Dissertation

submitted to the

Combined Faculty of Mathematics, Engineering and Natural Sciences

of Heidelberg University, Germany

for the degree of

Doctor of Natural Sciences

Put forward by

Ido Siovitz

born in: Haifa, Israel

Oral examination: October 28, 2025

UNIVERSAL SCALING AND EMERGENT SYMMETRIES IN A SPIN-1 BOSE GAS FAR FROM EQUILIBRIUM

Ido Siovitz

Referees: Prof. Dr. Thomas Gasenzer

Prof. Dr. Tilman Enss

“You know,” said Arthur thoughtfully,
“all this explains a lot of things.
All through my life I’ve had this strange unaccountable feeling
that something was going on in the world, something big, even sinister,
and no one would tell me what it was.”

“No,” said the old man,
“that’s just perfectly normal paranoia.
Everyone in the Universe has that.”

— Douglas Adams, “ Hitchhiker’s Guide to the Galaxy “

ABSTRACT

Quantum many-body systems driven far from equilibrium can show universal self-similar scaling dynamics associated with an approach to a non-thermal fixed point. The characterisation of non-equilibrium universality classes remains an open problem. In this thesis, we investigate the far-from-equilibrium dynamics of a one-dimensional spin-1 Bose gas. First, we study its microscopic dynamics, identifying rogue waves in the velocity fields, which form real-time instantons in the transverse spin. Their statistics lead to an additional scaling exponent governing the time evolution of a characteristic timescale. We derive a low-energy effective field theory of the spin-1 gas, taking the form of a double sine-Gordon model for the spinor phase. This model accounts for the subdiffusive and diffusion-type scaling observed in the full microscopic theory. It demonstrates that scaling dynamics at non-thermal fixed points go beyond simple domain-size growth processes and connects the type of scaling behaviour to the occupation of the minima of the sinusoidal potential by the double sine-Gordon field. Numerical as well as experimental results support the validity of the effective model. Furthermore, we investigate the symmetry content of the spin-1 gas using symmetry witnesses derived from Ward identities. We show that the dynamical restoration of symmetry from an explicitly symmetry-broken state occurs long before thermalisation. We further demonstrate that different quenches can lead to two distinct non-thermal fixed points, each associated with a different emergent symmetry. Finally, three-dimensional simulations of a quasi-one-dimensional condensate reconcile the long-standing discrepancies between experimentally and numerically observed scaling exponents. These findings contribute to a deeper understanding of non-equilibrium physics, establishing a double sine-Gordon non-equilibrium universality class to which the spin-1 Bose gas belongs to, and underline the role of emergent symmetries in determining the non-thermal fixed point the system approaches.

ZUSAMMENFASSUNG

Quanten-Vielteilchensysteme, die weit aus dem Gleichgewicht getrieben werden, können eine universelle, selbstähnliche Skalierungsdynamik aufweisen, die mit einem nicht-thermischen Fixpunkt in Verbindung steht. Die Charakterisierung solcher Universalitätsklassen außerhalb des Gleichgewichts ist ein offenes Problem. Diese Arbeit untersucht die Dynamik eines eindimensionalen Spin-1 Bose Gases fernab vom Gleichgewicht. Die mikroskopische Dynamik des Gases wird analysiert, in der Kaustiken in den Geschwindigkeitsfeldern entstehen, die Echtzeit-Instantonen im transversalen Spin formen. Die Statistik der Instantonen lässt auf einen zusätzlichen Skalierungsexponenten schließen, der die Zeitentwicklung einer charakteristischen Zeitskala bestimmt. Eine effektive Feldtheorie des Spin-1 Bose Gases bei niedrigen Energien wird hergeleitet, was die Form einer erweiterten Sine-Gordon Theorie in der Spinorphase aufweist. Das effektive Modell gibt sowohl das subdiffusive als auch das diffusionsartige Skalierungverhalten der vollen mikroskopischen Theorie wieder. Aus der hergeleiteten Theorie wird geschlossen, dass die Skalierungsdynamik aufgrund eines nicht-thermischen Fixpunktes ein Phänomen ist, das über Domänenvergrößerungsprozesse hinausgeht. Der Wert des Skalierungsexponenten wird mit der Besetzung der Minima des periodischen Potentials durch das Sine-Gordon Feld verbunden. Numerische sowie experimentelle Ergebnisse bestätigen die Reduzierung der Dynamik auf das effektive Modell. Weiter wird der Symmetrieinhalt des Systems mithilfe von Ward-Identitäten untersucht und damit gezeigt, dass die dynamische Wiederherstellung der Symmetrie aus einem explizit symmetriegebrochenen Zustand viel schneller ist als die Thermalisierung. Es wird zudem gezeigt, dass durch unterschiedliche Anfangsbedingungen zwei verschiedene nicht-thermische Fixpunkten erreicht werden können, die jeweils mit einer anderen emergenten Symmetrie verbunden sind. Mit Hilfe dreidimensionaler Simulationen eines quasi-eindimensionalen Rubidiumkondensats wird die langjährige Diskrepanz zwischen den experimentell gemessenen und numerisch beobachteten Skalierungsexponenten erklärt. Die Ergebnisse dieser Arbeit tragen zu einem tieferen Verständnis der Nichtgleichgewichtsphysik bei, indem sie eine erweiterte Sine-Gordon Universalitätsklasse außerhalb des Gleichgewichts etablieren, zu der das Spin-1 Bose Gas gehört, und die Rolle emergenter Symmetrien bei der Bestimmung des nicht-thermischen Fixpunkts untermauern.

PUBLICATIONS

In this thesis, I present the findings of the following publications:

[1] I. Siovitz, S. Lannig, Y. Deller, H. Strobel, M.K. Oberthaler and T. Gasenzer *"Universal dynamics of rogue waves in a quenched spinor Bose condensate"*, Phys. Rev. Lett. **131**, 183402 (2023)

[2] I. Siovitz, A.-M. E. Glück, Y. Deller, A. Schmutz, F. Klein, H. Strobel, M.K. Oberthaler and T. Gasenzer *"Double sine-Gordon class of universal coarsening dynamics in a spin-1 Bose gas"* Phys. Rev. A. **112**, 023304 (2025)

[3] A.N. Mikheev, V. Noel, I. Siovitz, H. Strobel, M.K. Oberthaler and J. Berges *"Extracting the symmetries of nonequilibrium quantum many-body systems"*, SciPost Phys. **18**, 044 (2025)

In addition, I discuss results from ongoing work:

[4] Y. Deller, A. Schmutz, R. Schäfer, A. Flamm, F. Schmitt, I. Siovitz, T. Gasenzer, P.G. Kevrekidis, H. Strobel and M.K Oberthaler, *"Observation of sine-Gordon solitons in a spinor Bose-Einstein condensate"*

[5] I. Siovitz, L. Heck, V. Noel and T. Gasenzer *"Symmetry crossover in the universal scaling dynamics of a spin-1 Bose gas"*

For [1, 2], I formulated the core ideas and developed the theoretical frameworks. I performed all numerical simulations and subsequent numerical data analysis, carried out a large part of the analytical calculation and wrote most of the manuscript. In [3], I performed all numerical simulations and contributed to key ideas and discussions.

For [4], I derived the theory and provided key ideas. In [5], I performed the numerical simulations and data analysis, and discuss results from the Bachelor thesis of L. Heck, which I supervised.

Furthermore, publications in which I took part, but are not presented in this thesis:

[6] S. Lannig, M. Prüfer, Y. Deller, I. Siovitz, J. Dreher, T. Gasenzer, H. Strobel, M.K. Oberthaler *"Observation of two non-thermal fixed points for the same microscopic symmetry"*, arXiv:2306.16497

[7] A.N. Mikheev, I. Siovitz and T. Gasenzer *"Universal dynamics and non-thermal fixed points in quantum fluids far from equilibrium"*, Eur. Phys. J. Spec. Top. **232**, 3393–3415 (2023)

The latter being a review paper, upon which Sect. 2.1 is based on and some results from [1] are also presented.

CONTENTS

LIST OF FIGURES

INTRODUCTION

לא גמור , לא תמיד מכוון
השיר הזה מתחיל כאן

– Ehud Banai, "Yotze El Ha'Or"

The study of relaxation dynamics of closed quantum many-body systems quenched far away from equilibrium has seen increased interest in recent years. Physical settings include the evolution of the early universe after the inflation epoch [8–10], thermalisation and hadronisation of a quark-gluon plasma [11, 12], as well as the relaxation of ultracold atomic quantum gases in extreme conditions studied in table-top experiments [13–15]. A great variety of different scenarios has been proposed and observed, such as prethermalisation [16–23], generalised Gibbs ensembles [13, 21, 24–28], critical and prethermal dynamics [29–32], decoherence and revivals [33], dynamical phase transitions [34–38], many-body localisation [39–43], relaxation after quantum quenches in quantum integrable systems [44–46], wave turbulence [47–50], superfluid or quantum turbulence [51–54], universal scaling dynamics and the approach of a non-thermal fixed point [53–58], and prescaling in the approach of such a fixed point [59–62]. The broad spectrum of possible phenomena occurring during the evolution reflects many differences between quantum dynamics and the relaxation of classical systems.

Out of the many intriguing observed phenomena, the universal scaling dynamics of closed quantum many-body systems far from equilibrium has garnered special attention in modern research. This thesis investigates the self-similar scaling dynamics associated with an approach to a non-thermal fixed point, using numerical simulations of an ultracold spin-1 Bose gas. The central objective of this thesis is to deepen our understanding of universal non-equilibrium phenomena, with particular emphasis on the identification and characterisation of universality classes far from equilibrium.

Generally, universal scaling dynamics associated with a non-thermal fixed point is signalled by the self-similar spatio-temporal scaling of order-parameter correlations in the system. This framework significantly reduces the complexity of the time evolution far from equilibrium, where the dynamics of the two-point correlators can now be described by a universal scaling function and two universal exponents alone. Such an approach seeks to describe non-equilibrium universal phenomena as a generalisation of the notion of universality in equilibrium, where critical slowing down is observed near a phase transition, corresponding to a fixed point in the renormalisation group flow. In recent years, the research of non-equilibrium universality has seen extensive theoretical [17, 59, 60, 63–96], as well as experimental research [6, 18, 27, 31–33, 49–57, 97–101],

exploring the nature of universal spatio-temporal scaling of correlations, to a large part in the field of ultracold atoms, thus underlining the importance of universality in non-equilibrium physics. Although self-similar scaling behaviour can emerge from a plethora of physical phenomena, such as the conserved redistribution of collective excitations or the dynamics of topological excitations, the effective description remains universal, governed by only a few parameters. The universal nature of this phenomenon hence enables the study of otherwise experimentally inaccessible systems by investigating more controllable platforms, such as ultracold Bose gases.

Ultracold Bose gases offer many advantages as an experimental platform for exploring non-equilibrium dynamics in quantum many-body systems. Their high degree of experimental control makes them ideal quantum simulators, serving as well-controlled toy models to study fundamental physics under conditions that are often challenging to realise in other settings. Unlike high-energy systems, such as the quark-gluon plasma, where non-equilibrium dynamics must be resolved on extremely short timescales and measurements are typically limited to asymptotic output states, ultracold Bose gases allow direct and time-resolved access to equal-time correlation functions. This is possible in tabletop experiments, as opposed to the vast and highly specialised infrastructure required for particle accelerators in high-energy physics. The extraction of non-equilibrium equal-time correlations is enabled by the ability to repeat ultracold atom experiments with high precision, maintaining a high degree of control over experimental parameters such as atom number, temperature, and interaction strength. In particular, interaction strength can be finely tuned using Feshbach resonances, providing a powerful tool for probing how universal certain dynamical features truly are [101]. Furthermore, the ability of modern experiments to imprint spatial defects, such as solitons or vortices, opens a direct route to studying the influence of topological excitations on universal dynamics.

As in all fundamental theories in modern physics, symmetries play a central and crucial role in the description of the non-equilibrium dynamics of the system as well. Dating back to 1918, Emmy Noether had derived one of the most important aspects of symmetry, stating that each continuous symmetry of a physical model is associated with a conservation law [102]. Each conservation law is then associated with a conserved charge and current which obey a continuity equation. On the quantum level, Noether's theorem can be generalised, where now the continuous symmetries of the system imply a set of relations between correlations of the system. These are known as the Ward-Takahashi identities [103], or, for the non-Abelian case, as Slavnov-Taylor identities [104, 105]. However, in contrast to equilibrium, non-equilibrium physics require a subtle distinction between the symmetries of the quantum state and that of the microscopic model. This distinction raises important questions about the role of emergent symmetries, including the possibility of (asymptotically) restoring symmetries that are explicitly broken at the microscopic level.

Knowledge of the underlying (or emergent) symmetry of the system is crucial information for the derivation of effective field theories. These encapsulate the dominant mechanisms governing the non-equilibrium dynamics of the system. Quantum many-body systems, such as the spin-1 Bose gas handled in this thesis, often consist of many degrees of freedom, making a full analytical investigation of their non-equilibrium physics challenging. However, the universal scaling

dynamics often arises from only a subset of these degrees of freedom. For such cases, one may derive an effective theory for the relevant degrees of freedom from the microscopic model, thus simplifying the analytical analysis substantially. For example, in U(N) symmetric ultracold Bose gases, density fluctuations are strongly suppressed in the low-energy limit, while fluctuations in the complex phases dominate the dynamics, which show a rich excitation spectrum [106]. The low-energy effective theory of these models takes the form of a Luttinger liquid, where an analytical kinetic theory approach was able to predict the universal scaling exponents governing the self-similar scaling of correlations. Therefore, the reduction of a system's description to its low-energy effective theory may open a path to deeper analytical insights on the underlying mechanisms behind the universal behaviour.

In this thesis, we present numerical and analytical studies of the spin-1 Bose gas driven far out of equilibrium by a quench across a second-order phase transition from the polar phase to the easy-plane ferromagnetic phase, where the system is known to exhibit self-similar scaling of transverse spin correlations in one and two dimensions [55, 75, 77]. We show numerical simulations of the one-dimensional spin-1 Bose gas and observe the existence of rogue waves in the transverse spin degree of freedom. We employ the framework of propagating wavefronts in random media, where the noisy potential arises from the time-evolving spin-interaction terms of the underlying equations of motion. We find that, when considering additionally the spatio-temporal scaling of correlations, this framework gives rise to a second exponent which governs the coarsening of a timescale in the system. Furthermore, the rogue wave events are shown to be associated with topological real-time instanton defects, which take the form of vortices in space and time. To better understand these dynamics, we derive a low-energy effective theory for the system in the easy-plane phase, in the form of a double sine-Gordon model for the so-called spinor phase. This effective theory captures both types of scaling behaviours observed in the spinor gas, representing a significant simplification of the underlying complexity. Finally, using derived symmetry witnesses, we demonstrate the restoration of symmetry in the easy-plane phase from an initially symmetry-broken state. We explore the implications of this restoration for the system's non-equilibrium dynamics and propose the existence of a symmetry crossover, i.e., a transition in the effective symmetry that emerges when quenching to different points within the same quantum phase, or in other words, within the same microscopic symmetries of the Hamiltonian. We connect this crossover with two distinct scaling behaviours.

This thesis contributes to a deeper understanding of universal self-similar scaling dynamics far from equilibrium by employing effective descriptions to find the dominant mechanisms and addressing long-standing puzzles in the field. In particular, we find that the effective mapping of the spinor gas to a double sine-Gordon model places the universal dynamics into a sine-Gordon-type non-equilibrium universality class. It delivers an explanation for the anomalously slow scaling dynamics of the spinor gas and substantiates the difference between domain-size growth and self-similar scaling due to a non-thermal fixed point. Furthermore, we establish a direct connection between the dynamically emergent symmetry and distinct scaling behaviors. Finally, this work bridges the gap between experimental and numerical results obtained for the self-similar scaling in the one-dimensional spinor gas, offering an explanation as to the cause of this discrepancy.

OUTLINE OF THE THESIS

This thesis is organised in four parts, each covering a certain aspect of the far-from-equilibrium dynamics of the spin-1 Bose gas.

The first part introduces the theoretical background for this thesis.

Chapter 2 discusses the theoretical concepts for the various subjects in this thesis, starting with a comprehensive review of non-thermal fixed points. Then, the spin-1 Bose gas is introduced: its basic properties, mean-field description and various excitations. The theory of topology is briefly outlined. Finally, equal-time functional methods for non-equilibrium physics are presented.

Chapter 3 describes the numerical methods used for simulating the spin-1 Bose gas and the double sine-Gordon model. The concept of mass parallelisation on graphics processing units is briefly discussed.

In the second part, we consider the post-quench universal dynamics of the spin-1 Bose gas from the perspective of microscopic and effective theories.

Chapter 4 investigates the appearance of rogue wave excitations in the universal post-quench dynamics of the spin-1 gas. Their dominant timescale and its connection to the scaling of the correlations is studied. Then, the existence of real-time instantons in the system is discussed, showing that they follow the same spatial and temporal scaling given by the rogue waves.

Chapter 5 showcases that the double sine-Gordon model accounts for subdiffusive (i.e., slow) as well as diffusion-type scaling. It is derived as a low-energy effective model for the spinor phase of the spin-1 gas. Using this derivation, it is shown that pattern coarsening as seen in non-thermal fixed points can be a more intricate process than simple domain-size growth. The subdiffusive scaling is connected to the field configuration spreading across the sinusoidal potential.

In the third part, we turn to the discussion of symmetry identities and the aspects of symmetry in the far-from-equilibrium dynamics of the spin-1 Bose gas.

Chapter 6 explores the role of effective symmetries in non-equilibrium. Using a set of symmetry identities for a spontaneously broken SO(2) symmetry, it is shown that the dynamical restoration of symmetry in the system on the level of lower-order correlation functions occurs on a timescale which is much faster than the equilibration timescale. This approach is used to identify spontaneous symmetry breaking far from equilibrium on experimental data.

Chapter 7 presents results from work in progress, connecting to the subjects discussed in this thesis. A possible symmetry crossover in the spin-1 Bose gas is discussed, showcasing that the quench parameter controls the emergent symmetry and with it, the scaling behaviour. Finally, dimensional considerations are shown to significantly alter the scaling behaviour of the system within the quasi-one-dimensional regime, thus reconciling the long-standing discrepancy between theory and experiment.

In the fourth and final part, we summarise and give an outlook for the future in Chap. 8.

Part I

THEORETICAL BACKGROUND

2 THEORETICAL CONCEPTS

멈춰서도 괜찮아
아무 이유도 모르는 채 달릴 필요 없어

– BTS, "Paradise"

In this chapter, we briefly introduce and discuss the core theoretical concepts relevant for this thesis. The aim of this chapter is not to rigorously derive the methods used in this thesis, but to rather give a comprehensive overview of the key ideas of the employed frameworks. We begin by introducing the concept of non-thermal fixed points in Sect. 2.1. In Sect. 2.2, we shift our discussion to the main characteristics of the physical system with which we probe non-equilibrium dynamics of quantum many-body systems: the spin-1 Bose gas. There, we concentrate on the mean-field description of the system, discussing the mean-field phase diagram and the relevant quantum phase transition we will be utilising to bring the system out of equilibrium. We give the main results of Bogoliubov theory in the polar and easy-plane phases, discussing the dispersion relation for quasiparticle excitations for the two phases. We continue by introducing the relevant SU(2) subspaces, giving a useful tool for visualising the spin-1 gas dynamics. In Sect. 2.3, we briefly discuss the concept of topology, homotopy groups and winding numbers, giving the relevant examples of the spin-1 gas and the resulting instanton defects. We conclude this chapter by introducing the analytical framework of the equal-time functional methods of non-equilibrium dynamics in Sect. 2.4, deriving general symmetry identities with which we can probe the symmetry content of quantum many-body systems.

2.1 NON-THERMAL FIXED POINTS

A great part of the work done in this thesis was made with the aim to further the understanding of non-equilibrium universality, predominantly by considering the phenomenon of self-similar scaling of correlations far from equilibrium. Such power-law scaling of correlations has been observed in a variety of contexts, including wave-turbulence [47, 48], pattern coarsening dynamics [107] and driven-dissipative systems [108]. The plethora of systems which exhibit scaling has drawn researchers to search for a unifying framework to better handle this phenomenon and understand its implications. One such framework hypothesises the existence of so-called non-thermal fixed points (NTFP). In this section, we take it upon us to provide a detailed introduction to the concept of non-thermal fixed points, further going over recent developments in this field of research. This short introduction is based on [7], with some parts, such as the figure captions, taken verbatim.

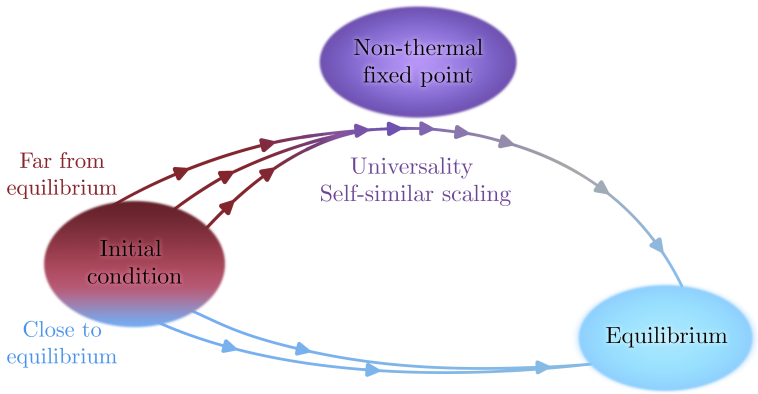

Figure 2.1: Schematics of a non-thermal fixed point, based on the ideas of a renormalisation group flow. For a range of initial conditions, a system brought out of equilibrium can approach an hypothesised non-thermal fixed point during its time evolution towards equilibrium. In the vicinity of such a fixed point, the system experiences a slowing down in the time evolution, (indicated by the tightly packed purple arrows) where correlation functions $C(k,t)$ show self-similar scaling behaviour in space and time according to $C(k,t) = t^{\alpha} f_{\mathrm{s}}(t^{\beta}k)$, with a universal scaling function f_{s} which depends on momentum alone. The scaling evolution is characterised by two universal scaling exponents α and β. Figure taken and adapted from [116].

The concept of non-thermal fixed points aims at generalising the well-known and celebrated concept of renormalisation group theory (RG) to a non-equilibrium framework [63, 109–113]. In equilibrium, or near it, the structure of the system is, in the RG framework, investigated under various spatial (or momentum) resolutions, i.e., the variation of the spatial scale upon which the system is observed [114, 115]. Considering correlation functions of the system, such as the two-point correlation function of two spatial points with a distance x between them, one finds that near a phase transition, the correlations retain their shapes, yet rescale according to $C(x;s) = s^{\zeta} f_{\mathrm{s}}(x/s)$, with some universal scaling function f_{s}. Hence, near or at criticality, the shape of the function does not depend on the resolution with which we observe the system. The exponent ζ is said to be universal for a class of systems, constituting a universality class, which is typically associated with the symmetry of the underlying Hamiltonian.

Quantitatively, in RG, one derives a so-called renormalisation flow, i.e., a set of differential equations which determine the change of the system with the spatial resolution. These differential equations show how the various couplings in the system's action change with the scale. One can then perform a fixed-point analysis, i.e., find where the differential equations vanish. There, the flow is said to stop, meaning that at every scale, the correlations of the system remain unaltered. At the fixed point, the system is scale independent and the universal scaling function takes the form of a pure power law. We note however that for realistic finite systems, there is always a scale present, such that a system can only approximately approach the fixed point. Performing a linearised analysis about the fixed points, one obtains, after some linear algebra, the scaling exponents of the various correlations w.r.t. the couplings. For further details, we refer the reader to [117, 118].

The generalisation of this approach to non-equilibrium physics leads to the consideration of real time t as the scale parameter. Adapting the same concepts as equilibrium RG, there should be some functional flow, where one may find a so-called non-thermal fixed point. Near such a fixed point, the correlations of the system scale self-similarly in time as $C(x,t) = t^{\tilde{\alpha}} f_s(t^{-\beta}x)$ with now two universal exponents $\tilde{\alpha}$ and β. In this case, one observes that a length scale of the system, the correlation length of the correlation function, scales as a power-law in time $\ell_\Lambda(t) \sim t^\beta$, i.e., the patterns in the system grow in size in time.

The strength of such a framework lies within its universal nature. It allows us to characterise various systems according to their *non-equilibrium universality class*, reducing the microscopic often very intricate and analytically inaccessible dynamics into a finite set of parameters given by the universal scaling function and the two universal exponents. Hence, should various systems belong to the same universality class, one is able to learn about one system while investigating the other, allowing for the study of experimentally inaccessible systems, such as the Universe, with the help of a tabletop experiment, e.g., an ultracold Bose gas.

In the following, we give a relevant example to gain better intuition to the notion of NTFPs in the area of ultracold gases: the three-dimensional one-component Bose gas after a strong cooling quench. The cooling quench here means that the initial condition of the occupation number $n(0,\boldsymbol{k})$ reflects a box distribution with some cutoff momentum scale Q, above which it vanishes

$$n(0,\boldsymbol{k}) = n_0\Theta(Q - |\boldsymbol{k}|). \tag{2.1}$$

This constitutes an extreme non-equilibrium initial condition, where the mode distribution is overoccupied in particular modes in contrast to the equilibrium distribution. Such an overpopulation results in a transport process of particles into lower momenta, i.e., towards the condensate, while the energy is transported to higher wavenumbers, see Fig. 2.2. This transport process is then captured by a universal function depending on momentum alone, which asymptotically reaches a power law. Interestingly, the transport in the infrared (IR) and ultraviolet (UV) result in a bidirectional scaling behaviour, meaning that there are two sets of universal exponents governing the transport of particles in the IR and energy in the UV, respectively. Each range of momenta shows the scaling of the occupation number w.r.t. some reference time t_{ref} according to $n(k,t) = (t/t_{\text{ref}})^\alpha n_s([t/t_{\text{ref}}]^\beta k)$, where the exponents α and β now govern the transport of particles and energy, respectively. The values of the scaling exponents α and β are constrained by global conservation laws in the underlying self-similar dynamics in the vicinity of a NTFP. Such laws lead to a relationship between the exponents, for example, quasi-particle conservation in the IR implies $\alpha = d\beta$, for d spatial dimensions.

The fact that, at later times, the entire transport process can be captured by a simple power-law behaviour in space and time reflects the universal nature of the time-evolution of the system, which exhibits the same behaviour, regardless of the exact initial condition. This behaviour can emerge from very different underlying physical configurations and processes, such as the conserved redistribution of quasiparticle excitations, e.g., as in weak wave turbulence [119, 120] but also by the reconfiguration of spatial patterns like magnetisation domains [121, 122] or by the annihilation of (topological) defects populating the system [65, 72]. Hence, even though the notion

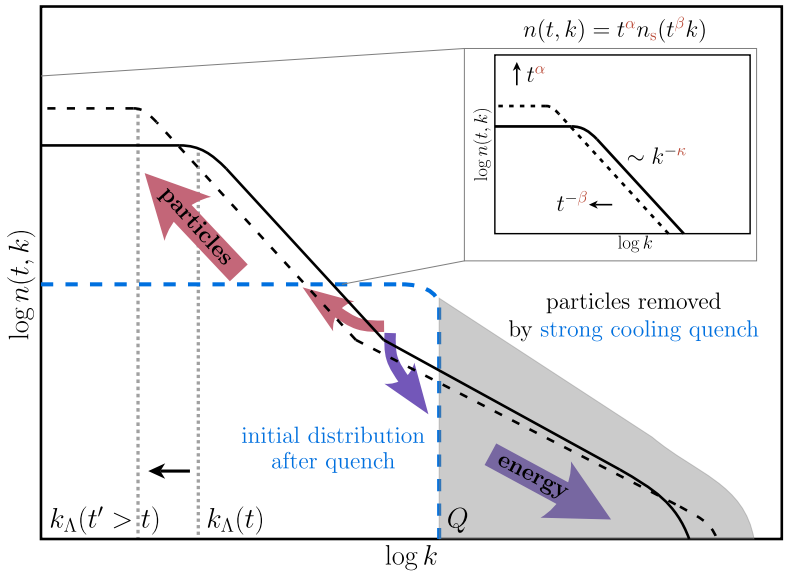

Figure 2.2: Sketch of self-similar scaling in time and space close to a non-thermal fixed point on a double logarithmic scale. The time evolution of the occupation number momentum distribution $n(k,t)$ of a Bose gas for two different times t is shown (solid and short-dashed line). Starting from an extreme initial distribution marked by the blue long-dashed line, being the result of a strong cooling quench, a bidirectional redistribution of particles in momentum space occurs as indicated by the arrows. Particle transport towards zero momentum as well as energy transport to large momenta are characterised by self-similar scaling evolutions in space and time according to $n(k,t) = (t/t_{\mathrm{ref}})^{\alpha} n_s([t/t_{\mathrm{ref}}]^{\beta} k)$, with universal scaling exponents α and β, in general, different for both directions. Here, t_{ref} is some reference time within the temporal scaling regime. The infrared transport (red arrow) conserves the particle number which is concentrated at small momenta when $\kappa \geq d$. In contrast, the energy, being concentrated at high momenta, where $\kappa' \leq d+2$, is conserved in the redistribution of short-wavelength fluctuations (purple arrow). Figure taken and adapted from [119].

of universality implies the characterisation of a system using only a few macroscopic parameters such as scaling exponents and the universal scaling function, the understanding of the microscopic processes governing the scaling of the system gives valuable insight into the possible types and characteristics of various non-equilibrium universality classes.

We note that pattern coarsening is also discussed thoroughly within the framework of phase-ordering kinetics [107], i.e., the dynamics after a quench across a phase transition. There, scaling laws are derived via the use of general phenomenological models stemming from the dynamics of domain walls of conserved and non-conserved fields in two or more spatial dimensions. These models make use of either diffusion-type equations, accounting for the scaling of a dominant length scale in the system with $\beta = 1/2$, or Cahn-Hilliard equations, accounting for conserved redistributions of excitations resulting in $\beta = 1/4$. The concept of non-thermal fixed points, though, goes beyond such theories, which it is expected to include as well.

Finding, characterising and understanding non-equilibrium universality classes, especially with regard to their self-similar scaling behaviour, is the subject of extensive research in experiment and theory and is largely an open problem. A major challenge in researching non-equilibrium phenomena comes from the fact that, in contrast to equilibrium studies, where only asymptotic in-

and output states are considered, non-equilibrium quantum field theories are formulated as initial value problems, with the initial density matrix playing a crucial role in the subsequent dynamics of the system. As a consequence, the derivation and solution of the full equations of motion for correlation functions out of equilibrium is a highly complicated and analytically cumbersome task, which requires the derivation and solution of equations of motion of unequal-time quantities known as Kadanoff-Baym equations [123].

Recent theoretical studies of non-thermal fixed points have tried to overcome the challenging nature of this problem, developing various frameworks to investigate and better understand non-equilibrium physics. Analytically, a *large-N kinetic theory approach* is used, based on the derivation of a Boltzmann-type equation for the occupation number distribution $\partial_t n(\boldsymbol{k}, t) = I[n](\boldsymbol{k}, t)$ of N-component field theories, where $I[n]$ is a scattering integral containing the occupation number self-energy, which can handled in a non-perturbative manner using a $1/N$ expansion of the two-particle irreducible (2PI) effective action for large-N [124]. This approach has been able to successfully predict scaling exponents observed in numerical studies [71, 119, 120]. In particular, the application of this approach to a derived *low-energy effective theory* for multi-component U(N) symmetric Bose gases has yielded the correct scaling exponents [106]. As a consequence, the use of analytically accessible effective models derived from the full microscopic theory allows one to pinpoint the relevant mechanisms underlying the scaling evolution and investigate the theory in a simplified manner. An especially interesting result derived from a kinetic theory concerns the scaling analysis for sine-Gordon-type theories. There, a resummation of the 2PI effective action considering infinite-order vertices has shown that, depending on the spread of the field configuration, two possible scaling solutions exist within the same system [85]. We finally note that a key aim for the analytical handling of NTFP sees the development of a functional renormalisation group theory encapsulating the flow to a non-thermal fixed point. Such a theory would provide a powerful tool to find NTFPs *a priori* on the grounds of symmetries, ultimately mapping all possible fixed points a system can reach. First steps into such a theory were made in [125], using the single-component Bose gas as a platform.

Numerical simulations of non-equilibrium dynamics provide an alternative means of investigating scaling phenomena far from equilibrium. In addition to confirming analytical predictions, they are able to expand upon the existing analytical framework and reveal phenomena which go beyond the analytical predictions. Such phenomena, such as distinctly subdiffusive scaling exponents, result from the dynamics of non-linear and topological excitations in the system. The aforementioned kinetic theory approach generically assumes the absence of such excitations to make predictions for the universal scaling behaviour of the system, concentrating on scaling phenomena driven by wave excitations manifested as, e.g., compressible phase fluctuations in Bose gases [106]. Numerical simulations of strong quenches give rise to strong non-linear and topological excitations dynamically, allowing for the discovery of new scaling solutions and the controlled investigation of strong excitations in the system. In various numerical studies, far-from-equilibrium universal scaling was observed in relativistic O(N) theories, as well as non-relativistic U(N) theories. A special focus of these numerical studies lies on understanding the difference between scaling phenomena associated with non-linear wave propagation, and the scal-

ing associated with the dynamics of topological defects. For example, in a two-dimensional single-component Bose gas it was found that for two different ensembles of vortex defects, two different scaling solutions are obtained. One subdiffusive with $\beta = 1/5$ and one with diffusion-type scaling $\beta = 1/2$ [72]. The former exponent was attributed to three-body-collision dynamics inside tightly packed vortex clusters, whereas the latter exponent was attributed to simple diffusion-type dynamics of random vortices. These findings were expanded to include the two-dimensional dipolar gas as well, showing the universal nature of this scaling phenomenon [96]. In relativistic O(N) theories, the use of persistent homology underlines the importance of topological defects in the possible scaling solution found in the system [86]. Recently, the role of quantised Kelvin waves in the scaling dynamics of an O(1) system in two and three spatial dimensions was discussed [87]. As a final, and very relevant example, the one-dimensional spin-1 Bose gas was found to exhibit bi-directional scaling of transverse spin correlations with a distinctly subdiffusive exponent $\beta = 1/4$ [75]. In contrast to the aforementioned systems, the correlations of a spin observable scale self-similarly and not the occupation number connected with the density of the condensate. In two dimensions, spin vortices in the spinor condensate were also found to give rise to self-similar scaling with $\beta = 1/2$ [77].

Experimentally, ultracold atom experiments show self-similar scaling after a quench of the system through a continuous phase transition. The investigation of a three-dimensional Bose gas after a cooling quench has shown self-similar scaling with exponents $\beta \approx 0.34$ and $\alpha \approx 3\beta = 1.15$ [54], while for the one-dimensional case, self-similar scaling with an anomalously slow exponent $\alpha = \beta \approx 0.1$ was found [56]. The numerical prediction of two distinct scaling behaviors depending on the distribution of vortices in a two-dimensional Bose gas was experimentally confirmed [53]. Utilising a quasi-one-dimensional spinor condensate, self-similar scaling far from equilibrium was shown for the system after a quench from the polar phase to the easy-plane phase with an exponent of $\beta = 1/2$ [55]. Recently, the same experiment has shown the possibility of several basins of attraction for various NTFPs within the same Hamiltonian. These basins are connected to different initial conditions, each leading to dynamics exhibiting different scaling behaviors [6].

To summarise, the scaling behaviour with time as a dynamical scaling parameter is found in many systems far from equilibrium. The spatio-temporal scaling of correlations is reminiscent of critical slowing down in equilibrium at a continuous phase transition, where correlations are shown to rescale in space as a power law in time. To a certain extent, slowed-down dynamics and scaling in the evolution time can be seen as a generalisation of the notion of universality in equilibrium critical phenomena, extending it into non-equilibrium systems. The main focus of this thesis is to deepen the understanding of NTFPs by investigating their connection to emergent symmetries in the dynamics of the system, using the knowledge to derive underlying effective theories which allow us to gain valuable insight into the mechanisms and characterisation of non-equilibrium universality classes.

2.2 SPIN-1 BOSE GAS

The far-from-equilibrium dynamics of multi-component spin-1 gases has been a subject of extensive numerical as well as experimental study due to the spin-dependent interactions present in the system, which give rise to intricate, non-trivial and unexplained phenomena in the non-equilibrium time evolution of the system. In this thesis, we use the spin-1 Bose gas as a platform to investigate, in detail, phenomena ranging from distinctly slow (or subdiffusive) scaling, to universal dynamics of rogue waves, as well as the restoration of symmetry in a time-evolving system out of equilibrium.

In the following, we briefly introduce the theoretical description of the spin-1 Bose gas. We give the Hamilton operator and discuss its terms in Sect. 2.2.1, followed by a discussion of the mean-field description, including the mean-field phase diagram in Sect. 2.2.2. We then continue to outline an effective low-dimensional description in Sect. 2.2.4. We give the main results of the Bogoliubov analysis of the spin-1 gas in the polar and easy-plane phases in Sect. 2.2.5 and conclude with a brief visual representation of the triplet state on two SU(2) subspaces. For an exhaustive review of spinor condensates, we refer the reader to [126, 127].

2.2.1 THE MODEL HAMILTONIAN OF THE SPIN-1 GAS

The spin-1 gas is described by a triplet state $\hat{\boldsymbol{\Psi}}(\boldsymbol{x},t) = \left(\hat{\Psi}_{-1}(\boldsymbol{x},t), \hat{\Psi}_0(\boldsymbol{x},t), \hat{\Psi}_1(\boldsymbol{x},t)\right)^T$, where each component represents one of the three magnetic sub-levels $m_\mathrm{F} \in \{-1,0,1\}$ of the $F = 1$ spin manifold. The three bosonic field operators, corresponding each to their respective magnetic sub-level, satisfy the bosonic commutation relations

$$\left[\hat{\Psi}_i(\boldsymbol{x},t), \hat{\Psi}_j(\boldsymbol{y},t)\right] = \left[\hat{\Psi}_i^\dagger(\boldsymbol{x},t), \hat{\Psi}_j^\dagger(\boldsymbol{y},t)\right] = 0, \tag{2.2}$$

$$\left[\hat{\Psi}_i(\boldsymbol{x},t), \hat{\Psi}_j^\dagger(\boldsymbol{y},t)\right] = \delta_{ij}\,\delta(\boldsymbol{x}-\boldsymbol{y}). \tag{2.3}$$

The Hamiltonian of the spin-1 Bose gas of particles with mass M reads as follows

$$\begin{aligned}\hat{H} = \int \mathrm{d}\boldsymbol{x} \Bigg\{ &\hat{\boldsymbol{\Psi}}^\dagger(\boldsymbol{x},t)\left[-\frac{\hbar^2}{2M}\nabla^2 + V(\boldsymbol{x}) + q f_z^2\right]\hat{\boldsymbol{\Psi}}(\boldsymbol{x},t) \\ &+\frac{1}{2}c_0 :\hat{n}^2(\boldsymbol{x},t): + \frac{1}{2}c_1 :\hat{\boldsymbol{F}}^2(\boldsymbol{x},t):\Bigg\},\end{aligned} \tag{2.4}$$

where :: denotes normal ordering and we have defined the number density operator

$$\hat{n}(\boldsymbol{x},t) = \hat{\boldsymbol{\Psi}}^\dagger(\boldsymbol{x},t)\hat{\boldsymbol{\Psi}}(\boldsymbol{x},t), \tag{2.5}$$

accounting for density-density interactions with coupling strength c_0 and the spin density operator

$$\hat{\boldsymbol{F}} = \hat{\boldsymbol{\Psi}}^\dagger(\boldsymbol{x},t)\cdot\boldsymbol{f}\cdot\hat{\boldsymbol{\Psi}}(\boldsymbol{x},t), \tag{2.6}$$

where the vector $\boldsymbol{f} = (f_x, f_y, f_z)$ contains the three generators of the $\mathfrak{so}(3)$ Lie algebra in the three-dimensional, $F = 1$ fundamental representation

$$f_x = \frac{1}{\sqrt{2}}\begin{pmatrix} 0 & 1 & 0 \\ 1 & 0 & 1 \\ 0 & 1 & 0 \end{pmatrix}, \qquad f_y = \frac{\mathrm{i}}{\sqrt{2}}\begin{pmatrix} 0 & -1 & 0 \\ 1 & 0 & -1 \\ 0 & 1 & 0 \end{pmatrix}, \qquad f_z = \begin{pmatrix} 1 & 0 & 0 \\ 0 & 0 & 0 \\ 0 & 0 & -1 \end{pmatrix}. \tag{2.7}$$

The spin density operator is a SO(3) symmetric interaction term, breaking the U(3) symmetry of a spin-1 Hamiltonian subject to density-density interactions alone. It describes spin changing collisions with a coupling strength c_1, which in turn lead to an especially intricate non-linear dynamic in the system. Allowing for scattering channels with even total spin only, the two couplings constants are given, assuming pure contact interactions, by

$$c_0 = \frac{4\pi\hbar^2(a_0 + 2a_2)}{3M}, \qquad c_1 = \frac{4\pi\hbar^2(a_2 - a_0)}{3M}, \tag{2.8}$$

where a_F are the corresponding s-wave scattering lengths for the $F = 0$ and $F = 2$ channels, respectively. The quadratic term containing q denotes the contribution from the quadratic Zeeman shift, governing the detuning between the $m_\mathrm{F} = 0$ and the $m_\mathrm{F} = \pm 1$ components. The spin-changing collisions and the quadratic Zeeman terms break the U(3) symmetry of the Hamiltonian into either a $\mathrm{U}(1)_\phi \times \mathrm{SO}(3)_f$ symmetry for $c_1 \neq 0$ and $q = 0$, or a $\mathrm{U}(1)_\phi \times \mathrm{SO}(2)_f$ symmetry for $c_1 \neq$ and $q \neq 0$, where all symmetries are to be understood as global symmetries. The subscripts ϕ and f denote that the symmetry lives in the condensate or spin sector, respectively. Note that strictly speaking, a term linear in f_z representing the linear Zeeman effect should also appear in the Hamiltonian. This term can be absorbed into the fundamental fields by considering a rotating frame of reference.

Finally, the term $V(x)$ accounts for an external trapping potential, which must be present in every realistic experimental setting. The exact shape of the potential is determined by the trap geometry and can take on several forms, where most common trap utilised is an harmonic trap, leading to a spatially inhomogeneous Thomas-Fermi density profile.

2.2.2 MEAN-FIELD DESCRIPTION

In this thesis, we mainly study the far-from-equilibrium dynamics of the spinor gas by means of numerical simulations. We employ a semi-classical, Monte-Carlo method known as the truncated Wigner approximation. Semi-classical methods make use of a mean-field description to propagate the classical equations of motion of the fields, whilst sampling quantum noise which is added to the initial condition, see Sect. 3.3 for more details. To guarantee the validity of such an approximation, one must ensure high occupations of the wave function, weak interactions in the Hamiltonian and very low temperature [128].

In the following, we outline the mean-field description of the spin-1 Bose gas. We plug in the mean-field values of the quantum operators in Eq. (2.4), $\psi_{m_\mathrm{F}}(\boldsymbol{x},t) = \left\langle \Psi_{m_\mathrm{F}}(\boldsymbol{x},t) \right\rangle = \sqrt{\rho_{m_\mathrm{F}}} e^{\mathrm{i}\varphi_{m_\mathrm{F}}} \in \mathbb{C}$, where ρ_{m_F} and φ_{m_F} denote the density and the complex phase of the wave function, respectively.

The mean-field spin-1 Hamiltonian then reads

$$H = \int \mathrm{d}\boldsymbol{x} \left\{ \psi^*(\boldsymbol{x},t) \left[-\frac{\hbar}{2M}\nabla^2 + V(\boldsymbol{x}) + q f_z^2 \right] \psi(\boldsymbol{x},t) + \frac{1}{2} c_0 n^2(\boldsymbol{x},t) + \frac{1}{2} c_1 \boldsymbol{F}^2(\boldsymbol{x},t) \right\}, \quad (2.9)$$

where the operators $n(\boldsymbol{x},t)$ and $\boldsymbol{F}(\boldsymbol{x},t)$ are defined as the mean-field analog to Eq. (2.5) and (2.6), respectively. The mean-field spin operators are defined as

$$F_x = \frac{1}{\sqrt{2}} \left[\psi_0^* (\psi_1 + \psi_{-1}) + \text{c.c.} \right], \quad (2.10)$$

$$F_y = \frac{\mathrm{i}}{\sqrt{2}} \left[\psi_0^* (\psi_1 - \psi_{-1}) + \text{c.c.} \right], \quad (2.11)$$

$$F_z = |\psi_1|^2 - |\psi_{-1}|^2, \quad (2.12)$$

where c.c. stands for the complex conjugate. Lastly, we obtain the classical equations of motion, the spin-1 Gross-Pitaevskii equations (GPEs) via a variation of Eq. (2.9) w.r.t. the conjugate field

$$\mathrm{i}\hbar \partial_t \psi_{m_\mathrm{F}}(\boldsymbol{x},t) = \frac{\delta H}{\delta \psi^*_{m_\mathrm{F}}}, \quad (2.13)$$

yielding a set of three coupled non-linear differential equations

$$\mathrm{i}\hbar \partial_t \psi(\boldsymbol{x},t) = \left[-\frac{\hbar^2}{2M}\nabla^2 + V(\boldsymbol{x}) + q f_z^2(\boldsymbol{x},t) + \frac{1}{2} c_0 n(\boldsymbol{x},t) + \frac{1}{2} c_1 \boldsymbol{F}(\boldsymbol{x},t) \cdot \boldsymbol{f} \right] \psi(\boldsymbol{x},t). \quad (2.14)$$

2.2.3 MEAN-FIELD PHASE DIAGRAM

The U(3) symmetry breaking terms, given by q and c_1, respectively, give rise to rich dynamics in the system, as the particle interchange between the various magnetic sublevels and the strength of the detuning of these collisions result in a phase diagram spanned by the two couplings. In other words, the terms containing q and c_1 are energy scales determining the ground state of the system, i.e., the preferred spin configuration. The resulting mean-field phase diagram for a homogenous gas exhibits four ground states of the system, each representing a different quantum phase separated by first-order quantum phase transition lines, with the exception of the phase transition between the easy-plane and polar phase, which is of second order.

Easy-axis phase

For ferromagnetic interactions, i.e., $c_1 < 0$ and a negative quadratic Zeeman shift $q < 0$, the system shows a spontaneously broken $\mathbb{Z}_2$ symmetry w.r.t. the magnetisation in F_z direction. This

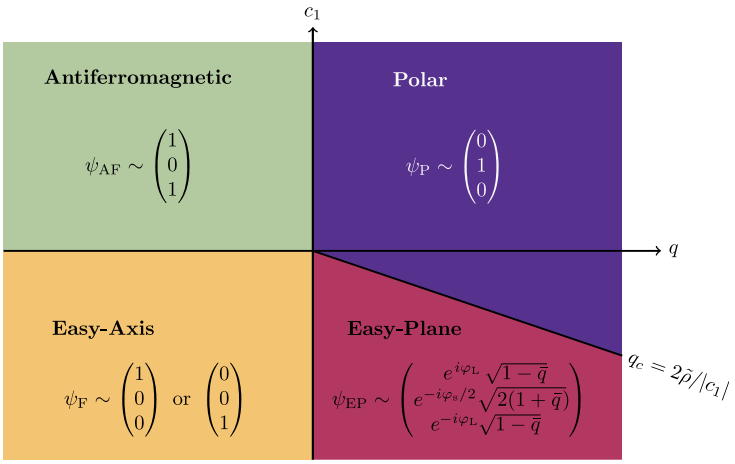

Figure 2.3: Mean-field phase diagram of the spin-1 Bose gas in absence of a trapping potential and $\langle F_z \rangle = 0$. Note that this implicitly accounts for the degeneracy of the ground state in the easy-axis phase. For $c_1 > 0$ and $q > 0$, the system is in the polar phase, whereas for $c_1 > 0$ and $q < 0$, the system is in the antiferromagnetic phase. The first-order quantum phase transition occurs at $q = 0$. For ferromagnetic interactions, i.e., $c_1 < 0$, three phases exist. In case of $q > 2\tilde{\rho}|c_1| = q_{\mathrm{c}}$, the system is still in the polar phase. Lowering q across the second-order transition line, $0 < q < q_{\mathrm{c}}$, the system finds itself in the easy-plane phase. Note that $\bar{q} = q/q_{\mathrm{c}}$. For $q < 0$, it is in the easy-axis phase, where the first-order transition is at $q = 0$.

leads to an arbitrarily chosen ground state which is fully magnetised in the $F_z = \pm 1$ direction. The spinor thus reads

$$\psi_{\mathrm{F}} = e^{\mathrm{i}\theta}\sqrt{\tilde{\rho}}\begin{pmatrix} 1 \\ 0 \\ 0 \end{pmatrix}, \quad \text{or} \quad \psi_{\mathrm{F}} = e^{\mathrm{i}\theta}\sqrt{\tilde{\rho}}\begin{pmatrix} 0 \\ 0 \\ 1 \end{pmatrix}, \tag{2.15}$$

where θ is a global U(1) phase of the system and $\tilde{\rho}$ is the homogeneous mean-field total density of the condensate.

Anti-ferromagnetic phase

For $c_1 > 0$ and $q < 0$, the condensate is in a state of complete symmetric occupation of the $m_{\mathrm{F}} = \pm 1$ modes, thus leading to a vanishing total magnetisation $\langle |\boldsymbol{F}| \rangle = 0$. The spinor takes the form

$$\psi_{\mathrm{AF}} = \sqrt{\tilde{\rho}}\begin{pmatrix} e^{\mathrm{i}\varphi_1} \\ 0 \\ e^{\mathrm{i}\varphi_{-1}} \end{pmatrix}. \tag{2.16}$$

Polar phase

For $c_1 > 0$, and $q > 2\tilde{\rho}|c_1| =: q_c$, the system is characterised by a macroscopic occupation of the $m_F = 0$ component, also leading to a vanishing total magnetisation $\langle |\boldsymbol{F}| \rangle = 0$:

$$\psi_P = e^{i\theta}\sqrt{\tilde{\rho}}\begin{pmatrix}0\\1\\0\end{pmatrix}. \tag{2.17}$$

Easy-plane phase

Lastly, As the system approaches $q = q_c$ from the polar phase, the spin changing collisions become resonant, allowing for scattering processes which transfer particles from the $m_F = 0$ component to the $m_F = \pm 1$ components. At this point, the system undergoes a second-order phase transition into the easy-plane phase. Therefore, for $c_1 < 0$ and $0 < q < q_c$, the SO(2) symmetry of the system is spontaneously broken [126, 129], leading to a redistribution of atoms between the components. In the mean field, we expect symmetric occupations of the $m_F = \pm 1$ components with a relative phase, $\varphi_L = (\varphi_1 - \varphi_{-1})/2$, known as the Larmor phase, and a finite occupation of the $m_F = 0$ mode. The ground state reads

$$\psi_{EP} = \sqrt{\tilde{\rho}}\frac{e^{i\theta/2}}{2}\begin{pmatrix} e^{i\varphi_L}\sqrt{1-q/q_c} \\ e^{-i\varphi_s/2}\sqrt{2(1+q/q_c)} \\ e^{-i\varphi_L}\sqrt{1-q/q_c}\end{pmatrix}. \tag{2.18}$$

Notice that we have defined the phase of the $m_F = 0$ component to be the so-called spinor phase $\varphi_s = \varphi_1 + \varphi_{-1} - 2\varphi_0$, after taking out a global phase $\theta = \varphi_1 + \varphi_{-1}$. This specific choice of variables serves the discussion in Chap. 5. In the easy-plane phase, the dynamics of the system are restricted to the F_x-F_y plane, and the system exhibits no magnetisation in the F_z direction. The spontaneously broken SO(2) symmetry (which is isomorphic to U(1)) leads to a complex scalar order parameter known as the transverse spin

$$F_\perp = F_x + iF_y = \sqrt{2}\left(\psi_1^*\psi_0 + \psi_0^*\psi_{-1}\right), \tag{2.19}$$

with a q-dependent mean-field spin length

$$|F_\perp|/\tilde{\rho} = \left(1 - \bar{q}^2\right)^{1/2}, \tag{2.20}$$

with

$$\bar{q} = \frac{q}{q_c} = \frac{q}{2\tilde{\rho}|c_1|} = 1 - \frac{4n}{\tilde{\rho}}, \quad n = \left\langle \frac{|\psi_{-1}|^2 + |\psi_1|^2}{2} \right\rangle. \tag{2.21}$$

2.2.4 ONE-DIMENSIONAL DESCRIPTION

The focus of this thesis lies on the quasi-one-dimensional spinor Bose-Einstein condensate (BEC). The term quasi-one-dimensional refers to the experimental reality that quantum gases in realistic settings can only take an effectively one-dimensional form, keeping the transversal extent of the system minimal. Numerically, we have the freedom of choice to either simulate a true one-dimensional setting by considering only a one-dimensional numerical grid, or to recreate the experimental setting by simulating a highly anisotropic three-dimensional grid, elongating the BEC along the longitudinal direction (here chosen to be x). Simulating a true one-dimensional system requires an adjustment of the aforementioned mean-field description to accommodate for the change in dimensionality.

Experiments typically employ a strong harmonic trap, setting the transversal trap frequencies to be large enough, such that an effectively one-dimensional description is suitable. Consider a harmonic potential

$$V(\boldsymbol{x}) = \frac{1}{2}\omega_\perp^2 r^2 + \frac{1}{2}\omega_\parallel^2 x^2, \tag{2.22}$$

where $r = y^2 + z^2$, and $\omega_{\perp,\parallel}$ are the harmonic trap frequencies in the transverse and longitudinal direction, respectively. The condition for an effective one-dimensional description is

$$\hbar\omega_\perp \gg \tilde{\rho}|c_0|,\ \tilde{\rho}|c_1|. \tag{2.23}$$

Alternatively, we may write down the criterion in terms of the density healing length $\xi = (2M\tilde{\rho}c_0)^{-1/2}$ and the spin healing length $\xi_s = (2M\tilde{\rho}|c_1|)^{-1/2}$, by demanding that the oscillator length in the transverse direction $a_\perp = \sqrt{\frac{\hbar}{M\omega_\perp}}$ be much smaller than the relevant length scales

$$a_\perp \ll \xi, \xi_s. \tag{2.24}$$

This effectively freezes the dynamics in the transverse direction. By further demanding that the longitudinal trap frequency $\omega_\parallel$ is much smaller than the transverse trap frequency $\omega_\perp$, we achieve an elongated trap geometry. When these conditions are satisfied, the wave-function in the transverse directions can be treated as being in the ground state of the harmonic oscillator, i.e., takes the form of a Gaussian. We can then perform the Gaussian integrals in the transverse directions and obtain the GPE with modified density and spin couplings

$$c_{0,1}^{1D} = \frac{c_{0,1}}{2\pi a_\perp^2}. \tag{2.25}$$

2.2.5 BOGOLIUBOV THEORY

In the following, we give a brief introduction into the spin-1 Bogoliubov theory, i.e., a beyond-mean-field theory encapsulating small field fluctuations, here in the absence of trapping poten-

tials. Expanding the Hamiltonian (2.4) to second order in the fields at non-vanishing momenta $k \neq 0$, we obtain an eigenvalue problem known as the Bogoliubov de-Gennes equations. Solving these equations, i.e., diagonalising the second-order Hamiltonian in momentum space, leads to quasi-particle dispersion relations for the various degrees of freedom of the spin-1 Bose gas. In particular, we concentrate on both the polar and easy-plane phase dispersions. We begin with the polar phase Bogoliubov spectrum, for which we now give a short outline of its derivation. For a more detailed discussion, see Ref. [126].

First, we write the wave functions of the magnetic components as

$$\hat{\psi}_{m_\mathrm{F}} = \frac{1}{\sqrt{\Omega}} \sum_{\boldsymbol{k}} \hat{a}_{\boldsymbol{k},m_\mathrm{F}} e^{i\boldsymbol{k}\boldsymbol{x}}, \tag{2.26}$$

where Ω denotes the volume of the system and the coefficients $\hat{a}_{\boldsymbol{k},m_\mathrm{F}}$ are the bosonic annihilation operators of the m_F-th magnetic sub-level with wave vector $\boldsymbol{k}$. Demanding that most of the particles are found in the condensate, i.e., in the $|\boldsymbol{k}| = 0$ mode, we can write the fixed particle number as a sum of creation and annihilation operators, where we consider the occupation of higher modes to be very small

$$N_0 + \sum_{\boldsymbol{k}\neq 0} \sum_{m_\mathrm{F}} \hat{a}^\dagger_{\boldsymbol{k},m_\mathrm{F}} \hat{a}_{\boldsymbol{k},m_\mathrm{F}} = N. \tag{2.27}$$

We now define annihilation and creation operators of the spin degrees of freedom via superpositions of the fundamental operators as

$$\hat{a}_{\boldsymbol{k},f_x} = \frac{1}{\sqrt{2}} \left(\hat{a}_{\boldsymbol{k},1} + \hat{a}_{\boldsymbol{k},-1}\right), \quad \hat{a}_{\boldsymbol{k},f_y} = \frac{\mathrm{i}]}{\sqrt{2}} \left(\hat{a}_{\boldsymbol{k},1} - \hat{a}_{\boldsymbol{k},-1}\right), \tag{2.28}$$

and plug these operators into the Hamiltonian, expanding up to second order

$$\begin{aligned} \hat{H}_\mathrm{BdG} = \frac{\Omega\tilde{\rho}^2 c_0}{2} + \sum_{\boldsymbol{k}\neq 0} \Bigg[& (\epsilon_k + \tilde{\rho}c_0)\hat{a}^\dagger_{\boldsymbol{k},0}\hat{a}_{\boldsymbol{k},0} + \frac{\tilde{\rho}c_0}{2}\left(\hat{a}^\dagger_{\boldsymbol{k},0}\hat{a}^\dagger_{-\boldsymbol{k},0} + \hat{a}_{\boldsymbol{k},0}\hat{a}_{-\boldsymbol{k},0}\right) \\ & + \sum_{f=f_x,f_y} \left\{ (\epsilon_k + q + \tilde{\rho}c_1)\hat{a}^\dagger_{\boldsymbol{k},f}\hat{a}_{\boldsymbol{k},f} + \frac{\tilde{\rho}c_1}{2}\left(\hat{a}^\dagger_{\boldsymbol{k},f}\hat{a}_{-\boldsymbol{k},f} + \hat{a}_{\boldsymbol{k},f}\hat{a}_{-\boldsymbol{k},f}\right) \right\} \Bigg], \end{aligned} \tag{2.29}$$

where $\epsilon_k = \hbar^2 k^2/2M$ and $\tilde{\rho} = N/\Omega$ is the homogeneous density. The obtained Hamiltonian can now be diagonalised in momentum space by solving the Bogoliubov de-Gennes equation, thus defining new quasi-particle annihilation and creation operators as

$$\hat{b}_{\boldsymbol{k},0} = \sqrt{\frac{\epsilon_k + \tilde{\rho}c_0 + \omega_{\boldsymbol{k},0}}{2\omega_{\boldsymbol{k},0}}}\hat{a}_{\boldsymbol{k},0} + \sqrt{\frac{\epsilon_k + \tilde{\rho}c_0 - \omega_{\boldsymbol{k},0}}{2\omega_{\boldsymbol{k},0}}}\hat{a}^\dagger_{-\boldsymbol{k},0}, \tag{2.30}$$

$$\hat{b}_{\boldsymbol{k},f} = \sqrt{\frac{\epsilon_k + q + \tilde{\rho}c_1 + \omega_{\boldsymbol{k},f}}{2\omega_{\boldsymbol{k},f}}}\hat{a}_{\boldsymbol{k},f} + \sqrt{\frac{\epsilon_k + q + \tilde{\rho}c_1 - \omega_{\boldsymbol{k},f}}{2\omega_{\boldsymbol{k},f}}}\hat{a}^\dagger_{-\boldsymbol{k},f}, \tag{2.31}$$

with energy eigenvalues $\omega_{\boldsymbol{k},0}$ and $\omega_{\boldsymbol{k},f}$. We then obtain the Bogoliubov de-Gennes Hamiltonian in the polar phase

$$\hat{H}_{\mathrm{BdG}} = E_0 + \sum_{\boldsymbol{k}\neq 0}\left[\omega_{\boldsymbol{k},0}\hat{b}^\dagger_{\boldsymbol{k},0}\hat{b}_{\boldsymbol{k},0} + \omega_{\boldsymbol{k},f}\left(\hat{b}^\dagger_{\boldsymbol{k},f_x}\hat{b}_{\boldsymbol{k},f_x} + \hat{b}^\dagger_{\boldsymbol{k},f_y}\hat{b}_{\boldsymbol{k},f_y}\right)\right], \tag{2.32}$$

with

$$\omega_{\boldsymbol{k},0} = \sqrt{\epsilon_{\boldsymbol{k}}(\epsilon_{\boldsymbol{k}} + 2\tilde{\rho}c_0)}\,, \tag{2.33a}$$

$$\omega_{\boldsymbol{k},f} = \sqrt{(\epsilon_{\boldsymbol{k}} + q)(\epsilon_{\boldsymbol{k}} + q + 2\tilde{\rho}c_1)} \tag{2.33b}$$

and E_0 is the ground state energy, which is regarded as a constant. We therefore obtain two dispersion relations, one for density phonons (2.33a) and one for transverse spin excitations (2.33b). Notice that the quasi-particle spectrum corresponding to density phonons is gapless, and due to $c_0 > 0$ does not give rise to any dynamical instabilities as we quench q. In contrast to that, the transverse spin spectrum is a gapped spectrum which can become imaginary when $q < q_{\mathrm{c}}$, thus indicating the phase transition between the polar phase and easy-plane phase. As we quench the system through the phase transition, dynamical instabilities will arise due to the Bogoliubov spectrum becoming imaginary, leading to unstable k modes in the transverse spin which grow exponentially. Such instabilities are the seed for the emergent structure in the post-quench dynamics of the system.

The easy-plane phase, on the other hand, shows a different dispersion relation. The spontaneous breaking of SO(2) and U(1) symmetry leads to the appearance of two Goldstone modes and a gapped mode. Solving the Bogoliubov de-Gennes equations for an easy-plane ferromagnetic condensate, we find the following dispersion relations

$$\omega_{k,0} = \sqrt{\epsilon_k(\epsilon_k + q)}\,, \tag{2.34a}$$

$$\omega_{k,\pm 1} = \sqrt{\epsilon_k^2 + (c_0 - c_1)\tilde{\rho}\epsilon_k + 2(\tilde{\rho}|c_1|)^2(1-\bar{q}^2) \pm \Lambda_k}\,, \tag{2.34b}$$

$$\Lambda_k = \sqrt{[(c_0 + 3c_1)\tilde{\rho}\epsilon_k - 2(\tilde{\rho}|c_1|)^2(1-\bar{q})]^2 + 4c_1(c_0 + 2c_1)\tilde{\rho}^2\bar{q}^2\epsilon_k^2}\,. \tag{2.34c}$$

The two Goldstone modes $\omega_{k,0}$ and $\omega_{k,-1}$ correspond to excitations in the Larmor phase φ_{L} and global phase θ, respectively, while the gapped mode corresponds to excitations in the transverse spin length, in particular excitations of the spinor phase φ_{s}. Notice that density fluctuations may also give rise to transverse spin length excitations, yet in the low-energy regime of an ultracold Bose gas, they are rendered subdominant compared to excitations of the complex phases. A visual representation of the excitations can be obtained from the transverse spin contribution in Eq. (2.9) which takes the form of a champagne bottle type potential landscape [130]. There, the Larmor phase, taking the role of a Goldstone mode, explores the valley of the transverse spin potential landscape, and the spinor phase, acting as a massive Higgs-type mode, goes up and down the valley.

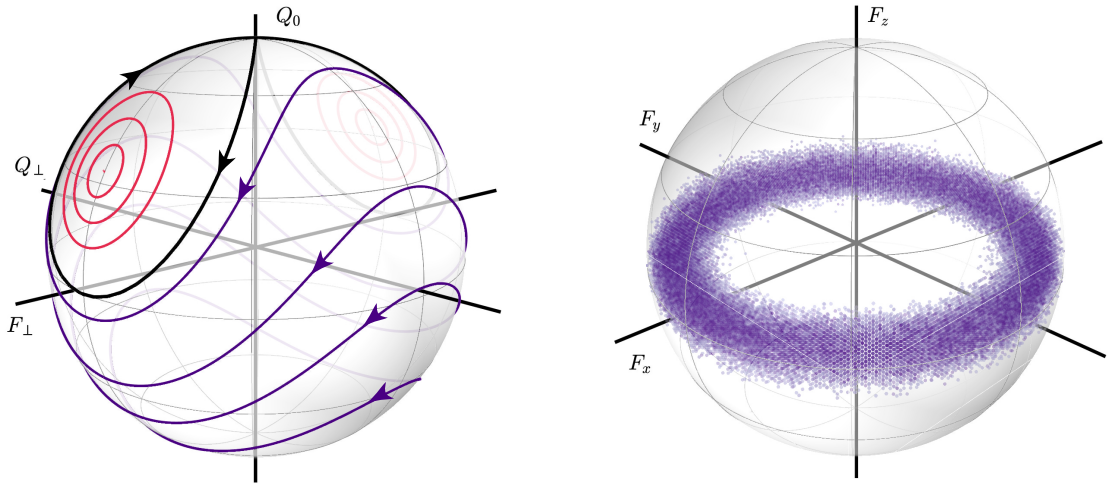

Figure 2.4: Spin and spin-nematic spheres. (Left) the spin-nematic sphere spanned by $\{F_\perp, Q_\perp, Q_0\}$. Mean-field single-mode trajectories are plotted on the surface. Near the fixed point of the Hamiltonian flow, the trajectories (red) oscillate about the mean transverse spin length. In black, the separatrix is shown. Beyond the separatrix, trajectories run across the sphere (purple). Such trajectories allow, e.g., for interpolation solutions like phase kinks in the spinor phase φ_s which describes the orientation angle in the $F_\perp$-$Q_\perp$ plane. (Right) The spin sphere spanned by $\{F_x, F_y, F_z\}$. In the easy-plane phase, the dynamics lead to the filling of the ring in the F_x-F_y plane due to the spontaneously broken SO(2) symmetry, with the orientation at each spatial point, i.e., the Larmor phase φ_L, chosen spontaneously. The thickness of the ring shows that F_z fluctuations are small as well as the spin length fluctuations are small.

2.2.6 SU(2) SUBSPACES

After having introduced the spin-1 gas in and beyond the mean field, we turn our the discussion to the full set of spin-1 observables. A spin-1 state can be fully represented by the $\mathfrak{u}(3)$ Lie algebra, constructed by eight generators, where we have already introduced three of these generators as the spin matrices (2.7). The remaining five are known as the nematic (or quadrupole) operators, defined as

$$\hat{Q}_{ij} = f_i f_j + f_j f_i - \frac{4}{3}\delta_{ij}. \tag{2.35}$$

A full characterisation of the density matrix of any state in the spinor system must include all 8 operators. Notice that in this section, we denote operators as $\hat{O}_i$ and their mean-field value as $O = \psi^\dagger \hat{O}_i \psi$.

Three relevant quadrupole operators, which span several important SU(2) subspaces are given by

$$\hat{Q}_{xz} = \frac{1}{\sqrt{2}}\begin{pmatrix} 0 & 1 & 0 \\ 1 & 0 & -1 \\ 0 & -1 & 0 \end{pmatrix}, \quad \hat{Q}_{yz} = \frac{i}{\sqrt{2}}\begin{pmatrix} 0 & -1 & 0 \\ 1 & 0 & 1 \\ 0 & -1 & 0 \end{pmatrix}, \quad \hat{Q}_{zz} = \begin{pmatrix} \frac{2}{3} & 0 & 0 \\ 0 & -\frac{4}{3} & 0 \\ 0 & 0 & \frac{2}{3} \end{pmatrix}. \tag{2.36}$$

For convenience, we shift the $\hat{Q}_{zz}$ operator by a constant to center it around the $m_F = 0$ component, thus defining a new operator

$$\hat{Q}_0 = -\frac{1}{3}\mathbb{1}_3 - \hat{Q}_{zz} = \begin{pmatrix} -1 & 0 & 0 \\ 0 & 1 & 0 \\ 0 & 0 & -1 \end{pmatrix}, \quad Q_0 = \rho_0 - \rho_1 - \rho_{-1}. \tag{2.37}$$

We now further define the transverse spin and transverse quadrupole operators for a given Larmor phase, i.e., the spin orientation in the F_x-F_y plane,

$$\hat{F}_\perp = \cos(\varphi_L) f_x + \sin(\varphi_L) f_y \,, \tag{2.38}$$

$$\hat{Q}_\perp = \cos(\varphi_L)\hat{Q}_{yz} - \sin(\varphi_L)\hat{Q}_{xz} \,. \tag{2.39}$$

The so-defined three operators fulfil the SU(2) commutation relations under the assumption that the probabilities of finding particles in the $m_F = \pm 1$ states are equal, i.e., $\langle F_z \rangle = 0$ [131], which is the case for the polar and easy-plane phases [126]. Hence, in addition to the spin commutation relations for the spin matrices $[f_i, f_j] = 2i\epsilon_{ijk} f_k$, the following identities hold

$$[\hat{Q}_0, \hat{Q}_\perp] = 2i\hat{F}_\perp, \quad [\hat{F}_\perp, \hat{Q}_0] = 2i\hat{Q}_\perp, \quad [\hat{Q}_\perp, \hat{F}_\perp] = 2i\hat{Q}_0. \tag{2.40}$$

With that, we obtain two SU(2) subspaces, which can be represented on their respective SO(3) spheres. The visualisation of the spin state in this manner is helpful in understanding the processes in the post-quench dynamics of the spinor gas. In the following, we give a short visual overview of the states on these two spheres (see Fig. 2.4), while a detailed discussion is found in Chap. 4 and Chap. 5.

A state in the polar phase can be seen as a coherent distribution beginning on the north pole of the spin-nematic sphere (left panel of Fig. 2.4), while the spin configuration is in the origin of the spin sphere (right panel of Fig. 2.4), reflecting an SO(2) symmetric state. The main discussion point in this thesis, though, is dynamics in the easy-plane phase, concentrating on the dynamics of both the Larmor and spinor phases, each representing the orientation angle in the F_x-F_y and $F_\perp$-$Q_\perp$ planes, respectively. On the spin sphere in the easy plane, one finds a well defined q dependant transverse spin length with an arbitrarily chosen orientation in the F_x-F_y plane, reflecting the spontaneously broken SO(2) symmetry. In particular, after a quench from the polar phase, the field probability distribution results in a thin torus distribution, where F_z excitations are strongly suppressed, see purple distribution on the right panel of Fig. 2.4. To gain intuition as to the dynamics on the spin nematic sphere, we compute mean-field single-mode trajectories of a particle subject to a Hamiltonian given by the spin-interaction term of Eq. (2.4), See Ref. [131, 132] for more details. We obtain two possible fixed points, corresponding to the q-dependent transverse spin length. Other than the fixed points, we find two kinds of possible trajectories on the sphere: closed oscillations about the fixed points, shown as red lines in Fig. 2.4 and 'runaway' open trajectories shown as purple lines in Fig. 2.4 which traverse the sphere. Hence, in the easy-plane phase, we expect the probability distribution of the field configuration to be centred around the fixed

points, reflecting weak fluctuations of the spin length. We note though that the open trajectories give rise to the possible formation of, e.g., phase defects in the spinor phase such as phase kinks interpolating between the two fixed points.

2.3 TOPOLOGY

As often discussed in the context of pattern coarsening and phase-ordering kinetics, topological excitations play a central role in the analysis of scaling phenomena. Often, the redistribution and annihilation of these objects leads to the time evolution of a dominant length scale in the system, typically identified as the mean defect distance [53, 72, 86, 87, 96]. In the following, we briefly outline the concepts of topology and apply them to the spin-1 gas to obtain the possible topological excitations in the system. Here, the symmetry, or rather the broken symmetry of the system plays a major role. For a comprehensive discussion of the topic, we refer the reader to Ref. [133, 134].

2.3.1 HOMOTOPY THEORY

Homotopy groups are fundamental constructs in topology. Broadly speaking, they classify equivalence classes of continuous maps from spheres into a topological space Y, often based at a point in a space X. Concretely, let X and Y be two manifolds without boundary. Two maps $\Psi_1 : X \mapsto Y$, $\Psi_2 : X \mapsto Y$ are called *homotopic* if there exists a continuous map

$$\tilde{\Psi} : X \times [0,1] \mapsto Y, \tag{2.41}$$

with a parameter τ in the interval $[0,1]$ such that $\tilde{\Psi}|_{\tau=0} = \Psi_1$ and $\tilde{\Psi}|_{\tau=1} = \Psi_2$. In other words, two maps are said to be homotopic if they may be continuously deformed into each other. Such a relation represents an equivalence relation, and hence a set of homotopic maps constitute an *homotopy class*. Since most of the discussions in this thesis concentrate on a one-dimensional periodic system, we define the base manifold X to be the unit circle S^1. We further denote the set of homotopy classes of based maps $\Psi : \mathrm{S}^1 \mapsto Y$ by $\pi_1(Y)$, commonly referred to as the *fundamental homotopy group*. The identity element is the constant map $\mathrm{S}^1 \mapsto y_0$, where y_0 a fixed base point on the manifold Y. If every loop in Y can be continuously deformed to y_0, then $\pi_1(Y)$ is said to be homotopic to the identity element, and the group is trivial, which is denoted by $\pi_1(Y) = 0$. A relevant physical example of such a construction would be field configurations in the system, which can be continuously mapped to the ground state of the system. Such field configurations may be long-lived and highly non-linear, but they are not protected by any topological considerations.

This thesis mainly discusses broken $\mathrm{SO}(2)$ or $\mathrm{U}(1)$ symmetries. Hence, we now specify Y to also be the unit circle S^1, the manifold of the aforementioned Lie groups. One can show that the fundamental homotopy group is given by

$$\pi_1(\mathrm{S}^1) = \mathbb{Z}, \tag{2.42}$$

where each homotopy class is characterised by one integer also known as a winding number. For completeness, we give a central result concerning possible homotopy classes:

$$\pi_n(S^m) \cong \begin{cases} \mathbb{Z} & \text{if} \quad m = n \geq 1 \\ 0 & \text{if} \quad m > n \geq 1. \end{cases} \tag{2.43}$$

Geometrically speaking, one is not able to wrap an m sphere by going over an n sphere with $n < m$. The case of $n > m$ is not trivial and should be investigated for each case by itself. This relation, for example, shows the existence of spin vortices in the Larmor phase of a two-dimensional spin-1 Bose gas in the easy plane.

2.3.2 HOMOTOPY GROUPS OF THE SPIN-1 BOSE GAS

To find the possible homotopy groups of the spinor BEC, we must consider the so-called vacuum manifold of each phase of interest. That is, the manifold $\mathcal{V}$ spanned by the possible ground-state field configurations. Mathematically speaking, the field configuration defines a map from the unit sphere S^{d-1}, where d is the spatial dimension, to the ground-state submanifold $\mathcal{V} \subset \mathbb{R}^n$

$$\psi : S^{d-1} \mapsto \mathcal{V}. \tag{2.44}$$

Hence, the homotopy class determining the topological nature of a field ψ is given by $\psi \in \pi_{d-1}(\mathcal{V})$.

Notice that given a single ground state, the manifold $\mathcal{V}$ is a single point, meaning that the homotopy class is necessarily the trivial one. This is the case for a symmetric system (e.g., a Bose gas above the critical temperature, or the spinor gas in the polar phase). If the symmetry is spontaneously broken, the ground state manifold takes a non-trivial configuration, typically a $n-1$-sphere in many physical systems. Thus, the homotopy group is given by $\pi_{d-1}(S^{n-1})$. This heavily restricts the possible topological excitations in the system given its dimensionality and possible ground states, as seen in Eq. (2.43).

The spin-1 gas quenched from the polar phase to the easy-plane phase results in a spontaneously broken SO(2) symmetry in spin space. Furthermore, since we consider dynamics at zero temperature, we find ourselves with a spontaneously broken U(1) symmetry, reflecting condensation. Hence, the order parameter manifold, or manifold of broken symmetries, is

$$\mathcal{V}^{\mathrm{EP}} = \mathrm{S}^1_{f_z} \times U(1)_\phi, \tag{2.45}$$

where the index f_z indicates that the broken symmetry is w.r.t. the spin in z direction, i.e. rotations in the F_x-F_y plane, governed by the Larmor phase φ_{L}. Therefore, in one spatial dimension, we find field configurations in the Larmor phase with non-trivial winding numbers, as given by the homotopy group

$$\pi_1(\mathcal{V}^{\mathrm{EP}}) = \mathbb{Z}. \tag{2.46}$$

This winding number constitutes a topological charge, which can be derived by a conserved topological current constructed from the spatial variation of the order parameter. For a one-dimensional system, the topological current j^μ associated with the phase field $\varphi_\mathrm{L}(x)$ can be defined as

$$j^\mu = \frac{1}{2\pi}\epsilon^{\mu\nu}\partial_\nu\varphi_\mathrm{L}, \tag{2.47}$$

where $\epsilon^{\mu\nu}$ is the antisymmetric Levi-Civita tensor in two dimensions and μ and ν denote indices going over time and space. The conservation law $\partial_\mu j^\mu = 0$ follows identically, reflecting that the winding number is a topological invariant independent of the system's dynamics. Integrating the zeroth component of this current over space yields the winding number Q_w,

$$Q_\mathrm{w} = \int_0^L \mathrm{d}x\, j^0 = \frac{1}{2\pi}\int_0^L \mathrm{d}x\, \partial_x\varphi_\mathrm{L} \in \mathbb{Z}, \tag{2.48}$$

where L is the size of the system. Hence, Q_w counts how many times the phase φ_L winds around the circle S^1 as one moves along the spatial dimension. This integer classifies the distinct homotopy classes seen above and is robust against continuous deformations, serving as a fundamental descriptor of topological excitations.

2.3.3 INSTANTONS

In the previous section, we discussed the conservation of topological charges. While this is generally true in equilibrium, this does not necessarily hold true for non-equilibrium physics. In equilibrium, time is Wick-rotated into the imaginary plane, taking on a periodic nature. Hence, the topology of a space-time manifold is fundamentally changed, as the time dimension is now a standard Euclidean dimension.

In a Euclidean space-time manifold, topological defects named instantons exist, which, in imaginary time, interpolate between field configurations with different winding numbers. Due to the Euclidean nature of the system, the instanton charge is conserved like any other topological defect defining a winding number. In Minkowskian dynamics, time is a set with open boundary conditions, changing the topology of the space-time manifold. As a consequence, if one would be able to analytically continue the imaginary time instanton solution into real time, one would experience a change in winding number in the dynamics of the system, i.e., the topological charge is not conserved in real time. In this thesis, we discuss the appearance of real-time instantons in the post-quench dynamics of the spinor gas, as they appear as a result of rogue-wave excitations in the Larmor phase. In the following, we briefly outline the concepts of instantons using an imaginary-time Yang-Mills theory, i.e., pure gauge theory, to better acquaint ourselves with the notion of this special topological defect.

Consider a pure gauge field

$$A_\mu = -\mathrm{i}U(\boldsymbol{x})\partial_\mu U^\dagger(\boldsymbol{x}), \tag{2.49}$$

where $U(\boldsymbol{x})$ is an element of the Lie group of interest. We impose a condition that the pure gauge $U(\boldsymbol{x})$ reaches a constant value at spatial infinity to compactify the configuration space, allowing us to consider the gauge transformations as maps between spheres, as we have previously discussed. Consider the Euclidean Yang-Mills action

$$S_E = \frac{1}{4}\int \mathrm{d}^d x F_{\mu\nu}F^{\mu\nu}, \tag{2.50}$$

where $F_{\mu\nu} = \partial_\mu A_\nu - \partial_\nu A_\mu$. Pure gauge fields as defined by Eq. (2.49) minimise the Yang-Mills action and thus represent a vacuum state. A pure gauge field with winding number n can be defined by a pure gauge transformation $U_n(\boldsymbol{x})$, for example:

$$U_n(\boldsymbol{x}) = \exp\left(\mathrm{i}\pi n \frac{\boldsymbol{x}}{|\boldsymbol{x}|}\boldsymbol{T}\right), \tag{2.51}$$

$$A_\mu^{(n)} = -\mathrm{i}U_n(\boldsymbol{x})\partial_\mu U_n^\dagger(\boldsymbol{x}), \tag{2.52}$$

where $\boldsymbol{T}$ are the generators of the gauge group. Gauge transformations with $U_n(\boldsymbol{x})$ connect physically equivalent configurations via continuous transformations, thus equating the field configurations in the sense of an homotopy class. A continuous transformation from distinct vacuum states $A_\mu^{(n)}$ to $A_\mu^{(m)}$ with $m \neq n$ without leaving the pure gauge is, in fact, not possible. Therefore, any transformation interpolating between two such vacua must overcome an energy barrier, since the Yang-Mills action is minimised by pure gauges. Such transformations can be interpreted as tunnelling events between various possible pure gauge vacua of the system, separated by some potential barrier. These are known, in imaginary time, as instantons. The instanton charge is given by the change of the winding number of the gauge field coming and going to infinite imaginary time $Q_\mathrm{I} = Q_\mathrm{w}(\tau = \infty) - Q_\mathrm{w}(\tau = -\infty) \in \mathbb{Z}$. Therefore, an instanton is simply a phase kink in the imaginary time direction, which now acts as an additional spatial dimension. The direct analytical continuation into real-time is non-trivial and, in general, not always possible, hence little is known about the dynamics of instantons in real time.

Returning to our discussion of the one-dimensional spin-1 gas, a pure SO(2) gauge field, which is isomorphic to U(1), can be constructed using $U(x) = \exp(\mathrm{i}\varphi_\mathrm{L}(x))$, which in turn gives rise to the gauge field $A_\mu = \partial_\mu \varphi_\mathrm{L}$, leading to winding numbers as in Eq. (2.48). An instanton in this context is seen as the change of the winding number of the Larmor phase in (imaginary) time.

2.4 NON-EQUILIBRIUM QUANTUM FIELD THEORY

In the previous sections, we have briefly introduced the physical system which we investigate and discussed its topological properties. We mentioned the notion of symmetry and underlined

its importance regarding a renormalisation flow or possible topological excitations in the system. In the following, we would like to lay down the foundation for an analytical formulation of non-equilibrium physics, which will be crucial for the derivation of symmetry identities akin to Noether's theorem. In Sect. 2.1, we mentioned the importance of the initial condition for the far-from-equilibrium dynamics of any system. In other words, the symmetry on the level of the observables is important for the possible subsequent dynamics. It is exactly this notion which we would like to investigate further in chapters 6 and 7.

2.4.1 EQUAL-TIME FORMULATION

In non-equilibrium physics, one extends the notion of the Feynman path integral to take its values on a so-called Schwinger-Keldysh contour, inspired by the unitary time evolution in the interaction picture. There, the time evolution is seen as an evolution on a closed contour spanning from a time t_0 to a time t and back, thus doubling the degrees of freedom in the system, as the field values on each time branch must be considered separately [123]. In the Schwinger-Keldysh formalism, correlation functions often include terms which are *non-local* in time. Such correlations, whilst accessible numerically when one has access to the entire time-evolution of the fundamental fields, are experimentally difficult to access. Many experiments in ultracold atoms make use of destructive measurements to extract data from their system, with the consequence that only snapshots in time are available and the time series is only represented statistically.

It is hence more instructive to employ an equal-time formulation for non-equilibrium quantum field theory, deriving correlations which are *local* in time [135]. This formulation is equivalent to the Schwinger-Keldysh formalism and is based upon the time evolution of the density matrix, or its Wigner functional [136]. In the following, we aim to give a brief overview of this approach and use it to derive the Ward-Takahashi identities for a quantum field theory.

We begin by introducing the non-equilibrium equal-time generating functional

$$Z_t[J_\varphi, J_\pi] = \mathrm{Tr}\left\{\hat{\rho}_t \exp\left[\int_x J_\varphi(x)\varphi(x) + J_\pi(x)\pi(x)\right]\right\}, \tag{2.53}$$

where J_φ and J_π are source terms, $\hat{\rho}_t$ is the system's density matrix at time t, and φ and π are canonically conjugate fields. This generating functional, in analogy to the Schwinger-Keldysh formalism, allows for a functional integral representation

$$Z_t[J_\varphi, J_\pi] = \int \mathcal{D}\varphi\mathcal{D}\pi\mathcal{W}_t[\varphi,\pi] \exp\left[\int_x J_\varphi(x)\varphi(x) + J_\pi(x)\pi(x)\right], \tag{2.54}$$

where we define the Wigner functional as

$$\mathcal{W}_t[\varphi,\pi] = \int \mathcal{D}\tilde{\varphi}\left\langle \varphi - \frac{\tilde{\varphi}}{2}\middle|\hat{\rho}_t\middle|\varphi + \frac{\tilde{\varphi}}{2}\right\rangle \exp\left[-\mathrm{i}\int_x \pi(x)\tilde{\varphi}(x)\right]. \tag{2.55}$$

The transformation of the density matrix to the Wigner functional is called a Weyl transformation, or Weyl symbol. Generally, such a transformation connects quantum operators with a classical

phase-space function, which then gives a natural functional integral form. From the discussion above, we may conclude that knowledge of the time evolution of the Wigner functional, beginning from some initial density matrix $\hat{\rho}_0$, allows one to access all the correlations of the system via the generating functional (2.54). Unfortunately, as in many cases, the time-evolution of the Wigner functional is a highly complex problem, forcing us to resort to approximation methods. One such method, the truncated Wigner approximation, is discussed in Chap. 3 in more detail.

From the generating functional, one may derive arbitrary correlation functions by taking functional derivatives w.r.t. the source terms, ultimately setting them to zero, e.g.

$$\left.\frac{\delta^2 Z_t}{\delta J_\varphi(x)\delta J_\varphi(y)}\right|_{J_\varphi, J_\pi = 0} = \langle \varphi(x)\varphi(y)\rangle\,, \tag{2.56}$$

which is equivalent to taking an expectation value as usual, $\mathrm{Tr}\{\hat{\rho}_t \varphi(x)\varphi(y)\}$. We further define the equal-time Schwinger functional, which is the generating functional for connected correlations

$$E_t[J_\varphi, J_\pi] = \log Z_t[J_\varphi, J_\pi]. \tag{2.57}$$

Finally, we define the one-particle irreducible (1PI) effective action via a Legendre transform as

$$\Gamma_t[\Pi, \Phi] = \sup_{J_\varphi, J_\pi}\left[\int_x J_\varphi \Phi(x) + J_\pi \Pi(x) - E_t[J_\varphi, J_\pi]\right], \tag{2.58}$$

where Φ and Π are the expectation values of the fundamental fields in the presence of the sources J_φ and J_π. Equations (2.57) and (2.58) define the quantum equations of motion as

$$\left.\frac{\delta\Gamma_t[\Phi]}{\delta\Phi}\right|_{\Phi=\Phi_J} = J_\varphi(x), \qquad \left.\frac{\delta E_t[J]}{\delta J(x)}\right|_{J=J_\varphi} = \Phi(x). \tag{2.59}$$

2.4.2 SYMMETRY TRANSFORMATIONS

The celebrated Noether's theorem states that each continuous symmetry of a Hamiltonian or Lagrangian, induces a conservation law, each with its own conserved current and charge. Broadly speaking, the quantum field theory analog of these conservation laws are known as the Ward-Takahashi identities. They are derived as identities, or restrictions on the level of correlation functions calculated from the action of the quantum field theory in question. In contrast to the derivation of such identities in equilibrium field theory, non-equilibrium dynamics contain contributions stemming from the initial condition. In order to understand the consequences of these contributions, we consider an infinitesimal continuous transformation given by:

$$\tilde{\varphi}^a = \varphi^a + \mathrm{i}\epsilon_k \mathcal{F}_k^a, \quad \tilde{\pi}^a = \pi^a + \mathrm{i}\epsilon_k \mathcal{P}_k^a. \tag{2.60}$$

with $\mathcal{F}_k^a$ and $\mathcal{P}_k^a$ being the generators of the transformation group and the index a represents the components of the fields. Plugging the transformation into Eq. (2.54), we see that the source terms transform as $J_a\varphi^a \to J_a(\varphi^a + \mathrm{i}\epsilon_k \mathcal{F}_k^a)$ and that the Wigner functional must also obtain

some change which is not further specified. Assuming the functional integral measure does not change under the symmetry transformation, we can pull the logarithm of the Wigner functional into the exponential and expand everything to first order in ϵ_k. We then use that ϵ_k is arbitrary and obtain the non-equilibrium equal-time Ward-Takahashi identities

$$\left\langle \left[\frac{\delta \log \mathcal{W}_t}{\delta \varphi(x)} + J^a_\varphi(x) \right] \mathcal{F}^a_k[x;\Omega] + \left[\frac{\delta \log \mathcal{W}_t}{\delta \pi(x)} + J^a_\pi(x) \right] \mathcal{P}^a_k[x;\Omega] \right\rangle_{\mathcal{W}_t, J_\varphi, J_\pi} = 0, \tag{2.61}$$

where we have introduced the field $\Omega = (\varphi^1, ..., \varphi^n, \pi^1, ..., \pi^n)$ and the average is to be understood with respect to the functional integral in the presence of the sources J_i and Wigner functional. Note that Eq. (2.61) is equivalent to the Ward-Takahashi identities one could derive from the Schwinger-Keldysh formalism, where they are derived from the conserved Noether current of the action.

At this stage, the question arises as to the distinction between the symmetry of the system, and the symmetry of the initial density matrix, which in turn gives rise to the symmetry of the observables. There are several cases to consider, the first being where both the initial condition and the system respect the same symmetry. In this case, it is possible to show that the unitary time evolution of the system will never break the initial symmetry of the Wigner functional [125]. Hence, the change of the Wigner functional in Eq. (2.61) will vanish at all times, and one obtains a set of symmetry identities connecting correlation functions. Plugging the quantum equations of motion Eq. (2.59) into Eq. (2.61), allows us to obtain arbitrary orders of correlation function identities from the derivatives of the quantum effective action $\Gamma[\Omega]$ or of the Schwinger functional $E_t[J]$. Such relations allow for the construction of symmetry witnesses, which quantify the symmetry content of a dynamical system.

Such witnesses are useful for the interesting case where the initial density matrix, i.e., the initial condition, explicitly breaks the symmetry of the Hamiltonian. In this case, the symmetry will never be truly restored, as shown rigorously in [125]. Yet, the symmetry can be approximately restored during the time evolution of the Wigner functional, a fact which would be represented by how well the symmetry identities are fulfilled. Such questions may seem abstract, yet the importance of symmetry is fundamental: it tells us about the possible excitations in the system and hints at the underlying effective theory governing the dynamics. The latter is especially relevant when trying to identify the dominant mechanisms and possible universality classes of a system far from equilibrium. Such an underlying effective theory, connected to the symmetry of the dynamics as well as the system itself, would in principle be able to define a non-equilibrium universality class.

3 NUMERICAL METHODS

Half algorithm, half deity
Glitches in the code or gaps in a strange dream
Tell me you guessed my future and it mapped onto your fantasy

– Vessel, "Ascenionism"

In the following chapter, we briefly overview the numerical methods used in the simulations done for this thesis. These methods are an essential tool for the study of systems that are analytically inaccessible far from equilibrium. We begin by introducing a pseudo-spectral method used for solving the spin-1 GPE in Sect. 3.1. There, we introduce the discretisation of the spin-1 field on a one-dimensional lattice and then discuss the splitting scheme and integration step used in the course of this thesis. Then, in Sect. 3.2 we very briefly present a second solver, the leapfrog algorithm, used to solve the double-sine Gordon model. Then, we outline the truncated Wigner approach to obtain beyond-mean-field results from classical equations of motion in Sect. 3.3. Finally, we introduce and briefly dive into the main optimisation tool used in this thesis: mass parallelisation on graphics processing units in Sect. 3.4.

3.1 SOLVING THE SPIN-1 GPE

In order to numerically solve the spin-1 GPE, we employ a pseudo-spectral splitting scheme, also known as the split-step-Fourier method. In the following, we introduce the grid discretisation in one dimension and detail the integration step, over which we iterate.

3.1.1 GPE ON A DISCRETE ONE-DIMENSIONAL GRID

The equations of motion (2.14) must first be discretised in order to be solved numerically. In our one-dimensional description of the GPE, the wave functions $\psi(x)$ take their values on a discrete grid of N_g grid points. We define the grid spacing as $\Delta x_g = L/N_\mathrm{g}$, where L is the physical size of the system. Accordingly, the time scale is given by $\omega_g = \hbar/M\Delta x_g^2$. We hence define the dimensionless numerical quantities as

$$\bar{x} = \frac{x}{\Delta x_g}, \quad \bar{t} = \omega_g t, \quad \bar{c}_{0,1} = \frac{c_{0,1}}{\hbar\omega_g \Delta x_g}, \quad \bar{\omega}_{\parallel,\perp} = \frac{\omega_{\parallel,\perp}}{\omega}, \quad \bar{q} = \frac{q}{\hbar\omega}, \quad \bar{\psi}_{m_\mathrm{F}} = \sqrt{\Delta x_g}\psi_{m_\mathrm{F}}\,. \tag{3.1}$$

For the rest of this thesis, we will omit the bars and discuss quantities in their numerical units, unless specified otherwise.

We utilise a sinusoidal discretisation of momentum space, in order to obtain an implementation which is equivalent to finite differences methods. To do so, we compute the discrete numerical Laplacian via a discrete Fourier transform (DFT). Decomposing the wave function into plane waves with wave number k, we obtain the Laplacian for $\psi_{m_\mathrm{F}}(x_j) = \psi^j_{m_\mathrm{F}}$ as

$$k^2\psi^j_{m_\mathrm{F}} = \Delta\psi^j_{m_\mathrm{F}} = \frac{\psi^{j+1}_{m_\mathrm{F}} - 2\psi^j_{m_\mathrm{F}} + \psi^{j-1}_{m_\mathrm{F}}}{\Delta x_g^2}. \tag{3.2}$$

Upon inserting the wave expansion for the wave function in Eq. (3.2), we obtain the lattice momenta

$$k_n = \frac{2}{\Delta x_\mathrm{g}} \sin\left(\frac{\pi n}{N_\mathrm{g}}\right), \tag{3.3}$$

where $n \in [-N_\mathrm{g}/2 + 1, N_\mathrm{g}/2]$. This definition leads to a denser momentum spacing in the ultraviolet (UV) and a nearly linear spacing in the infra-red (IR).

3.1.2 SPLIT-STEP FOURIER

In this section, we give a brief outline of the integration scheme used to propagate all simulations done with the spin-1 Bose gas. For a more detailed discussion, we refer the reader to [137, 138]. Generally, a Schrödinger-type time evolution following a classical equation of motion of the form

$$\mathrm{i}\frac{\partial\psi}{\partial t} = \mathcal{H}\psi, \tag{3.4}$$

with some differential operator $\mathcal{H}$, can be decomposed into the kinetic part $\mathcal{D}$ containing the differential operator and a part containing the non-linear terms $\mathcal{N}$

$$\mathcal{H} = \mathcal{D} + \mathcal{N}. \tag{3.5}$$

The formal solution of the Schrödinger-type equation is given by the application of the time-evolution operator $U(t) = \exp[-\mathrm{i}\mathcal{H}t]$ to the initial condition. We consider a single small discrete time step Δt, where the time evolution takes the form

$$\psi(x, t + \Delta t) = e^{-\mathrm{i}\Delta t\mathcal{H}}\psi(x, t) = e^{-\mathrm{i}\Delta t(\mathcal{D}+\mathcal{N})}\psi(x, t). \tag{3.6}$$

The Matrices $\mathcal{D}$ and $\mathcal{N}$ are, in general, non-commuting operators. Hence, the time evolution operator is a numerically costly matrix multiplication, on the order of N_g^2. The efficiency of the algorithm comes from taking advantage of the spectral properties of the operator. If one is able to split the operator into two operators, one containing the kinetic part and the other containing the parts in position space, one is able to diagonalise the kinetic operator by Fourier transforming the expression. This reduces the numerical complexity to that of simple scalar multiplication on the order of N_g. To achieve such a construction, one splits the exponential operator using the Baker-

Campbell-Hausdorff formula, neglecting the second order term, thus considering an error of the order $O(\Delta t^2)$,

$$\psi(x, t + \Delta t) = \left(e^{-\mathrm{i}\Delta t\,\mathcal{D}}\right)\left(e^{-\mathrm{i}\Delta t\,\mathcal{N}}\right)\psi(x,t) + O(\Delta t^2). \tag{3.7}$$

The kinetic part $\mathcal{D}$ in Fourier space takes the simple form $\mathcal{D} = \frac{k^2}{2}$ in the unitless description.

We now turn to applying the above method to the spin-1 Bose gas. The spin-1 Gross-Pitaevskii equations are given by

$$\begin{aligned} i\hbar\partial_t\psi_1 = \Bigg[&-\frac{\hbar^2}{2m}\nabla^2 + V(x) + q + (c_0 + c_1)(|\psi_1|^2 + |\psi_0|^2) \\ &+ (c_0 - c_1)|\psi_{-1}|^2\Bigg]\psi_1 + c_1\psi_{-1}^*\psi_0^2, \end{aligned} \tag{3.8}$$

$$\begin{aligned} i\hbar\partial_t\psi_0 = \Bigg[&-\frac{\hbar^2}{2m}\nabla^2 + V(x) + (c_0 + c_1)(|\psi_1|^2 + |\psi_{-1}|^2) \\ &+ c_0|\psi_0|^2\Bigg]\psi_0 + 2c_1\psi_0^*\psi_{-1}\psi_1, \end{aligned} \tag{3.9}$$

$$\begin{aligned} i\hbar\partial_t\psi_{-1} = \Bigg[&-\frac{\hbar^2}{2m}\nabla^2 + V(x) + q + (c_0 + c_1)(|\psi_{-1}|^2 + |\psi_0|^2) \\ &+ (c_0 - c_1)|\psi_1|^2\Bigg]\psi_{-1} + c_1\psi_1^*\psi_0^2. \end{aligned} \tag{3.10}$$

Promoting Eq. (3.4) to a matrix equation generalises the aforementioned arguments also to a set of differential equations such as the spin-1 GPE. The non-linear part of the spin-1 GPE contains coupling between the various components, making the propagation in real space non-trivial. The propagation of the kinetic term, on the other hand, remains the same. We employ the following splitting scheme for the spin-1 GPE:

$$\mathrm{i}\partial_t\psi_{m_\mathrm{F}}(x,t) = -\frac{1}{2}\nabla^2\psi_{m_\mathrm{F}}(x,t), \tag{3.11a}$$

$$\mathrm{i}\partial_t\psi_{m_\mathrm{F}}(x,t) = \left[V(x) + f_{m_\mathrm{F}}(|\psi_0|^2, |\psi_1|^2, |\psi_{-1}|^2)\right]\psi_{m_\mathrm{F}}(x,t), \tag{3.11b}$$

$$\mathrm{i}\partial_t\boldsymbol{\psi}(x,t) = S[\boldsymbol{\psi}(x,t)]\boldsymbol{\psi}(x,t), \tag{3.11c}$$

where Eq. (3.11a) is the kinetic part, f_{m_F} in Eq. (3.11b) is a function containing all the terms which do not change the single-component densities and Eq. (3.11c) contains the spin-changing collisions, denoted by the matrix $S[\boldsymbol{\psi}(x,t)]$.

The integration of the kinetic part ist straight forward in Fourier space. Hence, using fast Fourier transforms (FFTs), we may transform the field to momentum space and propagate it with a multiplicative factor, transforming it back after the kinetic integration step

$$\psi_{m_\mathrm{F}}(x_j, t_{n+1}) = \mathscr{F}^{-1}\left\{e^{-\mathrm{i}\Delta t k_j^2/2}\mathscr{F}\left[\psi_{m_\mathrm{F}}(x_j, t_n)\right]\right\}, \tag{3.12}$$

where $\mathscr{F}[\cdots]$ denotes a Fourier transform. We then integrate a half-step in the 'diagonal' part

$$\psi_{m_F}(x_j, t_{n+1}) = e^{-i\left[V(x_j)+f_{m_F}(|\psi_0(x_j,t_n)|^2,|\psi_1(x_j,t_n)|^2,|\psi_{-1}(x_j,t_n)|^2)\right]\Delta t/2}\psi_{m_F}(x_j, t_n). \tag{3.13}$$

We now turn to the spin-changing collisions part, which in matrix form reads

$$i\partial_t\boldsymbol{\psi}(x,t) = S\boldsymbol{\psi}(x,t) = c_1\begin{pmatrix} 0 & \psi_{-1}^*\psi_0 & 0 \\ \psi_{-1}\psi_0^* & 0 & \psi_0^*\psi_1 \\ 0 & \psi_0\psi_1^* & 0 \end{pmatrix}\boldsymbol{\psi}(x,t), \tag{3.14}$$

where we have omitted the spatial and time dependence inside the matrix for brevity. For the integration of the off-diagonal part, we neglect that the matrix $S(x,t)$ does not commute with itself at various time steps. This leads to the approximation of a Dyson ordered time series using a simple Euler step to approximate the integral

$$\begin{aligned}\boldsymbol{\psi}(x_j, t_{n+1}) &\approx \exp\left\{-i\int_{t_n}^{t_{n+1}} dt\, S[\boldsymbol{\psi}(x_j,t)]\right\}\boldsymbol{\psi}(x_j,t_n) \\ &\approx \exp\left\{-\frac{i}{2}\left(S[\boldsymbol{\psi}(x_j,t_n)] + S[\boldsymbol{\psi}(x_j,t_{n+1})]\right)\Delta t\right\}\boldsymbol{\psi}(x_j,t_n) \\ &\approx \exp\left[-i\frac{1}{2}\left(S[\boldsymbol{\psi}(x_j,t_n)] + S[\tilde{\boldsymbol{\psi}}(x_j)]\Delta t\right)\right]\boldsymbol{\psi}(x_j,t_n),\end{aligned} \tag{3.15}$$

with $\tilde{\boldsymbol{\psi}} = \boldsymbol{\psi} - iS\boldsymbol{\psi}$. We note that this approximation constrains the accuracy of the algorithm to remain on the order of $O(\Delta t^2)$, even though we are using a three-way splitting scheme, which usually would give accuracy up to order $O(\Delta t^3)$. The propagation thus takes the form of a 3×3 matrix multiplication

$$\boldsymbol{\psi}(x_j, t_{n+1}) = e^{ic_1\Lambda\Delta t}\boldsymbol{\psi}(x_j, t_n), \tag{3.16}$$

$$\Lambda = \frac{1}{2}\begin{pmatrix} 0 & \left[\psi_{-1}^*\psi_0 + \tilde{\psi}_{-1}^*\tilde{\psi}_0\right] & 0 \\ \left[\psi_0^*\psi_{-1} + \tilde{\psi}_0^*\tilde{\psi}_{-1}\right] & 0 & \left[\psi_0^*\psi_1 + \tilde{\psi}_0^*\tilde{\psi}_1\right] \\ 0 & \left[\psi_1^*\psi_0 + \tilde{\psi}_1^*\tilde{\psi}_0\right] & 0 \end{pmatrix}. \tag{3.17}$$

We define $a = \frac{1}{2}\left[\psi_{-1}^*\psi_0 + \tilde{\psi}_{-1}^*\tilde{\psi}_0\right]$, $b = \frac{1}{2}\left[\psi_0^*\psi_1 + \tilde{\psi}_0^*\tilde{\psi}_1\right]$ and $\lambda = \sqrt{|a|^2 + |b|^2}$ and obtain the integration step of the off-diagonal part (3.11c)

$$\boldsymbol{\psi}(x, t_{n+1}) = \begin{pmatrix} \frac{|a|^2\cos(\lambda c_1\Delta t)+|b|^2}{\lambda^2} & -ia\frac{\sin(\lambda c_1\Delta t)}{\lambda} & ab\frac{\cos(\lambda c_1\Delta t)-1}{\lambda^2} \\ -ia^*\frac{\sin(\lambda c_1\Delta t)}{\lambda} & \cos(\lambda c_1\Delta t) & -ib\frac{\sin(\lambda c_1\Delta t)}{\lambda} \\ a^*b^*\frac{\cos(\lambda c_1\Delta t)-1}{\lambda^2} & -ib^*\frac{\sin(\lambda c_1\Delta t)}{\lambda} & \frac{|a|^2+|b|^2\cos(\lambda c_1\Delta t)}{\lambda^2} \end{pmatrix}\boldsymbol{\psi}(x, t_n). \tag{3.18}$$

Upon performing this step, we propagate an additional half-step in the diagonal part in real space (3.13).

3.2 SOLVING THE DOUBLE SINE-GORDON EQUATION

In Chap. 5, we simulate the dynamics of the double sine-Gordon model obeying the equations of motion

$$\ddot{\varphi} = c_s^2 \Delta\varphi - \lambda \sin(\varphi) + \lambda_s \sin(2\varphi). \tag{3.19}$$

In this case, we must numerically integrate a second-order partial differential equation. A broad range of well-established integrators exist for the solution of such differential equations, with various degrees of accuracy. It might seem even cynical then, that we would choose the simple leapfrog algorithm, yet its ease of implementation, efficiency, accuracy and symplectic nature are of great advantage.

The leapfrog algorithm is a second order symplectic integrator. Its symplectic nature is especially practical when dealing with Hamiltonian systems such as Eq. (3.19), as it obeys the same mathematical structure. As a consequence, the algorithm intrinsically conserves the total energy of the system. We note that, even though well-known algorithms such as the celebrated fourth order Runge-Kutta (RK4) algorithm have a higher accuracy, they, in general, lead to a loss of energy with each integration step, which is undesirable when dealing with closed quantum systems. Furthermore, being fourth order, the computation costs of the RK4 algorithm are significantly higher than those of the leapfrog algorithm. Since we here simulate dynamics for very long times, these computational costs are an important factor.

Before we continue to the integration scheme, we first discretise the field on a grid with a grid spacing of 1, $\varphi(x) = \varphi(x_j) \equiv \varphi^j$. Then, we make use of simple finite differences methods to discretise the spatial derivative term for one and two dimensions. The Laplacian hence reads

$$\text{1D:} \quad \Delta\varphi = \varphi^{j+1} + \varphi^{j-1} - 2\varphi^j\,, \tag{3.20a}$$

$$\text{2D:} \quad \Delta\varphi = \varphi^{j-1,\ell} + \varphi^{j+1,\ell} + \varphi^{j,\ell-1} + \varphi^{j,\ell+1} - 4\varphi^{j,\ell}\,. \tag{3.20b}$$

The concept of the integration scheme is based on simple Euler half-time steps, alternating between the field $\varphi(x_j, t_n) \equiv \varphi_n^j$ and its conjugate momentum $\dot{\varphi}(x_j, t_n) \equiv \dot{\varphi}_n^j$. A single integration step of the discretised fields takes the form

$$\dot{\varphi}^j_{n+1/2} = \dot{\varphi}^j_{n-1/2} + \left[-\lambda \sin\left(\varphi_n^j\right) + \lambda_s \sin\left(2\varphi_n^j\right) + \Delta\varphi_n\right] \Delta t\,, \tag{3.21}$$

$$\varphi^j_{n+1} = \varphi^j_n + \dot{\varphi}^j_{n+1/2} \cdot \Delta t. \tag{3.22}$$

This integration scheme gives an error of the order $O(\Delta t^2)$, and when parallelised on graphics processing units, especially utilising shared block memory, the efficiency is increased substantially (see Sect. 3.4.2).

3.3 TRUNCATED WIGNER APPROXIMATION

In our discussion of far-from-equilibrium functional methods in Sect. 2.4, we used the Wigner functional to compute the equal-time correlation functions of the dynamical system. Therefore, knowledge of the Wigner functional at time t encapsulates the full state of the system at that time and gives access to observables. The time evolution of the Wigner functional is governed by the so-called *Moyal equation*, a generalisation of the famous *von Neumann* equation. The Moyal equation is, in general, not analytically solvable and one must resort to approximation methods to be able to recover beyond-mean-field results for closed quantum many-body systems. In the following, we briefly outline the concepts and approximations considered in the truncated Wigner method for the numerical simulation of quantum many-body systems. For a comprehensive review of the subject, we refer the reader to [139].

We begin by considering the equations of motion for the quantum mechanical density matrix, given by the von Neumann equation

$$\mathrm{i}\hbar\frac{\partial\hat{\rho}}{\partial t} = \left[\hat{H},\hat{\rho}\right]. \tag{3.23}$$

Applying the Weyl transform to this equation yields the equations of motion for the Wigner functional (2.55)

$$\mathrm{i}\hbar\frac{\partial\mathcal{W}}{\partial t} = 2H_W \sinh\left[\frac{\Lambda}{2}\right]\mathcal{W}, \tag{3.24}$$

where H_W is the Weyl symbol of the Hamiltonian of the system and we defined

$$\Lambda = \sum_j \frac{\overleftarrow{\partial}}{\partial\psi_j}\frac{\overleftarrow{\partial}}{\partial\psi_j^*} - \frac{\overrightarrow{\partial}}{\partial\psi_j}\frac{\overrightarrow{\partial}}{\partial\psi_j^*}, \tag{3.25}$$

where the arrows above the differential operators indicate the direction on which they operate. In order to solve this equation, we perform a series expansion of the hyperbolic sine in Λ, truncating the series at some relevant order. For large occupancies, i.e., large modulus of the wave function, one can show that it is sufficient to truncate the series at leading order [139]. Thus, one arrives, at leading order, at the classical Liouville equation

$$\mathrm{i}\hbar\frac{\partial\mathcal{W}}{\partial t} = \{H_W,\mathcal{W}\}_P, \tag{3.26}$$

where $\{\cdot,\cdot\}_P$ denotes the Poisson brackets. We note that in the case of non-linear Schrödinger equations with quartic interactions, such as the spin-1 model, the series would be exact at third order already, since all higher orders vanish after taking more than three derivatives of the field. On the other hand, this is not the case for the sine-Gordon model where the non-linearity persists in all orders due to the cosine potential.

The Liouville equation, as it stands, may be solved by the method of characteristics, bringing the equations of motion of the Wigner function into a familiar Schrödinger-type time evolution for the fundamental field

$$i\hbar\frac{\partial\psi}{\partial t} = \frac{\partial H_W}{\partial\psi^*}. \tag{3.27}$$

Hence, rather than time-evolving the full Wigner function, we evolve an ensemble of mean-field classical field configurations in time according to Eq. (3.10), with added quantum noise which is drawn from the Wigner distribution in the initial condition. Therefore, Eq. (3.27) traces the path of a single such realisation of the fields. In the relevant case of a Bose-Einstein condensate, the initial state is given by a coherent state, where the Wigner function is a positive definite probability distribution function, taking the form of a Gaussian distribution with a variance of half a particle. The quantum dynamics beyond the mean field are then recovered by considering observables after averaging over many independent truncated Wigner realisations.

3.4 PARALLELISATION ON GRAPHICS PROCESSING UNITS

All simulations discussed in this thesis have been performed using high-level parallelisation on graphics processing units (GPUs). In the following section, I would like to very briefly introduce fundamental concepts related to GPU computing, highlighting their strengths, limitations and key characteristics. This overview is not intended to be an exhaustive or technical treatment of the hardware, but rather a concise introduction to the key ideas we exploit in our research. While this section is not directly tied to the physical discussion in this thesis, the technical developments presented in this section played a crucial role in enabling the scale of the simulations presented. The achieved performance gains are the result of constant optimisation efforts carried out over several years, beginning from C.-M. Schmied's work [140]. I chose to include this aspect to highlight the considerations that went into achieving the current performance. Such aspects, while often behind the scenes, were essential to supporting the scientific results.

3.4.1 CENTRAL PROCESSING UNITS

First, in order to understand the advantages of computing on a GPU, we must consider the basic architecture of a central processing unit (CPU). The CPU, also called *the host* in the context of GPU accelerated computing, is the primary component responsible for executing instructions within a computer. Its architecture is designed to handle a variety of tasks with a very strong single-threaded performance. Plainly speaking, the CPU excels at executing a single task quickly and sequentially, rather than many small tasks in parallel.

A CPU consists of one or more processing cores, each capable of executing instructions independently and sharing a unified memory space for instructions and data. Each core contains an arithmetic logic unit (ALU) for executing mathematical operations (such as addition, multi-

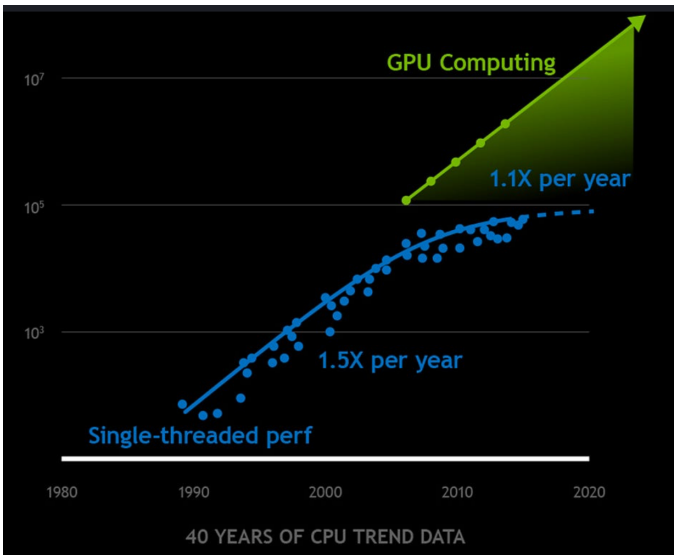

Figure 3.1: Moore's law, stating that the number of microtransistors doubles every two years, and with it the computation power of CPUs (blue dots) doubles every eighteen months. In recent years, difficulties in sustaining Moore's law on CPUs has led to the focus shifting towards GPUs. The appearance of GPU powered computing is said to continue Moore's law (green dots), hence dubbing this development colloquially as Huang's law, after Nvidia CEO at the time of writing, Jensen Huang. Figure is taken and adapted from [141]

plication and comparison), control logic for instruction sequencing and branching, and a set of so-called registers, i.e. small and fast memory locations, allowing for very fast storage and fetching of variables and hence the rapid execution of arithmetic operations.

A central feature of CPU performance lies in its memory hierarchy. Modern CPUs include several layers of cache, typically called L1, L2, and L3 caches. The cache hierarchy sees them to be progressively larger but slower, to compensate for the high latency of accessing main memory (RAM). This hierarchy is not exclusive to the CPU, also a GPU makes use of a similar hierarchy and the concept remains the same: The memory hierarchy can be likened to a storage system with varying access speeds. Accessing data from RAM is relatively slow, comparable to retrieving an item from a distant storage room in a large facility. In contrast, L1 cache operates like a small, back-room storage area, readily accessible for frequently used data. Registers represent the fastest form of storage, analogous to tools immediately available to a worker on their tool-belt, requiring minimal effort to access, but cannot contain much data.

While CPUs are particularly well-suited for serial calculations involving strong dependencies between computation steps, their sequential nature poses a certain drawback. Although modern CPUs support multi-threading and can execute multiple tasks in parallel (e.g., using OpenMP or MPI across cores or nodes), the total number of cores is still relatively limited, often ranging from 4 to 64 in typical research hardware. This makes the CPU ideal for simulation tasks that are either too irregular or too sequential for massive parallelisation but still demand high precision and stability. This drawback, stemming from physical and architectural limitations, has made it increasingly difficult to sustain the famous Moore's Law, which states that the number of transistors on a chip doubles approximately every two years, implying a near doubling of processing

Figure 3.2: Architecture of a Nvidia A100 GPU streaming multiprocessor. The FP64 cores can access a small register for fast storage. Cores within the SMs that are assigned to a block gain access to a shared memory cache for optimised memory access. Figure taken and adapted from [144].

power every eighteen months [142, 143]. In recent years, attention has shifted toward the use of GPUs, which offer massive throughput via massive parallelism, thereby continuing the exponential growth in performance, as illustrated in Fig. 3.1. This trend has been colloquially referred to as Huang's Law, named after Nvidia CEO, at the time of writing, Jensen Huang. Accelerated computing on GPUs has attracted significant attention, driven by advances in machine learning and artificial intelligence, which have in turn fuelled the development of increasingly powerful GPU architectures.

3.4.2 GRAPHICS PROCESSING UNITS

While the CPU excels at performing complex, sequential computations with high flexibility, the GPU, also called *the device*, is designed around the fundamentally different principle of massive parallelism. This architectural difference makes GPUs especially well-suited for physics simulations involving large datasets and operations that can be performed independently across many elements, such as solving the spin-1 GPE on a spatial lattice using the truncated Wigner approximation, as done in this thesis. Here, the parallelisation occurs on two levels: First, the use of pseudo-spectral methods enables parallel execution of local, independent operations across the spatial grid. Second, the truncated Wigner realisations are independent of one another, allowing them to be computed in parallel as well.

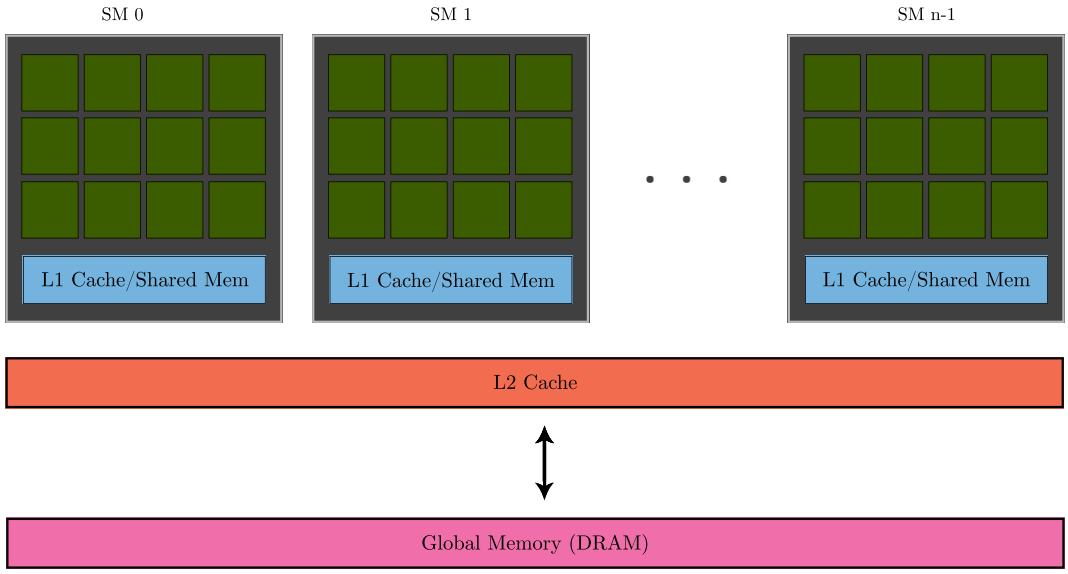

Figure 3.3: Memory hierarchy of a GPU. Multiple SMs, each containing their own shared memory perform the tasks, they can access a L2 cache to exchange information if needed, though this is rather small. Further memory can be accessed via the global device memory.

A GPU consists of a vast array ($\sim 10^3$) of smaller processing cores, organised into groups called streaming multiprocessors (SMs) (See Fig. 3.2). Each core is individually much less powerful than a CPU core in the sense of, e.g., processing power of double precision floating point operations (FP64), but due to their high degree of parallelism, they can achieve much higher throughput when performing the same operation over many data points, thus massively accelerating the program executed.

GPUs operate using a hierarchical model of parallel execution, built around the concepts of threads, blocks, and grids: A thread is the smallest unit of execution and performs the operations for a single data element (e.g., computing the forward integration step on a single spatial point via multiplication). Threads are grouped into blocks, which can share fast *on-chip* shared memory and can synchronise with each other. Blocks are organised into a grid, allowing for the execution of thousands of threads in parallel.

One of the key advantages of this type of block and grid architecture is how memory is handled. While CPUs rely heavily on the aforementioned large, hierarchical caches to reduce latency for memory access, GPUs are designed for high-bandwidth memory access. They benefit from efficient memory sharing, where threads read or write adjacent data in memory at the same time. The most prominent advantage comes from the so-called *shared memory* within a block. Shared memory resides on-chip and is shared among all threads in a thread block. It is much faster than global memory and enables data exchange between threads in the same block. In the context of our simulations, for example, using the leapfrog algorithm (see Sect. 3.2), shared memory is especially valuable for reusing data across threads, such as storing portions of a grid that multiple threads need to access. This can dramatically reduce the number of slow global memory accesses in finite difference methods, where a block of threads can load neighbouring cell values (as seen

in Eq. (3.20)) into shared memory once, then perform multiple operations on that data locally, minimising expensive reads from global memory. However, shared memory is relatively small (typically 48–100 KB per block on modern GPUs at the time of writing) and must be managed carefully. It is explicitly controlled by the user, unlike caches, which are managed automatically by hardware.

Furthermore, each thread also has access to a small number of registers, which are the fastest form of memory but are private to the thread and extremely limited in size. These are used for storing temporary values during execution, much like registers in CPUs. Lastly, at the top level, a GPU provides global memory (DRAM), which is large ($\sim$ 80GB for the Nvidia A100 used in simulating the data for this thesis), but relatively slow to access compared to other types of on-chip memory.

One must keep in mind, however, that with all the great advantages of mass parallelisation and incredible speed due to such memory management, this model also imposes some limitations. GPUs are less efficient at handling tasks with heavy control flow, irregular memory access, or deep interdependencies between operations, areas where the CPUs offer much better performance. As such, optimal use of a GPU often involves reformulating simulation problems to emphasise independent operations. An especially helpful analogy is to compare the use of a GPU to that of an elevator: while it can transport ten people to the upper floors efficiently, it does not make the trip any faster for just one person. Many integrators of partial differential equations offer an optimal factorisation of the computational problem. In our case, the split-step Fourier method makes heavy use of fast fourier transforms which are a perfect example of an algorithm that can be executed swiftly and independently for each grid point.

Writing a program to be executed on the device is a process of constant optimisation and there are a few factors one has to take into account. First, there is no automatic communication between the host and the device in the sense of memory transfer. The user has to manually allocate and manage memory on the device and copy any data from the host onto the device and back. This memory allocation and transfer is the slowest process possible in GPU accelerated programs. One must take extra care to minimise memory transfer between the host and the device as to assure that the bulk of the program is executed on the GPU without interruption.

Secondly, the correct settings of block sizes and grid sizes is also crucial for the efficiency of the program. The optimal size of a block and a grid are *a priori* not clear. This is a parameter which should be optimised via testing and is individual to each problem. In our case, where we distribute the threads across a one-dimensional spatial grid with many parallel realisations, we connect the device grid size to the size of the spatial grid and number of parallel truncated Wigner realisations, e.g. for the spatial dimension, $\text{gridsize} = \left\lceil \frac{N_g}{\text{blocksize}} \right\rceil$. The block size, though, has no universal rule and has to be optimized individually for each problem.

In summary, GPU-powered computing has become a significant tool for accelerating numerical simulations. In the context of this thesis, the use of GPU accelerated computing substantially improved the performance of our simulations. Utilising Ampere architecture GPUs (A100) to parallelise one-dimensional simulations across the spatial grid, as well as for executing independent truncated Wigner runs, resulted in a speed-up of $\sim 10^2$ compared to CPU computations.

Part II

MICROSCOPIC AND EFFECTIVE THEORIES

In this part, we thoroughly study the dynamics of the spin-1 Bose gas after a quench from the polar phase to the easy-plane phase from the perspective of its microscopic behaviour and derive an effective description for its macroscopic behaviour. The quench through the second-order phase transition was first simulated and analysed by C.-M. Schmied et al. [75]. There, self-similar scaling of the transverse spin order parameter was observed, persisting for several orders of magnitude in time. The resulting scaling exponents were numerically predicted to be $\alpha = \beta \approx 1/4$. The Rubidium BEC experiment performed by M. Prüfer et al. [55] studied the same quench in a quasi-one-dimensional spin-1 condensate with an elongated cigar-shaped trap geometry. By utilising their novel readout scheme [145], the experiment is able to spatially resolve the spin in x and y direction simultaneously, allowing them to calculate equal-time spatial correlation functions of the transverse spin. This led to the experimental observation of self-similar scaling in the spin condensate, albeit with a different scaling exponent $\beta \approx 1/2$. We would like to note here that the readout scheme employed by the experiment is not restricted to resolving only spins. The quadrupole operators, and with them also the spinor phase can also be experimentally extracted in this way, see [131, 145] for more details. The discrepancy between the numerical and experimental results is a long-standing problem and the effort to reconcile these differences led to the detailed study of the dynamics post-quench done in this thesis, in part to better facilitate a theory which encapsulates both options. We note that the explanation for this discrepancy is given in the next part, in Chap. 7.

In Chap. 4, we first investigate the microscopic dynamics of the one-dimensional spin-1 gas post-quench, concentrating on isolating the excitations which give rise to the shape of the order parameter spectrum. We observe the presence of extreme rogue wave events in the velocity fields of the Larmor phase of the spinor gas and study their statistics with regards to the universal scaling dynamics found in the system. We find that the scaling of the characteristic length scale is distinctly different from the scaling of the characteristic timescale, presenting two mutually dependent scaling exponents governing the time evolution of their respective scales. The exponent for the timescale is extracted utilising the framework of rogue wave propagation in disordered media, which is found to accurately describe the statistics. We then examine the emerging topological defects in the system, which take the form of space-time vortices, or real-time instantons in the Larmor phase. These excitations seem to give rise to the spatial structure seen in the order-parameter correlation function.

Remarkably, we find that the system continues to exhibit self-similar scaling of the transverse spin correlations even in the absence of the topological defects. Consequently, we conjecture that these excitations are a proxy for the true underlying mechanism. Therefore, in order to sift through the wide range of excitations present in the noisy dynamic post-quench, a low-energy effective theory is derived in Chap. 5, taking the form of a sine-Gordon-type model for the spinor phase. We show that this effective model reproduces the self-similar scaling dynamics of the spin-1 Bose gas in one and two dimensions. In light of this, this part of the thesis presents a shift in focus from the investigation of excitations of the Larmor phase, to the study of sine-Gordon type excitations in the spinor phase as a prime mechanism for scaling. Our results mark a notable

development in the research of non-equilibrium universality, pointing towards a sine-Gordon-type universality class, to which the spin-1 Bose gas in the easy-plane belongs to. Such a universality class is of particular interest, since the sine-Gordon model is a fundamental model appearing in many contexts, including false vacuum decay [146–148], dynamics of Coulomb gases and spin chains [149–151].

UNIVERSAL DYNAMICS OF ROGUE WAVES IN A SPIN-1 GAS

I'm a mess mess mess mess mess mess mess mess
I'm a mess mess mess mess mess mess mess mess

– Huh Yunjin, "Eve, Psyche & the Bluebeard's Wife"

In this chapter, we numerically investigate the microscopic phenomena present during the post-quench dynamics of the spin-1 gas. Recall that isolated many-body systems far from equilibrium may exhibit scaling dynamics with universal exponents indicating the proximity of the time-evolution to a non-thermal fixed point (NTFP). Here, we find universal dynamics connected with the occurrence of extreme wave excitations in the mutually coupled magnetic components of a spinor gas which propagate in an effectively random potential comprised of the spin interaction part of the spin-1 Gross-Pitaevskii equation (GPE). The frequency of these rogue-waves is affected by the time-varying spatial correlation length of the potential which is a reflection of the aforementioned universal scaling dynamics, thus giving rise to an additional exponent $\delta_c \simeq 1/3$ for temporal scaling, which is different from the exponent $\beta_V \simeq 1/4$, characterising the scaling of the correlation length $\ell_V \sim t^{\beta_V}$ in time. As a result of the caustics, i.e., focusing events, real-time instanton defects appear in the Larmor phase of the spin-1 system as vortices in space and time. The temporal correlations governing the instanton occurrence frequency scale as t^{δ_I}. This suggests that the universality class of a NTFP could be characterised by different, mutually related exponents defining the evolution in time and space, respectively.

The chapter is organised as follows: In Sect. 4.1.1, we describe the numerical preparation of the system, explaining the quench parameters and the initial condition used in all the discussed simulations in this chapter. Then, Sect. 4.1.2 describes the short-time dynamics of the system during its approach to the self-similar scaling regime, expanding upon the various excitations present in the system by discussing the spin and spin-nematic spheres as visualisation tools. Furthermore, in Sect. 4.2 we discuss the appearance and characterisation of rogue-wave events in the velocity fields of the magnetic components of the spin-1 gas. Thereupon, we give a sketch of a general derivation of the underlying timescale to first caustics in Sect. 4.2.1, followed by a generalisation to Bogoliubov excitations in the spin-1 gas subject to a random potential given by the spin interactions detailed in Sect. 4.2.2. After deriving the rogue wave timescale, we discuss

the effect of the spatio-temporal scaling of the order-parameter correlations on the coarsening of this timescale and provide a numerical analysis to support this in Sect. 4.2.3. We discuss the appearance of instantons, i.e. topological excitations, resulting from the rogue waves in the Larmor phase in Sect. 4.3. We investigate their structure and characterisation w.r.t. both spin and spin-nematic spheres in Sect. 4.3.1. We then study their spatio-temporal scaling in Sect. 4.3.2. Finally, we provide a short discussion and outlook in Sect. 4.4.

The content of this chapter is taken and adapted from [1]. I stress that some parts are taken verbatim from the publication, yet the content was reorganised and expanded upon to better accommodate the context of this thesis, especially regarding work done post-publication. Note also, that to ensure consistency across this thesis, the notation was slightly altered as well.

4.1 POST-QUENCH DYNAMICS OF THE SPIN-1 GAS

The dynamics of the spin-1 Bose gas after a quench from the polar phase to the easy-plane phase exhibit rich structure formation and non-equilibrium behaviour which is yet to be fully understood. The universal self-similar scaling phenomenon attributed to the vicinity of the system's time evolution to a NTFP is a hallmark of this particular quench. A better understanding of phenomena emerging during the far-from-equilibrium dynamics presents a unique opportunity to shed light onto the underlying mechanisms driving these processes. Hence, to gain valuable insight into such possible scaling mechanisms, we perform a detailed analysis of the microscopic excitations present in the system, with the intention of better understanding the universality class to which the spin-1 Bose gas belongs to and its characteristics.

In the following discussion, we normalise all observables with respect to the total density $\tilde{\rho}$ of the spinor condensate, i.e., $\bar{\psi}(x,t) = \psi(x,t)/\sqrt{\tilde{\rho}}$. In further discussions, we omit the bar and all observables are to be understood as normalised quantities unless specified otherwise. Furthermore, distances are given in units of the spin healing length $\xi_s = (2M\tilde{\rho}|c_1|)^{-1/2}$ and time is given in units of spin-collision time $t_s = 2\pi/(2M\tilde{\rho}|c_1|)$.

4.1.1 INITIAL CONDITION

We consider a quench from the polar ($c_1 < 0$, $q > 2\tilde{\rho}|c_1|$) to the easy-plane phase ($c_1 < 0$, $0 < q < 2\tilde{\rho}|c_1|$), where we expect the spin degrees of freedom to be dominantly oriented in the F_x-F_y-plane, giving rise to a complex scalar order parameter, the transverse spin

$$F_\perp \equiv F_x + \mathrm{i}F_y = |F_\perp| e^{\mathrm{i}\varphi_L}. \tag{4.1}$$

Recall that $\varphi_L = (\varphi_1 - \varphi_{-1})/2$ is the Larmor phase as introduced in Sect. 2.2.3. We simulate a condensate of $3 \cdot 10^6$ Rubidium atoms on a 4096-point grid subject to periodic boundary conditions, corresponding to a length of $L = 220\mu\mathrm{m} \approx 550\xi_s$. Prior to the quench, the atoms are

prepared in the mean-field polar phase, which is characterised by a full macroscopic occupation of the $m_F = 0$ component $\psi_0(x) = 1$, while the $m_F = \pm 1$ magnetic levels are empty, leading to an overall zero magnetisation. Upon initialisation, we add quantum noise to the Bogoliubov modes of the initial state

$$\psi(x) = \begin{pmatrix} 0 \\ \tilde{\rho} \\ 0 \end{pmatrix} + \sum_k \begin{pmatrix} a_{k,1} e^{ikx} \\ a_{k,0} u_k e^{ikx} - a^*_{k,0} v_k e^{-ikx} \\ a_{k,-1} e^{ikx} \end{pmatrix}, \tag{4.2}$$

where the functions a_{k,m_F} are complex Gaussian random variables with a variance of half a particle

$$\langle a^*_{k,m_F}, a_{k',m'_F} \rangle = \frac{1}{2} \delta_{m_F,m'_F} \delta_{k,k'}, \tag{4.3}$$

and u_k and v_k are the Bogoliubov mode functions defined as

$$u_k = \sqrt{\frac{k^2 + c_0}{2\sqrt{k^2(k^2 + 2c_0)}} + \frac{1}{2}}, \quad v_k = \sqrt{u_k^2 - 1}, \tag{4.4}$$

as seen in [75] . Subsequently, we quench the quadratic Zeeman shift through the second-order phase transition to a final value of $q_f = 0.9\,\tilde{\rho}|c_1|$. The dynamics are simulated utilising truncated Wigner simulations as introduced in Sect. 3.3. The simulations are performed in an experimentally realistic parameter regime for ^{87}Rb, i.e., $|c_1| \ll c_0$, albeit in the absence of a trapping potential and with an increased homogeneous density as to ensure the validity of the truncated Wigner approximation.

4.1.2 SHORT-TIME DYNAMICS

Following the quench, Bogoliubov instabilities lead to a fast build-up of strong excitations in the relative phases between the different magnetic components. It is instructive to study the short-time dynamics from the point of view of two SO(3) spheres: the spin sphere and the spin-nematic sphere, recall Sect. 2.2.6.

The initial condition can be seen as a coherent distribution beginning on the north pole of the transverse spin-nematic sphere (see left panel of Fig. 2.4). As the system is quenched through the second-order phase transition between the polar phase and easy-plane phase, the effective potential landscape changes. On the spin-nematic sphere, the fixed point at $Q_0 = 1$ becomes unstable, and two additional fixed points appear at the equilibrium mean-field value of the transverse spin length. This change of potential landscape leads to a squeezing dynamic on the spin-nematic sphere [131], as the phase-space distribution begins to spread across the separatrix (see, e.g. Fig. 5.5), before finally settling down into the fixed points of the spin-nematic sphere. The bifurcation of the probability distribution function on the spin-nematic sphere manifests itself as all manner of strong spin-wave excitations or as quasi-topological excitations.

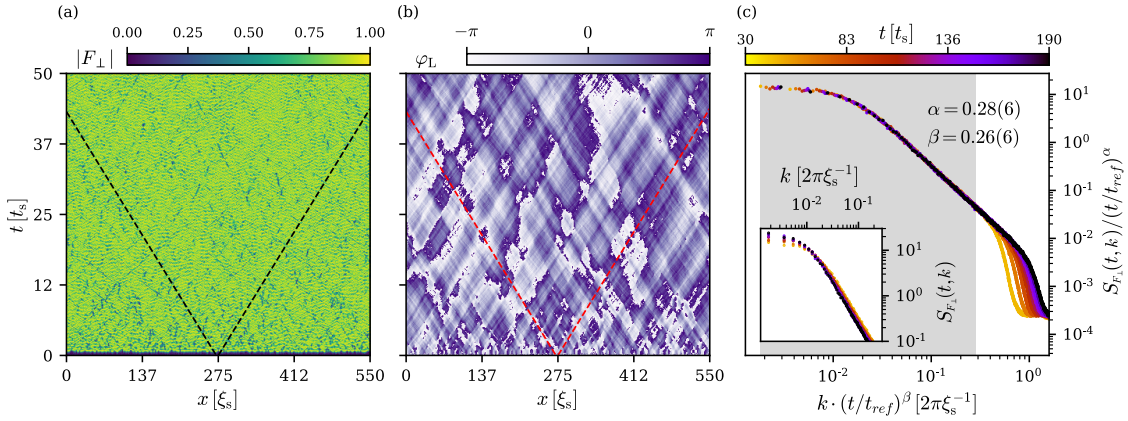

Figure 4.1: Time evolution (a) of the spin length $|F_\perp|$ of the transverse spin $F_\perp = F_x + \mathrm{i}F_y$ and (b) the Larmor phase $\varphi_L = \arg(F_\perp)$. The spin speed of sound $c_s = (\tilde{\rho}|c_1|/2M)^{1/2}$ is depicted by the black and red dashed lines. (c) The coarsening of spin-wave patterns seen mostly in the Larmor phase is reflected by the spatio-temporal scaling (4.6) of the structure factor (4.5) with universal exponents $\beta = 0.26(6)$ and $\alpha = 0.28(6) \simeq d\beta$ in $d = 1$ spatial dimension and universal scaling function $f_s(k)$. The scaling exponents confirm, within the error bounds, the findings of [75].

On the other hand, on the spin sphere we observe the sudden formation of a ring-like distribution in the F_x-F_y plane due to spontaneous breaking of SO(2) symmetry. We also notice very weak fluctuations in the F_z directions, rendering them subdominant. The resulting excitations in the transverse spin manifest as various spin textures, where, due to the immediate spontaneous symmetry breaking of SO(2) symmetry, patches of causally disconnected regions of approximately equal order parameter form. These patches are separated by strong almost domain-wall-like excitations in the Larmor phase, whereas the spin length only fluctuates weakly (cf. Fig. 4.1a, b). Recall that excitations in the Larmor phase correspond to massless Goldstone bosons, allowing the Larmor phase to fluctuate strongly, exploring the valley of the potential. In contrast, excitations in the radial direction on the spin sphere, i.e., Higgs-type modes, are gapped spinor phase excitations, which live on the spin-nematic sphere in the $F_\perp$-$Q_\perp$ plane. There, the potential landscape allows the spinor phase to fluctuate weakly around the fixed points, resulting in small fluctuations in the spin length.

It is important to note at this point that the mass gap of the spinor phase dispersion relation is still on the order of the spin interaction energy, allowing for events where the spinor phase can locally tunnel from one fixed point to the other, thus making the overall fluctuations of the spinor phase large as well, should one spatially unwind the phase. More details can be found in Chap. 5.

Lastly, we recall that the short-time dynamics starting from $Q_0 = 1$ and quickly reaching $Q_0 \ll 1$, implies that also large density fluctuations are present in the system at very early times, as the particles redistribute from the $m_F = 0$ component to the $m_F = \pm 1$ components. The system quickly relaxes into a state where the bulk of the dynamics happen within the relative phases of the complex fields, reflecting the process of spatial redistributions of bosons under the interaction-induced constraint of a nearly constant total density $\tilde{\rho}$, due to $|c_1| \ll c_0$ [75]. These dynamics reflect the system's attempt to adjust to the new quantum phase, as it strives to reach long-ranged order via a reduction of the number of the aforementioned causally disconnected patches.

4.1.3 SELF-SIMILAR SCALING DUE TO NTFP

As reported in Ref. [75], the patterns seen in the transverse spin, during the late-time evolution, cause the structure factor

$$S_{F_\perp}(t,k) = \langle F_\perp(t,k)^\dagger F_\perp(t,k)\rangle \tag{4.5}$$

to scale in time and (momentum) space according to the universal form

$$S_{F_\perp}(t,k) = (t/t_{\mathrm{ref}})^\alpha f_{\mathrm{s}}([t/t_{\mathrm{ref}}]^\beta k)\,. \tag{4.6}$$

Here f_{s} is a universal scaling function, which depends only on the momentum k, t_{ref} is a reference time within the scaling interval and the scaling exponents $\alpha = 0.28(6)$ and $\beta = 0.26(6)$ are, within errors, related by $\alpha = d\beta$, $d = 1$, ensuring the momentum integral over $S_{F_\perp}(t,k)$ to be conserved, see Fig. 4.1c. This is understood to signal the approach of a non-thermal fixed point characterised by the quoted universal scaling exponents as well as the scaling function $f_{\mathrm{s}}(k)$. Universality here means that, within a certain range of initial conditions and parameter values chosen, the time evolution leads to the same kind of scaling behaviour in time and space, irrespective of the details of the initial condition and the details of the chosen parameter values. We emphasise that the microscopic reason for the observed scaling exponents quoted above is unknown to date.

4.2 CAUSTICS IN THE SPINOR GAS

While utilising the notion of universality to obtain a macroscopic theory is the main aim of current research into NTFPs, a possible path to understanding and categorising the various universality classes lies within the investigation of microscopic dynamics in order to isolate the relevant mechanisms underlying the scaling evolution. As we have seen, the noisy dynamics of the spinor gas post-quench exhibits many forms of excitations, one of which can be investigated thoroughly using the notion of caustics and rogue waves, i.e., events of extreme intensity arising from the focusing of wave-fronts propagating through noisy media.

We observe that the highly excited system in its post-quench time evolution generates focusing of magnetic excitations into momentaneous rogue waves in the $m_{\mathrm{F}} = 0$ density, giving rise to density dips in the $m_{\mathrm{F}} = \pm 1$ modes, and thus to rogue-wave-like peaks in the velocity fields $v_{m_{\mathrm{F}}} \sim \partial_x \varphi_{m_{\mathrm{F}}}$ (Fig. 4.2). These rogue waves can be characterised as caustics [152–159], which are signalled by the scintillation index

$$S_v(t) = \frac{\langle |v_{\mathrm{L}}|^2\rangle_x}{\langle |v_{\mathrm{L}}|\rangle_x^2} - 1 \tag{4.7}$$

as rare extreme events in the velocity fields, where $\langle\cdots\rangle_x$ denotes the spatial average and $v_{\mathrm{L}} = 2\partial_x\varphi_{\mathrm{L}} = v_1 - v_{-1}$. At times where the system shows strong phase kinks, we expect a strong sudden rise in the scintillation index (see Fig. 4.3b). We observe that at certain times, a localised

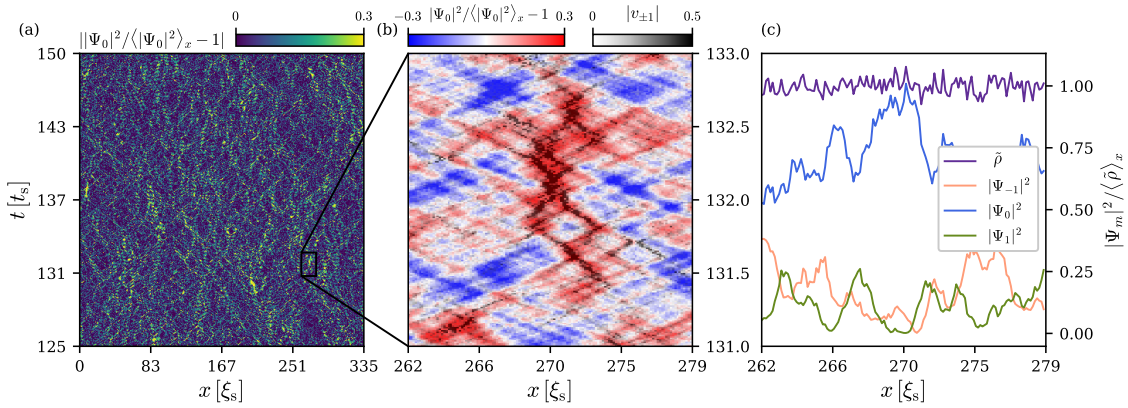

Figure 4.2: (a) Time evolution of the relative fluctuations $||\Psi_0|^2/\langle|\Psi_0|^2\rangle_x - 1|$ of the $m_F = 0$ field amplitude around the spatial average $\langle|\Psi_0|^2\rangle_x$. Caustics show up as spikes in the relative density. (b) Magnification of a set of caustics demonstrating this spatio-temporal correlation. The deviation of the density $|\Psi_0|^2$ from its average is shown in blue to red color scale. Overlayed on top are the velocity spikes $|v_{\pm1}|$, demonstrating the correlation of a rise in density with the phase defects in the magnetic side modes. (c) The total density being approximately flat implies that the spikes seen in panel (a) correlate with dips in the magnetic side modes $m_F = \pm1$.

wave in the velocity field of the $m_F = 1$ component meets a different localised wave in the velocity field of the $m_F = -1$ component. When the two waves meet, they create a spike in the velocity field associated with the Larmor phase v_L, resulting in a rogue wave in the transverse spin degree of freedom. The importance of the rogue wave excitations appearing during the post-quench dynamics lies within the understanding of their statistical properties.

4.2.1 UNIVERSAL STATISTICS OF ROGUE WAVES IN RANDOM MEDIA

An important question typically considered in the theory of caustics in random media concerns the relation between the temporal and spatial scales characterising the frequency of the occurrence of rogue waves and their mean separation in space, respectively. To this end, one determines, starting from some random initial state, the mean *time to first caustics* on the basis of the spatio-temporal correlations of the random noise potential. We give here a rough sketch of the derivation of the time to first caustics as presented by the arguments of [152–155] in order to gain intuition into this process, before we present the spin-1 case in the next section.

The time to first caustics is inferred from the solution of the classical equations of motion of point particles in the random potential V,

$$dx(t)/dt = p_x(t)/m\,, \qquad dp_x(t)/dt = -\partial V(x,t)/\partial x\,, \tag{4.8}$$

i.e., integrating over time, from

$$x(t) = x_0 + \frac{p_0}{m}(t - t_0) - \int_{t_0}^{t} \mathrm{d}t' \int_{t_0}^{t'} \mathrm{d}t'' \frac{\partial V(x,t'')}{\partial x}\,, \tag{4.9}$$

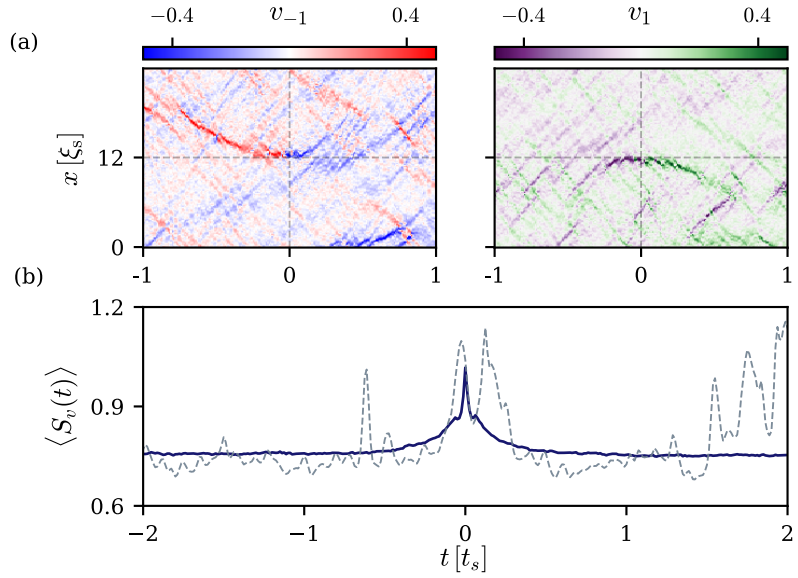

Figure 4.3: Characteristics of caustics in the system after a quench. (a) Excerpt of the space-time evolution of phase defects in the system. The phase gradients $v_1 = \partial_x\varphi_1$ (purple to green) and $v_{-1} = \partial_x\varphi_{-1}$ (red to blue) show the formation of rogue-wave-like excitations in the condensate which focus on a singular point marked by the cross. (b) The scintillation index $S_v(t)$, Eq. (4.7), around a rogue wave at $t = 0$. The blue solid line shows the scintillation profile averaged over $\sim 10^3$ (not normalised) rogue waves. The dashed line depicts $S_v(t)$ for the single truncated Wigner run in (a).

with $x_0 = x(t_0)$, $p_0 = p_x(t_0)$ defining the initial position and momentum. This is equivalent to considering the motion of particles with large linear velocity p_y/m in a weak two-dimensional random potential $V(x, y)$, in the paraxial approximation, $p_y \gg p_x$. Choosing $x_0 = p_0 = 0$, the mean squared variation of rays at time t results as

$$\left\langle x(t)^2 \right\rangle = \int_{t_0}^{t} \mathrm{d}t' \int_{t_0}^{t} \mathrm{d}\bar{t}' \int_{t_0}^{t'} \mathrm{d}t'' \int_{t_0}^{\bar{t}'} \mathrm{d}\bar{t}'' \left\langle \frac{\partial V(x,t'')}{\partial x} \frac{\partial V(x',\bar{t}'')}{\partial x'} \right\rangle \Bigg|_{x=x'}, \tag{4.10}$$

where the average is taken over many realisations of the noise potential.

In the theory of caustic formation, the temporal correlations are often assumed to be Markovian, i.e., proportional to a delta-distribution in the relative time,

$$C_V(\tau) = \langle V(x,t)V(x,t+\tau)\rangle = V_0^2(t)\tau_0\,\delta(\tau)\,, \tag{4.11}$$

with some time constant τ_0. Furthermore, the spatial correlations of the potential typically show some Gaussian or exponential fall-off, e.g.,

$$C_V(r) = \langle V(x,t)V(x+r,t)\rangle = V_0^2(t)\,\mathrm{e}^{-r/\ell_V(t)}\,. \tag{4.12}$$

We note that the analysis is not restricted to these forms of correlations. It can be shown that any correlation function $C_V(r, \ell_V)$ with a characteristic fall-off scale can be used in this derivation.

Finally, the time to first caustics t_c is estimated by evaluating the noise correlator, integrate it over time, and demand that the variance at time $t = t_0 + t_c$ is on the order of the correlation length squared ℓ_V^2 of the noise. This condition implies that caustics occur as the result of focusing of rays originating from a window around the focusing point the size of which corresponds to the scale on which the potential varies. From Eq. (4.10) one thus finds the scaling relation

$$t_c \sim \ell_V^{4/3}. \tag{4.13}$$

4.2.2 DERIVATION OF ROGUE-WAVE SCALING IN THE SPIN-1 GAS

In the spin-1 Bose gas considered here, all particles belong to one of the three magnetic sublevels. The underlying timescale of caustic focusing of strong wave excitations can be described in the framework of a stochastic non-linear Schrödinger equation (NLSE) [160–162]. Specifically, the system follows the classical field equation:

$$\mathrm{i}\partial_t \boldsymbol{\Psi} = \left[-\frac{\partial_x^2}{2M} + q f_z^2 + c_0 n + c_1 \boldsymbol{F}\cdot\boldsymbol{f}\right]\boldsymbol{\Psi}\,. \tag{4.14}$$

Due to the strong density-density interactions and the disordered behaviour of the spin-changing term, as seen in Fig. 4.1a,b, the last term of Eq. (4.14) can be considered as a fluctuating weak random potential added to a NLSE when neglecting backreaction,

$$V(x,t) \equiv c_1 \boldsymbol{F}(x,t)\cdot\boldsymbol{f} = c_1 \begin{pmatrix} F_z & F_\perp^* & 0 \\ F_\perp & 0 & F_\perp^* \\ 0 & F_\perp & -F_z \end{pmatrix}(x,t). \tag{4.15}$$

Hence, it comprises the spin-spin coupling, which, together with the quadratic Zeeman shift $\sim q f_z^2$, breaks the U(3) symmetry of the model by lifting the energy degeneracy and allowing for spin-changing collisions. Therefore, in order to estimate the time to first caustics, the full three-component equation needs to be taken into account. The matrix potential $V(x,t)$, due to $|c_1| \ll |c_0|$ and its non-linear dependence on the fluctuating fields, effectively takes the role of a weak noise which causes the spin-wave excitations to form caustics, as they propagate in time.

Analogously to the above introduced arguments of [152–155], we estimate the time to first caustics in a semi-classical way. Assuming the excitations leading to caustics are dominated by Goldstone-type excitations which redistribute particles within single magnetic sublevels while the total density $\tilde{\rho}$, subject to the density-density interactions $c_0\tilde{\rho}^2$ remains nearly constant, we aim to estimate the time to first caustics from the time evolution of the fields capturing the three sublevels. Note that all assumptions made during the derivation will be numerically justified in the next section.

We consider a caustic at some time t_0 in sublevel m, which is described by a distribution of the deviation $\delta\Psi_m(x,t_0) \equiv \Psi_m(x,t_0) - \langle\Psi_m\rangle$ from a stationary mean value $\langle\Psi_m\rangle$, peaked around a position x_0, with width

$$\langle[x-x_0]^2\rangle_{m,t_0} = \frac{\int \mathrm{d}x\,(x-x_0)^2|\delta\Psi_m(x,t_0)|^2}{\int \mathrm{d}x\,|\delta\Psi_m(x,t_0)|^2} \simeq \xi_\mathrm{s}^2 \tag{4.16}$$

being on the order of the spin healing length, as can be inferred from Fig. 4.2. The task is to estimate the temporal increase of the variance $\langle[x(t)-x_0]^2\rangle_m$ due to the evolution in the noisy potential formed by the other magnetic components. For this, we need to estimate the time evolution of the field starting from the caustic peak $\delta\Psi_m(x,t_0)$.

This evolution is governed by the Hamiltonian (2.4), which can be split into a Bogoliubov mean-field (MF) part and the rest, $H = H_\mathrm{MF} + \delta H_V$, where the Bogoliubov MF term, which is at most quadratic in the fields Ψ_m, gives rise to a coherent background evolution. As we can neglect, to a good approximation, Bogoliubov fluctuations of the total density $\tilde{\rho}$, the main contribution will arise from the gapless spin-wave excitations present in the easy-plane phase. Furthermore, as the width of the caustic peak is on the order of the spin healing length, wave numbers contributing to the packet are $k \lesssim k_{\xi_\mathrm{s}} \sim 1/\xi_\mathrm{s}$. Hence, the evolution with H_MF causes the wave packet to (split and) move, without dispersing, at the speed $c_\mathrm{s} = (\tilde{\rho}|c_1|/2M)^{1/2}$,

$$U_\mathrm{MF}^\dagger(t,t_0)\delta\Psi_m(x,t_0)U_\mathrm{MF}(t,t_0) \simeq \delta\Psi_m(x-c_\mathrm{s}[t-t_0],t_0)\phi_m(x,t)\,. \tag{4.17}$$

Here $U_\mathrm{MF}(t,t_0) = \exp\left(-\mathrm{i}\int_{t_0}^t \mathrm{d}t' H_\mathrm{MF}\right)$, and we neglect possible weak effects from dispersion in higher wave numbers. While the time evolution shifts the position of the wave packet, it in general also involves fast phase oscillations with a frequency on the order of $\sim \omega(k_{\xi_\mathrm{s}})$, which are taken into account by the, not further specified, multiplicative factor $\phi_m(x,t)$ which takes the form of a complex oscillating function of norm $|\phi_m(x,t)| \lesssim 1$, cf. Fig. 4.2.

Besides this coherent propagation of the packets with the speed of sound, the wave packet spreads out due to the motion in the noisy background potential which enters the interaction Hamiltonian $H_V(t) = \int \mathrm{d}x\,\Psi_m^\dagger(x)V_{mn}(x,t)\Psi_n(x)$ and thus the beyond-MF part $\delta H_V = H_V - H_{V,\mathrm{MF}}$. Note that we neglect beyond-MF contributions from the density-density interactions $\sim c_0\tilde{\rho}^2$ and that the potential V is taken to represent a time-varying background potential despite the fact that the field operators Ψ_m are evaluated at the fixed initial time t_0. The resulting beyond-MF Hamiltonian encodes the noisy background, which fluctuates on lengths scales set by the fluctuations of F_z and $F_\perp$, cf. Eq. (4.15).

Taking $\ell_\Lambda \gg \xi_\mathrm{s}$, we can Taylor expand the noise potential at the position of the caustic peak to first order around a constant background,

$$V(x,t) = V(x_0,t) + \left.\frac{\partial V}{\partial x}\right|_{x=x_0}(x-x_0) + \ldots\,, \tag{4.18}$$

and neglect the constant term, which causes the MF evolution to be corrected essentially to include a non-zero width of the dispersion.

The time-evolution operator $U(t,t_0) = \exp\left(-\mathrm{i}\int_{t_0}^{t} \mathrm{d}t' H\right)$ can be split into a fast mean-field part and a slow evolution caused by V,

$$U(t,t_0) = U_{\mathrm{MF}}(t,t_0) \times \exp\left[-\mathrm{i}\int_{t_0}^{t} \mathrm{d}t' U_{\mathrm{MF}}^{\dagger}(t'-t_0)\delta H_V(t') U_{\mathrm{MF}}(t'-t_0)\right]. \tag{4.19}$$

Combining the above expressions, we can now calculate the approximate broadening of the travelling wave packet due to the external noise V,

$$\begin{aligned}
&\left\langle [x - c_{\mathrm{s}}(t-t_0) - x_0]^2 \right\rangle_{m,t} \\
&\simeq \mathcal{N}_m^{-1} \int \mathrm{d}x\, [x - c_{\mathrm{s}}(t-t_0) - x_0]^2 \Big\{ |\delta\Psi_m(x - c_{\mathrm{s}}[t-t_0], t_0)|^2 \\
&+ \delta\Psi_m^*(x - c_{\mathrm{s}}[t-t_0], t_0) \int \mathrm{d}t'\, \mathrm{d}t''\, \left\langle \frac{\partial V_{ml}(x',t')}{\partial x'} \frac{\partial V_{ln}(x'',t'')}{\partial x''} \right\rangle_V \Big|_{x'=x''=x_0} \delta\Psi_n(x - c_{\mathrm{s}}[t-t_0], t_0) \\
&\quad \times [x - c_{\mathrm{s}}(t-t') - x_0]\, [x - c_{\mathrm{s}}(t-t'') - x_0] \Big\},
\end{aligned} \tag{4.20}$$

where $\mathcal{N}_m = \int \mathrm{d}x\, |\delta\Psi_m(x,t_0)|^2$ is a normalisation, the mean value $\langle \cdots \rangle_V$ denotes averaging over the noise potential and we have dropped terms linear in V, as they vanish when taking this average. We have also neglected any fast rotating phases, which will play a role in any single realisation of the potential but are expected to average out in the mean. Note that the covariance of the noise involves a matrix product of the potential, which takes the form

$$\begin{aligned}
C_V(r) &= \langle V(x,t) V(x+r,t) \rangle_V \\
&= \left\langle \begin{pmatrix} F_z(x)^* F_z(x+r) + F_\perp(x)^* F_\perp(x+r) & 0 & F_\perp(x)^* F_\perp(x+r)^* \\ 0 & F_\perp(x) F_\perp(x+r)^* + \text{c.c.} & 0 \\ F_\perp(x) F_\perp(x+r) & 0 & F_z(x)^* F_z(x+r) + F_\perp(x) F_\perp(x+r)^* \end{pmatrix} \right\rangle_V .
\end{aligned} \tag{4.21}$$

On average, the off-diagonal elements of this matrix vanish due to the recovery of the spontaneously broken SO(2) symmetry of the spin configuration in the easy plane, when averaging over many realisations of the potential, see the circle-shape histogram shown in the upper panel of Fig. 4.7d. Considering a spatial correlation with a characteristic fall-off scale ℓ_V and Markovian temporal correlations, we may integrate over t'', which thereby is set equal to t'. Finally, the spatial averaging done by integrating over x evaluates (4.20) to become

$$\left\langle [x - c_{\mathrm{s}}(t-t_0) - x_0]^2 \right\rangle_{m,t} \simeq \xi_{\mathrm{s}}^2 \left\{ 1 + \frac{\pi}{3} V_{0,m}^2 \frac{\ell_\tau c_{\mathrm{s}} t^3}{\ell_V^2} \right\}. \tag{4.22}$$

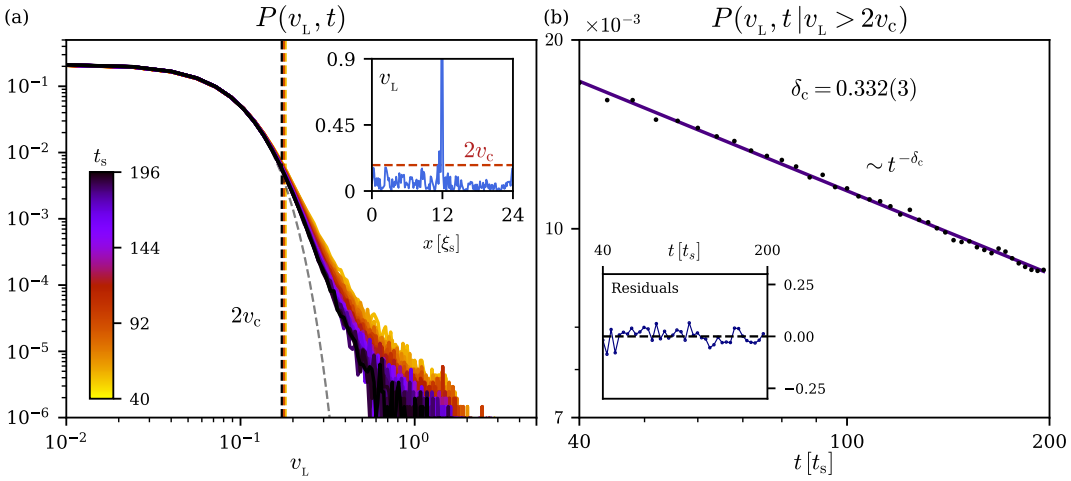

Figure 4.4: Statistics of caustics after a quench. (a) PDF of the local Larmor velocity $v_L = 2\partial_x\varphi_L = \partial_x(\varphi_1 - \varphi_{-1})$ for different times. The PDF takes the form of a Rayleigh exponential distribution (grey dashed line fit) with a heavy tail. The extreme events are characterised as those with an amplitude larger than $2v_c$, where v_c is the scale velocity, representing the mean of the upper tertile of events. The inset shows that $v_L > 2v_c$ at the focusing time (see Fig. 4.3). (b) The probability of finding an extreme event as a function of time. A power law decay $t^{-\delta_c}$, with $\delta_c = 0.332(3)$ is found. The inset shows the deviation of the fit from the data divided by the data point error.

For times $c_s t \gg \xi_s$, the term $\sim t^3$ dominates the width. Hence, as discussed above for the case of classical particles, demanding that the variance (4.22), at the time $t = t_c$ to first caustics, is on the order of ℓ_V^2, one obtains again the scaling relation for the mean time to first caustics,

$$t_c \sim \left(V_{0,m}^2 \ell_\tau c_s\right)^{-1/3} \ell_V^{4/3}\,. \tag{4.23}$$

4.2.3 ROGUE WAVE STATISTICS IN TRUNCATED WIGNER SIMULATIONS

We now turn to the numerical investigation of the coarsening dynamics of caustics in the spin-1 gas post-quench. Note that, as before, we characterise the intensity of caustics by means of the gradient of the Larmor phase.

It is well known that the probability distribution function (PDF) of intensities shows a long-tailed behaviour when rogue waves are present in the system [163–165]. Constructing such a PDF of the Larmor phase velocity field, we obtain a heavy-tailed Rayleigh exponential form, thus confirming the presence of rogue waves in the Larmor phase, see Fig. 4.4a. Furthermore, the PDF of $\ln v_L$ as shown in Fig. 4.5a corroborates that the formation of caustics in the system is characterised by the propagation of coherent waves in a random background [154], hence justifying our assumption in the previous section. From the PDF, one obtains a scale *velocity of significant waves*, v_c, as the mean of the upper tertile of the PDF. The criterion for rogue waves is then chosen to include those with an amplitude $v_L > 2v_c$, as is conventionally done in literature [165]. Fig. 4.4d shows that the probability of such rare events to occur decays in time as a power law, $P(v_L, t|v_L > 2v_c) \sim t^{-\delta_c}$, with a new exponent $\delta_c = 0.332(3)$.

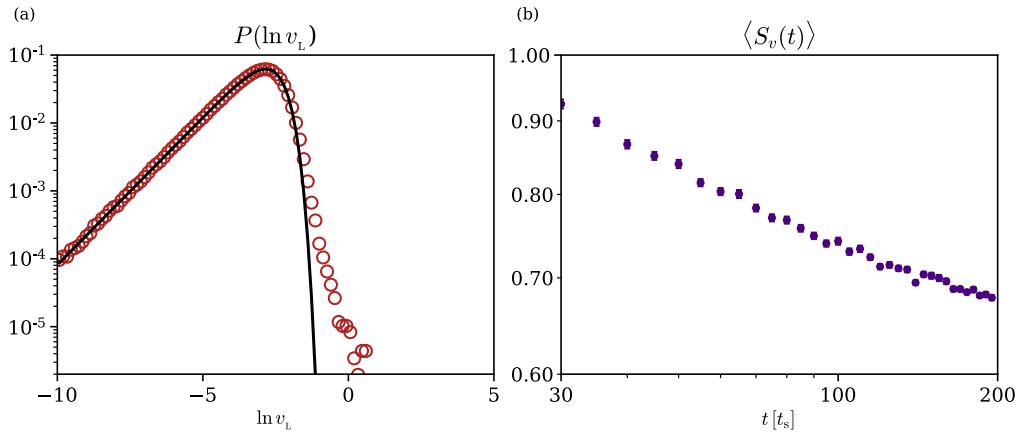

Figure 4.5: Statistics of caustics in the spin-1 gas. (a) PDF of $\ln v_{\perp}$ showing a Rayleigh exponential distribution with a heavy tail, in accordance with quantum dynamics of coherent wave packets [154]. (b) Time evolution of the scintillation index averaged over all realisations on a double logarithmic scale. The scintillation index decays over time, confirming the decrease in the occurrence of rogue wave events.

In order to explain the appearance of this new exponent, we study the statistical properties of the random potential (4.15). Recall that for propagation in random media, the time needed for the waves to focus, i.e., the mean time to caustics t_c, depends only on the correlation length and on the strength of the fluctuations of the random medium, as derived in the previous section. Our numerical simulations find that the diagonal elements of Eq. (4.21) exhibit, to a good approximation, correlations of exponential form in the diagonal elements

$$\langle \mathrm{Tr}[V(x,t)V(0,0)] \rangle = V_0^2 \exp\left[-x/\ell_V(t) \right], \tag{4.24}$$

with fluctuation strength V_0 and a correlation length scale ℓ_V.The off-diagonal elements of the correlation matrix vanish due to the recovery of SO(2) symmetry when averaging over statistical realisations. The recovery of SO(2) symmetry also results in a vanishing mean for the noise potential $\langle V \rangle = 0$. Thus, we find that the fluctuations of the Larmor phase and thus of $F_{\perp}$ dominate the correlations while those of F_z can be neglected. Furthermore, The temporal correlations show a nearly Markovian character (4.11), as is seen in Fig. 4.6b, where we fit a Lorentzian to the τ-dependence,

$$C_V(\tau) = \frac{V_0^2(t)}{1 + [c_s \tau/\ell_\tau(t)]^2}, \tag{4.25}$$

with $\ell_\tau(t)$ constant in time.

In contrast to the standard case studied in the context of caustics, the intricate non-linear interactions between the components of the condensate cause the correlation length ℓ_V to dynamically scale in time. This is a manifestation of the spatio-temporal scaling of the structure factor of the transverse spin (4.5), as seen in Fig. 4.1c. There, the infrared wave number $k_\Lambda \sim \ell_\Lambda^{-1}$ marking the onset of the plateau in the structure factor scales as $k_\Lambda \sim t^{-\beta_\Lambda}$, in accordance with the self-similar scaling of the spectra. Therefore, the universal scaling of the structure factor is reflected in the

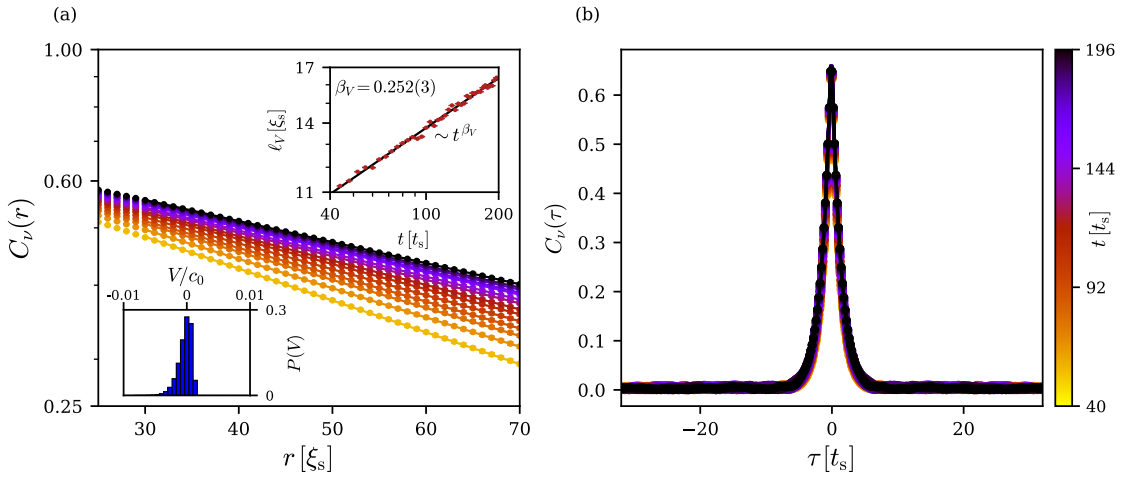

Figure 4.6: (a) Correlation function $C_V(r) = \left\langle \int \mathrm{d}x\, V(x,t)V(x+r,t) \right\rangle$ of the random potential term in Eq. (4.15). $C_V(r)$ takes the form of an exponential function $\exp(-r/\ell_V)$ with a time varying characteristic correlation length $\ell_V \sim t^{\beta_V}$, with $\beta_V = 0.252(3) \simeq \beta$ (upper inset). The lower inset shows the potential is weak in comparison to density fluctuations. (b) Temporal correlation function $C_V(\tau) = \left\langle \int \mathrm{d}x\, V(x,t)V(x,t+\tau) \right\rangle$. The correlation shows a fast decaying Lorentzian with constant correlation time ℓ_τ.

coarsening of the length scale which characterises the size of the coarsening patterns in the Larmor phase $\ell_\Lambda(t) \sim t^{\beta_\Lambda}$. The correlation length of the noise term Eq. (4.15) is then associated with ℓ_Λ, since the diagonal elements of Eq. (4.21) are given by the Fourier transform of the transverse spin structure factor. Our numerical simulations confirm that the noise correlation length scales with $\ell_V \sim t^{\beta_V}$ with $\beta_V = 0.252(3)$ (see Fig. 4.6a), hence corroborating $\beta_V \simeq \beta_\Lambda$ within the error bounds. Thus, the temporally growing correlation length scales as a power law in time with an exponent $\beta_V \simeq 1/4$, implying, according to Eq. (4.23), that the mean time to caustics scales in time as $t_c \sim t^{\delta_c}$, with $\delta_c = 4\beta_V/3 \simeq 1/3$.

Our results support the interpretation that a caustic in one of the magnetic sublevels is caused by the fluctuating potential, the respective other components effectively represent for its time evolution. While the non-linear coupling present in the three-component system eventually gives rise to the dynamics seen, a separation into single modes evolving in a fluctuating background formed by the respective other ones, allows for a basic characterisation of the observed relation between the temporal and spatial scales.

4.3 INSTANTONS IN THE SPIN-1 GAS

4.3.1 INSTANTON STRUCTURE AND CHARACTERISATION

The extreme events investigated in the previous section give rise to an interesting topological phenomenon in the Larmor phase of the spin-1 gas. We observe that at the intersection of phase kinks, where a strong rogue wave in the Larmor phase occurs, we witness a vortex in space-time, which gives rise to a change in the system's winding number, thus taking on the form of

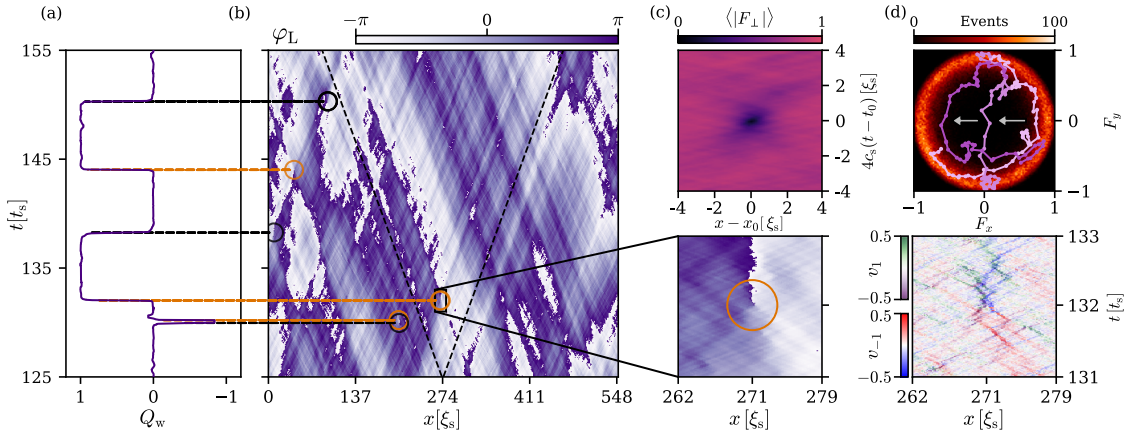

Figure 4.7: Structures and defects in the time evolution of the Larmor phase after a quench (units chosen as in Fig. 4.4). (a) Time evolution of the winding number Q_w for the run shown in panel (b). (b) Space-time evolution of the Larmor phase of the transversal spin $F_\perp = |F_\perp| \exp[i\varphi_L]$ across the entire system in a single truncated-Wigner (TW) run, with the spin speed of sound $c_s = \sqrt{\tilde{\rho}|c_1|/2M}$ (dashed line). In the strongly fluctuating system, vortex structures in space and time are observed, as the phase wraps around one point (cf. zoom in panel (c)). Instantons (orange) and anti-instantons (black), each cause an integer jump in the winding number $Q_w(t)$. (c) Structure of the real-time instanton. In the upper panel, the averaged $|F_\perp|$ profile of a defect located at x_0 at time t_0 is depicted. The lower panel shows the vortex-like nature of the defect in more detail, around which the Larmor phase winds by 2π. (d) The lower panel shows the corresponding intersection of two rogue waves in $v_{\pm1}$ at the position of the instanton, recall Fig. 4.4a. The upper panel exhibits the temporal evolution (bright to dark pink) of the $F_\perp$ field configuration in spin space, within the window shown in the lower panels. The outer circle represents a histogram (black to bright red color code) of spin orientations in the F_x-F_y plane averaged over 100 TW runs.

an instanton in real time. Instantons are of strong relevance in fundamental studies of quantum field theory and matter [166, 167], as well as various applications, including false vacuum decay [168–170]. Phenomena closely related to the real-time instantons we study here include coherence vortices [171] and phase slips [172–176].

One such instanton is shown in Fig. 4.7c at a time $t \simeq 132\,t_s$ and position $x \simeq 271\,\xi_s$. In Fig. 4.7a, b, we identify the direct correlation between a jump in the system's winding number and the appearance of such a vortex or anti-vortex structure in space-time. In the upper panel of Fig. 4.7d, we demonstrate that the defect manifests itself as a trajectory of the field configuration in the vicinity of this point propagating through the center of the transversal spin plane (or the spin sphere), causing a local reduction in spin length.

Interestingly, the trajectory on the spin sphere implies a sharp jump in the Larmor phase at the core of the space-time vortex. In contrast, this event does not show a topological character on the spin-nematic sphere. There, the field configuration leaves the $F_\perp$-$Q_\perp$ plane and acquires a non-zero Q_0 value, allowing it to connect to the opposite side of the sphere via a trajectory near the pole, see red curve in Fig. 4.8. Although the trajectory on the spin-nematic sphere exhibits a smooth interpolation between $\varphi_s \approx 0$ and $\varphi_s \approx 2\pi$, the corresponding path on the spin sphere involves a sudden π jump in the Larmor phase. This occurs since neighbouring points must now instantaneously flip their spin orientation to the opposite direction. Despite lacking any topologi-

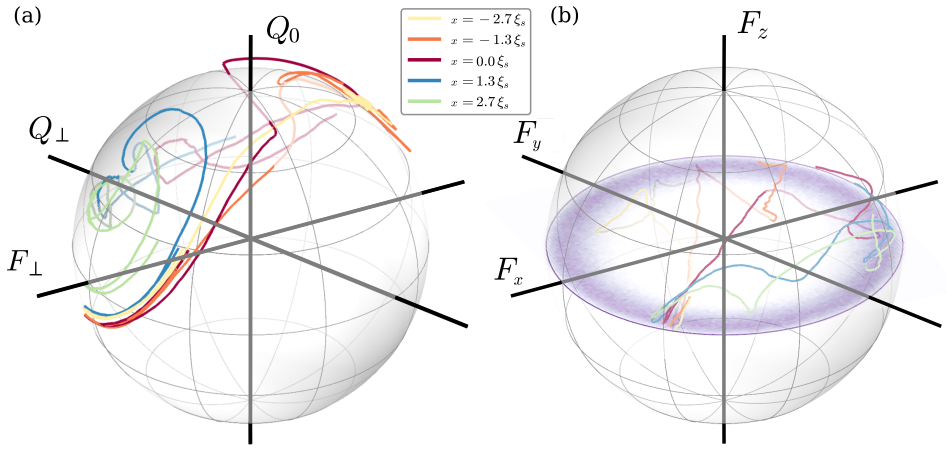

Figure 4.8: Instanton trajectory on the spin and spin-nematic spheres. (a) Trajectories in time for various spatial distances (yellow to green) from the instanton origin on the spin-nematic sphere. Far away enough from the instanton, the trajectories remain fluctuating near the fixed point. At the origin (red line, $x = 0$), the instanton trajectory goes over to the other side in time, by leaving the $F_\perp$-$Q_\perp$ plane and passing near the north pole of the sphere. (b) The same trajectories are shown on the spin sphere. As seen in Fig. 4.7, the trajectory in the origin of the instanton goes through the center of the spin sphere, thus creating a strong phase kink in the Larmor phase.

cal nature in the spinor phase, such processes are crucial to the formation of topological defects in the Larmor phase, as they push the field value to the next Riemann sheet. In Chap. 5 we shall see that these processes are a hallmark of the underlying effective model of the spin-1 gas in the easy plane.

As a result of this π jump, the Larmor phase wraps into the next Riemann sheet, giving rise to a change of the overall winding number of the Larmor phase,

$$Q_{\mathrm{w}} = \frac{1}{2\pi} \int_0^{\mathcal{L}} \mathrm{d}x \; \partial_x \varphi_{\mathrm{L}} \in \mathbb{Z}\,, \tag{4.26}$$

where $\mathcal{L}$ is the length of the system. With the help of a plaquette algorithm correlating jumps in the Larmor phase and dips in the spin length, we localise the instantons in space and time, allowing us to probe their statistics.

4.3.2 INSTANTON STATISTICS FOLLOWING ROGUE WAVE STATISTICS

During the evolution of the system following the quench, the density of (anti-)instantons decreases, and the probability of the system producing a topological defect reduces as it attempts to settle to a state with constant winding number, see the lower panel of Fig. 4.9a. We recall that such a reduction in instanton density is already signalled in Fig. 4.4 by the decreasing rogue-wave probability.

Due to the topological nature of these defects, they are robust and easily distinguishable from the noisy background, enabling us to isolate them from the plethora of excitations found in the system, thus making them a dependable observable to probe the system's dynamics. To extract

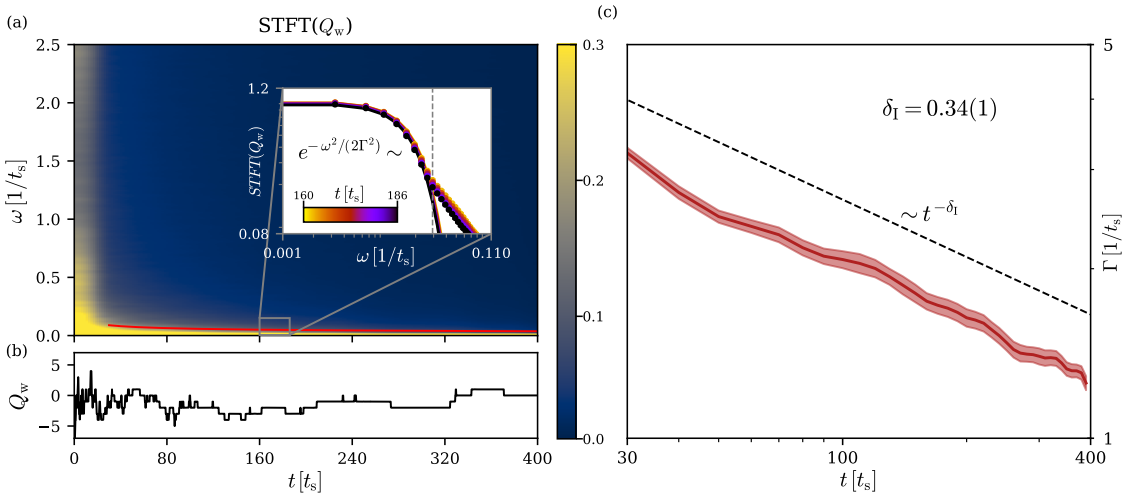

Figure 4.9: Statistics of the instantons after a quench. (a) Short-time Fourier transform (STFT) of the winding number $Q_w(t)$ (main panel, color scale), exhibiting a Gaussian fall-off for small frequencies (up to the grey dashed line in the inset) $\mathrm{STFT}[Q_w](t) \sim \exp\{-\omega^2/[2\Gamma^2(t)]\}$ (inset), with width decreasing as $\Gamma(t) \sim t^{-\delta_I}$, $\delta_I = 0.34(1)$ as seen in (c), confirming power-law coarsening dynamics of the governing timescale of Q_w as seen in (b). The lower panel shows the time evolution of the winding number Q_w for a single realisation.

the instanton probability decay, we first calculate the winding number $Q_w(t)$ over time for each truncated Wigner realisation and perform a short-time Fourier transform (STFT) of $Q_w(t)$ over time windows of width $\Delta t_{\mathrm{STFT}} = 70\,t_s$, averaging over $\sim 10^3$ realisations. The time window for the STFT was chosen such that it still contains the largest timescale in the system to avoid numerical artefacts. The resulting transform $\mathrm{STFT}[Q_w](t,\omega)$ is shown in color scale in Fig. 4.9a. We observe a down-chirp in the frequencies of the instanton appearances. At each time, the winding number jumps display a frequency spectrum with an approximate Gaussian fall-off (cf. inset of Fig. 4.9a)

$$\mathrm{STFT}[Q_w](t,\omega) \sim \exp\{-\omega^2/[2\Gamma^2(t)]\}\,, \tag{4.27}$$

with frequency scale Γ which is extracted via a least-squares fit. We find Γ to be decreasing in time as $\Gamma(t) \sim t^{-\delta_I}$, with $\delta_I = 0.34(1)$ (see Fig. 4.9b). Hence, by identifying the appearance of instantons as indicators of rogue-wave events, this analysis confirms the scaling of the underlying mean time to caustics within the error bounds.

To investigate the behaviour of the underlying spatial coarsening of the system, we recall the vortex structures shown in Fig. 4.7 giving rise to a length scale in φ_L via strong wave excitations that result from the defect. After such an event, strong kinks in the Larmor phase give rise to the domains of approximately equal order parameter. The detection of these Larmor phase textures and their propagation through the condensate is done with the help of the topological current $j_0 = \partial_t \varphi_L$. To quantify the spatial and temporal correlations of these defects, we identify their

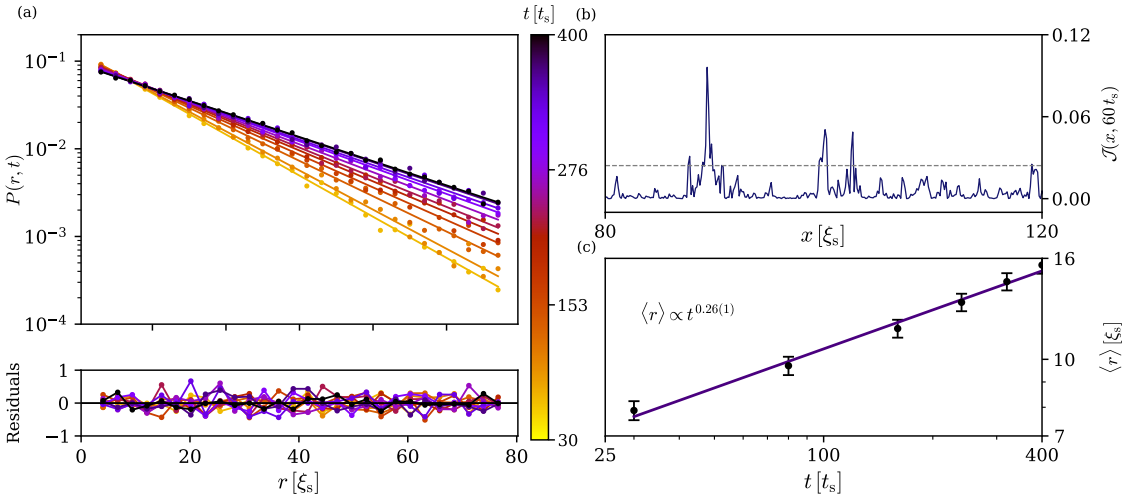

Figure 4.10: (a) The PDF of spatial defect separation is found to fall off exponentially, $P(r,t) \sim A(t)\exp[-r/\zeta(t)]$, with mean distance $\langle r\rangle(t) \sim t^{\beta_I}$, increasing from early times (yellow) to later times (black), exhibiting power-law coarsening with exponent $\beta_I = 0.26(1)$ (lower panel of (b)). The lower panel shows the difference of the data to the fit function divided by the standard deviation of each data point. (b) The upper panel shows the chosen threshold of the current $\mathcal{J}(x,t) = |\partial_x\varphi_L| \cdot (\langle|F_\perp|\rangle_x - |F_\perp|)$ for defect detection which corresponds to the top decile of amplitude.

positions by weighting the current with dips in the spin length, which results in the topological current

$$\mathcal{J}(x,t) = |\partial_x\varphi_L(x,t)| \cdot [\langle|F_\perp|\rangle_x - |F_\perp(x,t)|] \ . \tag{4.28}$$

where $\langle\cdots\rangle_x$ denotes the spatial average.

In order to calculate a characteristic length scale at each time, we utilise peak detection algorithms on the topological current $\mathcal{J}$, setting the peak values to be in the upper 10th percentile of its distribution function, ensuring that we detect extreme events, cf. the upper panel of Fig. 4.10b. In Fig. 4.10a, we depict the probability of the spatial separation of defects in the system, i.e., of the instantons of either charge. The resulting PDF exhibits a spatially exponential decay $P(r,t) \sim A(t)\exp[-r/\zeta(t)]$ with the mean separation increasing according to $\langle r\rangle(t) = \int \mathrm{d}r\, r\, P(r,t) \sim t^{\beta_I}$ with an exponent $\beta_I = 0.26(1)$, cf. the lower inset of Fig. 4.10b, corroborating the results obtained in [75]. We thus find, within the error bounds, the relation $\delta_c = 4\beta_V/3$ in the spatio-temporal scaling of the real-time instantons, which introduce a scale into the order parameter $F_\perp$.

4.4 CONCLUSION AND OUTLOOK

In this chapter, we have numerically investigated the microscopic dynamics of the spin-1 gas after a quench from the polar phase to the easy-plane phase. We observed the emergence of extreme rogue wave events in the velocity field of the Larmor phase, rising as a result of the propagation of Goldstone excitations through the disordered spin-changing dynamics, which act as an effectively random potential.

We analysed the statistics of rogue-wave events over time, and found that the probability of finding a rogue wave decays as a power law with a new exponent $\delta_c = 1/3$. To explain the appearance of this new exponent, we performed an analytical derivation of the time to first caustics, generalising the arguments of [152–155] to Bogoliubov excitations of coherent wave packets in the spin-1 gas. We saw that the timescale, being only dependent on the correlation of the noisy background, is found to scale as $t_c \sim \ell_V^{4/3}$. Interestingly, due to the intricate non-linear dynamics, self-similar scaling of the transverse spin correlations are observed in the dynamics. This phenomenon is captured by a coarsening of a correlation length of the transverse spin correlations in time with an exponent $\beta = 1/4$. The aforementioned derivation of the noisy potential shows that the diagonal elements of the correlation matrix are the only non-vanishing elements, and consist of precisely the transverse spin correlations. Hence, we obtain a time-varying correlation length $\ell_V \sim t^{\beta}$ which can be plugged into the varying timescale of mean time to caustics $t_c \sim t^{4\beta_V/3} \sim t^{1/3} \sim t^{\delta_c}$, thus explaining the appearance of this new exponent.

This result showcases that a non-thermal fixed point could be characterised by distinct, yet mutually connected scaling exponents, each governing the coarsening of the length– and timescales, respectively. Similarly, kinetic theory approaches used to obtain scaling exponents connect the appearance of the dynamical exponent z governing the dispersion relation $\omega(k) \sim k^z$ of the relevant excitations with the scaling of spatial scales. Such arguments usually predict $\beta = 1/z$ [120], which, e.g., for a standard diffusion type scaling, governed by free quasiparticle excitations would give $\beta = 1/2$. The connection of spatial and temporal scaling in our case may imply either a different dispersion relation, or that such arguments do not hold for the subdiffusive scaling in the presence of topological and highly non-linear excitations. A better understanding of this connection could aid possible analytical investigations aiming at predicting scaling exponents.

The focusing events in the Larmor phase velocity fields are observed to lead to a change in the overall winding number of the system in the Larmor phase, thus taking the form of an instanton in real-time. Such events are localised defects and can be observed as space-time vortices. The topological nature of these defects makes them easy to distinguish from the background, thus isolating the relevant excitation from the plethora of spin-textures present in this highly excited system, making them a reliable probe for the dynamics of rogue waves.

Performing a short-time Fourier transform on the winding number $Q_{\mathrm{w}}(t)$, we observe a down-chirp in the STFT spectrum, implying the decay in frequency of these events. The near-Gaussian fall-off of the frequency spectrum is shown to change its characteristic frequency scale as $\Gamma \sim t^{-0.34(1)}$ thus confirming the change in timescale of the rogue-wave appearance.

Furthermore, we investigated the spatial length scale of defect separation, as an instanton event brings about strong excitations in the transverse spin akin to domain walls. We obtain an exponential decay of defect separation probability with a changing length-scale over time $\langle r \rangle (t) \sim t^{1/4}$, confirming once more the spatio-temporal scaling of correlations as seen in the spectra of the transverse spin.

Our results present us with an important insight into the underlying mechanisms of the observed subdiffusive scaling. The investigation of the correlations shows that the scaling happens even when instantons are not present in the system, which happens at around $t \gtrsim 400 t_{\mathrm{s}}$. This implies

that instantons are mere proxy excitations, i.e., excitations that are carried by the dynamics, but not driving it. This substantiates the hypothesis that the subdiffusive scaling observed in the spinor gas is not topologically driven. The topological excitations in the Larmor phase make it possible to observe the length-scale and its coarsening in the transverse spin spectra, but the underlying reason for scaling must be a different one. In the next chapter, we discuss a possible explanation given by considering the dynamics of the spinor phase as the relevant degree of freedom. This shift in focus is already signalled by the structure of instantons in the spin-nematic sphere, where it is not of topological nature, but rather a strong non-linear excitation of the spinor phase. Should the spinor phase give rise to the scaling dynamics, then the instantons in the gas will follow the same scaling behaviour.

DOUBLE SINE-GORDON UNIVERSALITY CLASS OF THE SPIN-1 BOSE GAS

All my designs, simplified.

– Steven Wilson, "Arriving Somewhere but not Here"

In the previous chapter, we have seen the universal scaling dynamics of the spin-1 Bose gas. The presence of instanton defects in the system was discussed thoroughly, however a microscopic explanation to the scaling dynamics was yet to be identified. The development of a theory of coarsening resting on the microscopic properties of the system is a central long-standing problem in the research of far-from-equilibrium physics. Such a theory would allow the identification of the interaction mechanisms underlying a possible overarching universality class of the associated scaling dynamics. In quantum systems, this is complicated by the existence of non-linear and topological excitations due to the compact nature of phase degrees of freedom. In this chapter, we show that the double sine-Gordon model as a non-compact low-energy effective model of the spin-1 Bose gas accounts for subdiffusive coarsening dynamics, identifying field configurations spread over multiple wells of the sinusoidal potential as a precondition for the slow scaling. This is in contrast to diffusion-type scaling which the model is known to exhibit as well, where field configurations are seen to not extend over more than two wells. Experimental observations of a spinor BEC support these characteristics, thus constituting a platform for the investigation of sine-Gordon dynamics. Our results point to a path towards a classification of pattern coarsening in many-body systems on the basis of microscopic models.

This chapter is structured as follows: In Sect. 5.1, we give a brief introduction into the state of current research and the need for low-energy effective theories. We then proceed to discuss the subdiffusive scaling behaviour of the double sine-Gordon (DSG) theory in Sect. 5.2, and show that domain-size growth is not enough to explain subdiffusive coarsening. We show that the DSG also shows diffusion-type scaling in one spatial dimension, characterised by the occupation of only two minima. The DSG is then shown to be a low-energy effective theory of the spin-1 Bose gas in the easy-plane phase in Sect. 5.3, where we differentiate between a lowest-energy theory at vanishing momentum $k = 0$ and a theory at finite momenta. We compare numerical and experimental results in Sect. 5.4 and show that the DSG reproduces also the diffusion-type

scaling found in a spinor Bose gas in two spatial dimensions. Finally, we conclude with a short discussion and give an outlook at future projects stemming from this chapter in Sect. 5.5.

This chapter is taken and adapted from Ref. [2]. I stress that many parts are taken verbatim from the publication, yet the overall structure was reordered and the content was expanded upon to better fit the context of this thesis. This work was a theoretical and experimental collaborative effort. All numerical simulations and numerical data analysis were performed by me. The key idea of the analytical calculations as well as the calculations themselves were performed by me and A.-M. Glück. The experimental data was measured and analysed by Y. Deller, A. Schmutz, F. Klein and H. Strobel.

5.1 INTRODUCTION

The extensive study of universal phenomena far from equilibrium focusing on coarsening and phase-ordering kinetics has yet to develop a unifying scaling theory to account for these phenomena. Such a theory should ideally result from the underlying microscopic dynamics of the considered system, e.g., as a reduction to effective, relevant degrees of freedom. It would potentially lead beyond generalized diffusion models currently used to explain pattern coarsening in systems with two or more spatial dimensions. Such a framework would provide a scaling theory defining the universality class the coarsening process belongs to. A growing demand, as well as the potential for advancing such a framework is underlined by the extensive recent experimental [6, 18, 27, 31–33, 49–57, 97–101] and theoretical efforts [17, 59, 60, 63–96] exploring the nature of universal space-time scaling, to a large part in the field of ultracold atoms.

Coarsening and phase-ordering kinetics generically mean that order increases in a self-similar manner, characterised by the spatio-temporal scaling of order-parameter correlations. For example, in spinor quantum gases, which is the main focus of this thesis, subdiffusive, i.e, scaling with an exponent $\beta < 1/2$, as well as diffusion-type ($\beta = 1/2$) coarsening has been found in the structure of magnetic order. The task in question is to isolate the relevant degrees of freedom and their interactions that account for the specific scaling dynamics, thus possibly expanding upon the understanding of scaling dynamics in non-equilibrium systems. For multi-component Bose gases with interaction suppressed density fluctuations and U(N) symmetric interactions only, a low-energy effective theory (LEEFT), takes the form of a non-linear Luttinger-liquid type model of the phase excitations [106]. Assuming the absence of topological excitations, this effective theory makes it particularly easy to analytically account for the scaling exponents [106], which are confirmed numerically [120] and experimentally [6, 55], while their direct derivation from the full non-linear Schrödinger model is analytically cumbersome [119, 120]. If the pattern coarsening, however, involves topological excitations, one must take into account the compact phase of the quantum field in the statistical description of scaling. This is in particular the case for multi-component systems allowing inter-species exchange, such as spinor gases. There, non-linear excitations prevail, such as the instantons seen in Chap. 4, thus preventing an analytical scaling analysis so far [75, 77]. Hence, the reduction to an effective model explaining pattern coarsening is desirable, which accounts for the topological excitations in the underlying system.

5.2 DOUBLE SINE-GORDON DYNAMICS

In this section, we investigate the far-from equilibrium dynamics of the DSG model. To do so, we numerically simulate the DSG dynamics in one spatial dimension using a truncated Wigner approach [177], subsequently integrating the classical equations of motion with a simple leapfrog algorithm as introduced in Sect. 3.2.

5.2.1 SUBDIFFUSIVE SCALING IN 1+1D

Consider the DSG model with real-valued Lagrangian density

$$\mathcal{L} = \frac{1}{2}\dot{\varphi}^2 - \frac{c_\mathrm{s}^2}{2}(\nabla\varphi)^2 + \lambda\cos\varphi + \lambda_\mathrm{s}\sin^2\varphi\,, \tag{5.1}$$

with the free speed of sound c_s and DSG couplings λ and λ_s. From the Lagrangian (5.1), we can compute the classical equations of motion, reading

$$\ddot{\varphi} = c_\mathrm{s}^2\Delta\varphi - \lambda\sin\varphi + \lambda_\mathrm{s}\sin(2\varphi). \tag{5.2}$$

In order to achieve subdiffusive self-similar scaling far from equilibrium, we simulate a one-dimensional system with a numerical grid comprising of $N_\mathrm{g} = 4096$ points with $5\cdot 10^5$ particles. We further choose the couplings as $\lambda = 4\cdot 10^{-4} = 10\lambda_\mathrm{s}$ and $c_\mathrm{s} = 0.0262$ in numerical units. We initialise our fields in a general non-equilibrium momentum distribution chosen according to

$$\varphi(x,0) = \varphi_0 + \int_{-\infty}^{\infty}\frac{\mathrm{d}k}{2\pi}\sqrt{\frac{f_k+1/2}{\omega_k}}c_k\mathrm{e}^{\mathrm{i}kx}\,, \tag{5.3}$$

$$\dot{\varphi}(x,0) = \dot{\varphi}_0 + \int_{-\infty}^{\infty}\frac{\mathrm{d}k}{2\pi}\sqrt{(f_k+1/2)\omega_k}\tilde{c}_k\mathrm{e}^{\mathrm{i}kx}\,, \tag{5.4}$$

where $\omega_k = \sqrt{k^2+M^2}$, $M^2 = \lambda - 2\lambda_\mathrm{s}$ and the noise coefficients c_k, $\tilde{c}_k$ satisfy the relations

$$\left\langle c_k c_{k'}^*\right\rangle = 2\pi\delta(k-k'), \quad \left\langle c_k c_{k'}\right\rangle = \left\langle c_k^* c_{k'}^*\right\rangle = 0\,. \tag{5.5}$$

The latter constitutes the truncated Wigner noise for the numerical simulation of the system. The initial momentum distribution f_k is chosen as a distinctly non-equilibrium distribution

$$f_k = \begin{cases} \text{const.} & |k| < Q, \\ 0 & \text{elsewhere,} \end{cases} \tag{5.6}$$

resulting in an initial condition for the structure factor of the fundamental field $S(k,t) = \langle|\varphi(k,t)|^2\rangle$ reflecting a box distribution in momentum space with cutoff Q (Fig. 5.1a, blue line). We then cen-

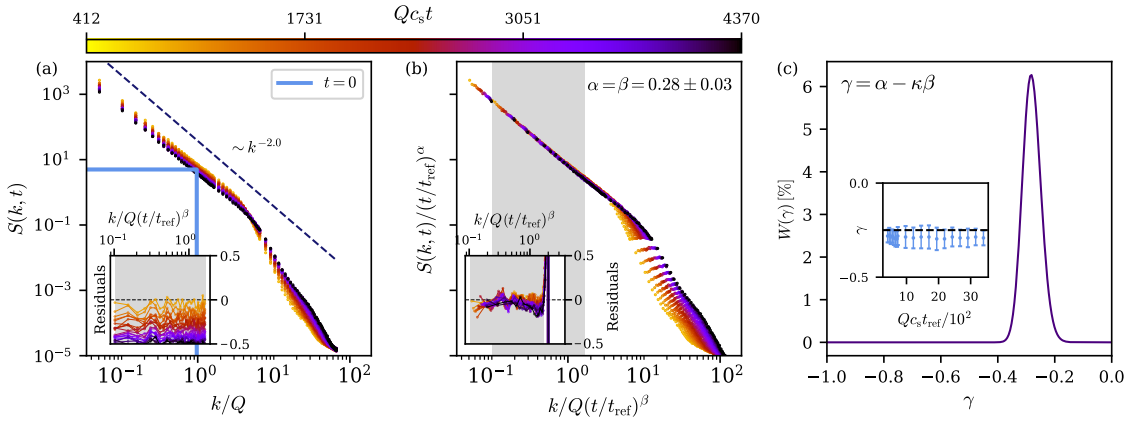

Figure 5.1: Subdiffusive self-similar scaling evolution near a non-thermal fixed point of the DSG model in (1+1)D. (a) Time evolution of the structure factor $S(k,t) = \langle|\varphi(k,t)|^2\rangle$ of the real scalar field. The initial $S(k,0)$ (blue line) is a box with cutoff Q. At long times, the redistribution of excitations towards the IR leads to a power-law shape $S(k,t) \sim k^{-\kappa}$ at large wave lengths. (b) The collapse of the curves to the universal scaling function according to $S(k,t) = (t/t_{\rm ref})^{\alpha} S([t/t_{\rm ref}]^{\beta}k, t_{\rm ref}) = (t/t_{\rm ref})^{\alpha-\kappa\beta}k^{-\kappa}$, to the reference time $t_{\rm ref} = 412/(Qc_{\rm s})$, with $c_{\rm s}$ denoting the free speed of sound, exhibits the spatio-temporal scaling of the correlator in the regime of low wave numbers, $k \ll k_{\xi_{\rm s}} = (2M\tilde{\rho}|c_1|)^{1/2} \approx 4Q$, with a resulting subdiffusive exponent $\alpha = \beta = 0.28(3)$, and with $\kappa \simeq 2.0$. The inset shows the residuals of the spectra w.r.t. the reference spectrum, calculated as the relative difference of the rescaled spectra and the spectrum at $t_{\rm ref}$, with the equal distribution of errors confirming the self-similarity of the scaling. (c) Likelihood function of the scaling exponent $\gamma = \alpha - \kappa\beta = (1-\kappa)\beta$, from which the error of the exponents was extracted. The inset shows the center and width of the likelihood function for different reference times.

ter the distribution around $\langle\varphi\rangle = \pi$, i.e., at a maximum of the cosine potential. This allows the system to randomly decay to the adjacent and further minima, accumulating in either of them at later times.

After the initial redistribution of particles to the various momenta, a pure power-law emerges in the infrared (IR), i.e., a fractal form reflecting the long-wave behaviour of the field in a single truncated Wigner realisation, as is generally expected for the correlator of a phase angle for symmetry reasons, as argued in [106, 125]. At sufficiently late times, in our case $t \gtrsim 412/(Qc_{\rm s})$, the system enters a self-similar scaling regime, with the structure factor exhibiting the pure power-law, $S(k,t) \sim k^{-\kappa} \sim k^{-2}$. Due to the shape of the universal scaling function being a pure power-law, we cannot independently determine the two scaling exponents α and β. Considering the conservation of the momentum integral over $S(k,t)$ for the scaling regime, we may set $\alpha = d \cdot \beta = \beta$ for $d = 1$. This brings the scaling function to an especially simple form, allowing for the rescaling of the spectra with only one exponent. Hence, we may rescale using

$$S(k,t) = (t/t_{\rm ref})^{\alpha} f_{\rm s}([t/t_{\rm ref}]^{\beta}k, t_{\rm ref}) = (t/t_{\rm ref})^{\alpha-\kappa\beta}k^{-\kappa} \tag{5.7}$$

by means of fitting $\gamma = (1-\kappa)\beta$. We find $\alpha = \beta = 0.28(3)$ (see Fig. 5.1b), confirming distinctly subdiffusive ($\beta < 1/2$) scaling. The inset of Fig. 5.1c shows the independence of the exponent of the reference time.

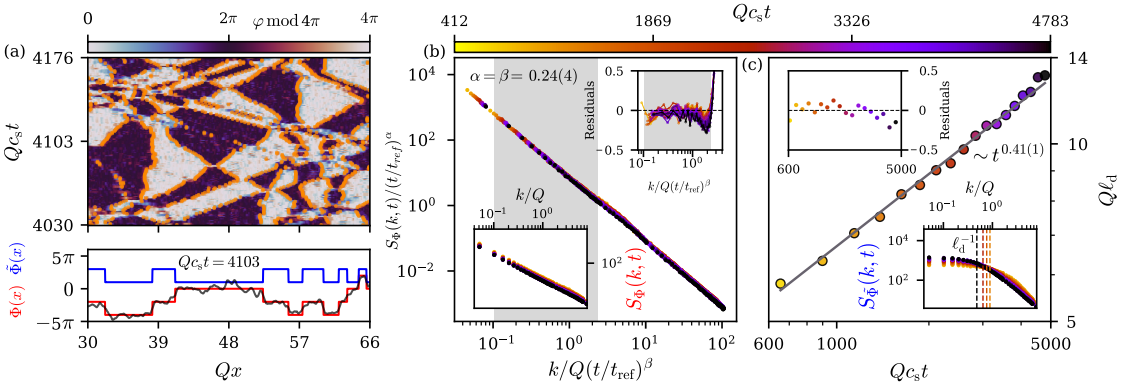

Figure 5.2: Defect coarsening in the dynamics of the DSG. (a) (upper panel) Excerpt of the time evolution of the DSG field φ in a single TW run with full system length $L = 122\,Q^{-1}$. For better visibility, we plot it modulo 4π. Domain walls are detected and denoted by orange markers. (lower panel) A function $\Phi(x)$ (red) is constructed by jumping by 2π (-2π) for each detected (anti-)kink. A function $\tilde{\Phi}(x) = \cos(\Phi(x)/2)$ (blue) alternates between ± 1 for each detected defect, regardless of their signs, encoding the length-scale of domains alone. The blue curve is scaled and shifted for better visibility. The fundamental field φ is shown in grey. (b) Spatio-temporal evolution of defect correlations. The spatial correlation in Fourier space is calculated as $S_\Phi(k,t) = \langle \Phi(k)\Phi(-k)\rangle$ and averaged over 10^3 realisations. In the IR, the correlation function shows, within the error bounds, the same scaling evolution as the spectra in Fig. 5.1. Upper inset: Residuals, i.e., the relative difference of the rescaled spectra and the reference spectrum at $t_{\mathrm{ref}} = 412/(Qc_s)$. Lower inset: Snapshots of the unscaled data. (c) Spatio-temporal evolution of domain sizes. We extract the IR length-scale associated with domain walls ℓ_d (cf. yellow to black dashed lines in lower inset) from the correlation function $S_{\tilde{\Phi}}(k,t) = \langle \tilde{\Phi}(k)\tilde{\Phi}(-k)\rangle$ and observe a power law coarsening with $t^{0.41(1)}$, differing from the scaling of the spectra in (b).

5.2.2 DOMAIN GROWTH VERSUS COARSENING DYNAMICS

In the short-time DSG dynamics, the system decays from the initial position on the maximum of the potential into the various minima of the periodic potential, with domains of the respective field values, corresponding to their respective minima, forming dynamically. Relatively sharply defined cross-over regions are found separating them, as seen in Fig. 5.2a. In the typical handling of phase-ordering kinetics, the argument for $d \geq 2$ spatial dimensions, considering either conserved or non-conserved fields, generically associates the coarsening dynamics with the deformation and hence growth of domain-sizes in the system [107]. These dynamics are governed by a simple diffusion-type or Cahn-Hilliard equation governing the transport of field values and thus the dynamics of the domain walls in the system. Therefore, it is instructive to investigate the time evolution of these domains in our system. Note that for $d = 1$ dimensions, there is no such intuitive picture and no generalised diffusion model of this sort was derived to date.

To further understand the coarsening mechanisms in one spatial dimension, we investigate the spatial configuration of the aforementioned domains by constructing a function $\Phi(x)$, which jumps by 2π (-2π) at each kink (anti-kink), thus isolating the effects of the domains themselves from other excitations, see Fig. 5.2b. The structure factor of Φ, $S_\Phi(k,t) = \langle \Phi(k)\Phi(-k)\rangle$, is found to exhibit a power-law spectrum with $\kappa \approx 2$ in the IR. Using the same rescaling algorithm as in Fig. 5.1, we obtain the scaling exponents $\alpha = \beta = 0.24(4)$ (cf. Fig. 5.2b). The residuals

in the upper inset of Fig. 5.2c indicate that this scaling is concentrated in the IR and that thus fluctuations across separate wells of the potential contribute to the universal dynamics of the full fundamental field.

We emphasise, though, that $\Phi(x)$ encodes more than the size of the domains seen in Fig. 5.2a. It captures the sequence of orientations of the kinks and thus the rescaling of the fractal pattern of steps as illustrated by the black and red lines in the lower panel of Fig. 5.2a. Hence, it embodies the overall long-wave structure of the DSG field spreading over many minima, which is possible due to the periodic symmetry of the non-compact DSG potential. The importance of this becomes clear when reducing the field to an alternating function $\tilde{\Phi}(x) = \cos(\Phi(x)/2)$, which alternates between ± 1 and thus encodes the domain length only. We construct the structure factor $S_{\tilde{\Phi}}(k,t) = \left\langle \tilde{\Phi}(k)\tilde{\Phi}(-k) \right\rangle$ and extract from it the mean domain length ℓ_d at each time, by fitting a function $f_s = 1/[1-(k/k_d)^2]$ with $k_d = 2\pi/\ell_d$ to the spectra (see inset of Fig. 5.2c). The evolution of the domain-size length scale exhibits a power-law evolution in time $\ell_d \sim t^{0.41(1)}$ with an exponent distinctly different from β, governing the coarsening of the fundamental field spectra, see Fig. 5.2c. This shows that the subdiffusive coarsening of the DSG field is a more intricate phenomenon than domain coarsening and underlines the relevance of the long-range structure of φ, which spreads over several to many minima of the sinusoidal potential.

5.2.3 DIFFUSION-TYPE SCALING IN THE (1+1)D DSG

As a contrast to the subdiffusive scaling discussed above, the DSG model in $d = 1$ spatial dimensions is found to also exhibit diffusion-type self-similar dynamics of the field correlations. For this, we perform a further simulation with different parameters for the DSG Lagrangian. We chose the couplings such that the potential landscape now shows a *local* maximum at $\langle\varphi\rangle = 2\pi\mathbb{Z}$, degenerate *global* maxima at $(2\mathbb{Z}+1)\pi$ and degenerate minima between them. We intialise the field with a momentum box distribution as before, yet in this case centered around $\langle\varphi\rangle = 0$. This results in a decay to the adjacent minima, but since the field is initialised on a local maximum, the system does not have enough energy to overcome the potential barrier given by the global maxima, hence constraining the dynamics to the two neighboring minima. As a result, the model reduces to an effective φ^4 model (see inset of Fig. 5.3a) for which diffusion-type scaling behavior is well known. Here, the correlations take the form of a universal scaling function with a plateau, showcasing the length scale of the binary domains which have formed in the dynamics. This allows us to rescale the spectra as in Fig. 4.1, determining the scaling exponents independently from one another. We find self-similar scaling of the fundamental field correlations with $\alpha = 0.53(5)$ and $\beta = 0.52(4)$, see Fig. 5.3. We hence conclude that the fractal pattern found in Fig. 5.1 which was the result of the field configurations being able to spread across many minima of the sinusodial potential defines its own distinct scaling behavior, other than when the field only occupies two minima.

We note that subdiffusive and diffusive scaling do not imply that the evolution is governed by a simple diffusion-type equation as is it is often chosen for the phenomenological description of pattern coarsening. There, a diffusion equation is used to describe self-similar scaling with

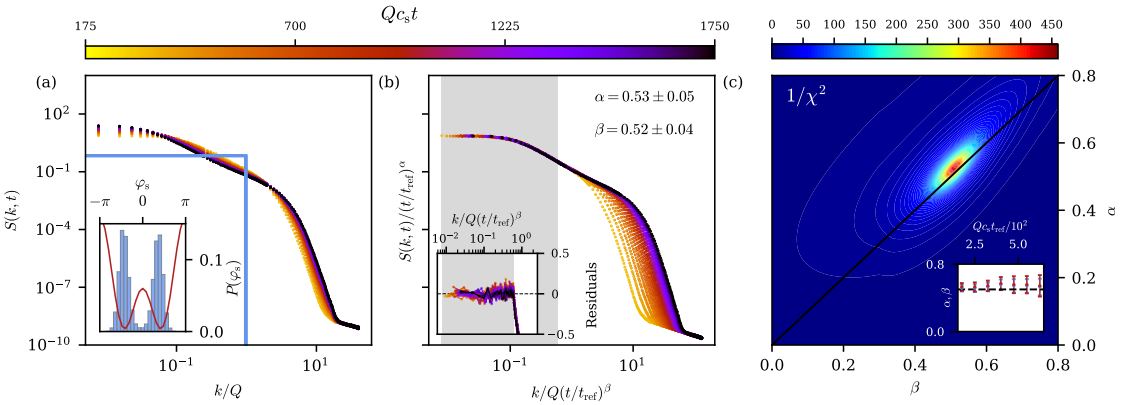

Figure 5.3: Self-similar scaling of the DSG model in (1+1)D with only two minima occupied. (a) Unscaled structure factor $S(k,t) = \langle \varphi(k,t)\varphi(-k,t)\rangle$ of the DSG dynamics, starting from the momentum box indicated by the blue line. The form differs from that of Fig. 5.1 and shows a plateau, hinting at a dominant coarsening length scale in the system. The inset shows the PDF (blue bars), which is centered only around two minima of the shown bare potential (red). (b) Rescaled structure factor. Using the same algorithm as in Fig. 5.1, we obtain diffusion-type scaling exponents $\alpha = 0.53(5)$ and $\beta = 0.52(4)$, obeying $\alpha = d\beta$ within errors, here for $d = 1$. The inset shows the residuals with an even distribution implying strict self-similarity. (c) Inverse χ^2 distribution showing the most likely distribution. The inset shows the stability of scaling w.r.t. the reference time, with the dashed line indicating the value 0.5.

$\beta = 1/2$, reflecting the combination of a first-order time derivative with a second-order spatial derivative, and, e.g., the Cahn-Hilliard equation governs scaling with $\beta = 1/4$, as it contains a fourth-order spatial derivative as a result of an additional conservation law. We emphasise, though, that the diffusion-type as well as the subdiffusive scaling observed in our numerics and considered in this thesis is not to be identified automatically with pattern coarsening phenomenologically or microscopically described by either of these diffusion-type equations. We rather point out that the description we aim at, in line with the microscopic description of the scaling close to a non-thermal fixed point, results in a description of the corresponding scaling on the grounds of the full non-linear evolution of the system. This typically requires an effective-theory description as introduced in the present work as well as a (non-)perturbative approach to the scaling analysis of such a model.

Such a scaling analysis was performed by [85, 178] on sine-Gordon-type models, utilising a kinetic theory approach and non-perturbative two-particle irreducible (2PI) resummation. It was found that, assuming both models admit scaling solutions, they both show solutions of the diffusion-type as well subdiffusive scaling, depending on the number of occupied minima. This can be easily understood by considering that for dynamics containing only a few minima, the dominant vertices are $2 \to 2$ vertices as in a φ^4 theory. When many minima are occupied, the full non-linearity comes into play, making $n \to n$ vertices with large n more relevant, thus altering the scaling behaviour. Our numerics support this distinction, and the obtained scaling exponents are close to the analytical prediction of $\beta = 1/(d+1)$ for subbdifusive and $\beta = 1/2$ for diffusion-type scaling. The discrepancy between the numerical results and analytics, though, is a subject to be investigated and goes beyond the scope of this thesis.

5.3 LOW-ENERGY EFFECTIVE THEORY

In the following, we derive the DSG model as a low-energy effective model of the spin-1 Bose gas. As mentioned above, the derivation of such a model leads to a significant reduction of complexity of the problem, isolating the relevant degrees of freedom leading to universal scaling dynamics in the spinor system. We integrate out the interaction-suppressed density fluctuations in the spin-1 Lagrangian to obtain low-energy effective theories for the spinor and Larmor phase, respectively. We show that we obtain two kinds of theories: one lowest-energy theory at vanishing momenta, and a theory at momenta near the spin healing length. With this derivation we show that the far-from equilibrium dynamics of the spin-1 Bose gas in the easy-plane phase belongs to a sine-Gordon-type non-equilibrium universality class.

The spin-1 Lagrangian is given by

$$\mathcal{L} = \frac{\mathrm{i}}{2}\left(\psi_a^*\partial_t\psi_a - \psi_a\partial_t\psi_a^*\right) - \frac{1}{2M}\nabla\psi_a^*\nabla\psi_a - q(f^z)^2_{ab}\psi_a^*\psi_b - \frac{c_0}{2}(\psi_a^*\psi_a)^2 - \frac{c_1}{2}\sum_{i\in\{x,y,z\}}(\psi_a^* f^i_{ab}\psi_b)^2\,, \tag{5.8}$$

where summation over the same indices is implied and once more ψ_a represent the magnetic sublevels with $m_\mathrm{F} = a \in \{-1, 0, 1\}$. Here and in the following we suppress the space-time arguments of all fields for brevity. The magnetic field components can be expressed in terms of their respective densities ρ_{m_F} and phase angles φ_{m_F} as $\psi_{m_F} = \sqrt{\rho_{m_F}}\exp\{\mathrm{i}\varphi_{m_F}\}$. Rewriting these by means of the total density $\tilde{\rho}$, as well as the mean side-mode density ρ and z-magnetisation $F_z = 2\epsilon$,

$$\tilde{\rho} = \rho_{-1} + \rho_0 + \rho_1\,, \quad \rho = \frac{\rho_1 + \rho_{-1}}{2}\,, \quad \epsilon = \frac{\rho_1 - \rho_{-1}}{2}\,, \tag{5.9}$$

and of the overall phase θ, the Larmor phase φ_L, and the spinor phase φ_s,

$$\theta = \varphi_1 + \varphi_{-1}\,, \quad \varphi_\mathrm{L} = (\varphi_1 - \varphi_{-1})/2\,, \quad \varphi_\mathrm{s} = \theta - 2\varphi_0\,, \tag{5.10}$$

yields

$$\psi_{\pm1} = \sqrt{\rho \pm \epsilon}\,\mathrm{e}^{\mathrm{i}(\theta/2 \pm \varphi_\mathrm{L})}\,, \quad \psi_0 = \sqrt{\tilde{\rho} - 2\rho}\,\mathrm{e}^{\mathrm{i}(\theta - \varphi_\mathrm{s})/2}\,. \tag{5.11}$$

We proceed by inserting the expressions (5.11) into the Lagrangian (5.8), which gives

$$\begin{aligned}\mathcal{L} = &-\frac{\tilde{\rho}}{2}\left(\dot{\theta} - \dot{\varphi}_\mathrm{s}\right) - 2\epsilon\,\dot{\varphi}_\mathrm{L} - \rho\,\dot{\varphi}_\mathrm{s} \\ &- \frac{\tilde{\rho} - 2\rho}{8M}(\nabla\theta - \nabla\varphi_\mathrm{s})^2 - \frac{\rho}{4M}(\nabla\theta)^2 - \frac{\rho}{M}(\nabla\varphi_\mathrm{L})^2 - \frac{\epsilon}{M}\nabla\varphi_\mathrm{L}\,\nabla\theta \\ &- \frac{1}{8M}\left\{(\rho - \epsilon)\left[\nabla\ln(\rho - \epsilon)\right]^2 + (\rho + \epsilon)\left[\nabla\ln(\rho + \epsilon)\right]^2 + (\tilde{\rho} - 2\rho)\left[\nabla\ln(\tilde{\rho} - 2\rho)\right]^2\right\} \\ &- 2q\rho - \frac{c_0}{2}\tilde{\rho}^2 - 2c_1\left[-2\rho^2 + \epsilon^2 + \rho\tilde{\rho} + \sqrt{\rho^2 - \epsilon^2}(\tilde{\rho} - 2\rho)\cos\varphi_\mathrm{s}\right].\end{aligned} \tag{5.12}$$

In the regime of low-energy excitations, density fluctuations are strongly suppressed. Hence, we assume the density fields to be given by their mean-field background values with small fluctuations added,

$$\tilde{\rho}(\boldsymbol{x},t) = \tilde{\rho} = \text{const.}\,, \quad \rho(\boldsymbol{x},t) = n + \delta\rho(\boldsymbol{x},t)\,, \quad \epsilon(\boldsymbol{x},t) = \bar{\epsilon} + \delta\epsilon(\boldsymbol{x},t)\,, \tag{5.13}$$

where $n = \text{const.}$ and, in the easy-plane phase of the spin-1 gas, the mean-field background solution of the density difference is $\bar{\epsilon} = 0$.

Before inserting this ansatz, we rewrite the terms in Eq. (5.12) which contain time and spatial derivatives in such a way that the coupling of the overall phase to the Larmor and spinor phases takes the following form,

$$\begin{aligned}
\mathcal{L} = & -\frac{\tilde{\rho}}{2}\left[\dot{\theta} - \left(1-\frac{2\rho}{\tilde{\rho}}\right)\dot{\varphi}_\mathrm{s} + 4\frac{\epsilon}{\tilde{\rho}}\,\dot{\varphi}_\mathrm{L}\right] \\
& - \frac{\tilde{\rho}}{8M}\left[\nabla\theta - \left(1-\frac{2\rho}{\tilde{\rho}}\right)\nabla\varphi_\mathrm{s} + 4\frac{\epsilon}{\tilde{\rho}}\,\nabla\varphi_\mathrm{L}\right]^2 - \frac{\rho}{4M}\left(1-\frac{2\rho}{\tilde{\rho}}\right)(\nabla\varphi_\mathrm{s})^2 \\
& - \frac{\rho}{M}(\nabla\varphi_\mathrm{L})^2 + \frac{2\epsilon^2}{M\tilde{\rho}}(\nabla\varphi_\mathrm{L})^2 - \frac{\epsilon}{M}\left(1-\frac{2\rho}{\tilde{\rho}}\right)\nabla\varphi_\mathrm{L}\,\nabla\varphi_\mathrm{s} \\
& - \frac{1}{8M}\left\{(\rho-\epsilon)^{-1}\left[\nabla(\rho-\epsilon)\right]^2 + (\rho+\epsilon)^{-1}\left[\nabla(\rho+\epsilon)\right]^2 + (\tilde{\rho}-2\rho)^{-1}\left[\nabla(\tilde{\rho}-2\rho)\right]^2\right\} \\
& - 2q\rho - \frac{c_0}{2}\tilde{\rho}^2 - 2c_1\left[-2\rho^2+\epsilon^2+\rho\tilde{\rho}+\sqrt{\rho^2-\epsilon^2}(\tilde{\rho}-2\rho)\cos\varphi_\mathrm{s}\right].
\end{aligned} \tag{5.14}$$

By setting the total density to be constant, we imply a conservation law in our system. Such a density conservation is connected with a U(1) current, which for Schrödinger-type equations is defined as

$$\boldsymbol{j} = -\frac{\mathrm{i}}{2M}\left(\psi_a^*\nabla\psi_a - \text{c.c.}\right) = \frac{\tilde{\rho}}{2M}\left[\theta - \left(1-\frac{2\rho}{\tilde{\rho}}\right)\varphi_\mathrm{s} + 4\frac{\epsilon}{\tilde{\rho}}\varphi_\mathrm{L}\right] \tag{5.15}$$

$$= \frac{\tilde{\rho}}{2M}\left[\theta - \left(1-\frac{2n}{\tilde{\rho}}\right)\varphi_\mathrm{s} + 4\frac{\bar{\epsilon}}{\tilde{\rho}}\varphi_\mathrm{L}\right] + O(\delta\rho,\delta\epsilon)\,. \tag{5.16}$$

In the last step, we have written the total U(1) Noether current in the mean field. The consequences of this conservation law hence become clear, when writing out the continuity equation

$$\partial_t\tilde{\rho} - \nabla\boldsymbol{j} = 0. \tag{5.17}$$

Considering a constant total density, and that the global phase θ does not contain topological excitations, which is a fair assumption when considering homogeneous density, the continuity equation then reads

$$\nabla\theta = \left(1-\frac{2n}{\tilde{\rho}}\right)\nabla\varphi_\mathrm{s} + 4\frac{\bar{\epsilon}}{\tilde{\rho}}\nabla\varphi_\mathrm{L} + O(\delta\rho,\delta\epsilon). \tag{5.18}$$

We now redefine the total phase by shifting it, as given by the continuity equation, by the spinor and Larmor phases, each multiplied with a constant, as

$$\theta \to \tilde{\theta} = \theta - \left(1 - \frac{2n}{\tilde{\rho}}\right)\varphi_{\mathrm{s}} + 4\frac{\bar{\epsilon}}{\tilde{\rho}}\varphi_{\mathrm{L}}\,. \tag{5.19}$$

Inserting (5.13) and (5.19) into (5.14), one finds that, in leading order, the spinor and Larmor phases decouple from the total phase, leaving only couplings between the gradients of the phases, which are linear in $\delta\rho$ and $\delta\epsilon$,

$$\begin{aligned}
\mathcal{L} = & -\frac{\tilde{\rho}}{2}\dot{\tilde{\theta}} - \delta\rho\,\dot{\varphi}_{\mathrm{s}} - 2\delta\epsilon\,\dot{\varphi}_{\mathrm{L}} \\
& - \frac{\tilde{\rho}}{8M}\left(\nabla\tilde{\theta}\right)^2 - \frac{n}{4M}\left(1 - \frac{2n}{\tilde{\rho}}\right)(\nabla\varphi_{\mathrm{s}})^2 - \frac{n}{M}(\nabla\varphi_{\mathrm{L}})^2 \\
& - \frac{\delta\rho}{4M}\left[\left(1 - \frac{4n}{\tilde{\rho}}\right)(\nabla\varphi_{\mathrm{s}})^2 + 4(\nabla\varphi_{\mathrm{L}})^2 + 2\nabla\tilde{\theta}\,\nabla\varphi_{\mathrm{s}}\right] - \frac{\delta\epsilon}{M}\left[\nabla\tilde{\theta}\,\nabla\varphi_{\mathrm{L}} + \left(1 - \frac{2n}{\tilde{\rho}}\right)\nabla\varphi_{\mathrm{L}}\,\nabla\varphi_{\mathrm{s}}\right] \\
& - \frac{1}{8M}\left\{\frac{(\nabla\delta\rho)^2}{\tilde{\rho} - 2n - 2\delta\rho} + \frac{2(n+\delta\rho)}{(n+\delta\rho)^2 - (\delta\epsilon)^2}\left[(\nabla\delta\rho)^2 + (\nabla\delta\epsilon)^2\right] - \frac{4\delta\epsilon}{(n+\delta\rho)^2 - (\delta\epsilon)^2}\nabla\delta\rho\,\nabla\delta\epsilon\right\} \\
& - 2q\delta\rho - 2c_1\left[(\tilde{\rho} - 4n)\delta\rho - 2\delta\rho^2 + \delta\epsilon^2 + \sqrt{\rho^2 - \delta\epsilon^2}(\tilde{\rho} - 2n - 2\delta\rho)\cos\varphi_{\mathrm{s}}\right] \\
& - 2qn - \frac{c_0}{2}\tilde{\rho}^2 - 2c_1 n\,(\tilde{\rho} - 2n)\,.
\end{aligned} \tag{5.20}$$

At this point, we see that the coupling of the global phase translates into a coupling of the two phases to each other. Interestingly, these couplings only happen on the level of the spatial gradients and are a pure beyond-mean-field effect. Numerical simulations using pure mean-field dynamics indeed confirm the decoupling of the phases from each other, unless one of the phases causes the spin orientation to flip its sign. Then, the other phase must also self-consistently accommodate this change via a π or 2π jump, as seen in Sect. 4.3.1.

Approximating the above Lagrangian now to leading order in the density fluctuations, neglecting terms of $O(\delta\rho_\alpha\nabla\delta\rho_\beta\nabla\delta\rho_\gamma)$, as well as terms of order $O(\delta\rho_\alpha\nabla\varphi_\beta\nabla\varphi_\gamma)$, with $\delta\rho_{\alpha,\beta,\gamma} \in \{\delta\rho, \delta\epsilon\}$, $\varphi_{\beta,\gamma} \in \{\tilde{\theta}, \varphi_{\mathrm{s}}, \varphi_{\mathrm{L}}\}$, we can write it in the following form,

$$\mathcal{L} = \mathcal{L}_{\tilde{\theta}} + \mathcal{L}^0 + \mathcal{L}^1 + \mathcal{L}^2 + O(\delta\rho_\alpha\nabla\delta\rho_\beta\nabla\delta\rho_\gamma, \delta\rho_\alpha\nabla\varphi_\beta\nabla\varphi_\gamma)\,, \tag{5.21}$$

with

$$\mathcal{L}_{\tilde{\theta}} = -\frac{\tilde{\rho}}{2}\dot{\tilde{\theta}} - \frac{\tilde{\rho}}{8M}\left(\nabla\tilde{\theta}\right)^2 , \tag{5.22a}$$

$$\mathcal{L}^0 = -\frac{n}{M}\left(\nabla\varphi_{\mathrm{L}}\right)^2 - \frac{n}{4M}\left(1-\frac{2n}{\tilde{\rho}}\right)\left(\nabla\varphi_{\mathrm{s}}\right)^2 - 2qn - \frac{c_0}{2}\tilde{\rho}^2 - 2c_1 n(\tilde{\rho}-2n)(1+\cos\varphi_{\mathrm{s}}) , \tag{5.22b}$$

$$\mathcal{L}^1 = \begin{pmatrix} -\dot{\varphi}_{\mathrm{s}} - 2q - 2c_1(\tilde{\rho}-4n)(1+\cos\varphi_{\mathrm{s}}) , & -2\dot{\varphi}_{\mathrm{L}} \end{pmatrix}\begin{pmatrix}\delta\rho\\ \delta\epsilon\end{pmatrix}, \tag{5.22c}$$

$$\mathcal{L}^2 = (\delta\rho\,,\delta\epsilon)\begin{pmatrix} \frac{\nabla^2}{4Mn}\frac{\tilde{\rho}}{\tilde{\rho}-2n} + 4c_1(1+\cos\varphi_{\mathrm{s}}) & 0 \\ 0 & \frac{\nabla^2}{4Mn} - c_1\left[2+(2-\tilde{\rho}/n)\cos\varphi_{\mathrm{s}}\right]\end{pmatrix}\begin{pmatrix}\delta\rho\\ \delta\epsilon\end{pmatrix}. \tag{5.22d}$$

As we disregard fluctuations of the total density, we may also neglect the contribution $\mathcal{L}_{\tilde{\theta}}$, which in the chosen approximation decouples from the remaining Lagrangian. Thus, the approximated Lagrangian takes the form of

$$\mathcal{L} = \mathcal{L}^0 + \boldsymbol{J}\cdot\boldsymbol{\delta\rho} + \frac{1}{2}\boldsymbol{\delta\rho}^T\cdot\boldsymbol{G}^{-1}\cdot\boldsymbol{\delta\rho} + O(\delta\rho^3,\delta\epsilon^3) , \tag{5.23}$$

where $\boldsymbol{\delta\rho} = (\delta\rho,\delta\epsilon)^T$ and

$$\boldsymbol{J} = (-\dot{\varphi}_{\mathrm{s}} - 2q - 2c_1(\tilde{\rho}-4n)(1+\cos\varphi_{\mathrm{s}}), -2\dot{\varphi}_{\mathrm{L}}) , \tag{5.24}$$

$$\boldsymbol{G}^{-1} = \begin{pmatrix} \frac{\nabla^2}{2Mn}\frac{\tilde{\rho}}{\tilde{\rho}-2n} + 8c_1(1+\cos\varphi_{\mathrm{s}}) & 0 \\ 0 & \frac{\nabla^2}{2Mn} - 2c_1\left(2+\left(2-\frac{\tilde{\rho}}{n}\right)\cos\varphi_{\mathrm{s}}\right)\end{pmatrix}. \tag{5.25}$$

The quadratic form allows us to integrate out the density fluctuations by carrying out the Gaussian integrals for $\delta\rho$ and $\delta\epsilon$ according to

$$\begin{aligned} Z &= \int \mathcal{D}\delta\rho\,\mathcal{D}\delta\epsilon\,\mathcal{D}\varphi_{\mathrm{s}}\,\mathcal{D}\varphi_{\mathrm{L}}\exp\left\{\mathrm{i}\int_{t,x}\left(\mathcal{L}^0 + \boldsymbol{\delta\rho}^T\boldsymbol{J} + \frac{1}{2}\boldsymbol{\delta\rho}^T\boldsymbol{G}^{-1}\cdot\boldsymbol{\delta\rho}\right)\right\} \\ &= C\int \mathcal{D}\varphi_{\mathrm{s}}\,\mathcal{D}\varphi_{\mathrm{L}}\underbrace{\exp\left\{\mathrm{i}\int_{t,x}\left[\mathcal{L}^0 - \frac{1}{2}\boldsymbol{J}^T\boldsymbol{G}\boldsymbol{J}\right] - \frac{1}{2}\log\det\boldsymbol{G}^{-1}\right\}}_{=\exp\{\mathrm{i}S^{\mathrm{eff}}\}}, \end{aligned}$$

and collecting the result in the effective action

$$S^{\mathrm{eff}} = \int_{t,x}\left[\mathcal{L}^0 - \frac{1}{2}\boldsymbol{J}^T\boldsymbol{G}\boldsymbol{J}\right] + \frac{\mathrm{i}}{2}\log\det\boldsymbol{G}^{-1} . \tag{5.26}$$

Furthermore, neglecting irrelevant constant terms in $\mathcal{L}^0$, this procedure yields the following real part of the effective Lagrangian, where the denominators containing derivatives are implied to denote the respective Green's functions:

$$\begin{aligned}\mathrm{Re}\,\mathcal{L}^{\mathrm{eff}} = &-\frac{n}{M}(\nabla\varphi_{\mathrm{L}})^2 - \frac{n}{4M}\left(1-\frac{2n}{\tilde{\rho}}\right)(\nabla\varphi_{\mathrm{s}})^2 - 2c_1 n(\tilde{\rho}-2n)\cos\varphi_{\mathrm{s}} \\ &-\frac{1}{2}\left\{\frac{\dot{\varphi}_{\mathrm{L}}^2}{\frac{\nabla^2}{2Mn}-2c_1[2+(2-\tilde{\rho}/n)\cos\varphi_{\mathrm{s}}]} + \frac{[\dot{\varphi}_{\mathrm{s}}+2q+2c_1(\tilde{\rho}-4n)(1+\cos\varphi_{\mathrm{s}})]^2}{\frac{\nabla^2}{2Mn}\frac{\tilde{\rho}}{(\tilde{\rho}-2n)}+8c_1(1+\cos\varphi_{\mathrm{s}})}\right\}.\end{aligned} \tag{5.27}$$

The imaginary part is given by

$$\mathrm{Im}\,\mathcal{L}^{\mathrm{eff}} = \frac{1}{2\Delta t(\Delta x)^d}\ln\left(\frac{(1+\cos\varphi_{\mathrm{s}})\,[2+(2-\tilde{\rho}/n)\cos\varphi_{\mathrm{s}}]}{2\,(4-\tilde{\rho}/n)}\right), \tag{5.28}$$

where Δt and Δx are the time- and length scales relevant for regularisation, defined by $\sum_{t,x} = (\Delta t)^{-1}(\Delta x)^{-d}\int_{t,x}$. As such, they are related to the system's volume in Fourier space. Moreover, we have normalised the imaginary part to vanish at $\varphi_{\mathrm{s}} = 0$, using that overall constants do not change the generating functional. As this imaginary term only leads to an overall damping of Z, we will focus on discussing the real part in the following.

It is, furthermore, useful to express the Lagrangian in terms of dimensionless space, time, and energy density,

$$\mathbf{x} = \frac{\bar{\mathbf{x}}}{k_{\xi_{\mathrm{s}}}}, \qquad t = \bar{t}\,\frac{2M}{k_{\xi_{\mathrm{s}}}^2}, \qquad \mathcal{L}^{\mathrm{eff}} = \bar{\mathcal{L}}^{\mathrm{eff}}\tilde{\rho}\,\frac{k_{\xi_{\mathrm{s}}}^2}{2M}, \tag{5.29}$$

where the spin healing wave number is defined as

$$k_{\xi_{\mathrm{s}}} = (2M\tilde{\rho}|c_1|)^{1/2}. \tag{5.30}$$

In terms of $\bar{x}$, $\bar{t}$ and $\bar{q}$, cf. Eq. (2.21), the real part of the effective Lagrangian in the easy-plane phase, i.e., for $c_1 < 0$, $0 < \bar{q} \leq 1$, takes the form

$$\begin{aligned}\mathrm{Re}\,\bar{\mathcal{L}}^{\mathrm{eff}} = &-\frac{1}{8}\left[4(1-\bar{q})\,(\nabla_{\bar{x}}\varphi_{\mathrm{L}})^2 + \frac{1}{2}(1-\bar{q}^2)(\nabla_{\bar{x}}\varphi_{\mathrm{s}})^2 - 2(1-\bar{q}^2)\cos\varphi_{\mathrm{s}}\right] \\ &-\frac{1}{2}\left\{\frac{1-\bar{q}}{\nabla_{\bar{x}}^2+1-\bar{q}-(1+\bar{q})\cos\varphi_{\mathrm{s}}}(\partial_{\bar{t}}\varphi_{\mathrm{L}})^2\right. \\ &\left.\frac{(1-\bar{q}^2)/8}{\nabla_{\bar{x}}^2-(1-\bar{q}^2)(1+\cos\varphi_{\mathrm{s}})}\,[\partial_{\bar{t}}\varphi_{\mathrm{s}}+4\bar{q}-2\bar{q}(1+\cos\varphi_{\mathrm{s}})]^2\right\}.\end{aligned} \tag{5.31}$$

For our low-energy effective theory, we consider only momenta which are much lower than the healing momentum of the system. Hence, we will eventually omit the momentum dependence of $\mathcal{L}^2$, such that the matrix elements of the Green's function $\mathbf{G}$ are given by the respective inverses of the matrix elements of $\mathbf{G}^{-1}$, Eq. (5.25). Yet, the resulting effective theory would be divergent

for $\varphi_\mathrm{s} = \pi$ and, depending on the ratio $\tilde{\rho}/n$ and thus $\bar{q}$, in general also at different values of $0 < |\varphi_\mathrm{s}| < \pi$. This can be seen as a manifestation of a constraint for the system: the spinor phase φ_s cannot 'hop' between degenerate ground states across the entire system. In the following, we will argue that, despite this constraint, there can be nevertheless such hopping between adjacent minima as long as this occurs locally, i.e., in higher momentum modes of the field.

We may now consider two limiting cases: A lowest-energy theory of very low momenta $k \approx 0$, where the field configuration is concentrated around $\varphi_\mathrm{s} \approx 2\pi N$, with $N \in \mathbb{Z}$, and a theory around the spin healing momentum $k = k_{\xi_\mathrm{s}}$, where we can also perform the expansion around $\varphi_\mathrm{s} \approx \pi N$.

Lowest-energy theory

We first turn to the former. In this case, we assume

$$k^2 \ll 4k_{\xi_\mathrm{s}}^2\,, \qquad \text{i.e.} \quad 0 \approx \bar{k}^2 \ll 4\,, \tag{5.32}$$

$\bar{k} = k/k_{\xi_\mathrm{s}}$, such that we can effectively neglect the Laplacian term in the denominators in the second and third lines of Eq. (5.31). The dynamics of the spin-1 gas in the easy-plane phase are then characterised by a weakly fluctuating spin length, which corresponds to φ_s fluctuating around one of its mean values $2\pi N$, with $N \in \mathbb{Z}$, i.e., to a fully elongated spin vector in the F_x-F_y-plane. Therefore, we can use

$$1 + \cos\varphi_\mathrm{s} = 2\left[1 - \sin^2(\varphi_\mathrm{s}/2)\right] \tag{5.33}$$

and expand the denominators in the effective Lagrangian in powers of $\sin^2(\varphi_\mathrm{s}/2)$ up to order $\sin^4(\varphi_\mathrm{s}/2)$. Moreover, together with this assumption and motivated by numerical results, we may also neglect any terms of order $\dot{\varphi}_j \sin^2(\varphi_\mathrm{s}/2)$ and $(\nabla\varphi_j)^2 \sin^2(\varphi_\mathrm{s}/2)$, $j \in \{\mathrm{L},\mathrm{s}\}$. With these approximations, we find that the effective actions for φ_L and φ_s decouple. For φ_s, it takes the form

$$\mathcal{L}_{\varphi_\mathrm{s}}^{\mathrm{eff}} = -\frac{1}{32c_1}\dot{\varphi}_\mathrm{s}^2 - \frac{n(\tilde{\rho}-2n)}{4M\tilde{\rho}}(\nabla\varphi_\mathrm{s})^2 - \left(2c_1 n(\tilde{\rho}-2n) - \frac{q^2}{16c_1}\right)\cos\varphi_\mathrm{s} + \frac{q^2}{32c_1}\sin^2\varphi_\mathrm{s}\,, \tag{5.34}$$

or, in its dimensionless form

$$\bar{\mathcal{L}}_{\varphi_\mathrm{s}}^{\mathrm{eff}} = \frac{1}{4}\left[\frac{1}{8}(\partial_{\bar{t}}\varphi_\mathrm{s})^2 - \frac{1-\bar{q}^2}{4}(\nabla_{\bar{x}}\varphi_\mathrm{s})^2 + (1-2\bar{q}^2)\cos\varphi_\mathrm{s} - \frac{\bar{q}^2}{2}\sin^2\varphi_\mathrm{s}\right]. \tag{5.35}$$

For φ_L, it takes the form

$$\mathcal{L}_{\varphi_\mathrm{L}}^{\mathrm{eff}} = \frac{2n}{q}\dot{\varphi}_\mathrm{L}^2 - \frac{n}{M}(\nabla\varphi_\mathrm{L})^2\,, \qquad \text{i.e.} \quad \mathrm{Re}\,\bar{\mathcal{L}}_{\varphi_\mathrm{L}}^{\mathrm{eff}} = \frac{1-\bar{q}}{4\bar{q}}(\partial_{\bar{t}}\varphi_\mathrm{L})^2 - \frac{1-\bar{q}}{2}(\nabla_{\bar{x}}\varphi_\mathrm{L})^2\,. \tag{5.36}$$

Thus, the effective theory for the Larmor phase is a quadratic, free model, while the spinor phase φ_s is described by a DSG Lagrangian, which exhibits, compared with a pure SG model, a distorted periodic potential for the phase field. We stress that, in our derivation, the periodic potential derives from the local spin-spin interactions, in contrast to standard cases, where it is caused by

a linear coupling due to an external field transverse to magnetisation [146, 179, 180] or results in a description dual to a 2D Coulomb gas [181–184]. In numerical units, the DSG couplings are given by $\lambda_{\text{spin}-1} = 1.9 \cdot 10^{-4} \approx 5.8\lambda_{\text{s,spin}-1}$ and $c_{\text{s}}^2 \approx 0.01$, which is comparable with the parameters used for the DSG simulations for subdiffusive scaling, see Sect. 5.2.1.

We emphasise that the presence of the $\sin^2\varphi_{\text{s}}$ term was found to be crucial for achieving scaling behaviour far from equilibrium, even if its relative amplitude is much smaller than that of the $\cos\varphi_{\text{s}}$ term. Truncating the expansion at the leading order would lead to a pure sine-Gordon model, yet all performed numerical simulations have shown that, in one spatial dimension, the power spectra remain static in that case. The underlying reason for this behaviour remains unclear. One possibility is that no suitable initial condition has *yet* been found which leads to a scaling solution within the sine-Gordon model. Another possibility is the breaking of classical integrability of the one-dimensional sine-Gordon model by the $\sin^2\varphi_{\text{s}}$ term. In this thesis, we utilise semi-classical methods to simulate the dynamics of the quantum system beyond the mean-field approximation. Such methods take into account quantum fluctuations in the initial condition, yet the time evolution of a single run follows the classical equations of motion which are integrable and deterministic. Classical integrable systems are known to generically conserve the shape of the momentum distribution at all times, due to the infinite conservation laws constraining the dynamics of the system [185]. This notion is further supported by numerical simulations of the single-component Bose gas in one spatial dimension governed by an integrable GPE. To date, there are no known semi-classical simulations exhibiting self-similar scaling, in contrast to results of the Rubidium experiment in Vienna conducted by S. Erne et al., showing a distinctly subdiffusive scaling of the single-component Bose gas in one spatial dimension [56].

Theory at non-vanishing momenta

From Eq. (5.31) it becomes clear that the derived DSG model we derived cannot be valid for $\varphi_{\text{s}} \approx (2n+1)\pi$, $n \in \mathbb{Z}$, because, in the limit $k \to 0$, the denominator in the terms involving a shifted $\dot{\varphi}_{\text{s}}$ vanishes in that case. Moreover, for $\cos\varphi_{\text{s}} = (1-\bar{q})/(1+\bar{q})$, the denominator of the $\dot{\varphi}_{\text{L}}$-dependent term vanishes, which is possible in the easy-plane phase ($0 \leq \bar{q} \leq 1$). As a result, long-wave-length fluctuations of the spinor phase, with $k \to 0$, will not interpolate between adjacent minima of the cosine potential, forcing these fluctuations to stay near its minima.

Hence, in order for the DSG model to be applicable for all values of φ_{s}, one needs to consider fluctuations with sufficiently large momenta, such that no divergences can appear in the above model. Superficially, one can estimate, from the denominator in the spinor-phase dependent terms of (5.27) and (5.31) that, in the easy-plane phase, one needs $k^2 \gtrsim 2k_{\xi_{\text{s}}}^2$ in order for the denominators to be regular throughout. For this estimate, we consider the most basic approximation, where one replaces the Laplacian in Eq. (5.27) by $k^2 \sim k_{\xi_{\text{s}}}^2$, (in (5.31) by $\bar{k} = k/k_{\xi_{\text{s}}} = 1$) neglecting therewith that the Green's function also depends non-linearly on the spinor phase. We note that in this approximation, we still neglect the coupling of the kinetic terms in Eq. (5.20), in order to gain intuition to the mechanism behind the momentum dependence. In this very rough approximation, one thus assumes that only the derivative terms show a momentum dependence, while $\cos\varphi_{\text{s}}$ is taken to be set by its constant mean-field value. After replacing the Laplacian in

the denominators of Eq. (5.31), $\nabla^2_{\bar{x}} \to -\bar{k}^2 = -1$, we may again expand these denominators, however now about the maxima of the periodic potential in the spinor phase, $\varphi_\mathrm{s} \approx (2n+1)\pi$, $n \in \mathbb{Z}$, and in powers of

$$1 + \cos([2n+1]\pi + \delta\varphi_\mathrm{s}) = 2\sin^2(\delta\varphi_\mathrm{s}/2) \tag{5.37}$$

up to $O(\sin^4(\delta\varphi_\mathrm{s}/2))$. Neglecting again any terms of the order $\dot{\varphi}_i(1+\cos\varphi_\mathrm{s})$ and $(\nabla\varphi_i)^2(1+\cos\varphi_\mathrm{s})$, $i = \mathrm{s}, \mathrm{L}$, as well as higher than quadratic terms in the derivatives, the theories for φ_s and φ_L decouple and we yet again obtain a free theory for φ_L with

$$\bar{\mathcal{L}}^{\mathrm{eff}}_{\varphi_\mathrm{L}} = \frac{1-\bar{q}}{16}\left[(\partial_{\bar{t}}\varphi_\mathrm{L})^2 - 8\,(\nabla_{\bar{x}}\varphi_\mathrm{L})^2\right] \tag{5.38}$$

and a DSG theory for φ_s,

$$\mathrm{Re}\,\bar{\mathcal{L}}^{\mathrm{eff}}_{\varphi_\mathrm{s}} = \frac{1-\bar{q}^2}{16}\left[(\partial_{\bar{t}}\varphi_\mathrm{s})^2 - (\nabla_{\bar{x}}\varphi_\mathrm{s})^2\right] + \bar{A}_R\cos\varphi_\mathrm{s} - \bar{B}_R\sin^2\varphi_\mathrm{s}\,, \tag{5.39}$$

with coefficients

$$\bar{A}_R = \frac{1-\bar{q}^2}{4}\left(1 - 2\bar{q}^2 + 4\bar{q}^2(1-\bar{q}^2) + 8\bar{q}^2(1-\bar{q}^2)^2\right), \tag{5.40}$$

$$\bar{B}_R = \bar{q}^2\frac{1-\bar{q}^2}{4}\left(1 + 4(1-\bar{q}^2) + 4(1-\bar{q}^2)^2\right). \tag{5.41}$$

This again represents a double sine-Gordon Lagrangian, albeit with different 'couplings'. We stress, however, that this is a very rough approximation used only to gain intuitive insight into the effects of the momentum dependence of the DSG couplings and is not intended to constitute a rigorous derivation.

Nevertheless, we can infer that field configurations in the spinor phase of the spin-1 gas must interpolate between the minima in a spatially localised manner, on the order of the spin healing length $\xi_\mathrm{s} = (2M\tilde{\rho}|c_1|)^{-1/2}$ only. Such interpolations are indeed observed in the universal scaling dynamics of the full spin-1 model as space-time vortex defects in φ_L and φ_s, as thoroughly discussed in Chap. 4. There, recall that the structure factor of the transverse spin was observed to scale with a distinctly subdiffusive exponent, which the DSG reproduces within the error bars (See Fig. 5.1 and Fig. 4.1). Our results demonstrate that the DSG dynamics of the spinor phase alone accounts for the subdiffusive scaling exhibited by the full spin-1 system, while there is no need to take into account the Larmor and total phases as, e.g., in [106].

Remarkably, we observe that the existence of topological charges, such as winding numbers seen in the non-equilibrium dynamics of the spin-1 gas, is translated to a non-compact effective theory, which does not enforce the 2π periodicity of the phase field φ_s. Most importantly, the DSG model reproduces the subdiffusive scaling of the spinor gas despite the absence of topological information, thus ultimately allowing for a further analytical study of scaling characteristics, as such approaches generically require the absence of topological excitations. This further substantiates the notion that the instanton excitations in the Larmor phase, which give rise to the coarsening

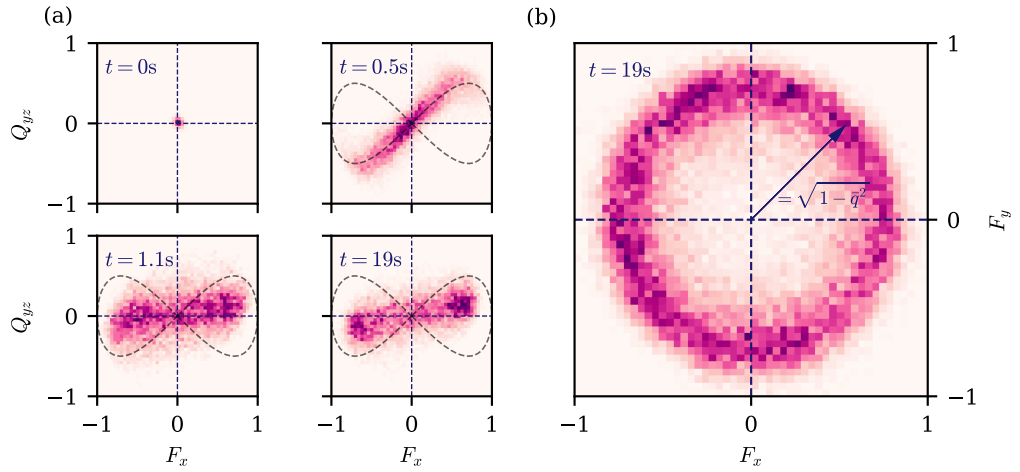

Figure 5.4: Experimental data after a quench from the polar into the easy-plane phase. (a) Time evolution of the probability distribution function in the F_x-Q_{yz} plane. The short-time dynamics are characterised by a redistribution along the separatrix, followed by a settling down near the mean-field expectation value, as seen in the lower right panel. Notice a systematic distortion for long evolution times compared to Fig. 5.5 which is attributed to a readout calibration error. (b) Probability distribution function in the transverse spin plane. The ring-shaped distribution of field values shows that the system is in the easy-plane phase. The spin length $|F_\perp|$ (the radius of the ring) allows for the estimation of the quadratic Zeeman shift according to $|F_\perp| = [1 - \tilde{q}^2]^{1/2}$, with $\tilde{q} = q/q_c = q/(2\tilde{\rho}|c_1|)$.

length scale seen in the transverse spin spectra, merely reflect the true underlying sine-Gordon-type universality class. In Sect. 4.3.1 we have shown that an instanton in the Larmor phase can be seen as an interpolating event of the spinor phase from one minimum of the DSG potential to another. Should these events also follow the spatial and temporal scales given by the DSG, then the length scale of the transverse spin as seen in the Larmor phase will follow suit.

5.4 COMPARISON WITH EXPERIMENTAL OBSERVATIONS

In the following, we show that the spin-1 Bose gas indeed shows DSG dynamics in the spinor phase by presenting numerical and experimental evidence. First, we briefly introduce the experimental system and methods that were employed for the acquisition of the experimental data. We then discuss the probability distribution function of the spinor phase post-quench and compare the experimental and numerical results supporting our derivation of the DSG model as a LEEFT of the spin-1 gas.

5.4.1 EXPERIMENTAL EXTRACTION OF OBSERVABLES

We prepare a Bose-Einstein condensate of $\sim 10^5$ ^{87}Rb atoms in a quasi-one-dimensional box-like trapping potential, for more details see [186]. We prepare all atoms in the state $F = 1$, $m_F = 0$ and initiate spin dynamics by quenching the quadratic Zeeman shift to $q_f \approx \tilde{\rho}|c_1|$ via off-

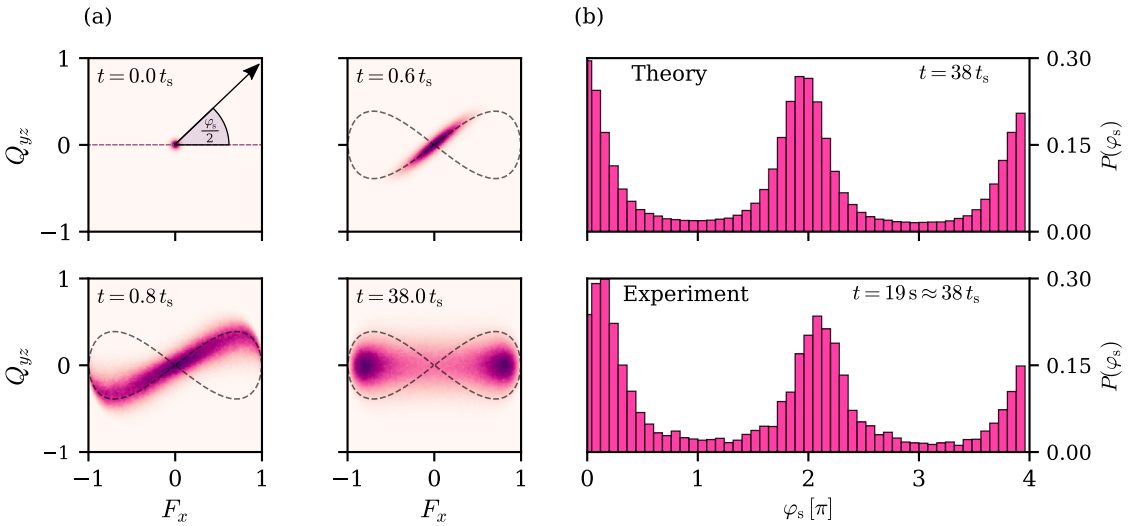

Figure 5.5: Spinor phase dynamics after a quench from the polar phase into the easy-plane phase. (a) Short-time evolution of the spinor phase probability distribution in the F_x-Q_{yz} plane. The upper left panel gives the visual interpretation of the spinor phase. The dashed black lines in the other three panels shows the separatrix on the spin-nematic sphere [131]. The distribution across a separatrix due to Bogoliubov instabilities ultimately leads to a settling of the field configuration in the values corresponding to the full spin orientation (lower right panel of (a)). Time is given in units of spin healing time $t_s = 2\pi/(\tilde{\rho}|c_1|) \approx 3/(Qc_s)$, where Q is the DSG initial-state momentum-box cutoff and c_s the DSG speed of sound. (b) The theoretical probability distribution function extracted via the angle in the F_x-Q_{yz} plane compared to the experimental one. The figure shows a larger occupation between the periodic potential minima, due to the method of extraction.

resonant microwave dressing. The observables are extracted from the measured atomic densities by employing a POVM-readout, see [145]. We extract the one-dimensional spatial profiles of F_x and Q_{yz} simultaneously in every experimental realisation. Many repetitions give rise to the phase-space distributions depicted in Fig. 5.4a. We bin the data according to the optical resolution of $\approx 1\,\mu$m and treat each bin as a separate point in the phase space spanned by F_x and Q_{yz}.

The system is initialised in a symmetric coherent state and, for short evolution times up to 0.5s, the measured distributions in F_x and Q_{yz} follow the so-called separatrix of the corresponding mean-field phase space trajectories [132], cf. Figs. 5.5a and 5.4a. For long evolution times, the system settles into a distribution with non-zero mean transversal spin length $F_\perp$, which can also be seen in Fig. 5.4b in the phase-space spanned by F_x and F_y, reflecting also the numerical distribution found in the upper panel of Fig. 4.7d. The dynamics of the measured phase-space distributions are in good qualitative agreement with the numerical simulations, as can be seen by comparing Fig. 5.5 and Fig. 5.4.

We estimate the value of q_f from the data shown in Fig. 5.4b by assuming that the configuration of the system has relaxed close to the mean-field ground state for late times. The positions of the minima of the mean-field potential in the easy-plane phase depend on q via $|F_\perp|_{\text{min}} = [1 - \tilde{q}^2]^{1/2}$. As the distribution in $F_\perp$ has a maximum at $|F_\perp| \approx 0.75$ at time $t = 19$s, we estimate $q_f \approx \tilde{\rho}|c_1|$. Note that, in contrast to the numerical data shown in figure Fig. 5.5, the measured phase-space distribution in F_x and Q_{yz} is systematically tilted from the F_x-axis for late evolution times. We

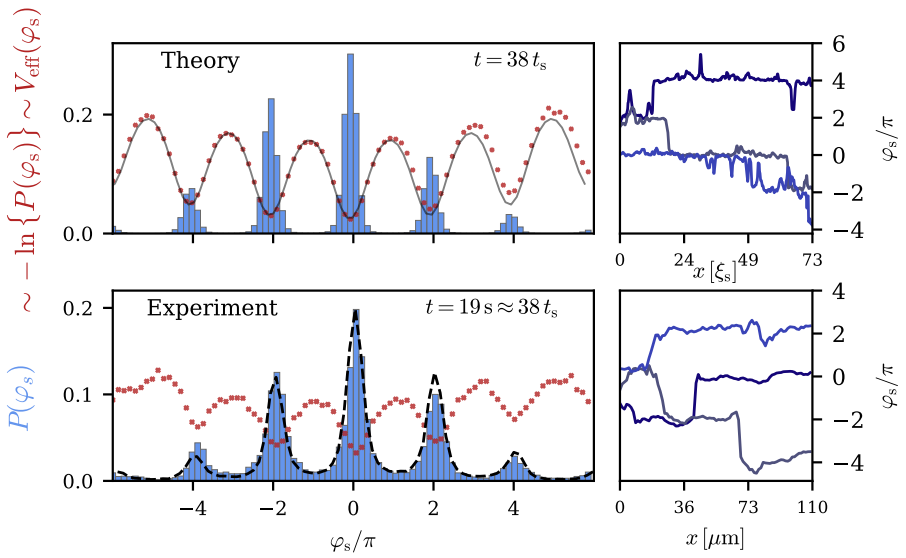

Figure 5.6: Probability distribution histogram (blue bars) of the spinor phase φ_s after a quench from the polar phase to the easy plane. (Upper left panel) Numerical result. After preparing the system in the polar phase, $q_i > 2\tilde{\rho}|c_1|$, we quench the quadratic Zeeman shift to $q_f = 0.9\,\tilde{\rho}|c_1|$, after which φ_s settles quickly into the minima of its effective potential (red crosses), thus underlining the reduction to the DSG model. This potential is extracted in a Boltzmann approximation as $V_{\mathrm{eff}}(\varphi_s) \sim -\ln(P(\varphi_s))$. The solid grey line is the analytical expression Eq. (5.34). Notice a small mean-field shift which forms dynamically and raises the potential for higher φ_s. We observe the occupation of many minima of the effective DSG potential. (Lower left panel) Experimentally extracted distribution of φ_s, having prepared $\sim 10^5$ atoms in a quasi-one-dimensional cigar-shaped trap with hard walls in the longitudinal direction, in the $m_F = 0$ state with quadratic Zeeman shift $q_i \gg 2\tilde{\rho}|c_1|$ and quenching to $q_f \approx \tilde{\rho}|c_1|$. The corresponding oscillating effective potential (red crosses) is evaluated after an evolution time $t = 19\mathrm{s} \approx 38\,t_s = 38 \cdot 2\pi/(\tilde{\rho}|c_1|) \approx 115\,(Qc_s)^{-1}$. The pedestal of the histogram can be attributed to the employed measurement scheme. The dashed line shows the theoretical PDF using the same extraction method as in the experiment, and taking into account a systematic calibration offset. The upper and lower right panels show the spatial configuration of φ_s for three different realisations denoted each by a different shade of blue. One observes that the field configuration interpolates between the DSG minima via localised phase kinks that cause the field to spread over several minima.

attribute this tilt to a systematic calibration error in the readout scheme. As a result, the readout axes are not perfectly orthogonal, which induces a distortion of the experimental distributions. For the spinor-phase histogram shown in Fig. 5.6 this leads to a shift of $\approx 0.083(3)\,\pi$ and was taken into account by shifting the numerical curve accordingly (dashed line in Fig. 5.6).

5.4.2 DSG DYNAMICS OF THE SPINOR PHASE

Fig. 5.6 (left panels) show the post-quench long-time probability distribution function (PDF) of the spatially resolved spinor phase profiles inferred from 10^3 truncated Wigner (upper) and 140 experimental runs (lower panel). The PDF is localised at multiples of 2π, corresponding to the minima of the effective DSG potential. We conclude that the approximation of small $\varphi_s - 2\pi\mathbb{Z}$,

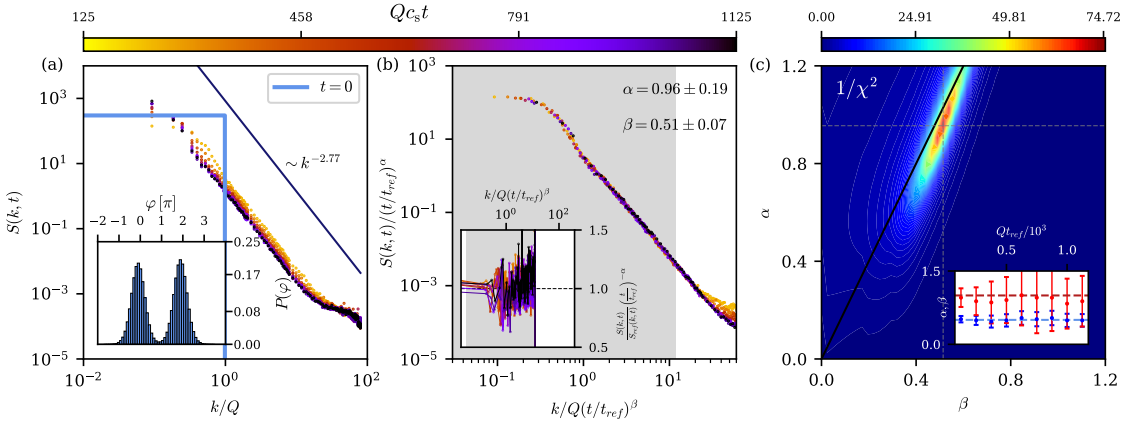

Figure 5.7: Self-similar scaling of the DSG model in (2+1)D. (a) Time evolution of the structure factor $S(k,t) = \langle|\varphi(k,t)|^2\rangle$. The initial condition (blue line) is a box with cutoff Q. The redistribution of excitations in the system leads to a power law in the IR, for momenta greater than a characteristic scale $k_\Lambda(t) \sim t^{-\beta}$. The inset shows the probability distribution histogram $P(\varphi)$ of the DSG field, demonstrating the occupancy of only two adjacent minima of the DSG potential in the simulations. (b) The collapse of the curves to the universal scaling function, with reference time $t_{\text{ref}} = 100\,(Qc_s)^{-1}$, shows the spatio-temporal scaling of the correlator with exponents $\alpha = 0.98(20)$ and $\beta = 0.51(7)$. The inset shows the residuals of the spectra w.r.t. the reference spectrum. The equal distribution of errors confirms self-similarity of the evolution. (c) Inverse χ^2 distribution showing the most likely scaling exponents. Notice the proximity of the scaling exponents to the $\alpha = d\beta = 2\beta$ line. The inset shows the stability of the scaling of α (red) and β (blue) w.r.t. the reference time. The blue and red dashed lines show the value 0.5 and 1, respectively.

chosen in the derivation of the LEEFT (5.34), is experimentally confirmed, thus underlining the reduction of the dynamics to a DSG model. Note that the experimental histograms show probabilities for the field configuration to take on a value at $(2\pi + 1)\mathbb{Z}$, in contrast to the numerical results. To explain this, we consider the experimental method for extracting the spinor phase. In Sect. 2.2.6, we discussed several SU(2) subspaces of the spin-1 manifold. Particular subspaces, under the assumption of $\langle F_z\rangle = 0$, are $\{F_x, Q_{yz}, Q_0\}$ and $\{F_y, Q_{xz}, Q_0\}$. For brevity, we constrain the discussion here to the former subsphere. The extraction of the spinor phase can be done by numerically directly accessing the complex phases of the fundamental fields. Yet, one may also employ the spin-nematic sphere and read out the orientation of the field in the F_x-Q_{yz} plane. The latter is the procedure which is implemented in the experiment. It is important to note that the full spinor phase dynamics is given only by considering both spin-nematic spheres simultaneously, thus eliminating the effect of the Larmor phase (as discussed in Sect. 2.2.6). By performing the readout of the coordinates in only one sphere, we obtain a non-vanishing probability of field configurations around $\varphi_s \approx \pi$. Fig. 5.5b showcases that numerically implementing this procedure reproduces the pedestals obtained from the experimental data in theory, see also the black dashed line in the lower left panel of. Fig. 5.6, corroborating a distribution of the experimental data according to the double sine-Gordon model.

The logarithm of the PDF, which in equilibrium is proportional to the free energy of the system, provides an estimate of the effective potential, coinciding qualitatively for the simulated and mea-

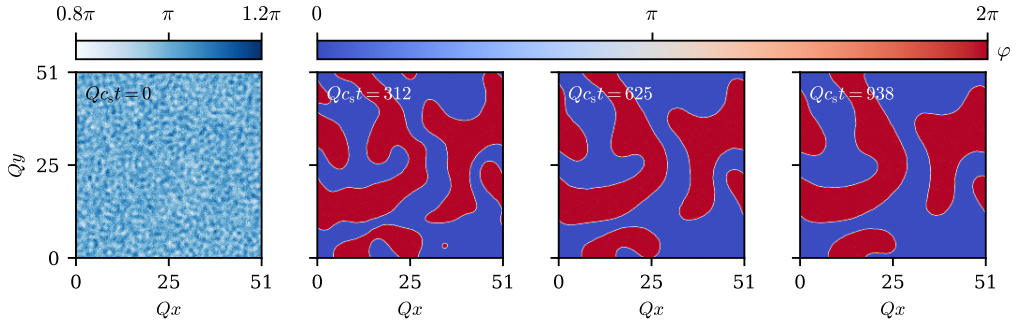

Figure 5.8: Time evolution of the spatial patterns of the DSG model in (2+1)D. Snapshots of the 2D system at 4 different evolution times $Qc_st \in \{0, 312, 625, 938\}$ of the coarsening evolution. In the initial state, the spinor phase is randomly distributed about $\varphi = \pi$, the value at a maximum of the DSG potential, fluctuating according to the box distribution shown in the left panel of Fig. 5.7. The system early-on develops closed domains where φ fluctuates around either of the two values 0 and 2π. With time proceeding these domains grow in size and eventually merge.

sured distributions. Most importantly, we find field configurations to spread over many minima of the periodic potential, as exemplarily shown in the right panels for 3 realisations each.

5.4.3 SCALING EVOLUTION ACCORDING TO THE TWO-DIMENSIONAL DSG MODEL

In contrast to the one-dimensional case, scaling dynamics resulting in a diffusion-type exponent in a two-dimensional spin-1 system [77] has been attributed to the dynamics of spin vortex patterns. To compare with this setting, we simulate the DSG model in two dimensions with couplings $\lambda = 1.6 = 100\,\lambda_s$ in numerical units, preparing again a momentum box of DSG field about a mean value $\langle\varphi\rangle = \pi$ chosen at a maximum of the cosine potential. An analysis of the ensuing evolution of the φ distribution in this case reveals that the DSG field φ is concentrated mainly across two minima of the periodic effective potential, see inset of Fig. 5.7a. This corresponds to the formation of spin-type magnetic domains as seen in Fig. 5.8b. At long evolution times, these domains coarsen, i.e., grow in size, corresponding to universal dynamical scaling evolution with $\beta \approx 0.5$, cf. Fig. 5.7. The time evolution and scaling collapse of the spectra $S(k, t)$ are shown in Figs. 5.7a,b. The presence of a weak plateau in the spectra allows us to rescale the spectra while optimising α and β independently, with larger errors on α than β due to the smallness of the plateau, see panel c. We obtain $\beta = 0.51(8)$, $\alpha = 0.98(20) \simeq d\beta$ and $\kappa = 2.76(1)$, corroborating the spin-1 results from [77] within the error bounds. Once more we find indications that the spread of the DSG field across the potential is crucial for the type of scaling found in the system.

5.5 CONCLUSION AND OUTLOOK

In this chapter, we have shown that the universal dynamics of the intricate spin-1 Bose gas after a quench of the quadratic Zeeman shift from the polar phase to the easy-plane phase can be recaptured by a real scalar field theory, which takes the form of a double sine-Gordon model for the spinor phase degree of freedom. This effective description is consistent with numerical and

experimental observations regarding the probability distribution function of φ_s. In our derivation, we have shown that we may obtain two sets of models: one lowest-energy model for low wavenumbers and a model for momenta on the order of the spin healing momentum. We have shown that the model naturally constrains the hopping between the degenerate minima of the periodic potential to happen in a highly localised manner on the order of the spin healing length, reflecting the reality seen in numerics and experiment. The far-from-equilibrium dynamics of the effective model shows pattern coarsening in the IR regime of wave numbers $k \ll k_{\xi_s}$, of the subdiffusive ($\beta < 1/2$), as well as the diffusion type ($\beta = 1/2$), consistent with previous findings of [1, 75, 77] for the full spin-1 gas. The subdiffusive and diffusion-type scaling are associated with field configurations spreading over many, or few minima of the sinusoidal potential, respectively. These results corroborate analytical findings of Refs. [85, 178]. Our results are crucial to the understanding of the dominant mechanisms leading to self-similar scaling far from equilibrium. The reduction to a non-compact field theory of a single real scalar field, advances our efforts towards the identification of far-from-equilibrium universality classes. They open a path for classifying subdiffusive [53, 56, 72, 78, 87, 187] vs. diffusion-type scaling [53, 55, 71, 77, 81, 100, 101, 120] also in other systems.

The appearance of the (double) sine-Gordon model as an effective model for many systems may constitute an overarching non-equilibrium universality class to which the aforementioned systems belong to, thus underlining the strength of a universal description for far-from-equilibrium dynamics. It is worth noting that the sine-Gordon model has a natural connection to the description of vortex dynamics, particularly in the context of the Berezinskii-Kosterlitz-Thouless (BKT) transition [180, 181, 188]. The emergence of this model in a setting where topological defects and their redistribution play a central role is unlikely to be coincidental. However, establishing a general non-equilibrium framework that connects a compact model such as the XY model to the non-compact sine-Gordon model, an approach which is well known in equilibrium studies, is a highly non-trivial task and lies beyond the scope of this thesis.

Our results furthermore open up the possibility to use the spin-1 Bose gas for experimentally investigating fundamental sine-Gordon dynamics. Currently, the experiment developed a new measurement scheme, enabled through the derivation of this effective theory, aimed at calibrating and stabilising control over the quadratic Zeeman shift (see Chap. 7 for further details). In Ref. [4], experimental efforts focus on exploring sine-Gordon dynamics by utilising the spinor gas as a platform. These studies concentrate on the dynamics of quasi-topological excitations, such as sine-Gordon solitons and their collisions [189], breathers and n-bounce solutions [190, 191]. These phenomena are hallmark solutions of the sine-Gordon model, and their emergence in the system provides compelling evidence for the validity of the effective theory in the easy-plane regime.

Part III

SYMMETRIES

In this part, we explore the importance of symmetry in dynamics far from equilibrium, using the spin-1 Bose gas as a platform. In equilibrium, the density matrix of a system is proportional to the exponential of the system's Hamiltonian, thus naturally obeying the same symmetries as the Hamiltonian. Therefore, symmetry identities constraining the field configurations on the level of correlations stem purely from the symmetry of the model. In contrast, the ability to break the symmetry in non-equilibrium via the introduction of a symmetry-violating initial density matrix leads to an important distinction of symmetry on the level of the observable and on the level of the Hamiltonian.

In the broader context of this thesis we have discussed approaches to characterise and identify non-thermal fixed points, which generically classify systems according to their symmetries. For example, the symmetry of a system contains valuable information crucial for the development of effective theories. Yet, the derivation of an effective theory for a system far from equilibrium is especially challenging, since symmetries in non-equilibrium systems may be a dynamical and emergent quantity. Hence, in order to obtain the effective theory underlying the far-from-equilibrium dynamics of a system, the emergent symmetry must be considered, in addition to that of the Hamiltonian.

In Chap. 6, we introduce a method for the extraction of the symmetry content in a dynamical system out of equilibrium and apply it to the spin-1 Bose gas in the easy plane. To this end, we derive a set of Ward-Takahasi identities of spin-operator correlations for a spontaneously broken SO(2) symmetry. Defining so-called symmetry witnesses, we numerically show that starting from an explicitly symmetry-broken initial condition of a non-Gaussian density matrix in the easy plane, the symmetry is dynamically asymptotically restored on a timescale much faster than the equilibration timescale. We find that lower-order correlations restore the symmetry content rather quickly, while higher-order correlations retain their memory of the initial state for longer times. Studying experimental data of a quenched spinor gas, we discuss the spontaneous symmetry breaking in the context of these symmetry witnesses.

In the final chapter of this thesis, Chap. 7, we present recently obtained results, which have not been published as of the time of writing. The developed approach to use Ward identities to define symmetry witnesses allows us to connect two scaling behaviours found in the spin-1 gas to the underlying symmetry emerging dynamically in the system. The change of the quench parameters is seen to give rise to a *symmetry crossover*, where the value of the scaling exponents changes rapidly due to a different symmetry emerging dynamically. Finally, we show that we are able to reconcile the discrepancy between numerically observed and experimentally measured results for the scaling behaviour of the post-quench spin-1 dynamics. We discuss the implications of these findings on the underlying sine-Gordon effective theory. This chapter is intended to provide a short, yet detailed outlook, highlighting promising directions for future research.

EXTRACTING THE SYMMETRIES OF NON-EQUILIBRIUM QUANTUM MANY-BODY SYSTEMS

By tomorrow, we forget the remains, we start over
That's the problem

– Kendrick Lamar, "The Heart Part 5"

Symmetries play a pivotal role in our understanding of the properties of quantum many-body systems. While there are theorems and a well-established toolbox for systems in thermal equilibrium, much less is known about the role of symmetries and their connection to dynamics out of equilibrium. This arises due to the direct link between a system's thermal state and its Hamiltonian, which is generally not the case for non-equilibrium dynamics. In this chapter, we present a pathway to identify the effective symmetries and to extract them from data in non-equilibrium quantum many-body systems. Our approach is based on exact relations between correlation functions involving different numbers of spatial points, which can be viewed as non-equilibrium versions of (equal-time) Ward identities encoding the symmetries of the system. We derive symmetry witnesses, which are particularly suitable for the analysis of measured or simulated data at different snapshots in time. To demonstrate the potential of the approach, we apply our method to numerical and experimental data for a spinor Bose gas. We investigate the important question of a dynamical restoration of an explicitly broken symmetry of the Hamiltonian by the initial state. Remarkably, it is found that effective symmetry restoration can occur long before the system equilibrates. We also use the approach to define and identify spontaneous symmetry breaking far from equilibrium, which is of great relevance for applications to non-equilibrium phase transitions. Our work opens new avenues for the classification and analysis of quantum as well as classical many-body dynamics in a large variety of systems, ranging from ultracold quantum gases to cosmology.

This chapter is structured as follows: We begin by giving a general introduction to the subject in Sect. 6.1, followed by a discussion of symmetry transformations in and out of equilibrium in Sect. 6.2. Next, in Sect. 6.3, we derive a set of symmetry identities for the spin-1 Bose gas in the

easy plane, finding relations between the correlations of the transverse spin components F_x and F_y, with which we define the so-called symmetry witnesses. Thereafter, in Sect. 6.4, we probe the dynamics of the spin-1 Bose gas in a non-equilibrium setting, having explicitly broken the symmetry in the initial condition. We observe and discuss the restoration of symmetry in this non-equilibrium setting and show the dependence of the results on the initial condition. Finally, we discuss spontaneous symmetry breaking, using experimental data from quench experiments of the BEC lab by Markus K. Oberthaler in Sect. 6.5.

This chapter is taken and adapted from [3], a collaborative publication including three groups. I stress that many parts of this chapter are taken verbatim from the publication, yet some parts were edited and expanded upon to better fit the context of this thesis. The development of symmetry witnesses and the analytical calculation of the identities were performed by A. N. Mikheev and V. Noel, whereas key ideas, all numerical simulations and parts of the data analysis were performed by me. The experimental data was measured by S. Lannig and H. Strobel, and analysed by V. Noel. This work has also been presented in the dissertation of V. Noel [116].

6.1 INTRODUCTION

As discussed in Chap. 4 and Chap. 5, the analytical study and analysis of dynamics far from equilibrium remains a challenging and, to date, largely unsolved problem. To gain a deeper insight to the relevant processes and mechanisms driving the system as it evolves in time towards equilibrium, various theoretical frameworks are utilised to simplify the dynamics to its essential components. As emphasised in the course of this thesis, the framework of deriving effective theories is of particular relevance when attempting to classify various models into non-equilibrium universality classes. Effective theories allow for the extraction of the relevant degrees of freedom in the dynamics, often mapping the system onto well-known field theories, such as a Luttinger liquid [106] or a sine-Gordon model [2, 147, 148]. Whether symmetries stem from the Hamiltonian or emerge dynamically from the non-equilibrium time evolution, they constitute, in principle, a key step towards extracting effective field theories from experimental and numerical data and thus a better understanding of the underlying non-equilibrium dynamics.

In this chapter, we describe a general pathway for extracting the effective symmetries of non-equilibrium quantum many-body systems using equal-time correlation functions. The approach takes into account that the density operator $\hat{\rho}_t$ describing a non-equilibrium state at any time t may not be directly related to the Hamiltonian $\hat{H}$, unlike in thermal equilibrium, where $\hat{\rho}_{\mathrm{eq}} \sim \exp\left(-\beta\hat{H}\right)$ for the example of a canonical ensemble. Instead, we exploit that the symmetries can be classified on the level of observables, i.e., expectation values $\mathrm{Tr}\left[\hat{\rho}_t\,\hat{O}(\boldsymbol{x}_1,\ldots,\boldsymbol{x}_n)\right]$ of n-point operators $\hat{O}(\boldsymbol{x}_1,\ldots,\boldsymbol{x}_n)$. We derive exact relations between expectations values of operators involving different numbers n of spatial points, which encode the symmetry properties of the system. Our equations can be viewed as non-equilibrium versions of (equal-time) Ward identities [103]. For the example of a spin-1 Bose gas, we show that extracting the n-point functions from spatially resolved data allows one to efficiently uncover the presence or absence of a given symmetry. For this, we define symmetry witnesses and apply our approach to analyse the dynamical effec-

tive restoration of explicit symmetry breaking. Remarkably, we observe that effective symmetry restoration can occur long before the system equilibrates, which is a crucial ingredient for the construction of effective theories for non-equilibrium evolutions. Importantly, we also demonstrate how the method can be used to define and identify spontaneous symmetry breaking even far from equilibrium, opening up numerous applications for non-equilibrium phase transitions.

While the approach can be used for any analytical or classical simulation technique of quantum many-body systems, we emphasize that it is particularly well suited for large-scale (analog) quantum simulations based on setups with ultracold quantum gases [192, 193]. These systems can realise a wide range of Hamiltonians with different symmetries, variable interactions and degrees of freedom based on atomic, molecular, and optical physics engineering. They offer high control in the preparation and read-out of the quantum dynamics, with the ability to explore new regimes even far from equilibrium [54–56] that are otherwise difficult to access directly.

6.2 SYMMETRIES AND DYNAMICS

For the following discussion, it will be important to distinguish symmetries of a state or density operator from symmetries of the Hamiltonian that governs the equations of motion [194]. A Hamiltonian $\hat{H}$ is symmetric under the group of transformations G if $[U, \hat{H}] = 0$ for every $U \in G$. This group can be either discrete or continuous, with U forming an (anti-)unitary representation of G on the Hilbert space of the system [195, 196]. In this chapter, we focus on the case of continuous unitary symmetries. In addition, we assume that the considered continuous symmetries have the structure of a Lie group, whose elements can be written as

$$U = \exp(\mathrm{i}\alpha_k T_k)\,, \quad [T_i, T_j] = \mathrm{i} f_{ijk} T_k\,, \tag{6.1}$$

where f_{ijk} are the structure constants that characterise the underlying Lie algebra, and the operators T_k are the generators of the group. For brevity we have restricted ourselves to elements of G that are simply connected to the unity element. Since U is unitary, the operators T_k are Hermitian and taken to correspond to physical observables. From Eq. (6.1) it immediately follows that $[T_k, \hat{H}] = 0$, implying that the generators of G are conserved quantities.

On the other hand, the state at time t, described by the density operator $\hat{\rho}_t$, is symmetric under G if $[U, \hat{\rho}_t] = 0$ for every $U \in G$. From this, one also concludes the following rigorous property for the unitary time evolution of quantum systems described by the von Neumann equation: If the density operator $\hat{\rho}_{t_0}$ explicitly breaks a symmetry of the Hamiltonian $\hat{H}$ at some given time t_0, then it cannot be restored on a fundamental level at any other time. Conversely, starting with a symmetric state and following a unitary evolution respecting the same symmetry, it will never be explicitly broken.

However, these strict statements are not in conflict with the assertion that typical observables may show emergent phenomena which involve the effective restoration of an initially broken symmetry or vice versa. In this chapter, we will consider expectation values $\mathrm{Tr}\big[\hat{\rho}_t\, \hat{O}(\boldsymbol{x}_1, \ldots, \boldsymbol{x}_n)\big]$ of n-point operators $\hat{O}(\boldsymbol{x}_1, \ldots, \boldsymbol{x}_n)$ as observables. An effective symmetry still remains a set of transformations which leave observable properties of the system unchanged, though the set of

observables becomes restricted in practice, which in our case will be related to finite numbers for n. For instance, the notion of effective or relevant symmetries for observable properties is at the heart of macroscopic theories for non-equilibrium evolutions, such as effective kinetic theories or hydrodynamics describing the long-time and long-distance behaviour of an underlying microscopic many-body system in terms of few-point functions only [12]. In this respect, the discussion also closely resembles the one concerning thermalisation in closed quantum systems with unitary time evolution [197].

So far we have distinguished the symmetries of the state from the those of the Hamiltonian with the possibility of explicit symmetry breaking. However, for many-body systems it is also important to distinguish an explicit breaking of a symmetry from the phenomenon of spontaneous symmetry breaking. The latter is crucial, e.g., for our understanding of typical phase transitions where an order-parameter can be defined to vanish on one side of the transition while taking on a non-zero value otherwise. Though this is of course well established in equilibrium, the definition and detection of spontaneously broken symmetries out of equilibrium is much less explored.

Spontaneous symmetry breaking implies that the symmetry of the system's state is reduced to a residual symmetry subgroup of G without explicit symmetry violation. Generally, the system will be in a superposition of degenerate states such that the symmetry breaking is not manifest. To efficiently characterise spontaneous symmetry breaking in terms of an order parameter, one needs to lift the degeneracy and favour one of the infinitely many symmetry-breaking configurations. This is typically achieved by adding a small symmetry-breaking perturbation to the Hamiltonian, such as $\hat{H} \to \hat{H} + \int J\,\hat{O}$ for a given order-parameter operator $\hat{O}$. To remove the explicit symmetry breaking in the end, such a bias is introduced as a limiting procedure. Spontaneous symmetry breaking is then identified by a non-vanishing expectation value

$$\lim_{J\to 0^+} \mathrm{Tr}\left[\hat{\rho}_t\,\hat{O}(\boldsymbol{x})\right] = v_t(\boldsymbol{x})\,. \tag{6.2}$$

Crucially, in the case of spontaneous symmetry breaking one finds a non-zero order parameter, $v_t(\boldsymbol{x}) \neq 0$, even in the limit of a vanishing perturbation, $J \to 0^+$. On the other hand, $v_t(\boldsymbol{x})$ is zero in the symmetric state. The choice of an order parameter operator is not unique, although often suggested by the physics of the spontaneous symmetry breaking. Here, we have restricted ourselves to cases that can be characterised by a local order parameter. For translationally invariant systems in space and/or time, the function $v_t(\boldsymbol{x})$ naturally reduces to a respective constant.

For non-equilibrium systems, there are interesting further options to introduce a symmetry-breaking bias, e.g., through the choice of an explicit symmetry-breaking state at a given initial time t_0 with

$$[U, \hat{\rho}_{t_0}] \neq 0\,, \quad [V, \hat{\rho}_t] = 0\,, \tag{6.3}$$

while the symmetry of the Hamiltonian remains unaffected with $[U, \hat{H}] = 0$. In this case, the initial explicit symmetry breaking is not restricted to small perturbations. In situations where the explicitly broken symmetry gets effectively restored dynamically during the time evolution, spontaneous symmetry breaking is still signalled by the emergence of a non-zero order parameter (6.2). Typically, this requires an evolution of the system to sufficiently late times such that the

initial explicit symmetry breaking is effectively reduced to a small perturbation. In the following sections, we will employ and discuss how symmetry can be broken through initial conditions in systems out of equilibrium. Specifically, we will introduce relationships between different n-point functions to identify symmetries and to distinguish between explicit and spontaneous symmetry breaking.

6.3 SYMMETRY IDENTITIES BETWEEN EQUAL-TIME CORRELATION FUNCTIONS

We are probing the symmetry content of our system via equal-time correlation functions. Since such correlators can be extracted from measurements at different snapshots in time, they are particularly convenient for studying cold atom systems and matching theory to experiment. In spinor Bose gases, a convenient choice of experimentally accessible observables are the spin operators $\hat{F}_i$. On a theoretical level, the corresponding equal-time correlation functions can then be conveniently extracted from the generating functional

$$Z_t[\boldsymbol{J}] = \mathrm{Tr}\left\{\hat{\rho}_t \exp\left[\int \mathrm{d}x\, \boldsymbol{J}(x)\cdot\hat{\boldsymbol{F}}(x)\right]\right\}, \tag{6.4}$$

where $\hat{\rho}_t$ is the density matrix of the system in the Schrödinger picture at time t, not necessarily normalised to unity. Symmetrically ordered equal-time spin correlation functions are obtained by taking derivatives with respect to $J_i(x)$ and setting the latter to zero:

$$\frac{Z^{(n)}_{t,i_1\ldots i_n}[0]\,(x_1,\ldots,x_n)}{Z_t[0]} = \frac{1}{n!}\sum_{\sigma\in S_n}\left\langle \hat{F}_{i_{\sigma_1}}(x_{\sigma_1})\ldots\hat{F}_{i_{\sigma_n}}(x_{\sigma_n})\right\rangle. \tag{6.5}$$

Here, the prefactor $1/Z_t[0]$ takes care of the density matrix normalisation, S_n denotes the set of all permutations of $\{1,\ldots,n\}$, $\langle\ldots\rangle \equiv \mathrm{Tr}\{\hat{\rho}_t\ldots\}$, and we have introduced the notation

$$Z^{(n)}_{t,i_1\ldots i_n}[\boldsymbol{J}]\,(x_1,\ldots,x_n) \equiv \frac{\delta^n Z_t[\boldsymbol{J}]}{\delta J_{i_1}(x_1)\ldots\delta J_{i_n}(x_n)}\,. \tag{6.6}$$

The correlation functions (6.5) contain disconnected, lower-order parts. To remove this redundant information and generate connected correlation functions, one can invoke an equal-time equivalent of the Schwinger functional,

$$E_t\,[\boldsymbol{J}] = \log Z_t\,[\boldsymbol{J}]\,. \tag{6.7}$$

As an example, a two-point connected symmetric spin correlation function generated by the functional E_t is given by

$$E^{(2)}_{t,xy}\,[0]\,(x_1,x_2) = \frac{1}{2}\left\langle \hat{F}_x(x_1)\,\hat{F}_y(x_2) + \hat{F}_y(x_2)\,\hat{F}_x(x_1)\right\rangle - \left\langle \hat{F}_x(x_1)\right\rangle \left\langle \hat{F}_y(x_2)\right\rangle, \tag{6.8}$$

and correspondingly for higher-order correlation functions.

Since the spin operators $\hat{F}_i$ transform trivially under $\mathrm{U}(1)$, we will focus on the $\mathrm{SO}(2)$ part and derive associated symmetry identities between different correlation functions. Following the discussion in the previous sections, we will assume that the initial state $\hat{\rho}_{t_0}$ is also $\mathrm{SO}(2)$-invariant, ensuring that the symmetry is fully respected on the dynamical level. In this case, the density matrix $\hat{\rho}_t$ remains formally symmetric at any time $t \geq t_0$, even in the case of spontaneous symmetry breaking. As pointed out above, to address the latter scenario, one has to introduce a symmetry-breaking bias to the system. In this work, the role of such a bias will be played by the sources J_i coupled to the spin operators in the definition (6.4) of the generating functional, which will be addressed in more detail in the following.

From (6.4) we conclude, together with $\hat{\rho}_t = U\,\hat{\rho}_t\,U^{-1}$, where $U \in \mathrm{SO}(2)$, that

$$Z_t[\boldsymbol{J}] = \mathrm{Tr}\left\{\hat{\rho}_t \exp\left[\int \mathrm{d}x\,\boldsymbol{J}(x)\cdot\left(U^{-1}\,\hat{\boldsymbol{F}}(x)\,U\right)\right]\right\}, \tag{6.9}$$

where we have used the cyclic property of trace and $U^{-1}\exp(A)\,U = \exp\left(U^{-1}A\,U\right)$.

The spin operators $\hat{F}_i$ live in the fundamental representation of the rotation group and thus transform as

$$\hat{F}_i \to R_{ij}(\epsilon)\,\hat{F}_j = \hat{F}_i + \mathrm{i}\epsilon T_{ij}\hat{F}_j + O\left(\epsilon^2\right),\; T = \begin{pmatrix} 0 & \mathrm{i} & 0 \\ -\mathrm{i} & 0 & 0 \\ 0 & 0 & 0 \end{pmatrix}, \tag{6.10}$$

where $R(\epsilon)$ denotes the rotation matrix by an angle ϵ about the F_z axis with its single generator T.

Together, Eqs. (6.4) – (6.10) imply $Z_t[\boldsymbol{J}] = Z_t[R^{-1}\boldsymbol{J}]$, and likewise $E_t[\boldsymbol{J}] = E_t[R^{-1}\boldsymbol{J}]$, where we have used the fact that $\boldsymbol{J}\cdot\left(R\hat{\boldsymbol{F}}\right) = \left(R^{-1}\boldsymbol{J}\right)\cdot\hat{\boldsymbol{F}}$. Taking R to be infinitesimal, this yields $E_t[J_x - \epsilon J_y, J_y + \epsilon J_x] - E_t[J_x, J_y] = 0$. Expanding it to linear order in the rotation angle ϵ, we finally derive the master symmetry identity:

$$\int \mathrm{d}x'\left[J_x(x')\,E^{(1)}_{t,y}[\boldsymbol{J}](x') - J_y(x')\,E^{(1)}_{t,x}[\boldsymbol{J}](x')\right] = 0\,. \tag{6.11}$$

By taking further J-derivatives one can generate an infinite hierarchy of symmetry identities encoding the $\mathrm{SO}(2)$ symmetry of the system.

Here and in the following, we assume that the mean field does not break spatial homogeneity. To emphasise the distinction between the fields $\hat{F}_x$ and $\hat{F}_y$, we then introduce the notation $(F_x, F_y) \to (\pi, \sigma)$, $(J_x, J_y) \to (J_\pi, J_\sigma)$, and accordingly $\langle\hat{\pi}\rangle = 0$ and $\langle\hat{\sigma}\rangle = v_t$. To allow for

a spontaneous symmetry breaking scenario, we first explicitly break the symmetry via a linear source term $\int \mathrm{d}x\, J\, \hat{\sigma}(x)$, cf. the discussion in Sect. 6.2:

$$\langle \hat{\sigma} \rangle = \lim_{J \to 0^+} E^{(1)}_{t,\sigma}[J_\pi = 0, J_\sigma = J] = v_t \,. \tag{6.12}$$

The symmetry-breaking case corresponds to $v_t \neq 0$, whereas $v_t = 0$ in the symmetric phase. For spin systems, this symmetry-breaking term allows for a simple physical interpretation as a deformation of the initial density matrix, which is discussed in more detail in App. A.2.

Differentiating the master symmetry identity (6.11) once with respect to J_π we get

$$\begin{aligned} \int \mathrm{d}x' \Big[& \delta(x' - x'')\, E^{(1)}_{t,\sigma}[\boldsymbol{J}](x') + J_\pi(x')\, E^{(2)}_{t,\sigma\pi}[\boldsymbol{J}](x', x'') \\ & - J_\sigma(x')\, E^{(2)}_{t,\pi\pi}[\boldsymbol{J}](x', x'') \Big] = 0 \,. \end{aligned} \tag{6.13}$$

Setting the sources to $(0, J)$ and going to Fourier space we obtain

$$E^{(1)}_{t,\sigma}[0, J] - J\, \tilde{E}^{(2)}_{t,\pi\pi}[0, J](p = 0, -p = 0) = 0 \,, \tag{6.14}$$

where we have introduced the notation

$$E^{(n)}_{t,i_1 \ldots i_n}(p_1, \ldots, p_n) \equiv 2\pi\delta\left(\sum_{i=1}^{n} p_n\right) \tilde{E}^{(n)}_{t,i_1 \ldots i_n}(p_1, \ldots, p_n) \,. \tag{6.15}$$

Similarly, differentiating the master symmetry identity (6.11) once with respect to both J_π and J_σ and then setting the sources to $(0, J)$ yields

$$\begin{aligned} J \lim_{q \to 0} \tilde{E}^{(3)}_{t,\pi\pi\sigma}[0, J]\,(q, p, -p - q) = {} & \tilde{E}^{(2)}_{t,\sigma\sigma}[0, J]\,(p, -p) \\ & - \tilde{E}^{(2)}_{t,\pi\pi}[0, J]\,(-p, p) \,. \end{aligned} \tag{6.16}$$

Taking the $J \to 0^+$ limit and using (6.12) and (6.14) we then find

$$v_t \lim_{q \to 0} \frac{\tilde{E}^{(3)}_{t,\pi\pi\sigma}(q, p, -p - q)}{\tilde{E}^{(2)}_{t,\pi\pi}(q, -q)} = \tilde{E}^{(2)}_{t,\sigma\sigma}(p, -p) - \tilde{E}^{(2)}_{t,\pi\pi}(-p, p) \,, \tag{6.17}$$

with $\tilde{E}^{(n)}_t \equiv \tilde{E}^{(n)}_t[J_\pi = 0, J_\sigma = 0]$. Here, we have taken into account that only the quotient of $\tilde{E}^{(3)}_{t,\pi\pi\sigma}(q, p, -p - q)$ and $\tilde{E}^{(2)}_{t,\pi\pi}(q, -q)$ may have a finite $q \to 0$ limit. While Eq. (6.17) connects

two- and three-point functions, additional symmetry identities relating higher-order correlation functions can be obtained by taking further derivatives:

$$v_t \lim_{k\to 0} \frac{\tilde{E}^{(4)}_{t,\pi\pi\sigma\sigma}(k,p,q,-k-p-q)}{\tilde{E}^{(2)}_{t,\pi\pi}(k)} = \tilde{E}^{(3)}_{t,\sigma\sigma\sigma}(p,q,-p-q) - \tilde{E}^{(3)}_{t,\pi\pi\sigma}(q,p,-p-q) - \tilde{E}^{(3)}_{t,\pi\pi\sigma}(p,-p-q,q)\,, \tag{6.18a}$$

$$v_t \lim_{k\to 0} \frac{\tilde{E}^{(4)}_{t,\pi\pi\pi\pi}(k,p,q,-k-p-q)}{\tilde{E}^{(2)}_{t,\pi\pi}(k)} = \tilde{E}^{(3)}_{t,\pi\pi\sigma}(p,q,-p-q) + \tilde{E}^{(3)}_{t,\pi\pi\sigma}(p,-p-q,q) + \tilde{E}^{(3)}_{t,\pi\pi\sigma}(q,-p-q,p)\,, \tag{6.18b}$$

and so forth.

Symmetry identities, akin to those derived in the present section, then serve as a manifestation of the system's symmetry properties on the level of correlation functions. Since n-point correlation functions can be readily extracted from numerically simulated data or experimental measurements, the symmetry identities can be explicitly checked. This makes them a powerful tool for analysing the symmetry content of quantum many-body systems, allowing to determine whether the symmetry is broken explicitly, spontaneously, or not broken at all.

Based on the above symmetry identities one can introduce symmetry witnesses, which provide efficient measures of the symmetry content of a given system. In particular, higher-order correlation functions are often difficult to visualise and the introduction of a norm as a measure can be very convenient. Defining the left- and right-hand sides of (6.17) as

$$f^{(3)}_{t,\pi\pi\sigma}(p) = v_t \lim_{q\to 0} \frac{\tilde{E}^{(3)}_{t,\pi\pi\sigma}(q,p,-p-q)}{\tilde{E}^{(2)}_{t,\pi\pi}(q,-q)}\,,$$
$$f^{(2)}_{t,\pi\pi\sigma}(p) = \tilde{E}^{(2)}_{t,\sigma\sigma}(p,-p) - \tilde{E}^{(2)}_{t,\pi\pi}(-p,p)\,, \tag{6.19}$$

we may encode the symmetry content by measuring a distance between the two functions using the standard L_1-norm, $\|f\| = \mathcal{L}^n \int \mathrm{d}p_1 \ldots \mathrm{d}p_n\, |f(p_1,\ldots,p_n)|$, with $\mathcal{L}$ being the system size setting the smallest unit of momentum $1/\mathcal{L}$. To avoid biasing the IR momentum region, where the correlation functions are typically larger, we normalise the difference by dividing it by double the average value of $|f^{(3)}|$ and $|f^{(2)}|$, which yields

$$Q^{(3)}_{\pi\pi\sigma}(t) = \lim_{\varepsilon\to 0^+} \left\| \frac{f^{(3)}_{t,\pi\pi\sigma} - f^{(2)}_{t,\pi\pi\sigma}}{\left|f^{(3)}_{t,\pi\pi\sigma}\right| + \left|f^{(2)}_{t,\pi\pi\sigma}\right| + \varepsilon} \right\|. \tag{6.20}$$

Here, ε is a regularisation parameter ensuring that $Q^{(3)}_{\pi\pi\sigma} = 0$ when $f^{(3)}_{t,\pi\pi\sigma} = f^{(2)}_{t,\pi\pi\sigma} = 0$, i.e., in the absence of both explicit as well as spontaneous symmetry breaking. In practice, the choice of ε is motivated by the value of statistical error, inevitable in any experimental or numerical setup.

Note that the normalisation choice implies $0 \leq Q^{(3)}_{\pi\pi\sigma} \leq 1$, with the upper bound following from the Cauchy–Schwarz inequality.

At each point in time, the quantity $Q^{(3)}_{\pi\pi\sigma}$, which we call a symmetry witness, connects one-, two-, and three-point correlation functions and quantifies the degree of violation of the symmetry identity (6.17). Analogously, one can introduce higher-order witnesses $Q^{(4)}_{\pi\pi\sigma\sigma}$ and $Q^{(4)}_{\pi\pi\pi\pi}$ using the identities (6.18a) and (6.18b), respectively, characterising the symmetry content with respect to the higher-order correlation functions. Geometrically, the connected correlation functions characterise the shape and the inner structure of the histograms like the ones depicted in Fig. 6.1. Such histograms consist of "sub-histograms", one for each spatial point x_i, or momentum mode p_i, in the system. The one-point functions correspond to their positions, the two-point functions are related to their widths and heights, while higher-order n-point functions reflect cross-correlations between the sub-histograms. Symmetry then puts constraints on their allowed shapes and cross-correlations, and symmetry witnesses represent how well these constraints are satisfied. The spatial correlation functions can be extracted from numerical simulations or experimentally by sampling read-outs of the transverse spin $F_\perp(x) = F_x(x) + \mathrm{i}F_y(x)$ [145]. As a result, probing symmetry properties of the system via exact relations between observable correlation functions proves to be an effective approach, as demonstrated in the following sections.

6.4 NON-EQUILIBRIUM SYMMETRY RESTORATION

In the following, we investigate the dynamics of the spin-1 Bose gas as introduced and discussed in the previous chapters, prepared in an explicitly symmetry-broken state. Whether the initially explicitly broken symmetry gets effectively restored during the dynamics will be analysed using the symmetry witnesses introduced above. We employ the truncated Wigner approximation (TWA), which describes the dynamics for highly occupied systems at not too late times and weak couplings [139]. The numerical integration of the system is done as in Chap. 4 with the methods introduced in Chap. 3.

6.4.1 INITIAL CONDITION

We start from an initial state with non-vanishing n-point spin correlations that violate the SO(2) rotational symmetry in the F_x-F_y plane. For this we consider the spinor condensate in the mean-field ground state of the easy-plane phase,

$$\psi_{\mathrm{EP}} = \frac{e^{\mathrm{i}\theta/2}}{2} \begin{pmatrix} e^{-\mathrm{i}\varphi_{\mathrm{L}}}\sqrt{1-\bar{q}} \\ e^{-\mathrm{i}\varphi_{\mathrm{s}}/2}\sqrt{2+2\bar{q}} \\ e^{\mathrm{i}\varphi_{\mathrm{L}}}\sqrt{1-\bar{q}} \end{pmatrix}, \tag{6.21}$$

with $\bar{q} = 0.9$. The state is characterised by a well-defined spin length and orientation in the $F_y = 1$ direction. In addition, we imprint a Gamma distribution function in momentum space in

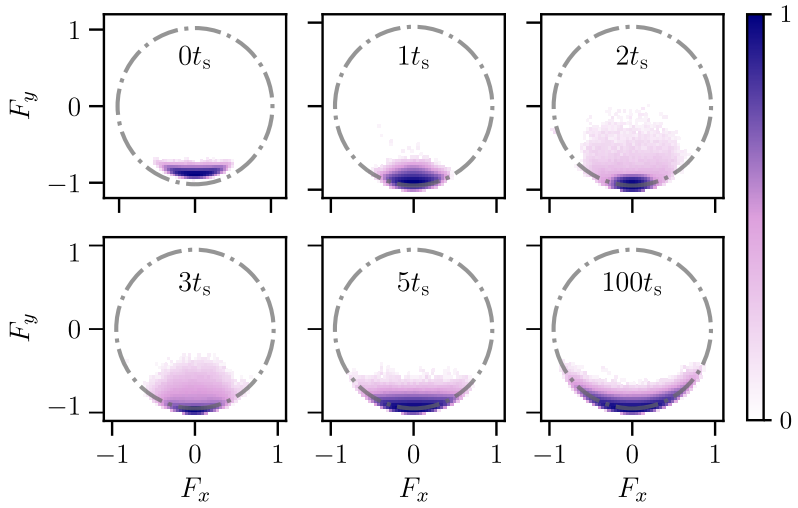

Figure 6.1: Histograms of the spin orientations in the F_x-F_y plane normalised by the atom number for $q_f = 0.6\tilde{\rho}|c_1|$ and averaged over 10^3 runs. The dash-dotted line represents the average spin length $\langle |F_\perp| \rangle = \sqrt{1-\bar{q}^2} \sim 0.95$.

the phases of the fundamental fields, resulting in non-Gaussian statistics in the spinor and Larmor phases, as to achieve a sizeable explicit symmetry breaking. Concretely, we define

$$c_p^{m_F} = \mathrm{d}\zeta_{m_F}\Gamma(p), \tag{6.22}$$

where $\mathrm{d}\zeta_{m_F}$ is a Γ distributed white noise with a variance of half a particle, and $\Gamma(p)$ is a Gamma probability distribution function in momentum space. We then Fourier transform the noise $c_x^{m_F} = \mathcal{F}[c_p^{m_F}]$ and rotate the fundamental fields by their respective noise terms.

$$\psi_{\pm 1} \to \psi_{\pm 1} e^{\pm \mathrm{i}c_x^1}, \qquad \psi_0 \to \psi_0 e^{-\mathrm{i}c_x^0}. \tag{6.23}$$

Notice that the $m_F = \pm 1$ components are rotated by the same noise, but with opposite signs, while the $m_F = 0$ component is subject to a rotation with an independent noise term. This is equivalent to

$$\varphi_L = \bar{\varphi}_L + c_x^1, \quad \varphi_s = \bar{\varphi}_s + 2c_x^0, \tag{6.24}$$

where $\bar{\varphi}$ is to be understood as the background mean-field solution, which is chosen to be $\bar{\varphi}_s = 0$ and $\bar{\varphi}_L = \pi/2$, i.e., full spin orientation in the F_y direction. Since we rotate both the Larmor and spinor phases, we imprint non-Gaussian statistics in the transverse spin degree of freedom, both in orientation, as well as its length (see upper left panel of Fig. 6.1), without imprinting any density excitations, thus remaining in a low-energy regime. After imprinting the noise, we quench the quadratic Zeeman shift from an initial value of $q_i = 0.9\tilde{\rho}|c_1|$ to a final value of $q_f = 0.6\tilde{\rho}|c_1|$, where we verified that no significant excitations of topological defects are present in the system.

The physical parameters of the simulations aim to resemble a cloud of ^{87}Rb atoms in a one-dimensional geometry as performed in the experiments [6, 198, 199], the main differences being

an increased homogeneous density $\tilde{\rho}$ compared to the experiment and a purely one-dimensional setting with no trapping potential. We simulate a cloud of $3 \cdot 10^6$ particles on a numerical grid containing $N = 4096$ points corresponding to a physical length of 220μm. The spin healing length is given by $\xi_s = (2M\tilde{\rho}|c_1|)^{1/2} = 8$ lattice units, and spin-changing collisions occur on a timescale of $t_s = 2\pi/(\tilde{\rho}|c_1|) = 696$ in numerical time units. Furthermore, the field operators are normalised with respects to the total density $\tilde{\psi}_m = \psi_m/\sqrt{\tilde{\rho}}$, which results in a normalisation of the spin vector as well $\tilde{\boldsymbol{F}} = \boldsymbol{F}/\tilde{\rho}$. In the following, the tilde is omitted and all values are to be understood as normalised values unless explicitly stated otherwise. Upon extracting the spin degrees of freedom F_x and F_y, we compute the relevant two-, three-, and four-point correlation functions appearing in the identities (6.17), (6.18a) and (6.18b).

6.4.2 SYMMETRY WITNESSES POST-QUENCH

It is instructive to first examine the probability distribution of local spins in real space by averaging over many realisations. In Fig. 6.1, we depict a probability density in spin configuration space in the F_x-F_y plane. From the left graph, one observes that the initial state is characterised by a sizeable spin length with a rather well-defined orientation. As a consequence, one may separate two types of excitations for the transversal spin $F_\perp$: a radial "Higgs"-like mode associated with perturbations of the spin length $|F_\perp|$, and a transverse "Goldstone"-like mode associated with perturbations of the angle φ_L, respectively. We would like to note that the fluctuations in the spin length can be attributed to both density fluctuations, as well as to fluctuations in the spinor phase, whereas the latter is energetically favourable. Since the state is initialised away from the minimum of the champagne bottle effective potential (recall Sect. 2.2.6), one observes dynamics in the radial direction, such that the spin length $|F_\perp|$ acquires a range of values which are also significantly smaller than the initial one. As seen in the histograms, this occurs predominantly during the first few characteristic spin-changing collision times t_s. During this time, the non-equilibrium "Higgs"-like mode explores the inner part of the effective potential, whose non-convex shape is expected to lead to a fast instability growth of the mode occupancy in a characteristic momentum range. However, after about $\sim 5\,t_s$, perturbations in $|F_\perp|$ are seen to become more and more suppressed. Instead, significantly slower dynamics for the transverse mode starts dominating, by which the spin distribution settles into a banana-like shape as it spreads out around the ring set by the minimum of the effective potential.

While the histograms indicate the different dominant excitations and timescales of the system, one needs further information to quantify the initial explicit symmetry breaking and its effective restoration. For instance, both the left graph of Fig. 6.1 at $0\,t_s$ and the right one at $100\,t_s$ indicate configurations with comparable spin length and rather small spread in the radial direction. However, their transverse extensions along the ring, which represent the "Goldstone"-like fluctuations, are significantly different. As described in Sect. 6.3, in the absence of explicit symmetry breaking, there exists a well-defined relation between the spin length and the fluctuations, which we will use in the following to quantify the symmetry content of the data.

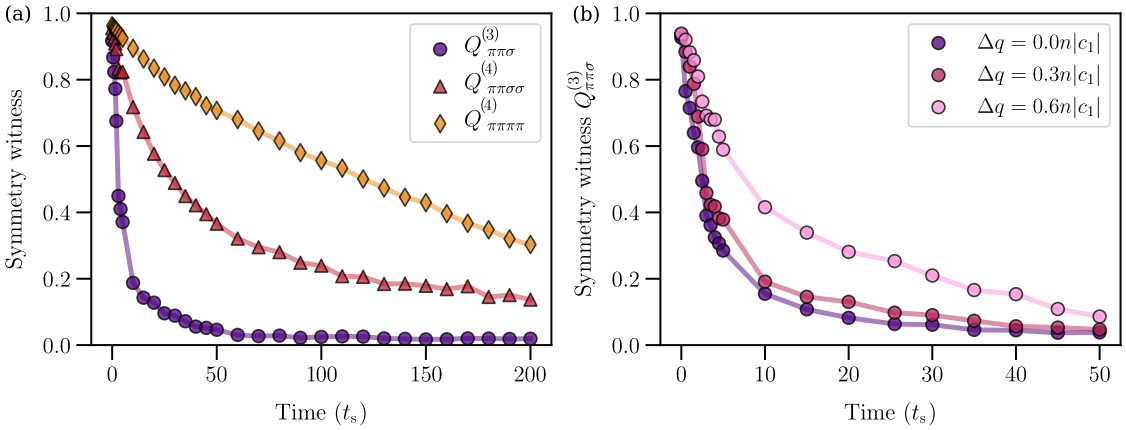

Figure 6.2: (a) Evolution of the symmetry witnesses $Q^{(n)}$ for a system prepared in a state which explicitly breaks the SO(2) symmetry of the Hamiltonian with a subsequent quench from $q_\mathrm{i} = 0.9\tilde{\rho}|c_1|$ to $q_\mathrm{f} = 0.6\tilde{\rho}|c_1|$, where $0 \leq Q^{(n)} \leq 1$. The value of $Q^{(n)} = 0$ corresponds to the absence of explicit symmetry violation. Here, $Q^{(3)}_{\pi\pi\sigma}$ is the identity connecting two- and three-point functions appearing in Eq. (6.17), while $Q^{(4)}_{\pi\pi\sigma\sigma}$ and $Q^{(4)}_{\pi\pi\pi\pi}$ connect three- and four-point functions. (b) Evolution of the symmetry witness $Q^{(3)}_{\pi\pi\sigma}$ for three different systems prepared in a symmetry-broken state. The dark purple curve represents the symmetry witness for a system that is not quenched initially, while the red- and pink curves correspond to initial quenches, with the pink one being a stronger quench. The middle curve for $Q^{(3)}$ shows the same data as in Fig. 6.2, but only up to $50\,t_\mathrm{s}$.

Fig. 6.2 shows the corresponding time evolution of the symmetry witnesses $Q^{(n)}$ defined in Eq. (6.20), where $0 \leq Q^{(n)} \leq 1$, with $Q^{(n)} = 0$ in the absence of explicit symmetry violation. The index n denotes the maximum number of spatial points involved in the correlation functions probing the symmetries. We show $Q^{(3)}_{\pi\pi\sigma}$ based on an identity connecting two- and three-point functions involving the "Goldstone"-like (π) and "Higgs"-like (σ) excitations appearing in Eq. (6.17), while $Q^{(4)}_{\pi\pi\sigma\sigma}$ and $Q^{(4)}_{\pi\pi\pi\pi}$ connect three- and four-point functions based on Eqs. (6.18a) and (6.18b), respectively.

As seen in Fig. 6.2, the systems starts out in a state that explicitly breaks the SO(2) symmetry of the underlying Hamiltonian very strongly, with the different $Q^{(n)}$ rather close to unity. While the unitary time evolution of the quantum system can never restore the symmetry exactly, one observes that important observable properties can nevertheless exhibit an effective symmetry restoration. The different witnesses based on n-point correlation functions probe more and more details as n increases. Correspondingly, we find that the lowest-order witness shown, $Q^{(3)}_{\pi\pi\sigma}$, approaches zero fastest (purple curve in Fig. 6.2a). In fact, after an initial rapid decrease until times of a few t_s, the restoration dynamics slows down, and the timescales are in close analogy to those observed from the histograms in Fig. 6.1.

The higher-order witnesses $Q^{(4)}_{\pi\pi\sigma\sigma}$ (red curve) and especially $Q^{(4)}_{\pi\pi\pi\pi}$ (gold curve) exhibit a comparably slower effective restoration of the initially broken symmetry. While $Q^{(4)}_{\pi\pi\sigma\sigma}$, involving both σ and π excitations, still shows a characteristic two-stage decay, which is relatively fast at early times and then slowing down at late times, this is much less pronounced in $Q^{(4)}_{\pi\pi\pi\pi}$, which involves predominantly the slow "Goldstone"-like modes. Nevertheless, all witnesses clearly exhibit the approach towards an effective restoration of the explicitly broken symmetry by the initial

state. We emphasise that this is much shorter than the timescale on which the approach to thermal equilibrium is observed, as the power spectrum $\langle |F_\perp|^2 \rangle$ starts to develop a thermal tail at higher momenta around $\sim 1400\, t_s$. This separation of time scales between the effective restoration of an explicitly broken symmetry and thermalisation may, in principle, be further diminished for sufficiently high-order correlation functions. However, thermalisation time is defined with respect to characteristic thermodynamic observables that typically do not involve arbitrarily high-order details since the time-translation invariant thermal state can never be reached on a fundamental level in systems with unitary dynamics. In practice, emergent theories that effectively describe dynamical behaviour, such as effective kinetic theories, are based on a reduced set of low-order correlation functions. In this context, our results demonstrate that effective symmetry restoration can occur long before the system equilibrates. The situation is reminiscent of thermalisation in isolated quantum systems, where local observables of the system, prepared in a non-equilibrium quantum state, eventually behave as if sampled from a thermal distribution. Similarly, while low-order symmetry witnesses show effective restoration, some higher-order witnesses, which encode finer statistical details of the system, will show symmetry violations at asymptotically late times. This is in accordance with the general statement regarding how the symmetry can never be fully restored by means of a unitary time evolution governed by a symmetric Hamiltonian, cf. Sec. 6.2.

It remains to investigate to what extent the results depend on the details of the initial state. Here we consider variations in the initial quench of the quadratic Zeeman shift with different strengths, or with no quench at all. As depicted in Fig. 6.2b, we find that the stronger the quench, the longer it takes to restore the SO(2) symmetry, and not quenching at all restores it the fastest. The witness based on the correlation functions from Eq. (6.17), as seen in Fig. 6.2b, corresponds to the middle red curve, with an initial quench from $q_i = 0.9\tilde{\rho}|c_1|$ to $q_f = 0.6\tilde{\rho}|c_1|$. Quenching stronger than this, to $q_f = 0.3\tilde{\rho}|c_1|$, takes longer to restore the symmetry (light pink curve), and not doing a quench takes the shortest (dark purple curve). Irrespective of the strength or the presence of the quench, the correlation functions and the restoration process look qualitatively very similar as shown in Fig. 6.2a.

The symmetry witnesses provide an efficient means to quantify the symmetry content of the data. However, further details can be investigated by looking directly at the underlying momentum-resolved correlation functions in the identity (6.17). In Fig. 6.3, we plot both the left-hand side (purple curve) and right-hand side (red curve) of Eq. (6.17) for four different time steps. Initially, we observe that the symmetry is strongly broken signalled by the unequal different n-point correlation functions. Within the span of a few t_s, these different correlation functions quickly approach each other, and by $\sim 50\, t_s$, they are nearly equal and the conclusions are as for the symmetry witnesses discussed before. In addition, one observes from the momentum-resolved correlation functions that, apart from the initial strong fluctuations at low momenta, an additional peak in the correlation functions develops at a higher momentum scale. The peak height settles quickly within a few t_s, during which the "Higgs"-like mode explores the inner part of the effective potential leading to a fast growth of fluctuations as discussed above.

The momenta of the correlation functions entering the identity (6.17) underlying $Q^{(3)}$ correspond to the momentum-conserving diagonals of the full momentum matrix. Likewise, the iden-

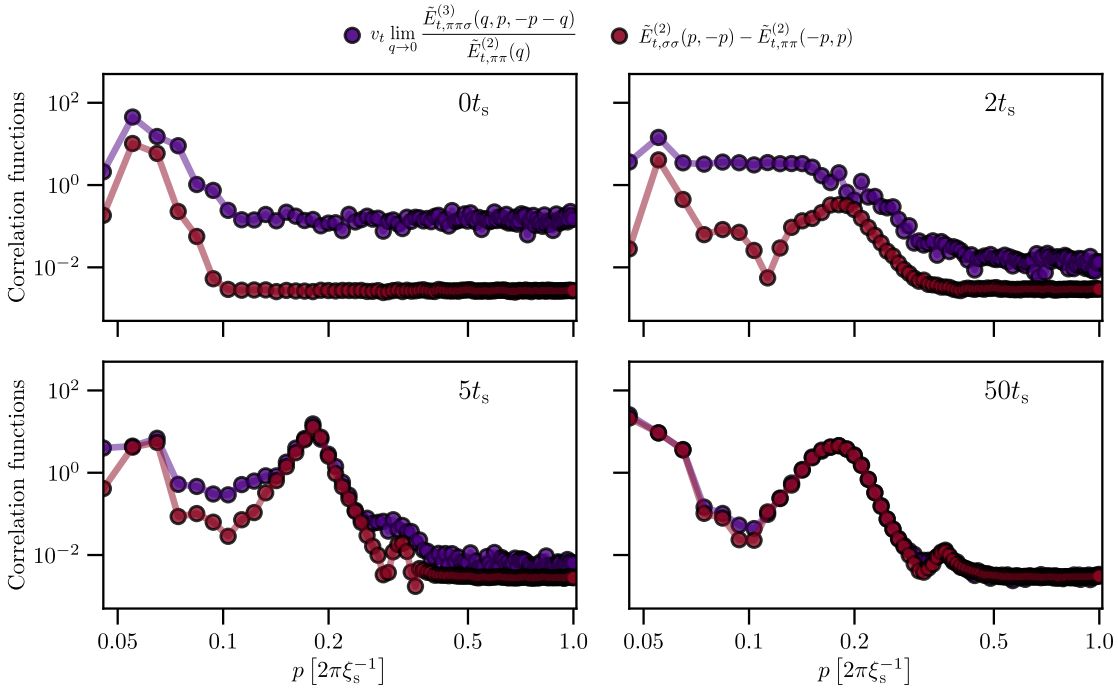

Figure 6.3: Data for the symmetry identity (6.17) with the correlation functions as a function of momentum at four different times during the dynamical evolution.

tities for $Q^{(4)}$ involve momentum-conserving surfaces. As an example, we show the surfaces of our numerical data corresponding to the symmetry identities (6.18a) in Fig. 6.4a and (6.18b) in Fig. 6.4b. In both cases, we see strong initial symmetry violation signalled by the different unequal n-point correlator surfaces. The cross-like shape is the dominant feature of these surfaces and is already present initially, although much stronger in the four-point surfaces. The appearance of the surfaces becomes gradually more equal with time in both Fig. 6.4a and b, however, we can visually confirm that it is not as quick as for the momentum-conserving diagonals above. Additionally, restoration is visibly slower for the identity (6.18b) since at $50\,t_s$ in Fig. 6.4b the dominant cross-like features are still at an increased amplitude in the four-point surface compared to the three-point one. This is consistent with what we have observed from the corresponding witnesses in Fig. 6.2.

6.5 Non-equilibrium spontaneous symmetry breaking

6.5.1 Experimental data

In the previous section, we discussed the explicit breaking of a symmetry of the Hamiltonian by the initial state, and its effective restoration long before the system equilibrates. However, even if explicit symmetry breaking is absent or dynamically restored, the symmetry may still be spontaneously broken. The notion of spontaneous symmetry breaking, in thermal equilibrium or dynam-

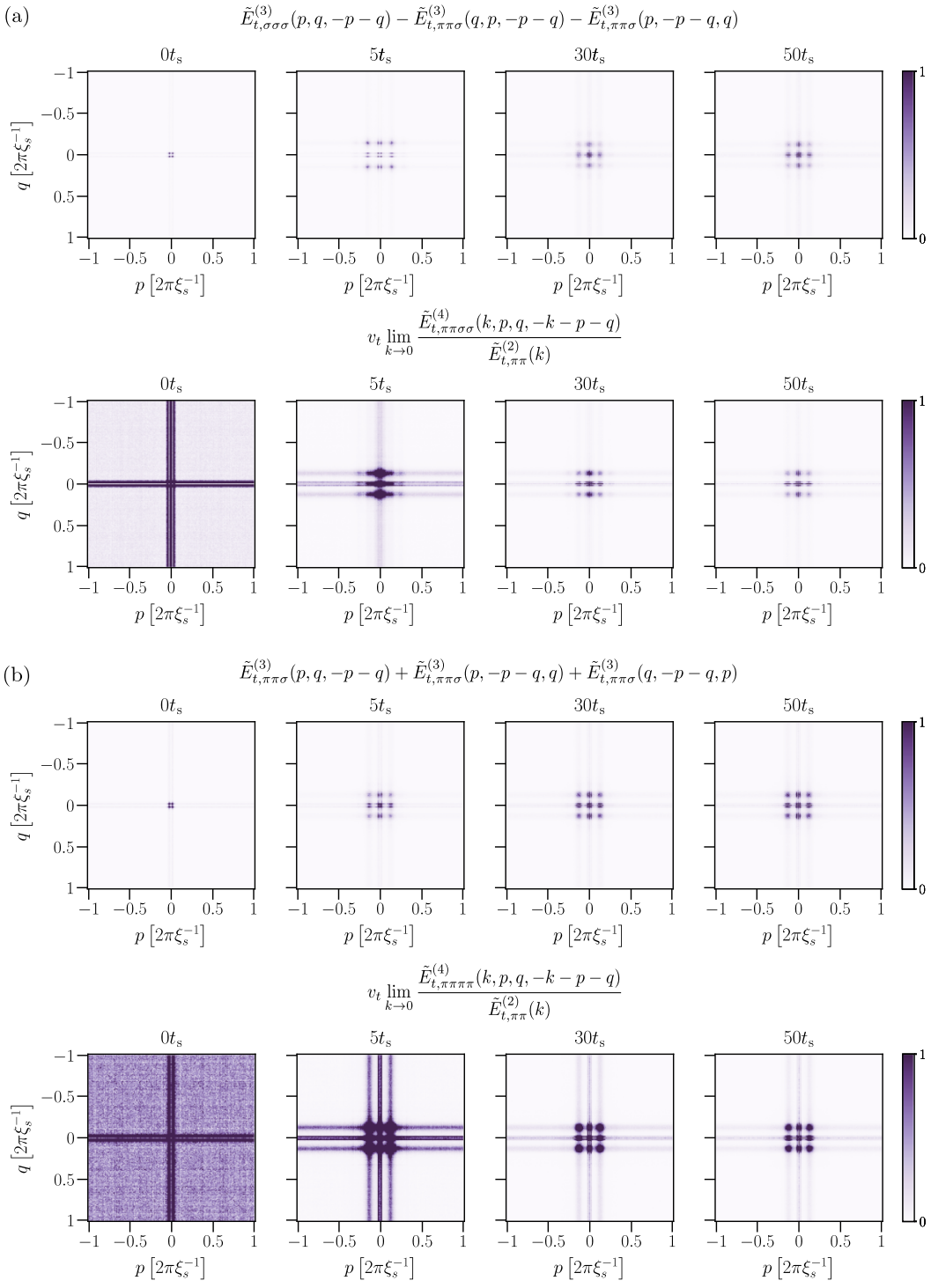

Figure 6.4: Momentum-conserving surfaces in the symmetry identities (6.18a) and (6.18b), respectively.

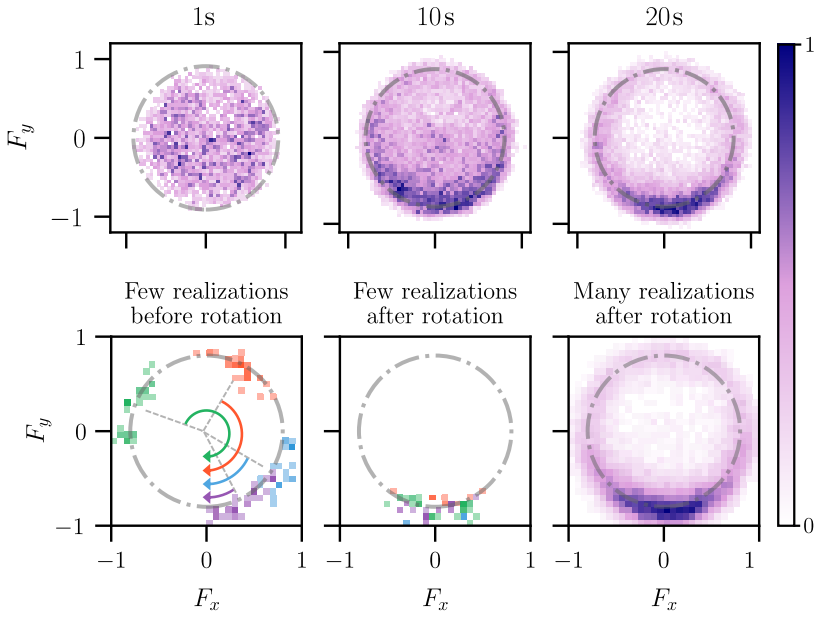

Figure 6.5: (upper panel) Histograms of the experimentally measured spin in the F_x-F_y plane taken from a quasi-one-dimensional ^{87}Rb experiment [6], normalised by the atom number, for different evolution times. The dash-dotted line represents $|F_\perp| = 0.85$. (lower panel) Histogram of the normalized spin at $t = 35$s. The left and middle figures show four different experimental realisations, each in different color, before (left) and after (middle) the rotation by the mean phases for each realization. On the right, the combination of all realisations with mean phase subtracted is displayed.

ically even far from equilibrium, is a central ingredient for our understanding of phase transitions. Spontaneous symmetry breaking is signalled by a non-zero order parameter (6.2) using a bias that does not break the symmetry explicitly in the end.

To analyse spontaneous symmetry breaking out of equilibrium in more detail, in the following we consider experimental data from measurements of a spinor Bose–Einstein condensate of ^{87}Rb atoms, recall Sect. 5.4.1 for the experimental methods, and see App. A.1 for further details. The system is initialised in the $|F, m_\mathrm{F}\rangle = |1, 0\rangle$ state, i.e., the polar state. Subsequently, the quadratic Zeeman shift q, is quenched to a value within the easy-plane phase thereby initiating the dynamics. In contrast to the initial state investigated in Sect. 6.4 in the context of explicit symmetry breaking, in the present case there is initially no well-defined spin length, with fluctuations solely in the F_x-F_y plane such that the initial state respects the SO(2) symmetry of the system. The initial conditions restrict the average longitudinal (z-axis) spin to be zero, and excitations build up in the F_x-F_y plane. This transversal spin degree of freedom is examined by the spatially resolved detection of the complex-valued field $F_\perp = F_x + \mathrm{i}F_y$ [6].

Fig. 6.5 shows histograms of the measured spin orientations in the F_x-F_y plane normalised by the atom number, at different times. While initially the measured values scatter, such that the average spin length is practically zero, this changes at later times. The average spin length settles around $|F_\perp| = 0.85$ represented by the dash-dotted line in the figure. In this case, the non-zero average spin plays the role of the order parameter signalling the spontaneous symmetry breaking

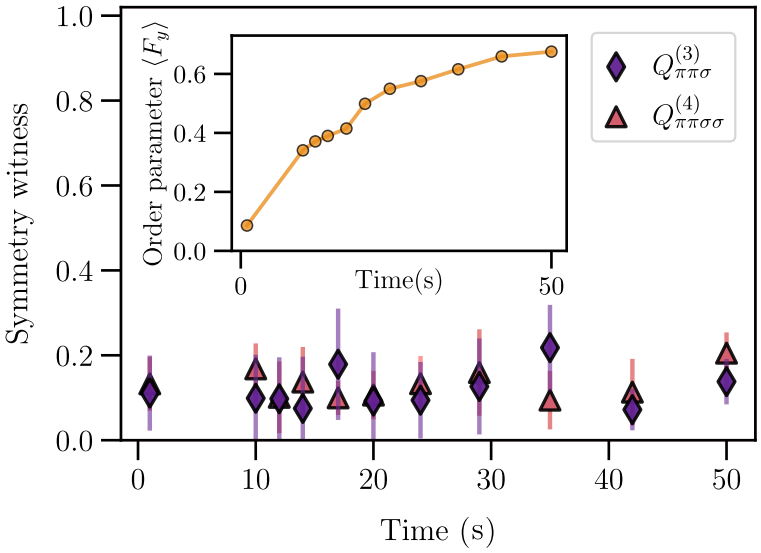

Figure 6.6: The symmetry witness based on two- and three-point correlation functions extracted from experimental data. The inset shows the average spin length $\langle F_y \rangle$. The witness $Q^{(4)}_{\pi\pi\pi\pi}$, which is not shown in order not to overcrowd the plot, gives comparable results to $Q^{(4)}_{\pi\pi\sigma\sigma}$. The error bars are obtained by bootstrapping and correspond to 80% confidence interval. The spin-changing collision time is $t_s = 2\pi/(n\,|c_1|) \sim 0.4$s for the experimental parameters used in this work.

of the SO(2)-symmetric system. Due to the underlying SO(2) symmetry, one can always align the expectation value along one of the axes, e.g., $\langle \hat{F}_x \rangle = 0$, $\langle \hat{F}_y \rangle = v_t$, which was done for Fig. 6.5. The alignment procedure of the spin expectation value for the experimental data is illustrated in the lower panel of Fig. 6.5. In the left graph, data from four experimental realisations is shown at late time ($t = 35$s). To understand the underlying dynamics leading to these configurations, it is helpful to consider them as corresponding to the top view of the pictorial representation of the champagne bottle effective potential. While in each realisation the spin distribution is expected to acquire a "blob" shape, as marked by the coloured distributions in the lower panel of Fig. 6.5, and settle in one of the many symmetry-breaking minima, many such blobs will form a symmetric ring (as in e.g., Fig. 4.7d). Hence, while there is a preferred direction in each experimental realisation individually, once we average over multiple realisations, the transverse spin is symmetrically distributed across the ring in the F_x-F_y plane. Correspondingly, one observes the different experimental realisations distributed along the ring as seen in the lower left graph of Fig. 6.5. However, by rotating each individual realisation by the global phase as shown in the lower middle panel of Fig. 6.5, there is a non-zero expectation value $\langle \hat{F}_y \rangle \neq 0$ and $\langle \hat{F}_x \rangle = 0$ when averaged over all the realisations. This is shown in the lower right graph of Fig. 6.5, which gives the average over many realisations. We emphasise that the global-phase rotation angle maintains translational invariance since this angle does not introduce any spatial bias, whereas, e.g., rotating by the phase of any specific point would do so.

While the histograms of Fig. 6.5 illustrate the dynamical build-up of a macroscopic spin length, a quantitative analysis of spontaneous symmetry breaking requires taking its fluctuations into account as well. In particular, the fluctuations can be used to distinguish data with underlying

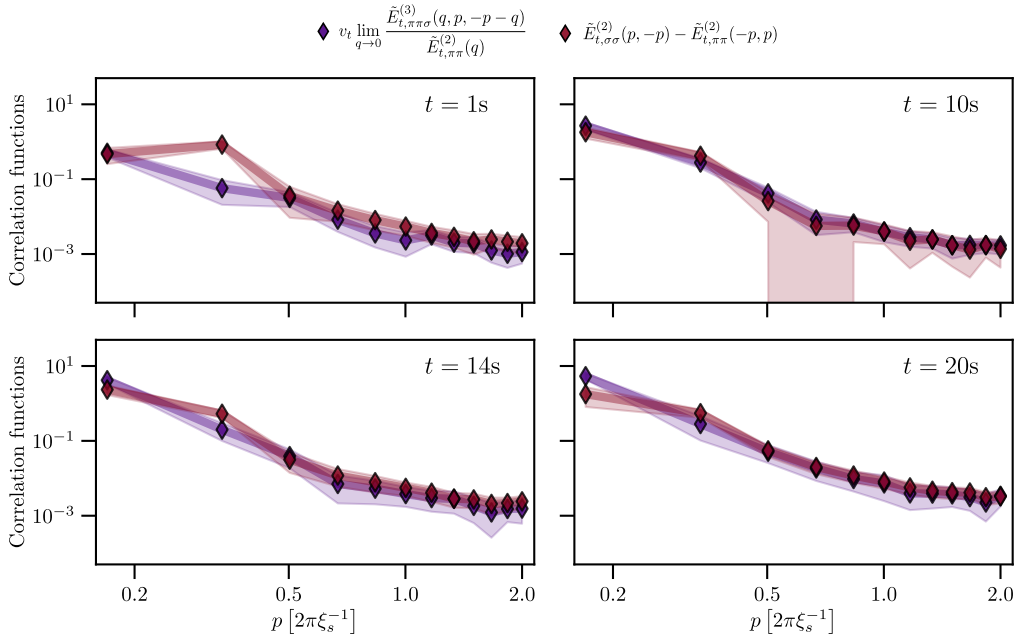

Figure 6.7: The left- and right-hand sides of the symmetry identity (6.17) using experimental data, with the momentum-resolved correlation functions at four different times during the dynamical evolution. The error bands represent 80% confidence intervals obtained from bootstrapping.

spontaneous symmetry breaking from situations where a macroscopic spin length arises due to explicit symmetry breaking, as exemplified on the left of Fig. 6.1. The fluctuations are encoded in the n-point correlation functions, which fulfill the symmetry identities for spontaneous symmetry breaking as derived in Sect. 6.3.

We examine the witnesses $Q^{(3)}_{\pi\pi\sigma}$ and $Q^{(4)}_{\pi\pi\sigma\sigma}$ according to Eq. (6.20) in Fig. 6.6. The minimum value of these quantities, and any of the higher-order witnesses is zero, which corresponds to a perfectly symmetric scenario including that of a spontaneously broken symmetric state, while the upper value is unity corresponding to a maximally and explicitly broken state. One observes that the value of the symmetry witnesses is clearly much smaller than unity, and near zero within errors. This indicates the absence of explicit symmetry breaking, which in principle can be improved with increasing statistics. We also give the average spin length $\langle F_y \rangle$ as an inset on top of the symmetry witness. The witness is seen to be near zero within errors independent of the magnitude of $\langle F_y \rangle$. One observes that the magnitude of $\langle F_y \rangle$ settles at later times, representing an order parameter for spontaneous symmetry breaking.

In order to test the momentum resolved symmetry identity (6.17), we consider the two- and three-point correlation functions by averaging over many realisations of single-shot measurements of the rotated $F_\perp(x)$. For more details on the data analysis procedure, see App. A.3. We plot four different time steps in Fig. 6.7 and observe that the left- and the right-hand sides of the identities are close within experimental errors at all times. Similarly, Fig. 6.8 shows momentum resolved surface plots for the symmetry identity (6.18a) connecting two-, three-, and four-point correlation functions calculated from experimental measurements. We emphasise once again that *a priori* there is no reason why these different n-point correlation functions should obey such

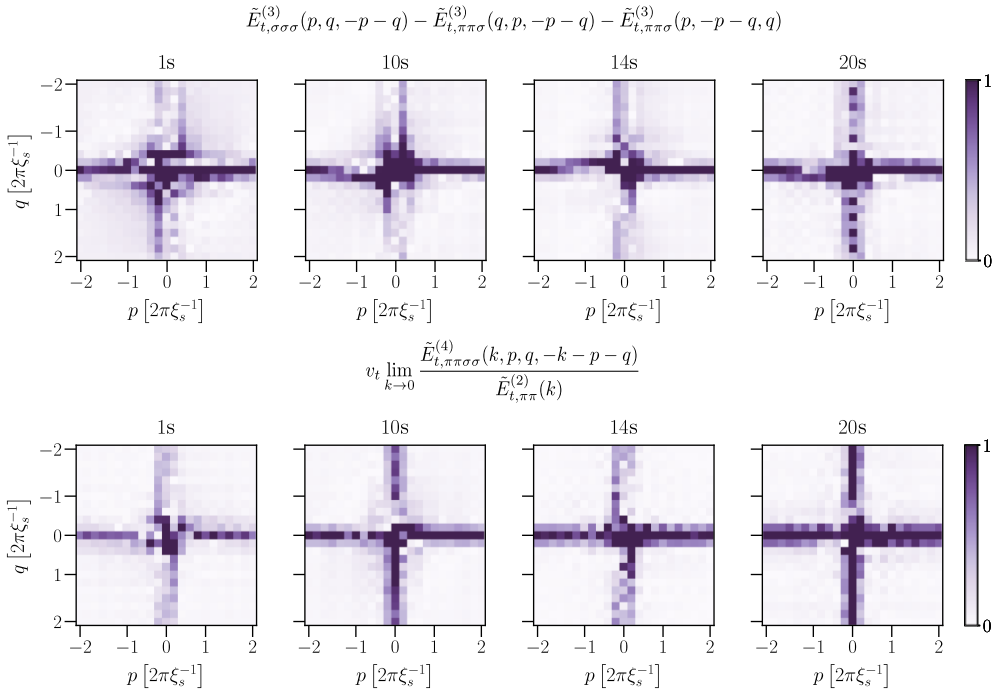

Figure 6.8: Data for the symmetry identity connecting two-, three-, and four-point correlation functions calculated from experimental measurements. The top four surface plots correspond to the right-hand side of the identity (6.18a), while the bottom ones correspond to the left-hand side of the equation. One observes the resemblance of these momentum-conserving surfaces, which involve different n-point correlation functions.

equalities, representing a quantitative manifestation of the emergence of spontaneous symmetry breaking.

6.6 CONCLUSION AND OUTLOOK

While symmetries of a Hamiltonian that are explicitly broken by the initial state cannot be restored on a fundamental level in closed quantum systems, we have shown that their effective restoration can be quantified in terms of symmetry identities for correlation functions. In particular, our results demonstrate that properties involving lower n-point correlation functions exhibit dynamical symmetry restoration earlier than those involving higher-order correlations. Moreover, our findings for a spinor Bose gas show that an initial explicit symmetry breaking gets restored on timescales much before the system thermalises. These are important ingredients for effective descriptions of non-equilibrium evolutions, which are typically based on lower-order correlation functions, where kinetic theory or Boltzmann equations for single-particle distribution functions extracted from two-point correlation functions represent a paradigmatic example [106].

Though the correlation functions appearing in the symmetry identities (6.17), (6.18a), and (6.18b) involve only few spatial points, in general, they also test extremely non-local properties, such as the ones encoded in their low-momentum behaviour in Fourier space. This is crucial for the identification of spontaneous symmetry breaking in the presence of a non-vanishing expectation value for the zero mode and condensation phenomena, which we have analysed for the example of the spinor Bose gas. In particular, our approach is not based on a spatial separation into subsystems, which can be difficult to define in fundamental descriptions, such as relativistic and gauge theories implementing local symmetries. Though we have not described the approach for local symmetries explicitly in this work, the formulation of non-equilibrium (equal-time) versions of Ward identities for gauge theories [103–105, 200] follows along the same lines as we described.

Our approach provides a general pathway to extract the symmetry content of non-equilibrium quantum as well as classical many-body systems based on a hierarchy of n-point correlation functions. This complements alternative approaches to the question of dynamical symmetry restoration, such as the entanglement asymmetry between spatial subsystems introduced as a measure of symmetry breaking in quantum systems [201–209], which has also been experimentally applied [210–212]. It would be interesting to establish a direct link between our symmetry witnesses based on correlations and the entanglement measure of symmetry breaking for quantum systems. While our work primarily focused on ultracold atoms, the approach could also give important further insights into applications and experimental data across various systems, ranging from the detection of new non-equilibrium phases in condensed matter systems to preheating dynamics in inflationary early-universe cosmology [12, 197, 213].

ASPECTS OF SYMMETRY IN NON-THERMAL FIXED POINTS

We'll ride the spiral to the end
And may just go where no one's been

– Maynard James Keenan, "Lateralus"

In the course of this thesis, the underlying symmetries of the spin-1 Bose gas model were used to investigate various aspects of its dynamics. The spontaneously broken SO(2) symmetry was explicitly used to derive the possible topological excitations present in the system post-quench, leading to the study of instantons in the Larmor phase of the system. Furthermore, it was shown that the consequences of the underlying (emergent) SO(2) symmetry of the dynamics, such as the suppression of F_z excitations and restriction of the spinor phase to values of $2\pi\mathbb{Z}$, are crucial considerations for the derivation of the double sine-Gordon model as the effective theory for a quench from the polar phase into the easy-plane phase. In this rather short chapter, we discuss two ongoing studies discussing the possible universality classes in the spin-1 system from the perspective of their emergent symmetries and dimensionalities. We present the main results of these studies as a short outlook for future work.

Following the results discussed in Chap. 6, we show in Sect. 7.1 that the non-equilibrium dynamics at low values of the quench parameter q_f show the recovery of higher effective symmetries, where symmetry witnesses uncover a behaviour closer to SO(3) or U(3) symmetric models. We discuss these findings, providing an argument for the existence of distinct non-thermal fixed points in the spinor gas, each connected to the emergent microscopic symmetry of the dynamics.

Lastly, we recall the discrepancy between the numerical results and experimental observation of the self-similar scaling of the spin-1 Bose gas. In Sect. 7.2, we present a possible explanation for this discrepancy and show that it can be solved by dimensional considerations. The quasi-1D cigar-shaped geometry of the experiment is fundamentally different from a strict one-dimensional grid with periodic boundary conditions in the sense of possible excitations and topology. We present numerical simulations utilising a thin box geometry in two and three spatial dimensions, ensuring that the transversal extent of the condensate is still below a spin-healing length. We find that we can reproduce the experimental results simply by changing the dimensionality of the grid.

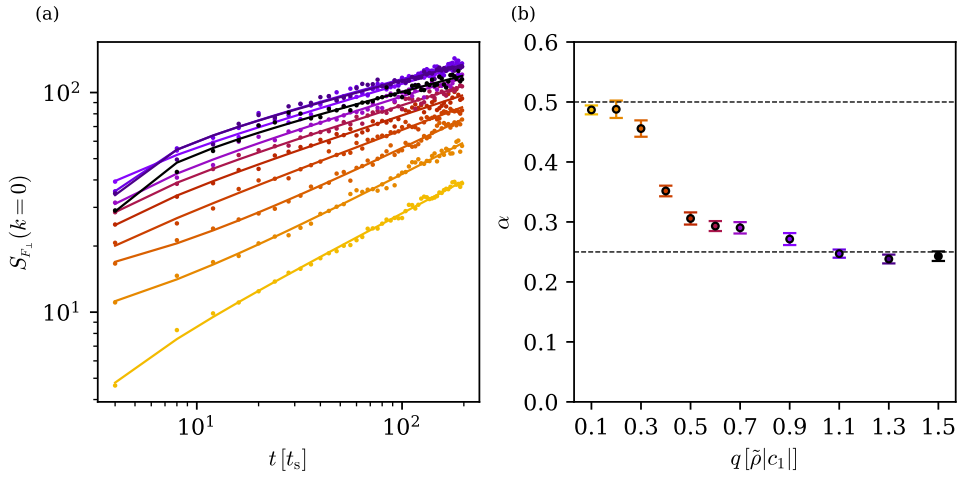

Figure 7.1: Scaling exponents of the transverse spin structure factor $S_{F_\perp} = \langle |F_\perp(k)|^2 \rangle$ for different values of q_f colour coded from yellow to black. (a) The exponents are extracted using the growth-rate of the $k = 0$ mode, fitting a function $S_{F_\perp}(k = 0) \sim (t - t_0)^\alpha$, with some non-universal constant t_0 and universal exponent α [100]. (b) Extracted scaling exponents. We observe a relatively sharp change in scaling exponent at around $q \approx 0.3\tilde{\rho}|c_1|$. The steepness of the crossover implies the approach to a different NTFP.

7.1 SYMMETRY CROSSOVER IN THE SPIN-1 GAS

In this section, we expand upon the discussion of Chap. 6 to explore the effects of emergent symmetries in the post-quench dynamics of the spin-1 gas. The type of effective theory governing the dynamics of the non-equilibrium physics strongly depends on the symmetry of the problem. For example, we have discussed the derivation of the double sine-Gordon (DSG) theory as an effective theory governing the post-quench dynamics of the spin-1 Bose gas in the easy plane, where a spontaneously broken SO(2) symmetry gives rise to the dynamics. It was discussed that for the derivation of this effective theory, it is crucial that the dynamics are concentrated on the ring in the F_x-F_y plane.

A question we have posed quite early in this work was the role the symmetries of observables play, or whether a connection between various non-thermal fixed-points and symmetry is possible. In [214], it was shown that a quench of the spinor gas into various final values of the quadratic Zeeman shift q_f, leads to a shift in the scaling exponents. In this work, we perform a more in-depth study of this phenomenon. To this end, we simulate various quenches from the polar phase into values $q_f \in [0.1, 1.5]\tilde{\rho}|c_1|$ in steps of $0.1\tilde{\rho}|c_1|$ up to $q_f = 0.7\tilde{\rho}|c_1|$, where we go over to steps of $0.2\tilde{\rho}|c_1|$. Notice that the case of $q_f = 0$ is not included, since this value lies on a first-order phase transition between the easy-plane and easy-axis phases (see Fig. 2.3), where we do not expect the system to obey the same symmetries of the easy-plane phase. All simulations were carried out using the same parameters as in Chap. 4 with the only difference being the quench parameters. To extract the scaling exponents, we analyze the growth rate of the $k = 0$ mode, which should grow as $S_{F_\perp}(k = 0, t) \sim (t - t_0)^\alpha$ [100], with some non-universal time constant t_0. The spectra are rescaled with the obtained exponent under the assumption of quasiparticle conservation, i.e. $\alpha = \beta$. We confirm the self-similarity of the scaling dynamics within the scaling regime, see

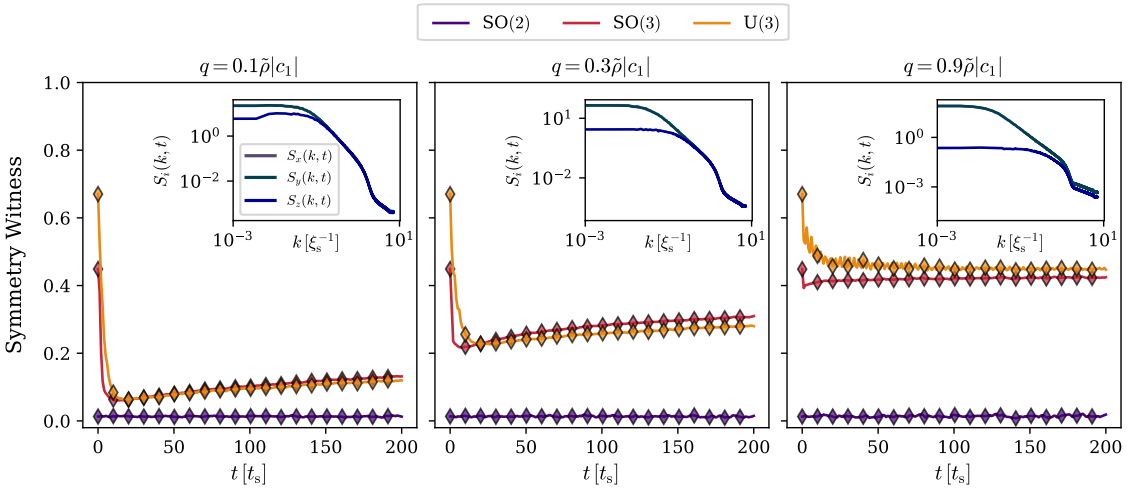

Figure 7.2: Symmetry witnesses of the spin-1 Bose gas after a quench to various values of q. For each quench, the symmetry identities for SO(2) (purple), SO(3) (red) and U(3) (gold) were calculated and their respective symmetry witnesses were defined. In the middle of the easy plane, the SO(2) symmetry is the dominant symmetry present in the system, allowing for the recovery of the DSG model and subdiffusive scaling. For low q_f, the symmetry breaking from the full U(3) symmetry of the gas is very weak, giving rise to the known diffusion-type exponents as derived in [106] for U(N) symmetric models. The insets show the two-point spin correlators $S_i(k,t)$ with $i \in \{x,y,z\}$ for $t = 100t_s$. One observes that S_x and S_y overlap in all three cases, while for low q_f values, the S_z correlator approaches those of the transverse spin.

App. B for details. As seen in Fig. 7.1, for low values of q_f, we obtain self-similar scaling of correlations with a diffusion-type exponent $\alpha = \beta \approx 0.5$. Interestingly, around $q_f \approx 0.3\tilde{\rho}|c_1|$, we observe a jump in the value of the scaling exponent, going over to the subdiffusive value of $\alpha = \beta \approx 0.25$. The jump in scaling exponents is continuous, yet relatively sharp and we attribute the width of the jump to the finite size of the system. The sharpness of the jump is an indication of a crossover event, where the system chooses to flow to one, or the other non-thermal fixed-point, whereas the obtained scaling exponents in the crossover regime are thought to be a result of mixed effects. This notion is further substantiated by considering the self-similarity of the spectra. For values of q_f in the crossover regime, the spectra show a slight deviation from self-similarity, signalled by the trends in the residuals, see Fig. B.1. Self-similarity is then restored on the other side of the crossover, indicating that now the system flows close to a different non-thermal fixed point.

The different scaling behaviors can be connected to different effective symmetries of the dynamics. In all cases, the initial condition is SO(2) symmetric. Strictly speaking, in all cases, the Hamiltonian is also SO(2) symmetric, since all values are within the easy-plane phase, where the spontaneously broken symmetry is restored when averaging over runs. To investigate the emergent symmetry content of the system as in Chap. 6, we utilise the Ward identities of SO(2), SO(3) and

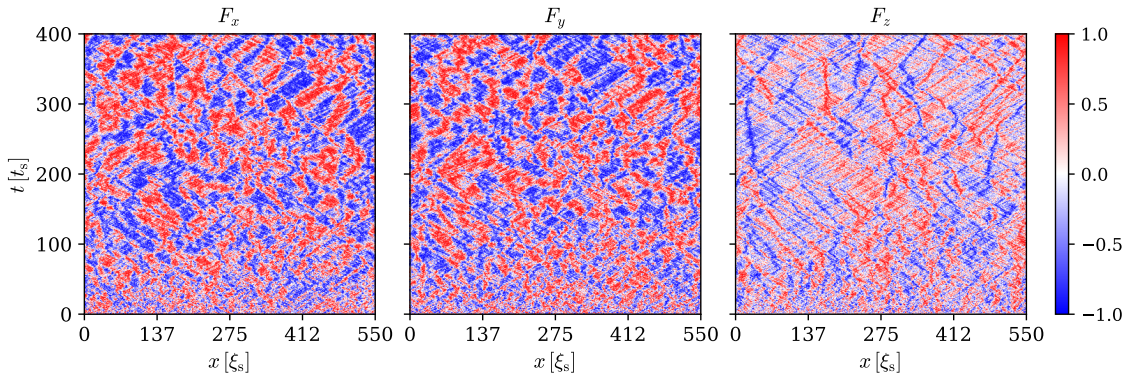

Figure 7.3: Time evolution of a one-dimensional spin-1 Bose gas after a quench from the polar phase into the easy plane to $q_f = 0.1\tilde{\rho}|c_1|$. We observes an abundance of F_z-excitations, which seem not to be of defect nature. The spin sphere is occupied across its entire surface, thus implying a higher symmetry than a simple SO(2) symmetry. These sound-wave-type excitations scale with $\beta \approx 0.5$.

U(3) field theories. On the level of the correlators and in the absence of spontaneous symmetry breaking, these yield

$$\text{SO(2)}: \quad \langle F_x(x)F_x(y)\rangle = \left\langle F_y(x)F_y(y)\right\rangle , \tag{7.1a}$$

$$\text{SO(3)}: \quad \langle F_x(x)F_x(y)\rangle = \left\langle F_y(x)F_y(y)\right\rangle = \langle F_z(x)F_z(y)\rangle , \tag{7.1b}$$

$$\text{U(3)}: \quad \left\langle \psi_1^*(x)\psi_1(y)\right\rangle = \left\langle \psi_0^*(x)\psi_0(x)\right\rangle = \left\langle \psi_{-1}^*(x)\psi_{-1}(y)\right\rangle . \tag{7.1c}$$

Using Eq. (7.1), we define the symmetry witnesses in a similar manner to Eq. (6.20). Given a correlation function $S_i(x,y) = \langle O_i(x)O_i(y)\rangle$, where the indices take the value $i, j \in \{x, y, z\}$ for spin correlations (7.1a), (7.1b) and $i, j \in \{-1, 0, 1\}$ for the occupation numbers (7.1c), we define the witness as

$$\mathcal{Q} = \frac{1}{\mathcal{N}} \sum_{ij} \frac{\big\| |S_i| - |S_j| \big\|}{\big\| |S_i| + |S_j| \big\|}, \tag{7.2}$$

where $\|\cdots\|$ denotes the L^1 norm, $\mathcal{N} = 1$ for the SO(2) identity and $\mathcal{N} = 3$ for the SO(3) and U(3) identities, thus normalizing the witness to unity for maximal symmetry breaking.

For quadratic Zeeman shifts close to the middle of the easy plane, e.g., $q_f = 0.9\tilde{\rho}|c_1|$, where we find subdiffusive scaling, we obtain a clear signal from the symmetry witnesses that the dynamics are well described by a SO(2) symmetric description. In contrast to that, the SO(3) and U(3) symmetry witnesses show a clear sign that these symmetries are (explicitly) broken. As we quench the system into lower values of the quadratic Zeeman shift, the symmetry witnesses reveal an interesting dynamic. At $q_f = 0.1\tilde{\rho}|c_1|$, we see that, while the SO(2) symmetry of the system is almost exactly preserved in the dynamics, the SO(3) and U(3) symmetries are weakly broken compared to the $q_f = 0.9\tilde{\rho}|c_1|$ quench. Hence, even though for both cases we start from a truly SO(2) symmetric state and quench to a SO(2) symmetric Hamiltonian, we observe different scaling exponents, each connected to a distinct *dynamical* symmetry content of the system. For

lower values of quadratic Zeeman shifts, the scaling comes from the distribution of excitations over the entire spin sphere, in contrast to the subdiffusive scaling we see for higher q_{f}. Here, we observe that excitations in the F_z direction are no longer energetically heavily suppressed, as seen in Fig. 7.3. Most importantly, the form of the excitations in F_z does not seem to be that of highly localised defects, as they usually spread across multiple healing lengths, see rightmost panel of Fig. 7.3. The departure of spin configurations from the F_x-F_y plane effectively changes the topology of the dynamics, as the ground-state manifold is now no longer a unit circle, but a two-sphere S^2. Therefore, the topology of the system is trivialised (recall Eq. (2.43)) due to the restorations of higher symmetries. As a result, the excitations on the spin sphere are thought to be predominantly collective spin excitations, for which a scaling theory has been derived. The scaling exponent obtained for low q_{f} values coincides, within error bounds, to the derived and numerically confirmed exponents for U(N) symmetric systems [106].

7.2 DIMENSIONALITY DEPENDENCE OF SCALING

As discussed in Chap. 1, a long-standing problem concerning the scaling dynamics of the spin-1 Bose gas quenched from the polar phase to the easy-plane phase has been the discrepancy between the numerically obtained scaling in $(1+1)d$ dimensions, and the experimentally measured exponents in a quasi-one-dimensional cloud of Rubidium atoms. Numerical simulations for the experimental parameters resulted in the distinct subdiffusive scaling for the polar quench [1, 75], yet the experiment observes diffusion-type scaling of $\beta \approx 1/2$ [55].

As seen in Sect. 7.1, a scaling exponent of $\beta \approx 1/2$ was numerically observed in the spinor gas for quenches to very low values of the quadratic Zeeman shift. Recently, experimental improvements in the stability of the microwave dressing and high-precision calibration measurements were made to address the possibility of the quadratic Zeeman shift being responsible for the discrepancy. Such calibration measurements make use of the mapping between the spin-1 gas and the sine-Gordon model derived in Chap. 5. In order to calibrate the $q = 0$ value, the experiment imprints sine-Gordon solitons in the spinor phase of the condensate and measures their time evolution. It can be shown that the velocity of sine-Gordon kinks in the spinor gas is linearly proportional to the quadratic Zeeman shift [4, 215]. Hence, at vanishing quadratic Zeeman shift, sine-Gordon solitons in the spinor phase are stationary, whereas for higher quadratic Zeeman shifts they begin to move, thus making it suitable as a precise tuning parameter. These high precision measurements have confirmed that the quenches performed in [55] were done to well-defined values of q, in agreement with the numerically simulated values.

A different hypothesis saw the dimensionality of the system as the culprit. Although the quasi-one-dimensional condition requires transverse confinement lengths to be smaller than the relevant healing length, this criterion is not fully satisfied in this experimental platform. The interaction terms of the Rubidium condensate show a separation of scales between the density and spin terms. Since the spin-dependent interaction is approximately two orders of magnitude weaker than the density-density interaction, the associated spin healing length ξ_{s} is much larger than the density

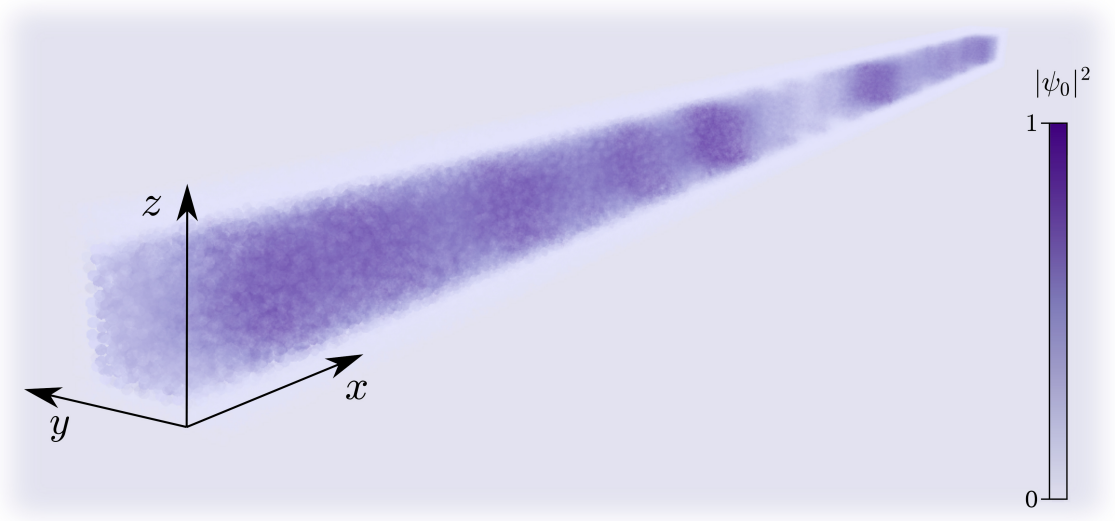

Figure 7.4: Excerpt of the density of the $m_\mathrm{F} = 0$ component of a quasi-one-dimensional condensate in a three-dimensional box trap. The numerical grid contains $2048 \times 32 \times 32$ grid points. The extension of the condensate in the transversal direction is about $0.5\xi_\mathrm{s}$, making the description in spin space effectively one-dimensional.

healing length ξ. In current experiments, the transverse confinement achieved sizes of $L^\perp_\mathrm{trap} \lesssim \frac{1}{2}\xi_\mathrm{s}$, thereby realising effective one-dimensionality for the spin sector. However, the density sector cannot take an effective one-dimensional description, since $\xi \approx 0.07\xi_\mathrm{s}$. Because the spin and densities are not fully decoupled, this dimensional crossover may influence the far-from-equilibrium spin dynamics, possibly altering the observed scaling behaviour.

To test this hypothesis, three-dimensional simulations of the spin-1 Bose gas in a trapped geometry are needed. However, such simulations are challenging for two primary reasons. First, the computational cost is substantial: Three-dimensional grids containing three complex fields demand significant memory resources, particularly when aiming for high resolution along the longitudinal axis while maintaining sufficiently large transverse dimensions to capture the relevant physics accurately and to avoid any cut-off dependencies and numerical artefacts.

Second, the validity of the truncated Wigner approximation becomes questionable when dealing with strongly inhomogeneous density distributions. The truncated Wigner approximation relies on large mode occupations for its semi-classical treatment to be valid. Yet, in harmonic traps, the low-density regions near the edges have low mode occupation. This issue is made worse in the transverse directions, where only a small number of modes are present due to the inhomogeneity of the numerical grid. In such cases, entire slices of the system, corresponding to low occupied modes, may be simulated inaccurately.

Fortunately, due to the rapid advancements in GPU technologies, large-scale simulations such as three-dimensional grids have become more accessible. Modern GPUs (at the time of writing) boast large memory capacities of between 80 to 92GB per device, as well as an extensive array of streaming multiprocessors to increase the parallelism. Utilising the power of these developments, we were able to compute the polar quench in two and three spatial dimensions to obtain new results.

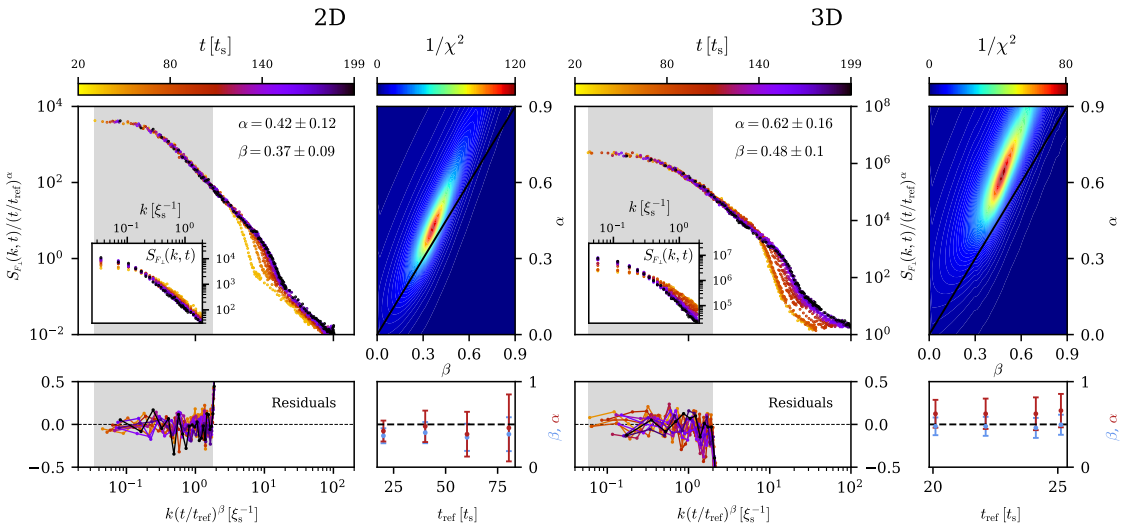

Figure 7.5: Self-similar scaling of a quasi-one-dimensional condensate. Simulations of a quench from the polar phase to the easy-plane phase done for two and three spatial dimensions, see main text for simulation parameters. A distinct change in scaling behaviour is observed via a change of dimensionality. Recall that $\beta \approx 0.25$ for a pure one-dimensional setting. For a two-dimensional grid, we obtain $\beta = 0.37(9)$ and $\alpha = 0.42(12)$. For a three-dimensional grid, we obtain $\beta = 0.48(10)$ and $\alpha = 0.62(16)$. The larger errors on α can be attributed to the smallness of the IR plateau. Notice also the slight deviation from $\alpha = \beta$, which we attribute to the extended dimensionality of the system. The self-similarity of the scaling is confirmed by the residuals in the lower left panels, whereas the stability of the scaling w.r.t. the reference time is shown in the lower right panels.

The second challenge was addressed by employing a hard-wall trap in all three spatial dimensions. To minimise boundary effects such as unphysical reflections, the walls are set to be sufficiently soft. Furthermore, the edge of the trap was ensured to be far enough from the ends of the grid to avoid aliasing artefacts from the Fourier transforms. Utilising a box trap geometry results in an homogenous density distribution, ensuring the validity of the truncated Wigner method across the entire condensate. Since we are not interested in the geometry of the trap, but rather focus on the dimensionality and lack of periodic boundary conditions, this approach proves sufficient. Notice also that the loss of periodic boundary conditions also results in a fundamental change of the base manifold topology. As a result, one is unable to define a topological charge.

We perform simulations in two as well as three dimensions, choosing a strongly anisotropic numerical grid to simulate a quasi-one-dimensional setting. In two dimensions, we simulate a grid of $N_g^x = 4096$ points in the longitudinal x direction corresponding to $L = 220\mu\text{m} = 280\xi_s$, and $N_g^y = 64$ in the transverse y direction. The grid spacing is determined by the longitudinal direction alone. The simulated trap contains $5 \cdot 10^5$ Rubidium atoms, which are quenched from the polar phase to easy-plane phase to a value of $q_f = 0.9\tilde{\rho}|c_1|$. The total density $\tilde{\rho}$ is to be understood as the homogeneous density of the trap, which extends to $L_{\text{trap}}^x \sim 240\xi_s$ in the longitudinal direction and $L_{\text{trap}}^y = 0.5\xi_s$ in the transverse direction.

In three dimensions, we choose a grid of $N_g^x = 2048$ points in the transversal direction, again corresponding to a physical length of $L = 220\mu\text{m} = 123\xi_s$ and $N_g^y = N_g^z = 32$. We quench a

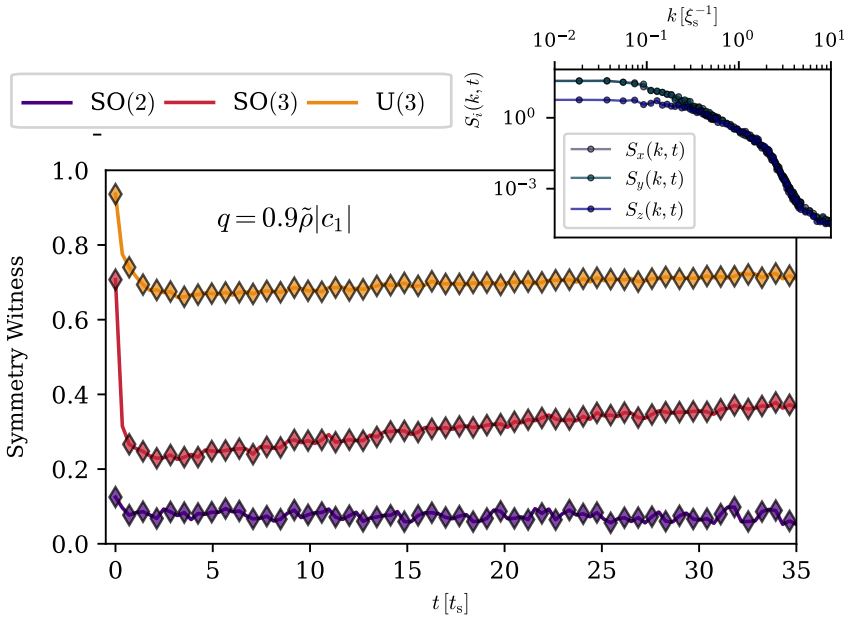

Figure 7.6: Symmetry witnesses for a quasi-one-dimensional condensate on a three-dimensional grid. The symmetry identities for SO(2) (purple), SO(3) (red) and U(3) (gold) were calculated and their respective symmetry witnesses were defined. As for the one-dimensional case, the SO(2) symmetry of the system is almost exactly realised, whereas the witnesses show that SO(3) and U(3) descriptions of the system are inadequate. The inset shows the spin spectra $S_i(k,t)$ at $t = 35t_s$, showing a good overlap in the UV, whereas the IR still remains different, reflecting the breaking of SO(3) symmetry.

cloud of $3 \cdot 10^5$ Rubidium atoms from the polar phase to the easy plane to a value of $q = 0.9\tilde{\rho}|c_1|$. The trap extends to $L^x_{\text{trap}} = 108\xi_s$ in the longitudinal direction and $L^\perp_{\text{trap}} = 0.5\xi_s$ in the transversal direction, as illustrated in Fig. 7.4.

Using the same rescaling algorithm as in Fig. 4.1, we extract the scaling exponents α and β independently, see Fig. 7.5. For the two dimensional case, we find $\alpha = 0.41(13)$ and $\beta = 0.36(9)$, whereas for the three-dimensional case, we find $\beta = 0.48(10)$ and $\alpha = 0.62(16)$, where, due to the smallness of the plateau, the errors on α are larger. We see that with the change of dimensionality, even though the description of the spin degree of freedom is, in fact, one-dimensional, the scaling behaviour of the system distinctly changes. Most interestingly, the value obtained for the scaling in the three-dimensional case corroborates the experimental results as found in [55].

To investigate these results further, we may turn to the two frameworks with which we have studied the dynamics of the spin-1 gas. Recall that in Chap. 5, we have indicated that the underlying effective model, i.e., the DSG model, can show different scaling exponents depending on the amount of occupied minima, where a diffusion-type scaling stems from the occupation of very few minima. The use of the DSG as an effective model for this quasi-one-dimensional description is justified by considering the emergent symmetries of the quench dynamics. Computing the symmetry witnesses (7.1), we obtain a similar case as in the one-dimensional description, where the SO(2) symmetry of the system is exactly fulfilled, while the witnesses for SO(3) and U(3) show strong deviations, on the order of what is seen in the rightmost panel of Fig. 7.2.

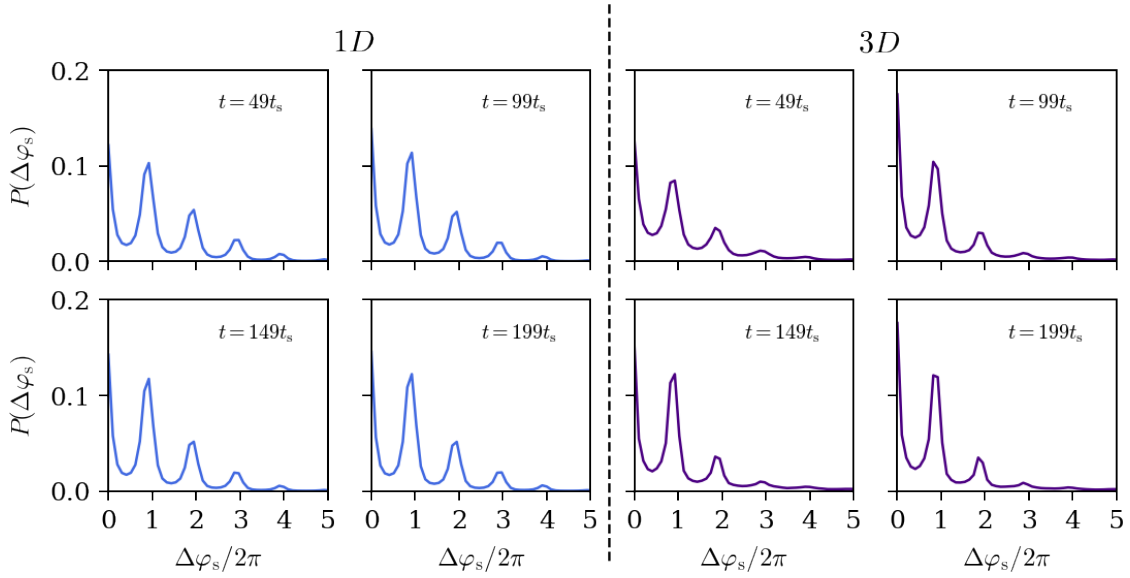

Figure 7.7: Autocorrelation of spinor phase histograms for one- and three-dimensional simulations. At each time and for each truncated Wigner realisation, the spinor phase probability distribution function (PDF) is calculated. Then, an autocorrelation of the PDF is calculated, describing the probability of distances between sine-Gordon minima in configuration space. We observe weaker occupations for larger distances in the three-dimensional case than for the one-dimensional space, presenting a possible explanation for the different scaling behaviour.

We study the spread of the spinor phase field configuration across the potential landscape, focusing on the number of occupied minima. To this end, we calculate a probability distribution function of the spinor phase field configuration for each truncated Wigner realisation at each time. Then, we compute the autocorrelation of this function with itself, averaging over the truncated Wigner realisations. As a result, we obtain a correlation function describing the probability of minima distances in configuration space, see Fig. 7.7. We obtain a peaked autocorrelation function for the one- and three-dimensional case. As seen in the left panels of Fig. 7.7, the one-dimensional case discussed in Chap. 4 and Chap. 5 shows probabilities to obtain field configurations spread over many minima. The right panels of Fig. 7.7 show the distribution for the three-dimensional case. There, we see that for earlier times, up to $\sim 50t_s$, we obtain occupations of up to four minima. Later, the transport processes in the dynamics lead to a lower probability to occupy more than three minima. We also notice that the probability to find field configurations spreading over three minima is reduced by a factor of two w.r.t. the one-dimensional case. To further substantiate this observation, simulations carried by L. Heck have shown that utilising a spin wave in the spinor phase, i.e., a linear phase gradient, one can occupy more minima in the sine-Gordon potential also in the three-dimensional simulations of the quasi-one-dimensional condensate [216]. These simulations have shown that at later times, up to five minima are strongly occupied at all times. A scaling analysis revealed that the self-similar scaling of correlations shows a distinctly slower scaling exponent $\beta = 0.35(8)$, in accordance to our conjecture in Chap. 5.

We would like to note, though, that the underlying reason for the change in scaling exponents may go beyond simple arguments for sine-Gordon scaling, since the density sector, as mentioned,

is not strictly one-dimensional. Analytical approaches for the derivation of scaling exponents must generally take into account the dimensionality of the system [119]. As a consequence, for our quasi-one-dimensional case, it might not be sufficient to consider the dynamics of the spinor phase alone, as effects of the density interactions due to a dimensional crossovers might also affect the scaling behaviour of the system.

Part IV

CONCLUSION

8 CONCLUDING REMARKS

I must lead the way to this conclusion
I let you inherit these words I sing to you

– Jonas Renske, "The One You are Looking for is Not Here"

8.1 SUMMARY

In this thesis, we have thoroughly investigated the post-quench far-from-equilibrium scaling dynamics of the spin-1 Bose gas. Using numerical simulations, we analysed the time evolution of the system, focusing on its microscopic dynamics, dynamical symmetry restoration and scaling behaviour under various parameters and dimensionalities. Furthermore, we derived an effective theory characterising the underlying non-equilibrium universality class.

To this end, the system was driven far out of equilibrium using a parameter quench of the quadratic Zeeman shift q into various final values q_f. This quench drives the system across a second-order phase transition from the polar phase to the ferromagnetic easy-plane phase. The resulting instabilities in the transverse spin degree of freedom lead to structure formation and, subsequently, also to self-similar scaling of correlations in time and space.

First, we have studied the microscopic excitations of the spin-1 Bose gas post-quench. We found that excitations in the form of rogue waves in the velocity fields give rise to topological real-time instanton excitations in the Larmor phase of the spin-1 gas. Using the topological nature of the instantons, we were able to numerically observe two distinct scaling exponents, each governing the scaling of the spatial and temporal scales with $\ell_V \sim t^\beta = t^{1/4}$ and $t_\mathrm{c} \sim t^\delta = t^{1/3}$, respectively. This scaling behaviour was described analytically in the framework of rogue waves in disordered media, where the disorder was given by the spin-changing collision term itself. The two exponents were found to be mutually connected via $\delta = 4\beta/3$. Interestingly, the connection of exponents governing spatial and temporal scaling is reminiscent of the arguments of kinetic-theory approaches, where the dynamical exponent z governing the dispersion relation $\omega(k) \sim k^z$ is connected to the spatial scaling exponent via $\beta = 1/z$. While previous studies attributed the observed one-dimensional subdiffusive scaling to the dynamics of topological excitations, our findings suggest that the coarsening dynamics cannot be explained by these excitations alone. In particular, an analysis of the system's dynamics reveals that scaling persists even in the absence of such excitations after $t \sim 400 t_\mathrm{s}$.

To better understand this behaviour, we derived a low-energy effective theory for the quenched spin-1 Bose gas in order to substantially reduce the complexity of the problem and better characterise the underlying universality class. In Chap. 5, we found that the low-energy effective theory

takes on the form of a double sine-Gordon (DSG) model in the spinor phase φ_s in the infrared. The DSG was found to account for subdiffusive ($\beta < 1/2$) as well as diffusion type ($\beta = 1/2$) scaling in one and two spatial dimensions, thus reproducing results from the full spin-1 model. Through this effective description, we have seen that the subdiffusive scaling seen in Chap. 4 and was first reported in [75], cannot be explained simply by the coarsening of magnetic-type domains, but is rather a product of the fractal form of the field configuration, underlining the importance of this highly non-linear model which allows the field to explore multiple minima of the sinusoidal potential. These results are consistent with the findings of Refs. [85, 178], where the type of scaling was found to be connected to either the occupation of two, or more minima of the cosine potential. This constitutes a significant step forward in the understanding of the non-equilibrium universality at play, situating the spin-1 Bose gas within a sine-Gordon universality class, to which many systems can be mapped onto.

Turning our attention towards symmetry arguments in Chap. 6, we derived symmetry witnesses for a spontaneously broken SO(2) symmetry, and applied them to investigate the symmetry content of the non-equilibrium dynamics of the spin-1 Bose gas. Beginning from an explicitly symmetry broken state in the easy-plane phase, we studied the dynamical asymptotic restoration of symmetry in the system with time. We numerically observed that low-order correlation functions show a fast restoration of symmetry, on timescales much faster than the equilibration timescale. Higher-order correlations, on the other hand, retain their memory of the initial condition for longer times. This emphasises the need for the construction of suitable observables when deriving effective theories, which typically are based on lower-order correlation functions. The role of dynamical symmetry restoration was further studied in Chap. 7 for quenches to lower values of the quadratic Zeeman shift, where the system is shown to scale with a diffusion-type exponent. The transition between the subdiffusive and diffusion-type scaling was observed to happen in a relative sharp crossover. Derived symmetry witnesses were used to show that, in this case, the system dynamically approaches a more U(3) symmetric case on the level of occupation number correlators. This suggested that the observed diffusion-type scaling arises from free quasiparticle excitations, consistent with expectations for U(N) symmetric models.

Finally, using three-dimensional simulations of a quasi-one-dimensional condensate in a box trap geometry, we have reconciled the long-standing discrepancy between numerical and experimental results for self-similar scaling in the quenched spinor gas. We have furthermore provided arguments using the derived effective theory for the difference in scaling behaviour.

The work done in this thesis advances our understanding of universal self-similar scaling dynamics far from equilibrium, establishing a sine-Gordon-type universality class to which the spin-1 Bose gas belongs to. In particular, the mapping of the scaling onto a non-compact field theory shows that even with the loss of topological information, subdiffusive scaling can be achieved and is not to be identified as domain-size growth alone. Additionally, emergent symmetries were shown to play a decisive role in determining the type of universal self-similar scaling observed in the system. The crossover of the system into effectively U(3) symmetric dynamics helps understand the dominant mechanisms, where free quasi-particle excitations are shown to dominate the dynamics, reducing the problem to an analytically identified scaling solution.

8.2 OUTLOOK

The advancements in the research of non-equilibrium physics presented in this thesis open up a path to explore interesting phenomena in theory and experiment.

The appearance of two distinct scaling exponents governing the universal scaling dynamics of the spin-1 Bose gas presents an opportunity for deeper understanding of non-equilibrium universality. Each exponent characterises the coarsening of spatial and temporal timescales, respectively. This can be compared with kinetic-theory approaches, where the dispersion relation $\omega(k) \sim k^z$ of dominant excitations determines the possible scaling exponent β. This raises the question: Does the presence of two mutually connected scaling exponents reflect a modified dispersion relation? Or does the relation $\beta = 1/z$ as derived in [109] not hold in the presence of strongly non-linear or topological excitations? Answers to this question may connect microscopic excitation spectra with the macroscopic scaling laws in far-from-equilibrium quantum many-body systems.

The derivation of the (double) sine-Gordon model as a low-energy effective theory of the spin-1 Bose gas in the easy plane enables the analytical investigation of self-similar scaling mechanisms at non-thermal fixed points and possible various scaling solutions. The (double) sine-Gordon model has been extensively studied over decades, providing a well-established theoretical framework from which we can advance the understanding of its non-equilibrium universality class. For example, a possible path would be to consider the decay of solitonic defects in the non-integrable DSG, where this could be linked to the presence of higher harmonics coupling to the phonon spectrum of the model. The decay rate of such excitations is thought to depend on which of the higher harmonics couples most strongly to the phonon modes [217]. The analytical derivation of such a timescale would prove a major step into deriving non-equilibrium scaling solutions in the DSG from first principles. Furthermore, the plethora of systems which can be mapped onto the DSG model allow for an overarching study of its universal properties, especially in the context of subdiffusive self-similar scaling, where this behaviour can be directly traced to field configurations in the DSG.

Experimentally, the results presented in Chap. 5 open up the possibility to use the spin-1 Bose gas as a platform probing (double) sine-Gordon physics. In Ref. [4], DSG dynamics are studied in the context of soliton collisions, by imprinting spinor-phase kinks. These kinks are shown to have the analytical sine-Gordon soilton form and behaviour. There, it is shown that elastic as well as inelastic collisions allow for the investigation of the DSG excitations. These experiments mark a significant step towards realising integrable dynamics in quantum many-body systems, while also offering a direct means to quantify the breaking of integrability via the $\sin^2 \varphi_s$ term in the DSG model. Furthermore, the insights gained into the preconditions for subdiffusive scaling in the system suggest a path towards experimentally accessing different scaling behaviours. A possible approach would be to imprint spinor phase kinks that spread over many minima of the sinusoidal potential, or the application of a spin wave across the entire system. This may allow the recovery of the numerically predicted subdiffusive scaling exponents.

The use of symmetry witnesses in quantum many-body systems represents a novel approach which may be used in the future to better characterise non-equilibrium universality classes on the

basis of their symmetry content. The derivation and understanding of underlying effective theories often relies on symmetry arguments and our approach can provide valuable insight into their development. Applying this framework to other systems exhibiting self-similar scaling, especially where the causes for the scaling remains unresolved, could offer a deeper understanding of the relevant mechanisms. In the case of the spin-1 Bose gas, a deeper investigation of the symmetry crossover observed at lower values of the quadratic Zeeman shift may advance our understanding of universality in far-from-equilibrium quantum many-body systems.

Part V

APPENDIX

APPENDIX TO CHAPTER 6

A.1 EXPERIMENTAL DETAILS AND ANALYSIS

For our analysis, we use data obtained with a ^{87}Rb spinor BEC of $\sim 10^5$ atoms in the $F = 1$ hyperfine manifold with initial state $|F, m_F\rangle = |1, 0\rangle$. The atom cloud is contained in a quasi one-dimensional trapping geometry, which consists of a dipole trap formed by a 1030nm laser beam with trapping frequencies $(\omega_\parallel, \omega_\perp) = 2\pi \times (1.6, 160)$ Hz, and with two end caps formed by beams at 760nm, confining the atoms within the central part of the harmonic potential. The longitudinal harmonic potential is constant to a good approximation over the employed sizes, leading to a 1D box-like confinement, with size $\sim 100\mu$m in the measurements used. The atom cloud is subjected to a uniform magnetic field of $B = 0.894$ G throughout the experiment which leads to a quadratic Zeeman splitting of $q_B \sim h \times 58$ Hz. The spin dynamics is controlled via off-resonant microwave dressing $q = q_B + q_{MW}$ with $q < 2\tilde{\rho}|c_1|$. The initial quench is implemented by the instantaneous switching on of the microwave power.

The transverse spin field $F_\perp = F_x + iF_y$ readout is obtained via spin rotations and microwave coupling to the initially empty $F = 2$ hyperfine manifold prior to a Stern–Gerlach pulse and spatially resolved absorption imaging. For a more detailed account on the experimental setup and on how the measurements were obtained, see the supplementary material of Ref. [6]. While the spatial degree of freedom is continuous, it gets discretized in the analysis procedure by the finite pixel size of the camera and imaging resolution ($\approx 1.2\mu$m per three pixels). Our analysis focuses on the central ~ 100 pixels of the data, since establishing long-range coherence across the entire system requires some time.

A.2 PHYSICAL INTERPRETATION OF THE SYMMETRY BREAKING PERTURBATION

Since the spin operators $\hat{F}_i$ are the generators of the rotational symmetry, they commute with a symmetric Hamiltonian and consequently with the evolution operator as well. This allows us to rewrite the generating functional as

$$\begin{aligned} Z_t[\boldsymbol{J}] &= \mathrm{Tr}\left\{\mathcal{U}(t, t_0)\, \mathrm{e}^{\int \mathrm{d}x \boldsymbol{J}(x)\cdot\hat{\boldsymbol{F}}(x)/2}\, \hat{\rho}_{t_0}\, \mathrm{e}^{\int \mathrm{d}x \boldsymbol{J}(x)\cdot\hat{\boldsymbol{F}}(x)/2} \mathcal{U}^\dagger(t, t_0)\right\} \\ &= \mathrm{Tr}\left\{\mathcal{U}(t, t_0)\, \hat{\rho}'_{t_0}(\boldsymbol{J})\, \mathcal{U}^\dagger(t, t_0)\right\}, \end{aligned} \tag{A.1}$$

Evolution time [s]	Number of realizations
1	68
10	237
12	236
14	237
17	236
20	239
24	238
29	269
35	296
42	298
50	296

Table A.1: Number of experimental realizations

where we have introduced the deformed initial density matrix

$$\hat{\rho}'_{t_0}(\boldsymbol{J}) \equiv \mathrm{e}^{\int \mathrm{d}x \boldsymbol{J}(x)\cdot\hat{\boldsymbol{F}}(x)/2}\, \hat{\rho}_{t_0}\, \mathrm{e}^{\int \mathrm{d}x \boldsymbol{J}(x)\cdot\hat{\boldsymbol{F}}(x)/2}\,. \tag{A.2}$$

Note that, provided the sources J_i are real, the deformed operator $\hat{\rho}'_{t_0}(\boldsymbol{J})$ is Hermitian. Furthermore, under the same condition, it is also positive semidefinite. Indeed,

$$\langle\psi|\, \hat{\rho}'_{t_0}(\boldsymbol{J})\, |\psi\rangle = \langle\psi_{\boldsymbol{J}}|\, \hat{\rho}_{t_0}\, |\psi_{\boldsymbol{J}}\rangle \geq 0\,, \tag{A.3}$$

with $|\psi_{\boldsymbol{J}}\rangle \equiv \mathrm{e}^{\int \mathrm{d}x \boldsymbol{J}(x)\cdot\hat{\boldsymbol{F}}(x)/2}\, |\psi\rangle$, and $\hat{\rho}_{t_0}$ is positive semidefinite being a density matrix by assumption. Thus, aside from normalization, $\hat{\rho}'_t$ satisfies all the conditions of a physical density matrix. This suggests a simple interpretation of the equal-time generating functional $Z_t[\boldsymbol{J}]$ in the absence of explicit symmetry violations: it represents the evolution of the symmetric density matrix $\hat{\rho}_{t_0}$ that has been deformed by means of linear sources coupled to the spin operators $\hat{F}_i$ at the initial time t_0, thus breaking the symmetry.

Let us remark that the above simple physical picture is, to a certain extent, unique for spin systems. The reason is that the linear-source term that enters the definition of the generating functional $Z_t[\boldsymbol{J}]$ and serves as a symmetry-breaking perturbation commutes, in this case, with the symmetric evolution operator $\mathcal{U}$ as the spin operators $\hat{F}_i$ are also generators of the symmetry group. Nevertheless, provided the linear source $\boldsymbol{J}$ in the definition of $Z_t[\boldsymbol{J}]$ is coupled to operators that transform nontrivially under the symmetry group in question, the formalism developed in this work can still be applied to define spontaneous symmetry breaking in nonequilibrium systems, albeit lacking the appealing interpretation of the symmetry-breaking perturbation as a deformation of the initial state.

A.3 CORRELATION FUNCTIONS

Both experimentally and in truncated Wigner simulations, we have N_s samples (measurements) of the spin observable F_i in datasets $\left\{F_i^{(s)} \mid s = 1, \ldots, N_s\right\}$, from which we infer n-th order correlation functions as

$$\langle F_{i_1} \cdots F_{i_n} \rangle \approx \frac{1}{N_s} \sum_{s=1}^{N_s} F_{i_1}^{(s)} \cdots F_{i_n}^{(s)}. \tag{A.4}$$

The information in all of the n-point correlation functions is equivalently stored in the generating functional $Z[J]$ as described in the context of Eq. (6.5). The truncated Wigner simulations involve periodic boundary conditions, and while the experimental setup considered is a finite system without periodic boundary conditions, we find approximate translational invariance, which simplifies the calculation of connected correlators in momentum space. We first perform a discrete Fourier transform (DFT) for the spin observables F_i to momentum space

$$F_i^{(s)}(p) = \mathrm{DFT}_{x \to p}\left[F_i^{(s)}(x)\right] \equiv \sum_{j=1}^{N} \mathrm{e}^{-\mathrm{i}pj} F_i^{(s)}(j)\,, \tag{A.5}$$

where $p \in [p_L, 2p_L, \ldots, Np_L]$, $p_L = 2\pi/L$, and L is the system size. Subsequently, we compute connected correlation functions in momentum space using the Julia language package Cumulants.jl [218].

We have verified that this procedure gives equivalent results to first computing connected correlators in position space, and then performing the DFT. The former approach, however, is much more memory-efficient. Indeed, computing higher-order correlation functions requires a considerable amount of computer memory: for instance, a four-point cumulant is an $N \times N \times N \times N$ array, so the amount of required memory scales quartically with the system size. At the same time, as evident from Eqs. (6.18a) and (6.18b), the four-point functions entering the symmetry identities have one of the momenta set to zero while the three remaining ones have to add up to zero due to momentum conservation. Therefore, one only needs a two-dimensional momentum-conserving surface, which can be encoded in an $N \times N$ matrix. By computing correlators directly in momentum space we avoid the need to store the full $N \times N \times N \times N$ array, and we can directly extract the relevant information by computing the two-dimensional momentum-conserving surface. For our numerical data, we consider correlation functions up to the inverse healing length, where the truncated Wigner description is expected to be reliable. For the plots, we have binned every 5 data points, while the correlators themselves were calculated on uncoarsened lattices.

Note that since perfect homogeneity and isotropy cannot be experimentally achieved, numerical artefacts always enter analyses. More specifically, in Eq. (6.17), while $E^{(2)}_{\pi\pi}(-p, p)$ and $E^{(2)}_{\sigma\sigma}(p, -p)$ are manifestly real, the three-point function $E^{(3)}_{\pi\pi\sigma}(0, p, -p)$ has in general a nonzero imaginary part. However, for the experimental data, the imaginary part is orders of magnitude below the real part, therefore the magnitude of the correlator is dominated by the contribution from the real part. We similarly observe this with numerical data, apart from the very early initial times of a few t_s, where the imaginary part is more pronounced. In this case, and in all other cases, the magnitude of complex quantities is plotted.

APPENDIX TO CHAPTER 7

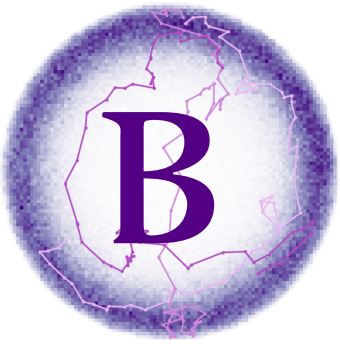

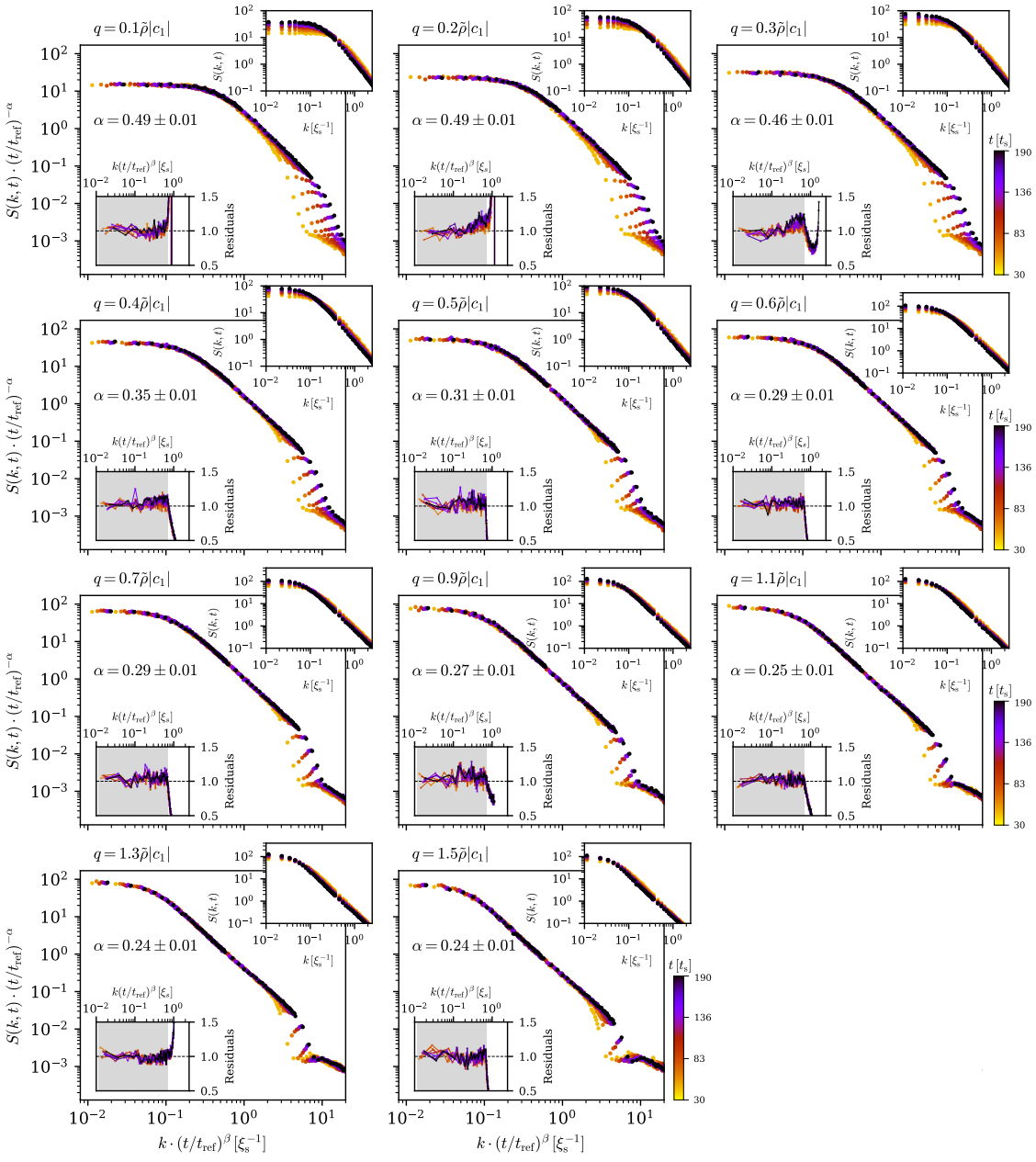

Figure B.1: Scaling exponents for different values of q.

Fig. B.1 shows the self-similar scaling dynamics of the transverse spin structure factor after a quench from the polar phase to the easy-plane phase for various values of the quench parameter q. The exponents are extracted using the growth-rate of the $k = 0$ mode, fitting a fuction $S_\perp(k = 0) \sim (t - t_0)^\alpha$, with some non-universal constant t_0 and universal exponent α as seen in Fig. 7.1. The obtained scaling exponents are then used to rescale the transverse spin correlations and the residuals are calculated to probe the self-similarity of the scaling. For q values which are far enough from the conjectured symmetry crossover, the residuals show no obvious trends and we conclude that the spectra scale self-similarly with the calculated exponents. For spectra within the crossover regime, i.e., at about $q \approx 0.3\tilde{\rho}|c_1|$, we observe a deviation from self-similarity, hence substantiating the notion that the self-similar scaling of correlations is due to the vicinity of the system to two distinct and discrete fixed points.

BIBLIOGRAPHY

[1] I. Siovitz, S. Lannig, Y. Deller, H. Strobel, M. K. Oberthaler and T. Gasenzer. "Universal Dynamics of Rogue Waves in a Quenched Spinor Bose Condensate." *Phys. Rev. Lett.* **131**, 183402 (2023).

[2] I. Siovitz, A.-M. E. Glück, Y. Deller, A. Schmutz, F. Klein, H. Strobel, M. K. Oberthaler and T. Gasenzer. "Double sine-Gordon class of universal coarsening dynamics in a spin-1 Bose gas." *Phys. Rev. A* **112**, 023304 (2025).

[3] A. Mikheev, V. Noel, I. Siovitz, H. Strobel, M. Oberthaler, J. Berges and N. None. "Extracting the symmetries of nonequilibrium quantum many-body systems." *SciPost Physics* **18**, 044 (2025).

[4] Y. Deller, A. Schmutz, A. Flamm, R. Schäfer, F. Schmitt, I. Siovitz, T. Gasenzer, P. Kevrekidis, H. Strobel and M. Oberthaler. "Observation of sine Gordo solitons in a spinor Bose-Einstein condensate." (2025). In preparation.

[5] I. Siovitz, L. Heck, V. Noel and T. Gasenzer. "Symmetry crossover in the universal scaling dynamics of a spin-1 Bose gas." (2025). In preparation.

[6] S. Lannig, M. Prüfer, Y. Deller, I. Siovitz, J. Dreher, T. Gasenzer, H. Strobel and M. K. Oberthaler. "Observation of two non-thermal fixed points for the same microscopic symmetry." (2023). arXiv: 2306.16497 [cond-mat.quant-gas].

[7] A. N. Mikheev, I. Siovitz and T. Gasenzer. "Universal dynamics and non-thermal fixed points in quantum fluids far from equilibrium." *Eur. Phys. J. Spec. Top.* **232**, 3393–3415 (2023).

[8] L. Kofman, A. D. Linde and A. A. Starobinsky. "Reheating after inflation." *Phys. Rev. Lett.* **73**, 3195 (1994).

[9] R. Micha and I. I. Tkachev. "Relativistic turbulence: A long way from preheating to equilibrium." *Phys. Rev. Lett.* **90**, 121301 (2003).

[10] R. Allahverdi, R. Brandenberger, F.-Y. Cyr-Racine and A. Mazumdar. "Reheating in Inflationary Cosmology: Theory and Applications." *Ann. Rev. Nucl. Part. Sci.* **60**, 27 (2010).

[11] R. Baier, A. H. Mueller, D. Schiff and D. T. Son. "'Bottom up' thermalization in heavy ion collisions." *Phys. Lett.* **B502**, 51–58 (2001).

[12] J. Berges, M. P. Heller, A. Mazeliauskas and R. Venugopalan. "QCD thermalization: Ab initio approaches and interdisciplinary connections." *Rev. Mod. Phys.* **93**, 035003 (2021).

[13] A. Polkovnikov, K. Sengupta, A. Silva and M. Vengalattore. "Colloquium: Nonequilibrium dynamics of closed interacting quantum systems." *Rev. Mod. Phys.* **83**, 863–883 (2011).

[14] N. Proukakis, S. Gardiner, M. Davis and M. Szymanska. "Quantum Gases: Finite Temperature And Non-equilibrium Dynamics." Imperial College Press, London, (2013). ISBN: 9781908979704.

[15] T. Langen, R. Geiger and J. Schmiedmayer. "Ultracold Atoms Out of Equilibrium." *Ann. Rev. Cond. Mat. Phys.* **6**, 201–217 (2015).

[16] G. Aarts, G. F. Bonini and C. Wetterich. "Exact and truncated dynamics in nonequilibrium field theory." *Phys. Rev. D* **63**, 025012 (2000).

[17] J. Berges, S. Borsanyi and C. Wetterich. "Prethermalization." *Phys. Rev. Lett.* **93**, 142002 (2004).

[18] M. Gring, M. Kuhnert, T. Langen, T. Kitagawa, B. Rauer, M. Schreitl, I. Mazets, D. A. Smith, E. Demler and J. Schmiedmayer. "Relaxation and Prethermalization in an Isolated Quantum System." *Science* **337**, 1318 (2012).

[19] T. Kitagawa, S. Pielawa, A. Imambekov, J. Schmiedmayer, V. Gritsev and E. Demler. "Ramsey Interference in One-Dimensional Systems: The Full Distribution Function of Fringe Contrast as a Probe of Many-Body Dynamics." *Phys. Rev. Lett.* **104**, 255302 (2010).

[20] T. Kitagawa, A. Imambekov, J. Schmiedmayer and E. Demler. "The dynamics and prethermalization of one-dimensional quantum systems probed through the full distributions of quantum noise." *New J. Phys.* **13**, 073018 (2011).

[21] T. Langen, T. Gasenzer and J. Schmiedmayer. "Prethermalization and universal dynamics in near-integrable quantum systems." *J. Stat. Mech.* **1606**, 064009 (2016).

[22] T. Mori, T. N. Ikeda, E. Kaminishi and M. Ueda. "Thermalization and prethermalization in isolated quantum systems: a theoretical overview." *J. Phys. B: At. Mol. Opt. Phys.* **51**, 112001 (2018).

[23] M. Ueda. "Quantum equilibration, thermalization and prethermalization in ultracold atoms." *Nature Rev. Phys.* **2**, 669–681 (2020).

[24] E. T. Jaynes. "Information Theory and Statistical Mechanics." *Phys. Rev.* **106**, 620–630 (1957).

[25] E. T. Jaynes. "Information Theory and Statistical Mechanics. II." *Phys. Rev.* **108**, 171–190 (1957).

[26] M. Rigol, V. Dunjko, V. Yurovsky and M. Olshanii. "Relaxation in a Completely Integrable Many-Body Quantum System: An Ab Initio Study of the Dynamics of the Highly Excited States of 1D Lattice Hard-Core Bosons." *Phys. Rev. Lett.* **98**, 050405 (2007).

[27] T. Langen, S. Erne, R. Geiger, B. Rauer, T. Schweigler, M. Kuhnert, W. Rohringer, I. E. Mazets, T. Gasenzer and J. Schmiedmayer. "Experimental observation of a generalized Gibbs ensemble." *Science* **348**, 207–211 (2015).

[28] C. Gogolin and J. Eisert. "Equilibration, thermalisation, and the emergence of statistical mechanics in closed quantum systems." *Rept. Prog. Phys.* **79**, 056001 (2016).

[29] S. Braun, M. Friesdorf, S. S. Hodgman, M. Schreiber, J. P. Ronzheimer, A. Riera, M. del Rey, I. Bloch, J. Eisert and U. Schneider. "Emergence of coherence and the dynamics of quantum phase transitions." *PNAS* **112**, 3641–3646 (2015).

[30] E. Nicklas, M. Karl, M. Höfer, A. Johnson, W. Muessel, H. Strobel, J. Tomkovic, T. Gasenzer and M. K. Oberthaler. "Observation of scaling in the dynamics of a strongly quenched quantum gas." *Phys. Rev. Lett.* **115**, 245301 (2015).

[31] N. Navon, A. L. Gaunt, R. P. Smith and Z. Hadzibabic. "Critical dynamics of spontaneous symmetry breaking in a homogeneous Bose gas." *Science* **347**, 167–170 (2015).

[32] C. Eigen, J. A. P. Glidden, R. Lopes, E. A. Cornell, R. P. Smith and Z. Hadzibabic. "Universal Prethermal Dynamics of Bose Gases Quenched to Unitarity." *Nature* **563**, 221–224 (2018).

[33] B. Rauer, S. Erne, T. Schweigler, F. Cataldini, M. Tajik and J. Schmiedmayer. "Recurrences in an isolated quantum many-body system." *Science* **360**, 307–310 (2018).

[34] S. Sharma, S. Suzuki and A. Dutta. "Quenches and dynamical phase transitions in a non-integrable quantum Ising model." *Phys. Rev. B* **92**, 104306 (2015).

[35] S. Smale, P. He, B. A. Olsen, K. G. Jackson, H. Sharum, S. Trotzky, J. Marino, A. M. Rey and J. H. Thywissen. "Observation of a transition between dynamical phases in a quantum degenerate Fermi gas." *Sci. Adv.* **5**, eaax1568 (2019).

[36] J. Zhang, G. Pagano, P. W. Hess, A. Kyprianidis, P. Becker, H. Kaplan, A. V. Gorshkov, Z. .-. Gong and C. Monroe. "Observation of a many-body dynamical phase transition with a 53-qubit quantum simulator." *Nature* **551**, 601–604 (2017).

[37] M. Heyl. "Dynamical quantum phase transitions: A brief survey." *Europhys. Lett.* **125**, 26001 (2019).

[38] J. Marino, M. Eckstein, M. S. Foster and A. M. Rey. "Dynamical phase transitions in the collisionless pre-thermal states of isolated quantum systems: theory and experiments." *Rept. Prog. Phys.* **85**, 116001 (2022).

[39] M. Schreiber, S. S. Hodgman, P. Bordia, H. P. Lüschen, M. H. Fischer, R. Vosk, E. Altman, U. Schneider and I. Bloch. "Observation of many-body localization of interacting fermions in a quasirandom optical lattice." *Science* **349**, 842–845 (2015).

[40] R. Nandkishore and D. A. Huse. "Many-Body Localization and Thermalization in Quantum Statistical Mechanics." *Ann. Rev. Cond. Matt. Phys.* **6**, 15–38 (2015).

[41] R. Vasseur and J. E. Moore. "Nonequilibrium quantum dynamics and transport: from integrability to many-body localization." *J. Stat. Mech.: Theor. Exp.* **6**, 064010 (2016).

[42] F. Alet and N. Laflorencie. "Many-body localization: An introduction and selected topics." *C. R. Phys.* **19**, 498–525 (2018).

[43] D. A. Abanin, E. Altman, I. Bloch and M. Serbyn. "Colloquium: Many-body localization, thermalization, and entanglement." *Rev. Mod. Phys.* **91**, 021001 (2019).

[44] D. Schuricht. "Quantum quenches in integrable systems: Constraints from factorisation." *J. Stat. Mech.* **1511**, P11004 (2015).

[45] F. H. L. Essler and M. Fagotti. "Quench dynamics and relaxation in isolated integrable quantum spin chains." *J. Stat. Mech.: Theor. Exp.* **6**, 064002 (2016).

[46] M. A. Cazalilla and M.-C. Chung. "Quantum quenches in the Luttinger model and its close relatives." *J. Stat. Mech.: Theor. Exp.* **6**, 064004 (2016).

[47] V. E. Zakharov, V. S. L'Vov and G. Falkovich. "Kolmogorov spectra of turbulence I." Springer, (2012). ISBN: 978-3-031-82728-0.

[48] S. Nazarenko. "Wave Turbulence." Springer, (2011). ISBN: 978-3-642-15942-8.

[49] N. Navon, A. L. Gaunt, R. P. Smith and Z. Hadzibabic. "Emergence of a turbulent cascade in a quantum gas." *Nature* **539**, 72–75 (2016).

[50] N. Navon, C. Eigen, J. Zhang, R. Lopes, A. L. Gaunt, K. Fujimoto, M. Tsubota, R. P. Smith and Z. Hadzibabic. "Synthetic dissipation and cascade fluxes in a turbulent quantum gas." *Science* **366**, 382–385 (2019).

[51] E. A. L. Henn, J. A. Seman, G. Roati, K. M. F. Magalhães and V. S. Bagnato. "Emergence of Turbulence in an Oscillating Bose-Einstein Condensate." *Phys. Rev. Lett.* **103**, 045301 (2009).

[52] W. J. Kwon, G. Moon, J.-y. Choi, S. W. Seo and Y.-i. Shin. "Relaxation of superfluid turbulence in highly oblate Bose-Einstein condensates." *Phys. Rev. A* **90**, 063627 (2014).

[53] S. P. Johnstone, A. J. Groszek, P. T. Starkey, C. J. Billington, T. P. S. and K. Helmerson. "Evolution of large-scale flow from turbulence in a two-dimensional superfluid." *Science* **364**, 1267–1271 (2019).

[54] J. A. P. Glidden, C. Eigen, L. H. Dogra, T. A. Hilker, R. P. Smith and Z. Hadzibabic. "Bidirectional dynamic scaling in an isolated Bose gas far from equilibrium." *Nature Physics* **17**, 457–461 (2021).

[55] M. Prüfer, P. Kunkel, H. Strobel, S. Lannig, D. Linnemann, C.-M. Schmied, J. Berges, T. Gasenzer and M. K. Oberthaler. "Observation of universal dynamics in a spinor Bose gas far from equilibrium." *Nature* **563**, 217–220 (2018).

[56] S. Erne, R. Bücker, T. Gasenzer, J. Berges and J. Schmiedmayer. "Universal dynamics in an isolated one-dimensional Bose gas far from equilibrium." *Nature* **563**, 225–229 (2018).

[57] A. D. Garc´ia-Orozco, L. Madeira, M. A. Moreno-Armijos, A. R. Fritsch, P. E. S. Tavares, P. C. M. Castilho, A. Cidrim, G. Roati and V. S. Bagnato. "Universal dynamics of a turbulent superfluid Bose gas." *Phys. Rev. A* **106**, 023314 (2022).

[58] S. Huh, K. Mukherjee, K. Kwon, J. Seo, J. Hur, S. I. Mistakidis, H. R. Sadeghpour and J.-y. Choi. "Universality class of a spinor Bose–Einstein condensate far from equilibrium." *Nature Physics* **20**, 402–408 (2024).

[59] C.-M. Schmied, A. N. Mikheev and T. Gasenzer. "Prescaling in a Far-from-Equilibrium Bose Gas." *Phys. Rev. Lett.* **122**, 170404 (2019).

[60] A. Mazeliauskas and J. Berges. "Prescaling and far-from-equilibrium hydrodynamics in the quark-gluon plasma." *Phys. Rev. Lett.* **122**, 122301 (2019).

[61] A. N. Mikheev, A. Mazeliauskas and J. Berges. "Stability analysis of nonthermal fixed points in longitudinally expanding kinetic theory." *Phys. Rev. D* **105**, 116025 (2022).

[62] J. Brewer, B. Scheihing-Hitschfeld and Y. Yin. "Scaling and adiabaticity in a rapidly expanding gluon plasma." *JHEP* **05**, 145 (2022).

[63] J. Berges and G. Hoffmeister. "Nonthermal fixed points and the functional renormalization group." *Nuclear Physics B* **813**, 383–407 (2009).

[64] T. Kodama, H. T. Elze, C. E. Aguiar and T. Koide. "Prethermalization and the effects of dynamical correlations." *Europhys. Lett.* **70**, 439 (2005).

[65] B. Nowak, J. Schole and T. Gasenzer. "Universal dynamics on the way to thermalization." *New Journal of Physics* **16**, 093052 (2014).

[66] J. Hofmann, S. S. Natu and S. Das Sarma. "Coarsening Dynamics of Binary Bose Condensates." *Phys. Rev. Lett.* **113**, 095702 (2014).

[67] A. Maraga, A. Chiocchetta, A. Mitra and A. Gambassi. "Aging and coarsening in isolated quantum systems after a quench: Exact results for the quantum O(N) model with $N \to \infty$." *Phys. Rev. E* **92**, 042151 (2015).

[68] L. A. Williamson and P. B. Blakie. "Universal Coarsening Dynamics of a Quenched Ferromagnetic Spin-1 Condensate." *Phys. Rev. Lett.* **116**, 025301 (2016).

[69] L. A. Williamson and P. B. Blakie. "Coarsening and thermalization properties of a quenched ferromagnetic spin-1 condensate." *Phys. Rev. A* **94**, 023608 (2016).

[70] A. Schachner, A. Piñeiro Orioli and J. Berges. "Universal scaling of unequal-time correlation functions in ultracold Bose gases far from equilibrium." *Phys. Rev. A* **95**, 053605 (2017).

[71] R. Walz, K. Boguslavski and J. Berges. "Large-N kinetic theory for highly occupied systems." *Phys. Rev. D* **97**, 116011 (2018).

[72] M. Karl and T. Gasenzer. "Strongly anomalous non-thermal fixed point in a quenched two-dimensional Bose gas." *New Journal of Physics* **19**, 093014 (2017).

[73] A. Chiocchetta, A. Gambassi, S. Diehl and J. Marino. "Universal short-time dynamics: Boundary functional renormalization group for a temperature quench." *Phys. Rev. B* **94**, 174301 (2016).

[74] A. Bourges and P. B. Blakie. "Different growth rates for spin and superfluid order in a quenched spinor condensate." *Phys. Rev. A* **95**, 023616 (2017).

[75] C.-M. Schmied, M. Prüfer, M. K. Oberthaler and T. Gasenzer. "Bidirectional universal dynamics in a spinor Bose gas close to a nonthermal fixed point." *Phys. Rev.A* **99** (2019).

[76] L. A. Williamson and P. B. Blakie. "Anomalous phase ordering of a quenched ferromagnetic superfluid." *SciPost Physics* **7**, 029 (2019).

[77] C.-M. Schmied, T. Gasenzer and P. B. Blakie. "Violation of single-length-scaling dynamics via spin vortices in an isolated spin-1 Bose gas." *Phys. Rev. A* **100**, 033603 (2019).

[78] D. Spitz, J. Berges, M. K. Oberthaler and A. Wienhard. "Finding self-similar behavior in quantum many-body dynamics via persistent homology." *SciPost Physics* **11**, 060 (2021).

[79] C. Gao, M. Sun, P. Zhang and H. Zhai. "Universal Dynamics of a Degenerate Bose Gas Quenched to Unitarity." *Phys. Rev. Lett.* **124**, 040403 (2020).

[80] M. T. Wheeler, H. Salman and M. O. Borgh. "Relaxation dynamics of half-quantum vortices in a two-dimensional two-component Bose-Einstein condensate." *EPL* **135**, 30004 (2021).

[81] L. Gresista, T. V. Zache and J. Berges. "Dimensional crossover for universal scaling far from equilibrium." *Phys. Rev. A* **105**, 013320 (2022).

[82] J. F. Rodriguez-Nieva, A. Piñeiro Orioli and J. Marino. "Universal prethermal dynamics and self-similar relaxation in the two-dimensional Heisenberg model." *PNAS* **119**, e2122599119 (2022).

[83] T. Preis, M. P. Heller and J. Berges. "Stable and Unstable Perturbations in Universal Scaling Phenomena Far from Equilibrium." *Phys. Rev. Lett.* **130**, 031602 (2023).

[84] P. Heinen, A. N. Mikheev, C.-M. Schmied and T. Gasenzer. "Non-thermal fixed points of universal sine-Gordon coarsening dynamics." (2022). arXiv: 2212.01162 [cond-mat.quant-gas].

[85] P. Heinen, A. N. Mikheev and T. Gasenzer. "Anomalous scaling at nonthermal fixed points of the sine-Gordon model." *Phys. Rev. A* **107**, 043303 (2023).

[86] V. Noel and D. Spitz. "Detecting defect dynamics in relativistic field theories far from equilibrium using topological data analysis." *Phys. Rev. D* **109** (2024).

[87] V. Noel, T. Gasenzer and K. Boguslavski. "Kelvin waves in nonequilibrium universal dynamics of relativistic scalar field theories." *Phys. Rev. Res.*, – (2025).

[88] R. Barnett, A. Polkovnikov and M. Vengalattore. "Prethermalization in quenched spinor condensates." *Phys. Rev. A* **84**, 023606 (2011).

[89] M. Marcuzzi, J. Marino, A. Gambassi and A. Silva. "Prethermalization in a Nonintegrable Quantum Spin Chain after a Quench." *Phys. Rev. Lett.* **111**, 197203 (2013).

[90] T. Langen, M. Gring, M. Kuhnert, B. Rauer, R. Geiger, D. A. Smith, I. E. Mazets and J. Schmiedmayer. "Prethermalization in one-dimensional Bose gases: Description by a stochastic Ornstein-Uhlenbeck process." *Eur. Phys. J. ST* **217**, 43–53 (2013).

[91] N. Nessi, A. Iucci and M. A. Cazalilla. "Quantum Quench and Prethermalization Dynamics in a Two-Dimensional Fermi Gas with Long-Range Interactions." *Phys. Rev. Lett.* **113**, 210402 (2014).

[92] P. Gagel, P. P. Orth and J. Schmalian. "Universal Postquench Prethermalization at a Quantum Critical Point." *Phys. Rev. Lett.* **113**, 220401 (2014).

[93] B. Bertini, F. H. L. Essler, S. Groha and N. J. Robinson. "Prethermalization and Thermalization in Models with Weak Integrability Breaking." *Phys. Rev. Lett.* **115**, 180601 (2015).

[94] M. Babadi, E. Demler and M. Knap. "Far-from-Equilibrium Field Theory of Many-Body Quantum Spin Systems: Prethermalization and Relaxation of Spin Spiral States in Three Dimensions." *Phys. Rev. X* **5**, 041005 (2015).

[95] M. Buchhold, M. Heyl and S. Diehl. "Prethermalization and thermalization of a quenched interacting Luttinger liquid." *Phys. Rev. A* **94**, 013601 (2016).

[96] N. Rasch, L. Chomaz and T. Gasenzer. "Anomalous non-thermal fixed point in a quasi-two-dimensional dipolar Bose gas." (2025). arXiv: 2506.01653 [cond-mat.quant-gas].

[97] G. Gauthier, M. T. Reeves, X. Yu, A. S. Bradley, M. A. Baker, T. A. Bell, H. Rubinsztein-Dunlop, M. J. Davis and T. W. Neely. "Giant vortex clusters in a two-dimensional quantum fluid." *Science* **364**, 1264–1267 (2019).

[98] D. A. Smith, M. Gring, T. Langen, M. Kuhnert, B. Rauer, R. Geiger, T. Kitagawa, I. Mazets, E. Demler and J. Schmiedmayer. "Prethermalization revealed by the relaxation dynamics of full distribution functions." *New J. Phys.* **15**, 075011 (2013).

[99] G. Martirosyan, C. J. Ho, J. Etrych, Y. Zhang, A. Cao, Z. Hadzibabic and C. Eigen. "Observation of Subdiffusive Dynamic Scaling in a Driven and Disordered Bose Gas." *Phys. Rev. Lett.* **132**, 113401 (2024).

[100] M. Gazo, A. Karailiev, T. Satoor, C. Eigen, M. Gałka and Z. Hadzibabic. "Universal Coarsening in a Homogeneous Two-Dimensional Bose Gas." (2024). arXiv: 2312.09248 [cond-mat.quant-gas].

[101] G. Martirosyan, M. Gazo, J. Etrych, S. M. Fischer, S. J. Morris, C. J. Ho, C. Eigen and Z. Hadzibabic. "A universal speed limit for spreading of quantum coherence." (2024). arXiv: 2410.08204 [cond-mat.quant-gas].

[102] E. N. and. "Invariant variation problems." *Transport Theory and Statistical Physics* **1**, 186–207 (1971).

[103] J. C. Ward. "An identity in quantum electrodynamics." *Physical Review* **78**, 182 (1950).

[104] A. A. Slavnov. "Ward identities in gauge theories." *Theor. Math. Phys.* **10**, 99–104 (1972).

[105] J. Taylor. "Ward identities and charge renormalization of the Yang-Mills field." *Nucl. Phys. B* **33**, 436–444 (1971).

[106] A. N. Mikheev, C.-M. Schmied and T. Gasenzer. "Low-energy effective theory of non-thermal fixed points in a multicomponent Bose gas." *Phys. Rev.A* **99** (2019).

[107] A. B. and. "Theory of phase-ordering kinetics." *Advances in Physics* **43**, 357–459 (1994).

[108] L. M. Sieberer, S. D. Huber, E. Altman and S. Diehl. "Dynamical Critical Phenomena in Driven-Dissipative Systems." *Phys. Rev. Lett.* **110**, 195301 (2013).

[109] T. Gasenzer and J. M. Pawlowski. "Towards far-from-equilibrium quantum field dynamics: A functional renormalisation-group approach." *Physics Letters B* **670**, 135–140 (2008).

[110] T. Gasenzer, S. Keßler and J. M. Pawlowski. "Far-from-equilibrium quantum many-body dynamics." *The European Physical Journal C* **70**, 423–443 (2010).

[111] J. Berges and D. Mesterházy. "Introduction to the nonequilibrium functional renormalization group." *Nuclear Physics B - Proceedings Supplements* **228**, 37–60 (2012).

[112] S. Mathey, T. Gasenzer and J. M. Pawlowski. "Anomalous scaling at nonthermal fixed points of Burgers' and Gross-Pitaevskii turbulence." *Phys. Rev.A* **92** (2015).

[113] L. Corell, A. K. Cyrol, M. Heller and J. M. Pawlowski. "Flowing with the temporal renormalization group." *Phys. Rev.D* **104** (2021).

[114] K. G. Wilson. "Renormalization Group and Critical Phenomena. I. Renormalization Group and the Kadanoff Scaling Picture." *Phys. Rev. B* **4**, 3174–3183 (1971).

[115] K. G. Wilson. "Renormalization Group and Critical Phenomena. II. Phase-Space Cell Analysis of Critical Behavior." *Phys. Rev. B* **4**, 3184–3205 (1971).

[116] V. Noel. "Far-from-equilibrium universality and dynamics of nonequilibrium quantum many-body systems." PhD thesis. Heidelberg University. (2025).

[117] P. Kopietz, F. Schutz and B. Lorenz. "Introduction to the functional renormalization group." Springer, (2010). ISBN: 978-3-642-26325-5.

[118] N. Goldenfeld. "Lectures on phase transitions and the renormalization group." CRC Press, (2019). ISBN: 9780429493492.

[119] I. Chantesana, A. P. Orioli and T. Gasenzer. "Kinetic theory of nonthermal fixed points in a Bose gas." *Phys. Rev.A* **99** (2019).

[120] A. Piñeiro Orioli, K. Boguslavski and J. Berges. "Universal self-similar dynamics of relativistic and nonrelativistic field theories near nonthermal fixed points." *Phys. Rev.D* **92** (2015).

[121] M. Karl, B. Nowak and T. Gasenzer. "Universal scaling at nonthermal fixed points of a two-component Bose gas." *Phys. Rev.A* **88** (2013).

[122] M. Karl, B. Nowak and T. Gasenzer. "Tuning universality far from equilibrium." *Scientific Reports* **3** (2013).

[123] L. P. Kadanoff and G. A. Baym. "Quantum statistical mechanics." Benjamin, (1962). ISBN: 978-0201410464.

[124] M. Alford, J. Berges and J. M. Cheyne. "Critical phenomena from the two-particle irreducible $1/N$ expansion." *Phys. Rev. D* **70**, 125002 (2004).

[125] A. N. Mikheev. "Far-from-equilibrium universal scaling dynamics in ultracold atomic systems and heavy-ion collisions." PhD thesis. Heidelberg University. (2023).

[126] Y. Kawaguchi and M. Ueda. "Spinor Bose–Einstein condensates." *Physics Reports* **520**, 253–381 (2012).

[127] D. M. Stamper-Kurn and M. Ueda. "Spinor Bose gases: Symmetries, magnetism, and quantum dynamics." *Rev. Mod. Phys.* **85**, 1191–1244 (2013).

[128] J. Berges and T. Gasenzer. "Quantum versus classical statistical dynamics of an ultracold Bose gas." *Phys. Rev. A* **76**, 033604 (2007).

[129] S. Uchino. "Spinor Bose gas in an elongated trap." *Phys. Rev. A* **91**, 033605 (2015).

[130] S. Lannig. "Vector Solitons and Different Scenarios of Universal Dynamics in a Spin-1 Bose-Einstein Condensate." PhD thesis. Heidelberg University. (2022).

[131] P. Kunkel. "Splitting a Bose Einstein condensate enables EPR steering and simultaneous readout of noncommuting observables." PhD thesis. Heidelberg University. (2019).

[132] C. D. Hamley, C. Gerving, T. M. Hoang, E. M. Bookjans and M. S. Chapman. "Spin-nematic squeezed vacuum in a quantum gas." *Nature Physics* **8**, 305–308 (2012).

[133] N. Manton and P. Sutcliffe. "Solitons — general theory." Cambridge University Press, (2004). ISBN: 9780511617034.

[134] F. Lenz. "Topological Concepts in Gauge Theories." (2005). ISBN: 978-3-540-31532-2.

[135] C. Wetterich. "Time Evolution of Nonequilibrium Effective Action." *Phys. Rev. Lett.* **78**, 3598–3601 (1997).

[136] R. Ott, T. V. Zache and J. Berges. "Equal-time approach to real-time dynamics of quantum fields." (2022). arXiv: 2204.06463 [cond-mat.quant-gas].

[137] W. Bao and Y. Zhang. "Dynamical Laws of the Coupled Gross-Pitaevskii Equations for Spin-1 Bose-Einstein Condensates." *Methods and Applications of Analysis* **17**, 49–80 (2010).

[138] G. R. Dennis, J. J. Hope and M. T. Johnsson. "XMDS2: Fast, scalable simulation of coupled stochastic partial differential equations." *Computer Physics Communications* **184**, 201–208 (2013).

[139] A. Polkovnikov. "Phase space representation of quantum dynamics." *Annals Phys.* **325**, 1790–1852 (2010).

[140] C.-M. Schmied. "Universal scaling dynamics at non-thermal fixed points in multi-component Bose gases far from equilibrium." PhD thesis. Heidelberg University. (2020).

[141] NVIDIA Corporation. "High Performance Computing (HPC)." Tech. rep. (2025).

[142] G. E. Moore. "Cramming More Components onto Integrated Circuits." *Electronics* **38**, 114–117 (1965).

[143] M. M. Waldrop. "The Chips Are Down for Moore's Law." *Nature* **530**, 144–147 (2016).

[144] NVIDIA Corporation. "NVIDIA Ampere Architecture Whitepaper." Tech. rep. (2020).

[145] P. Kunkel, M. Prüfer, S. Lannig, R. Rosa-Medina, A. Bonnin, M. Gärttner, H. Strobel and M. K. Oberthaler. "Simultaneous Readout of Noncommuting Collective Spin Observables beyond the Standard Quantum Limit." *Phys. Rev. Lett.* **123**, 063603 (2019).

[146] T. P. Billam, K. Brown and I. G. Moss. "False-vacuum decay in an ultracold spin-1 Bose gas." *Phys. Rev. A* **105**, L041301 (2022).

[147] A. C. Jenkins, J. Braden, H. V. Peiris, A. Pontzen, M. C. Johnson and S. Weinfurtner. "Analog vacuum decay from vacuum initial conditions." *Phys. Rev. D* **109**, 023506 (2024).

[148] J. Braden, M. C. Johnson, H. V. Peiris and S. Weinfurtner. "Towards the cold atom analog false vacuum." *Journal of High Energy Physics* **2018**, 14 (2018).

[149] S. Samuel. "Grand partition function in field theory with applications to sine-Gordon field theory." *Phys. Rev. D* **18**, 1916–1932 (1978).

[150] I. Affleck and M. Oshikawa. "Field-induced gap in Cu benzoate and other $S = \frac{1}{2}$ antiferromagnetic chains." *Phys. Rev. B* **60**, 1038–1056 (1999).

[151] E. Wybo, A. Bastianello, M. Aidelsburger, I. Bloch and M. Knap. "Preparing and Analyzing Solitons in the Sine-Gordon Model with Quantum Gas Microscopes." *PRX Quantum* **4**, 030308 (2023).

[152] L. Kaplan. "Statistics of Branched Flow in a Weak Correlated Random Potential." *Phys. Rev. Lett.* **89**, 184103 (2002).

[153] J. J. Metzger, R. Fleischmann and T. Geisel. "Universal Statistics of Branched Flows." *Phys. Rev. Lett.* **105**, 020601 (2010).

[154] J. J. Metzger, R. Fleischmann and T. Geisel. "Intensity Fluctuations of Waves in Random Media: What Is the Semiclassical Limit?" *Phys. Rev. Lett.* **111**, 013901 (2013).

[155] J. J. Metzger, R. Fleischmann and T. Geisel. "Statistics of Extreme Waves in Random Media." *Phys. Rev. Lett.* **112**, 203903 (2014).

[156] H. Degueldre, J. J. Metzger, T. Geisel and R. Fleischmann. "Random focusing of tsunami waves." *Nature Physics* **12**, 259–262 (2016).

[157] J. Mumford, W. Kirkby and D. H. J. O'Dell. "Catastrophes in non-equilibrium many-particle wave functions: universality and critical scaling." *Journal of Physics B: Atomic, Molecular and Optical Physics* **50**, 044005 (2017).

[158] W. Kirkby, J. Mumford and D. H. J. O'Dell. "Quantum caustics and the hierarchy of light cones in quenched spin chains." *Phys. Rev. Res.* **1**, 033135 (2019).

[159] W. Kirkby, Y. Yee, K. Shi and D. H. J. O'Dell. "Caustics in quantum many-body dynamics." *Phys. Rev. Res.* **4**, 013105 (2022).

[160] L. H. Ying and L. Kaplan. "Systematic study of rogue wave probability distributions in a fourth-order nonlinear Schrödinger equation." *Journal of Geophysical Research: Oceans* **117** (2012).

[161] M. Onorato, S. Residori, U. Bortolozzo, A. Montina and F. Arecchi. "Rogue waves and their generating mechanisms in different physical contexts." *Physics Reports* **528**, 47–89 (2013).

[162] G. Green and R. Fleischmann. "Branched flow and caustics in nonlinear waves." *New Journal of Physics* **21**, 083020 (2019).

[163] A. Safari, R. Fickler, M. J. Padgett and R. W. Boyd. "Generation of Caustics and Rogue Waves from Nonlinear Instability." *Phys. Rev. Lett.* **119**, 203901 (2017).

[164] A. Mathis, L. Froehly, S. Toenger, F. Dias, G. Genty and J. M. Dudley. "Caustics and Rogue Waves in an Optical Sea." *Scientific Reports* **5**, 12822 (2015).

[165] J. M. Dudley, F. Dias, M. Erkintalo and G. Genty. "Instabilities, breathers and rogue waves in optics." *Nature Photonics* **8**, 755–764 (2014).

[166] N. Seiberg and E. Witten. "Electric-magnetic duality, monopole condensation, and confinement in N=2 supersymmetric Yang-Mills theory." *Nuclear Physics B* **426**, 19–52 (1994).

[167] N. Seiberg and E. Witten. "Monopoles, duality and chiral symmetry breaking in N = 2 supersymmetric QCD." *Nuclear Physics B* **431**, 484–550 (1994).

[168] S. W. Hawking, I. G. Moss and J. M. Stewart. "Bubble collisions in the very early universe." *Phys. Rev. D* **26**, 2681–2693 (1982).

[169] J. Braden, J. R. Bond and L. Mersini-Houghton. "Cosmic bubble and domain wall instabilities I: parametric amplification of linear fluctuations." *Journal of Cosmology and Astroparticle Physics* **2015**, 007 (2015).

[170] J. R. Bond, J. Braden and L. Mersini-Houghton. "Cosmic bubble and domain wall instabilities III: the role of oscillons in three-dimensional bubble collisions." *Journal of Cosmology and Astroparticle Physics* **2015**, 004 (2015).

[171] T. P. Simula and D. M. Paganin. "Coherence vortices in one spatial dimension." *Phys. Rev. A* **84**, 052104 (2011).

[172] H. P. Büchler, V. B. Geshkenbein and G. Blatter. "Transport in a One-Dimensional Superfluid: Quantum Nucleation of Phase Slips." (1999). arXiv: cond-mat/9911301 [cond-mat.mes-hall].

[173] I. Danshita and A. Polkovnikov. "Quantum phase slips in one-dimensional superfluids in a periodic potential." *Phys. Rev. A* **85**, 023638 (2012).

[174] I. Danshita. "Universal Damping Behavior of Dipole Oscillations of One-Dimensional Ultracold Gases Induced by Quantum Phase Slips." *Phys. Rev. Lett.* **111**, 025303 (2013).

[175] C. D'Errico, S. S. Abbate and G. Modugno. "Quantum phase slips: from condensed matter to ultracold quantum gases." *Phil. Trans. Act. Roy. Soc. A: Math. Phys. Eng. Sci.* **375**, 20160425 (2017).

[176] J. Polo, R. Dubessy, P. Pedri, H. Perrin and A. Minguzzi. "Oscillations and Decay of Superfluid Currents in a One-Dimensional Bose Gas on a Ring." *Phys. Rev. Lett.* **123**, 195301 (2019).

[177] J. Berges. "Nonequilibrium Quantum Fields: From Cold Atoms to Cosmology." (2015). arXiv: 1503.02907 [hep-ph].

[178] H. Köper. "Approximations to the two-particle irreducible quantum effective action." Master's thesis. Heidelberg University. (2023).

[179] V. Gritsev, A. Polkovnikov and E. Demler. "Linear response theory for a pair of coupled one-dimensional condensates of interacting atoms." *Phys. Rev. B* **75**, 174511 (2007).

[180] S. Coleman. "Quantum sine-Gordon equation as the massive Thirring model." *Phys. Rev. D* **11**, 2088–2097 (1975).

[181] J. Kosterlitz and D. Thouless. "Ordering, metastability and phase transitions in two-dimensional systems." *J. Phys. C: Sol. St. Phys.* **6**, 1181 (1973).

[182] D. Amit, Y. Goldschmidt and S. Grinstein. "Renormalisation group analysis of the phase transition in the 2D Coulomb gas, Sine-Gordon theory and XY-model." *J. Phys. A: Mathematical and General* **13**, 585 (1980).

[183] T. Giamarchi. "Quantum Physics in One Dimension." Oxford University Press, (2003). ISBN: 9780198525004.

[184] M. A. Cazalilla, R. Citro, T. Giamarchi, E. Orignac and M. Rigol. "One dimensional bosons: From condensed matter systems to ultracold gases." *Rev. Mod. Phys.* **83**, 1405–1466 (2011).

[185] P. D. Lax. "Integrals of nonlinear equations of evolution and solitary waves." *Communications on Pure and Applied Mathematics* **21**, 467–490 (1968).

[186] M. Prüfer, D. Spitz, S. Lannig, H. Strobel, J. Berges and M. K. Oberthaler. "Condensation and thermalization of an easy-plane ferromagnet in a spinor Bose gas." *Nature Physics* **18**, 1459–1463 (2022).

[187] J. Schole, B. Nowak and T. Gasenzer. "Critical Dynamics of a Two-dimensional Superfluid near a Non-Thermal Fixed Point." *Phys. Rev. A* **86**, 013624 (2012).

[188] J. V. José, L. P. Kadanoff, S. Kirkpatrick and D. R. Nelson. "Renormalization, vortices, and symmetry-breaking perturbations in the two-dimensional planar model." *Phys. Rev. B* **16**, 1217–1241 (1977).

[189] X. Yu and P. B. Blakie. "Dark-soliton-like magnetic domain walls in a two-dimensional ferromagnetic superfluid." *Phys. Rev. Res.* **3**, 023043 (2021).

[190] D. K. Campbell, M. Peyrard and P. Sodano. "Kink-antikink interactions in the double sine-Gordon equation." *Physica D: Nonlinear Phenomena* **19**, 165–205 (1986).

[191] S. V. Dmitriev, P. G. Kevrekidis and Y. S. Kivshar. "Radiationless energy exchange in three-soliton collisions." *Phys. Rev. E* **78**, 046604 (2008).

[192] I. Bloch, J. Dalibard and S. Nascimbene. "Quantum simulations with ultracold quantum gases." *Nature Physics* **8**, 267–276 (2012).

[193] C. Gross and I. Bloch. "Quantum simulations with ultracold atoms in optical lattices." *Science* **357**, 995–1001 (2017).

[194] A. J. Beekman, L. Rademaker and J. van Wezel. "An Introduction to Spontaneous Symmetry Breaking." *SciPost Phys. Lect. Notes* **11**, 1 (2019).

[195] E. P. Wigner. "Group Theory and its Application to the Quantum Mechanics of Atomic Spectra." Academic Press, (1959). ISBN: 9780127505503.

[196] G. Chiribella, E. Aurell and K. Życzkowski. "Symmetries of quantum evolutions." *Phys. Rev. Res.* **3**, 033028 (2021).

[197] J. Eisert, M. Friesdorf and C. Gogolin. "Quantum many-body systems out of equilibrium." *Nature Phys.* **11**, 124 (2015).

[198] M. Prüfer, T. V. Zache, P. Kunkel, S. Lannig, A. Bonnin, H. Strobel, J. Berges and M. K. Oberthaler. "Experimental extraction of the quantum effective action for a non-equilibrium many-body system." *Nature Phys.* **16**, 1012–1016 (2020).

[199] M. Prüfer, D. Spitz, S. Lannig, H. Strobel, J. Berges and M. K. Oberthaler. "Condensation and thermalization of an easy-plane ferromagnet in a spinor Bose gas." *Nature Phys.* **18**, 1459–1463 (2022).

[200] Y. Takahashi. "On the generalized Ward identity." *Nuovo Cim.* **6**, 371–375 (1957).

[201] F. Ares, S. Murciano and P. Calabrese. "Entanglement asymmetry as a probe of symmetry breaking." *Nature Communications.* **14**, 2036 (2023).

[202] F. Ares, S. Murciano, L. Piroli and P. Calabrese. "Entanglement asymmetry study of black hole radiation." *Phys. Rev. D* **110**, L061901 (2024).

[203] B. Bertini, K. Klobas, M. Collura, P. Calabrese and C. Rylands. "Dynamics of charge fluctuations from asymmetric initial states." *Phys. Rev. B* **109**, 184312 (2024).

[204] L. Capizzi and V. Vitale. "A universal formula for the entanglement asymmetry of matrix product states." arXiv: 2310.01962 [quant-ph].

[205] F. Ares, S. Murciano, E. Vernier and P. Calabrese. "Lack of symmetry restoration after a quantum quench: An entanglement asymmetry study." *SciPost Phys.* **15**, 089 (2023).

[206] F. Ferro, F. Ares and P. Calabrese. "Non-equilibrium entanglement asymmetry for discrete groups: the example of the XY spin chain." *J. Stat. Mech.* **2402**, 023101 (2024).

[207] S. Yamashika, F. Ares and P. Calabrese. "Time evolution of entanglement entropy after quenches in two-dimensional free fermion systems: A dimensional reduction treatment." *Phys. Rev. B* **109**, 125122 (2024).

[208] S. Liu, H.-K. Zhang, S. Yin and S.-X. Zhang. "Symmetry Restoration and Quantum Mpemba Effect in Symmetric Random Circuits." *Phys. Rev. Lett.* **133**, 140405 (2024).

[209] D. J. Strachan, A. Purkayastha and S. R. Clark. "Non-Markovian Quantum Mpemba effect." arXiv: 2402.05756 [quant-ph].

[210] L. K. Joshi et al. "Observing the Quantum Mpemba Effect in Quantum Simulations." *Phys. Rev. Lett.* **133**, 010402 (2024).

[211] J. Zhang et al. "Observation of quantum strong Mpemba effect." arXiv: 2401.15951 [quant-ph].

[212] S. Aharony Shapira, Y. Shapira, J. Markov, G. Teza, N. Akerman, O. Raz and R. Ozeri. "Inverse Mpemba Effect Demonstrated on a Single Trapped Ion Qubit." *Phys. Rev. Lett.* **133**, 010403 (2024).

[213] M. A. Amin, M. P. Hertzberg, D. I. Kaiser and J. Karouby. "Nonperturbative Dynamics Of Reheating After Inflation: A Review." *Int. J. Mod. Phys. D* **24**, 1530003 (2014).

[214] I. Siovitz. "Topological Excitations and Universal Scaling of the One-Dimensional Spin-1 Bose-Einstein Condensate Far from Equilibrium." Master's thesis. Heidelberg University. (2022).

[215] X. Yu and P. B. Blakie. "Propagating Ferrodark Solitons in a Superfluid: Exact Solutions and Anomalous Dynamics." *Phys. Rev. Lett.* **128** (2022).

[216] L. Heck. "Sine-Gordon Universal Scaling Dynamics in a Quasi-One-Dimensional Spin-1 Bose Gas." Bachelor's thesis. Heidelberg University. (2025).

[217] I. V. Barashenkov and O. F. Oxtoby. "Wobbling kinks in ϕ^4 theory." *Phys. Rev. E* **80**, 026608 (2009).

[218] K. Domino, P. Gawron and Ł. Pawela. "Efficient computation of higher order cumulant tensors." *SIAM J. Sci. Comput.* **40**, A1590–A1610 (2018).

STATEMENT ON AI USAGE

AI tools (ChatGPT) have been used to restructure individual sentences, whilst the changes were done manually and selectively. ChatGPT was used for help in identifying bugs in the simulation code and generating some code snippets for the figures done with the Mayavi python package. It was not used in writing code for simulations nor data analysis.

ACKNOWLEDGMENTS

What I need... is a strong drink and a peer group.

— Douglas Adams, Life, the Universe and Everything

At this point, I would like to thank everyone who had supported me during the tumultuous times known as doctoral studies. This thesis is the culmination of my nine years physics studies here in Heidelberg university, all into a single work. I would like to take the time to thank the people that made this possible along my entire journey.

First and foremost, I would like to thank Thomas Gasenzer. The gratitude is extended two-fold: first, for allowing me to conduct my research on this challenging yet fascinating field of research. Thomas, you have given me immense support, spent hours of fascinating discussions about our mutual research and shown incredible patience. Your knowledge of the current and former state of research along with an enthusiastic approach combined with deep physical intuition are the backbone of my research. Second, on a more personal note, your approach for supervising and teaching in general is inspiring. At all times, I have felt appreciated and taken seriously, and saw how much you care for the group members' and your students' wellbeing.

Secondly, my sincere thanks go to Markus K. Oberthaler for the opportunity to collaborate with the labs under his supervision. The opportunity to be able to see theories I have developed being given a reality via experiment was deeply fulfilling. I thank you for long discussions, which helped me achieve a better quality of research, showing me different angles which I would not have considered otherwise. On a more personal note, I admire the spirit and enthusiasm for combining fascinating research with the human element of making sure everyone in the group feels comfortable and has fun while working here.

I would also like to thank Tilman Enss for kindly agreeing to be the second referee for this thesis.

I would like to express my deepest gratitude to my colleagues in the Gasenzer and Oberthaler groups. Dear Matterwavers, you made every day in the office a joy. I knew I made the right decision to join the group the day I noticed how much I enjoy coming to work, where I could laugh with you in incredibly long lunch breaks, discuss my research with you in even longer meetings, and still somehow wanted to spend time with you after work. I would like to thank you all for the incredible activities beyond work, from grill parties at the evening, to just a calm unwinding at the end of a work day. You all are a very special group of people that somehow all got together to form an incredible work environment. I would like to especially thank the members of the BEC

lab with whom I closely collaborated for my entire doctoral studies. Yannick, Stefan, Alex S., David, Luise, Raphael, Alex F. and Helmut. Each and every time I walked through your office door, I knew I would get new perspectives on my research and a good laugh whilst doing so.

I would like to thank current and former members of the Gasenzer group: Philipp, Aleksandr, Niklas, Hannes, Andreea, Florian, Anna-Maria G. and Martin. I'm especially thankful to Niklas and Hannes, with whom I shared an office for most of my time in the group. Thank you for the countless hours of physics discussions and hilarious distractions. Thank you for being not just colleagues, but also good friends. Andreea, I would like to thank you for many things, mainly for deciding to do your doctorate in our group, thereby enriching our lives with your presence, sharp humour and incredibly caring character. I would also like to express my gratitude to Victoria, with whom I collaborated in Chap. 6. Thank you for motivating discussions about physics, anime and your fundamental disapproval of my color schemes.

I would also like to thank the bachelor students I have supervised during my doctoral studies: Mai, Yvette, Anna-Maria L., Jasmin and Luisa. Supervising you was incredibly enriching, on a personal and professional level. Your ideas and approaches have helped me become a better researcher.

I extend my deepest thanks to my friends which have been with me since (almost) day one of my studies here in Heidelberg. First, my wonderful DnD group: Samantha, Michelle, (Dr.!) Sophia and (Dr.!) Jenny. Thank you for many many many hilarious, surreal days and evenings of fantastical story telling, weird plot twists and funny dice rolls. Thank you for your continued support, genuine care and fulfilling friendship. Louis and Finn, my trusty friends, from the first day of the mathematischer Vorkurs at the very beginning of our academic journey, your humour, wit and physical knowledge have carried me through the ups and downs of physics studies.

I would like to thank my parents back home for their unwavering support of my endeavours, even from afar. Your continuous support through my studies and doctoral studies was an island of solace in these times. There have been very difficult times for us during the last two years of this thesis, but together, we overcame them.

Last, but absolutely not least, I owe special thanks to my family here: My incredible wife Luci and, of course, my daughter Nele Lior, who was born during the writing of this thesis. Luci, there's a lot to say about your support and presence in my life. You are an anchor, my rock and my partner in crime. Whether needing a soft supporting shoulder or to laugh until my stomach hurts, I can always count on you to do the right thing and be there. I am incredibly happy to call you my wife and to have the privilege of raising our wonderful daughter Nele together with you.

Nele, if at some point of your life you would read this thesis for whatever reason, let me tell you what a huge source of light you are in my life. You are true to your name, Lior.